LA-7328-PR
Progress Report

Laser Fusion Program

July 1—December 31, 1977

University of California

LOS ALAMOS SCIENTIFIC LABORATORY
Post Office Box 1663 Los Alamos, New Mexico 87545

The four most recent reports in this series, unclassified, are LA-6510-PR, LA-6616-PR, LA-6834-PR, and LA-6982-PR.

This work was supported by the US Department of Energy, Office of Laser Fusion.

UNITED STATES
DEPARTMENT OF ENERGY
CONTRACT W-7405-ENG. 36

LA-7328-PR
Progress Report
UC-21
Issued: December 1978

Laser Fusion Program at LASL

July 1—December 31, 1977

Compiled by
Frederick Skoberne

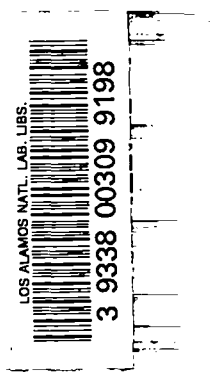

CONTENTS

LASER FUSION PROGRAM AT LASL
JULY 1—DECEMBER 31, 1977

Compiled by

Frederick Skoberne

ABSTRACT

Progress in the development of high-energy short-pulse CO_2 laser systems for fusion research is reported. Among the achievements discussed are an increase in on-target energy of the Two-Beam System to 375 J per beam; operation of one Eight-Beam System module at the design point of 1.2 kJ at a power of > 2 TW; and the on-schedule development of our 100- to 200-TW laser Antares. Technology and research efforts are summarized, which led to the incorporation of an effective broadband isolater in both the Two-Beam System and the Eight-Beam System.

Target designs based on the LASNEX code incorporating new theoretical insights are described, culminating in a double-shell exploding-pusher target that attains a high degree of symmetry through hot-electron transport in an exploding outer shell. Significant improvements in the fabrication and inspection of targets are reported, as well as advances in the development of promising new materials such as low-density, small-cell plastic foams and ammonia borane, which was formed successfully into microballoons for the first time.

Studies of laser light absorption are outlined, which confirmed that the values for CO_2 are nearly identical to those obtained with Nd:glass lasers, and that ion loss is not a severe concern for laser fusion application as had been feared earlier.

Unique diagnostics are described, which allow us to measure properties of x-ray emission not previously accessible, and which provide absorption data of sufficient accuracy for direct comparison with theory. Finally, various feasibility and systems studies are summarized, such as the successful modeling of short-pulse amplification in large three-pass CO_2 laser amplifiers, as verified experimentally.

SUMMARY

(R. B. Perkins and Laser Fusion Staff)

INTRODUCTION

The Laser Fusion Program at the Los Alamos Scientific Laboratory (LASL) is pursuing the dual goal of investigating military and commercial applications of inertial confinement fusion. For both goals it is essential to achieve scientific breakeven, that is, a fusion output that equals the laser energy incident on the target. For this purpose, we have invented, and are developing, high-power short-pulse carbon-dioxide gas lasers, which offer the advantage of exhibiting adequate efficiency combined with a repetition-rate capability that holds promise for their eventual use in commercial power plants. In support of pellet burning experiments, which we expect will successfully culminate in breakeven, we are expending significant effort in target design, target fabrication, laser facility support, and diagnostics development. A modest experimental effort directed toward military applications is under way to identify the feasibility of various types of relevant experiments. Finally, a systems group is exploring design concepts for future commercial fusion reactor systems and subsystems to identify potential problems at an early date.

CO_2 LASER PROGRAM

During the current reporting period we have made substantial progress in many areas. In the CO_2 laser program, we have continued the use of the Single-Beam System (SBS) and Two-Beam System (TBS) for target experiments. The upgrading of the TBS continued with incorporation of an improved saturable gas isolator cell between the laser final amplifier and the target chamber, permitting the on-target energy to be raised to 375 J per beam. The SBS was shut down at the end of November 1977, and the personnel was transferred within the division to support more urgent tasks.

Effort continued at a vigorous level on the Eight-Beam System (EBS) to meet facility completion in April 1978. Highlights of achievement include the evaluation of gaseous saturable absorbers and the development of a suitable mixture, which permitted us to operate the EBS at the design point of 1.2 kJ, at a power >2 TW on one module. The front end is essentially complete. The target chamber and optics are installed and the cryogenic vacuum system is operational. All four dual-beam modules are assembled and have been operating simultaneously through the computer operations program. The target insertion mechanism and vacuum interlock are installed.

Progress toward completion of the 100-kJ Antares laser continued, with the objective of extending present CO_2 laser capabilities to power levels at which fusion experiments can be expected to yield thermonuclear energy release in the range of scientific breakeven.

ANTARES

The Antares system comprises a six-beam, 100- to 200-TW CO_2 laser (100 kJ in 1 ns or 50 kJ in 0.25 ns) and associated target-irradiation facilities. Excellent progress was made in system design and in construction of the various large buildings to house the system. Most noteworthy were the successful conclusion of the prototype power-amplifier (PA) program; the start of all construction; the completion of the Antares PA optical and electromechanical design layouts to the point where detailed design was begun; and the release of specifications for the target vacuum system to the Department of Energy (DOE) in the form of a Request for Proposals (REP).

All objectives of the prototype PA programs have been attained. Evaluation of the electromechanical characteristics of the chambers and of the cylindrical electron gun; characterization of the gas discharges, with specific identification of magnetic effects; and laser gain measurements demonstrated the correctness of the designs. Operational tests of the improved electron-beam foil-support structure were completely successful. Parasitic-gain standoff in excess of Antares requirements was achieved.

The Antares PA design incorporated all operational and design experience gained in the prototype programs. In addition, an optical-path layout was developed that included optical design concepts that substantially reduced the sensitivity to misalignment, vibration, and mechanical deformations, and which will successfully control target backscatter, thereby eliminating damage to optical components. The design of long-lead-time hardware for the PAs was on schedule for fabrication early in 1978.

CO_2 LASER TECHNOLOGY

A modest CO_2 laser technology and research effort is continuing in support of all our present and future laser systems. A major achievement was the deployment of an effective broadband gas isolator in both the EBS and TBS, thus permitting operation of one EBS beam at design point. Additional studies to optimize such isolators and to better characterize their behavior are continuing. Theoretical studies of parasitic oscillation criteria in the TBS, EBS, and Antares systems indicate that the saturable gaseous absorbers, created for design-point operation of the TBS and EBS, will not be required in Antares, largely because of the great standoff distance between the laser and the target.

LASER FUSION THEORY, EXPERIMENTS, AND TARGET DESIGN

The design of laser fusion targets requires a theoretical understanding of the physics involved and their simulation in large computer programs. We continue to rely primarily on the LASNEX code to develop targets of specific design. By using a version of LASNEX that contains modifications generated at LASL, we developed numerous designs for the soon-to-be-completed EBS.

- Exploding-pusher glass microballoon targets are expected to produce yields in the range of 10^8 to 10^{11} neutrons;
- Target designs have been completed that will attain 20 times liquid density. Here, the major difficulty is the design of a target whose compression can be verified experimentally;
- Double-shell exploding-pusher targets have been designed to attain a high degree of symmetry through hot-electron transport in an exploding outer shell. Energy delivered to an inner shell by hot and cold electron transport and by hydrodynamic motions then drives an ablative implosion of the inner shell.

A computer code named DOC is now available for stability analysis of these and other designs and modifications to LASNEX have been made, including changes that will eventually allow LASNEX to run faster and cheaper on the CRAY-I supercomputer.

The theoretical support effort attempts to coordinate target diagnostics with various theoretical models and thereby develop improved models for use in target design calculations. The variety of numerical tools used in the support effort enables the microscopic investigation of the detailed processes associated with energy absorption and transport and their complex interaction, which would be intractable by purely analytic means. Significant progress was made in several areas.

- Detailed studies of the performance of ion pinhole cameras have shown that the quality of the image can be affected seriously by space charge in the pinhole.
- An inexpensive elementary model for computing the hot-electron distribution functions generated by resonant absorption has been developed.
- A detailed comparison of multigroup and Monte-Carlo transport methods has shown that the former can overestimate preheat and underestimate decoupling relative to the more accurate (and more costly) Monte-Carlo techniques.
- A two-component electron distribution in the pellet corona has been shown to cause the formation of a rarefaction shock that may be observable by interferometry. This phenomenon allows a more direct determination of the hot-electron spectrum in a target experiment.
- A computerized data file for recording and manipulating laser-target shot information has been developed, allowing a more rapid comparison and correlation of various target diagnostics.

LASER FUSION TARGET FABRICATION

Our ability to fabricate targets for laser fusion experiments has increased in several areas. Improvements in fabrication techniques have allowed us to produce several new types of targets, whereas improved plastic coating and radiographic inspection have increased target quality. The startup of our new high-pressure DT gas-fill system has greatly improved our response time for supplying gas-filled microballoons with custom pressures and DT/Ne mixtures. In the solid-fuel development effort we have fabricated microballoons of amonia borane (NH_3BH_3) for the first time. Our work on materials and production techniques for future targets has resulted in significant improvements in the development of low-density, small-cell plastic foams; *in situ* polymerized plastic coatings; and cryogenic target insertion mechanisms.

We have also improved our target assembly techniques; we can now mechanically drill clean pinholes and diagnostic holes with diameters ranging from 5 to 300 μm. We have extended the range of atomic numbers for materials we can either sputter or PVD-coat and have produced several types of flat targets of these materials. We are now filling microballoons with DT gas and with mixtures of DT and neon to pressures of 600 atm and temperatures of 673 K in a facility at our site. This permits much more rapid turnaround on special gas fills.

We have also improved the characterization and separation techniques for glass microballoons (GMB): The surface-acoustic-wave generator is now operating with a reliable microballoon feeder, and evaluation of this technique for microballoon separation is in progress. We have improved the photometrically analyzed microradiograph method for characterizing microballoons by adding a careful statistical comparison subroutine to the computer analysis of images formed by using a monochromatic x-ray source. Blemishes as small as 3 μm in diameter and wall-thickness variations as small as 0.02 μm can be analyzed automatically. In experiments designed to improve the surface quality and uniformity of GMBs, we have levitated, heated, and expanded single glass microballoons for the first time. The surface quality of these microballoons is being analyzed. We have solved the problem of short gas-retention half-lives in some GMB batches by storage at 193 K. Permeation studies at room temperature and below suggest that variation in gas loss rate from GMBs within a batch arise because of variations in chemical composition from shell to shell.

The development of advanced materials continued: Ammonia borane (NH_3BH_3), a potential solid fuel, was formed successfully into microballoons for the first time. The balloons range in diameter from 160 to 300 μm with wall thickness of 2.2 to 7.0 μm. Hydrogen evolution during partial decompositions of NH_3BH_3, which occurs near the melting point, provides the blowing agent for microballoon formation.

Small-cell plastic foams have been formed by two techniques: Water-extended polyester resin and aqueous gelatin/toluene emulsions were vacuum-dried to produce densities as low as 0.12 g/cm^3 and cell sizes of 1 to 3 μm. Both methods show promise for making hemispherical foam shells.

We have built an apparatus for coating stalk-mounted microballoons with parylene to a thickness of 5 μm, deviating from uniformity not more than 2%.

Cryogenic targets will be needed to realize the highest performance on the EBS and Antares. The fast isothermal freezing technique for producing uniform DT ice layers on the inside wall of a microballoon has been modified to permit gas vaporization with an electrical-resistance pulsed heater. However, this approach proved more erratic and less reliable than the previously used laser heating method. The design and drawing phases of the cryogenic-target insertion mechanism for the EBS laser have been completed and an experimental apparatus is being built. We have discovered a method of fabricating two-shell laser targets on a glass stalk, which permits repeated cycling to cryogenic temperatures without damage to the target.

High-power CO_2 lasers have been used successfully, both to repeat spherical implosion experiments previously demonstrated with Nd:glass lasers and to learn new information concerning basic physical processes relevant to laser-driven implosions. Because computations of complete laser-driven targets leading to breakeven require complex design codes such as LASNEX, experimental testing of computations for simpler geometries was

emphasized to aid in specifying key parameters in the code. In particular, experiments were chosen specifically to test calculations of electron transport and x-ray generation. Because electron transport is the dominant mode of energy transfer in laser-heated targets, it will remain an active area of research in future investigations. However, considerable progress has been made in identifying areas of concern as well as confirming particular models. A thorough study of laser light absorption by various targets yielded values that are nearly identical to those obtained with Nd:glass lasers.

A characterization of accelerated ion emission was completed. This ion loss was found to be limited to less than 10% of the absorbed laser energy and independent of target type or laser wavelength. Thus "fast-ion" loss is not a severe concern for laser fusion application as had been feared earlier.

The effects of prepulse damage to delicate targets were investigated in detail, and damage threshold levels for intensity were determined. These thresholds are higher than the prepulse values measured in the EBS and are also higher than those expected in the Antares System.

TARGET DIAGNOSTICS

Unique diagnostics have been developed to provide the essential data for understanding the behavior of laser-driven targets. Ultrafast x-ray diodes; spatially resolved, high-resolution x-ray line spectrographs; and filtering pinhole imaging arrays have allowed us to measure properties of x-ray emission not previously accessible. Special light-collecting mirrors and calorimeters have provided absorption data of sufficient accuracy for direct comparison with theory.

Accuracies of 15 μm in the alignment and focusing of CO_2 beams are now possible by using microscopes and pyroelectric vidicon cameras. These diagnostics have also been used to determine irradiance profiles within a focal spot.

Innovative diagnostics are being developed for future use in determining neutron yields and spectra, plasma expansion velocities and energy integrals, electron density profiles and motions, and vacuum uv (VUV) spectra and source distributions.

APPLICATIONS OF LASER FUSION

Progress was also made in our feasibility and systems studies. In inertial confinement fusion (ICF) reactor studies, we obtained new results in the modeling of transient pressure loadings and preliminarily assessed the requirements for understanding the characteristics of laser beam propagation through the reactor cavity environment. In laser studies, we successfully modeled the short-pulse amplification in large three-pass CO_2 laser amplifiers, as verified experimentally. A computer program, INDEXER, has improved and facilitated the economic modeling of ICF facilities by automating the computation of economic indexes used to project current costs into the future. Investigations of new laser fusion applications resulted in a preliminary characterization of the ICF reactor system and of the thermochemical cycle suitable for synthetic fuel production.

In conclusion, progress toward our goals during the second half of 1977 has met or exceeded our expectations. Probably of greatest significance has been the demonstration of design-point operation of one beam of the EBS. This achievement was the direct result of the development of a gaseous saturable absorber to improve parasitic stability. Completion of the full EBS at design point seems assured.

I. CO_2 LASER PROGRAM

The research and development programs on high-energy short-pulse CO_2 lasers were begun at LASL in 1969. Three large systems are now either operating or being installed. The SBS, a four-stage prototype, was designed in 1971 and has been in in operation since 1973 with an output energy of 250 J_2 in a 1-ns pulse. Target experimentation continued on the TBS, which will ultimately generate pulses of 2 to 4 TW for target-irradiation experiments, and construction is under way on the EBS, which is scheduled for completion in April 1978 and will then begin target experiments at 10 to 20 TW. A fourth system, Antares, is in the design and prototype stage. This system, described separately in Sec. II, will generate laser pulses of 100 to 200 TW, with the objective of demonstrating scientific breakeven.

SINGLE-BEAM SYSTEM (G. T. Schappert)

The SBS is operated as a service facility for single-beam laser-target interaction experiments at 10.6 μm with a 1.0-ns pulse and a developmental system for many aspects of operating and controlling high-energy CO_2 laser systems for target experiments. The SBS consists of a gated oscillator and four electron-beam-sustained amplifiers. The system delivers on target a maximum intensity of 7×10^{14} W/cm^2 and yields new information for fusion-target development.

The hot filament electron gun of Amplifier IV constantly required attention, rendering this last stage of amplification inoperative. Target experimentation was continued at a 2-to 5-J, 1-ns pulse level with Amplifiers I, II, and III. Troubleshooting and repair work on Amplifier IV proceeded on a reduced priority. The obvious fix for Amplifier IV would have been a cold cathode retrofit, but it proved to be too expensive.

Because of manpower limitations in the laser development and target experimentation areas, it was decided that the SBS facility should be phased out. Operation of the SBS for target experiments was terminated at the end of November 1977 and the facility was dedicated to Antares front-end design studies.

TWO-BEAM SYSTEM (J. V. Parker)

Introduction

The TBS is primarily devoted to target experimentation at energies up to 1 kJ in two beams in 1-ns pulses. This laser has been operational for 1 yr, but we are still in the process of studying, modifying, and upgrading its performance to maintain and improve its effectiveness. Along these lines, several projects were performed.

Laser Performance and Diagnostics (J. P. Carpenter, J. McLeod, J. V. Parker). A number of significant measurements relating to laser system performance have been made. Notably, the $\pm$ 50 μm pointing accuracy of the present Hartmann alignment system has been confirmed, the benefits of SF_6-Freon isolator gases in the target chamber cell have been evaluated, and calculations and measurements of leakage energy have verified that prepulse damage is not a problem in the current system and will not be a problem with any anticipated system

changes. A 5-GHz oscilloscope is now in routine use for pulse shape measurements on target irradiation shots. A statistical study of output pulse shape on the south beam characterized the system performance as follows (55 data traces):

Risetime	239 ± 36 ps
FWHM	1.13 ± 0.26 ns
Energy/Peak Power	1.35 ± 0.21 ns

Substantial reductions in the noise on the prelase detection system were achieved. A CO_2 line spectrograph was installed in the small-signal gain probe apparatus to monitor the line on which gain is measured. A second scan converter was installed in the Hartmann alignment system so that both beams can be aligned simultaneously, thus reducing the number of front-end shots required for alignment by a factor of about 2.

A new diagnostic instrument has been developed to quantitatively measure postlase energy. This instrument operates in the following manner: One of the two sample beams derived from the 15.2-cm-diam (6 in.) wedged salt beam splitter is directed onto a diffuser located at a point where the beam diameter is 1.3 cm. A Molectron P5-00 pyroelectric detector is located 2.5 cm behind the diffuser. At this position the diffused CO_2 radiation produces a signal proportional to the average incident intensity, independent of nonuniformities in the incident beam.

The pyroelectric detector is connected to a high-input impedance fast buffer amplifier with a 20 pF load on the detector. This acts as an integrator with a 4-to 5-ns risetime and a 40-μs decay time. The buffer amplifier output signal is therefore proportional to the total energy incident on the detector up to that time. The performance of this detector will be evaluated during the next quarter.

An experiment to verify the accuracy of the Hartmann alignment technique was conducted. Beam position was determined by melting a hole in a 200-μm-diam GMB using the front-end pulse attenuated to approximately 100 μJ level by an appropriate pressure of SF_{66} in the target chamber gas cells. Approximately 16 targets were shot with both beams. The dual-beam module was not fired for these tests, but the low-level pulse passed through the triple-pass amplifier. Before each GMB was shot, the flat turning mirrors in the target chamber were arbitrarily misaligned and then realigned with the Hartmann system. The GMB was shot and then the Hartmann test run again to check for noticeable drift. The south beam had observable drift three or four times. The period between Hartmann tests was approximately 1/2 h. The north beam was completely stable. The observed south-beam drift is probably due to a loose mount on the turning mirror in the target chamber.

Preliminary analysis of the data indicates an rms pointing error of approximately 45 μm, which is consistent with previous estimates based on x-ray pinhole pictures of irradiated targets.

Oscillator-Preamplifier System (P. D. Goldstone, V. O. Romero). No major problems were encountered in the operation of the oscillator and preamplifiers. However, the technique of preionization tested in preamplifier 1 (two flashboards only, using washers instead of square tabs) has been temporarily abandoned. After several weeks of operation, there was some evidence of insufficient preionization. Upon examination, erosion of the metal washers was evident. New flashboards will be produced using harder metal washers and this technique will be tried again.

We have tested simultaneous active and passive modelocking of the oscillator. In its standard operating configuration, running on P(20) only and modelocked with an acousto-optic loss modulator, pulses in the modelocked train have risetimes of approximately 700 ps and widths of approximately 1.5 ns FWHM. By using a piece of p-doped germanium as an output coupler to passively modelock the system along with the active acousto-optic modelocker, we have observed significant pulse sharpening. Using a p-doped germanium output coupler with $\alpha L = 0.34$ we obtained risetimes (10 to 90%) of 466 ± 20 ps and widths of 1.04 ± 0.08 ns. The use of p-doped germanium in the cavity should also decrease the energy between pulses in the modelocked train and improve the pulse onset. When simultaneous active and passive modelocking was implemented for regular operation, insertion of the p-doped germanium modelocker did not significantly change either energy or peak power out of the front end. Preliminary evidence suggests that pulse shape improvement may be less than was hoped, and that burning of the antireflection (AR)

coating on the germanium flat may be a serious problem. We will continue to study the use of p-doped germanium in the oscillator cavity during the coming quarter.

Power Amplifier System (J. Carpenter). A major operational limitation of the TBS has been the inability to put more than approximately 200 J/beam on flat targets, or approximately 300 J/beam on GMBs, due to the presence of parasitic oscillations. This has limited operation to a $g_oL < 4.4$, whereas the amplifier itself is stable without a target at the focal spot up to $g_oL \sim 5.5$. In the past, pure SF_6 has been used in a gas cell between the Dual-Beam Module (DBM) and the target to stand off the amplifier gain on P(20) and stabilize the amplifier for operation against targets. In addition, for flat targets it has been necessary to physically block the region of the beam that can participate in four-pass oscillations. With the development of multicomponent gas isolator mixes for use in the EBS, we have undertaken a series of experiments to determine both gain standoff and transmission of these mixes when used in the TBS between the amplifier and the target, and thereby determine the maximum energy on target using these mixes. The experiments on flat polyethylene targets were completed: using mix 804 (1.51% SF_6, 4.04% C_4F_8, 12.2% FC-115, 19.8% FC-1113, and 62.4% FC-12) we find an expected maximum on-target energy of 375 ± 41 J compared to the approximately 190 J previously available. Experiments on glass and goldcoated microballoons will follow.

The electron beam Marx generator has been mechanically changed to give better support to the internal components. The capacitor hv bushings are better protected against breakage by connecting the capacitors to the main current bus with thin copper sheeting. This should prevent further capacitor bushing failures.

EIGHT-BEAM LASER SYSTEM

Introduction (S. Singer)

The EBS represents the next generation of high-power short-pulse CO_2 laser systems we will use to study the interaction of intense light beams with matter, with emphasis on investigating problems relating to laser fusion. This system is designed to deliver 10 to 20 TW to a target—10 kJ in a 1-ns pulse or 5 kJ in a 0.25-ns pulse. The EBS will consist of an oscillator-preamplifier system that generates a 0.25-ns multiline optical pulse at the several-hundred-megawatt level, and which will drive four DBMs clustered around a target chamber. Each of the eight 35-cm-diam beams will deliver ~650 to 1250 J (depending on pulse length) to the target chamber, which will contain an optical system to focus these beams onto a target. The front end of this system is operational and is being used to support multiline energy extraction and pulse shape measurements on one side of the first DBM. Construction of the other DBMs is on schedule.

Oscillator-Preamplifier System (R. L. Carlson, D. E. Casperson, R. Quicksilver, M. Weber). The oscillator-preamplifier system, or front end, is operational as a complete four-beam system including diagnostics, and the output energy, pulse shape, line content, and energy contrast ratio have been measured. A shot counter for the oscillator and each preamplifier has been installed. This reveals that the front end is being used at a rate of greater than 500 shots per week in support of Triple Pass Amplifier (TPA) energy extraction, alignment, and development of front end and main floor diagnostics. The optical transport system of the front end has been adjusted to produce the proper beam waists at the TPA entrances.

The current front-end configuration is shown in Fig. I-1. The configuration will be used for the full power test of the EBS and initial target interaction studies. Preliminary tests producing retropulses from a target located in the target chamber indicate that the front-end components are protected against any retropulse damage.

The oscillator is operated with a 0:1:1:He:N_2:CO_2 mixture at 50 kV and a plasma tube pressure of 7.5 torr at a current of 3.5 mA. This condition produces a 500-to 600-mJ multiline output (P20, 18, 16, and 14) with a gain-switched pulse risetime of 20 ns and a FWHM of 80 ns. This energy has been attenuated down to 150 to 200 mJ incident on the first crystal face of the triple switchout system. After several

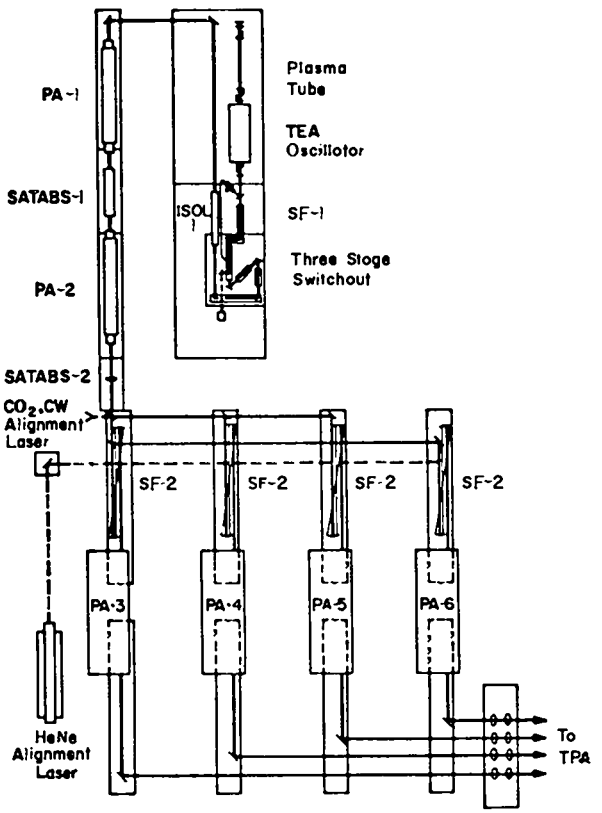

Fig. I-1.
EBS Oscillator-Preamplifier front end system: preamplifiers (PA), saturable absorbers (SATABS), isolators (ISOL), spatial filters (SF), to drive the four triple-pass amplifiers (TPA).

thousand shots there were only microscopic damage inclusions on the face of the CdTe crystal. It is concluded that essentially no damage occurs to the CdTe AR coating in an operational environment of several months and in excess of a thousand shots if the average energy density is kept below ≈500 mJ/cm^2.

In the present arrangement the triple Pockels cell switchout produces a 0.3 mJ-pulse with a 0.76-ns FWHM. The measured feedthrough energy (i.e., energy transmitted with the light-triggered spark gap off) is 8 nJ. This gives an energy contrast ratio of 4 x 10^4. The prepulse energy contrast ratio is three times higher than this because of the temporal distribution of the energy in the gain-switched pulse. Referring to Fig. I-1, the other front-end components operate as follows.

The lenses of ISOL-1 have been adjusted to give a beam waist w_o=1.2 cm after the second lens. SATABS No. 1 consists of a slab of p-doped germanium with an $\alpha_o L$ = 1.25 and a 10-to 15-torr-cm cell of SF_6 with an αL = 6-9. The second lens of SATABS No. 1 has been adjusted to give a beam waist w_o = 1.2 cm located approximately 100 cm in front of the first concave mirror of SF2. SATABS No. 2 is a slab of germanium having an $\alpha_o L$ = 4. This slab may be removed to supply more front-end energy for purposes of alignment. Typically, 15-20 mJ is available at each SF2 station with SATABS No. 2 in and 45-60 mJ with SATABS No. 2 out. The second concave mirrors of SF2 have been adjusted to produce a beam waist radius w_o = 1.2 cm at the TPA entrances.

The output of the final preamplifiers (PA3, 4, 5 and 6) after splitting 17% off the beam for diagnostics, is approximately 450 mJ with SATABS No. 2 out and approximately 175 mJ with SATABS No. 2 in. Using the spectrometer of the front-end diagnostics, a 5-line content has been observed having a typical relative distribution of 3, 22, 21, 40, and 4% for the lines P14 through P22, respectively. The multiline pulse shape is characterized by a 330-ps risetime with a 760-ps FWHM. The single line pulse shape has a 400-ps risetime with a 770 ps FWHM. The total front-end feedthrough energy per beam with no SF_6 in SATABS No. 1 and the triple switchout system OFF is 100 nJ. Assuming that one-third of this 100 nJ occurs as prepulse energy and that 15 torr-cm of SF_6 is used in SATABS No. 1, the estimated prepulse energy per beam is 4 pJ. This should give a prepulse energy on target of less than 10 μJ/beam.

Energy Extraction Measurements (J. S. Ladish, M. D. Montgomery, D. Casperson, R. F. Haglund, R. Ainsworth, R. L. Johnston). After considerable research and testing, a number of gas mixtures has been identified whose constituents are proportioned to provide a small signal loss vs frequency curve that matches in broad outline the gain curve of the EBS power amplifiers. One of these mixes, mix 804, was tested in TPA module 2A with considerable success for energy extraction.

Figure I-2 summarizes the results achieved with this mix; $\alpha_o \ell$ is the small-signal loss-length product of one pass through the absorber. The approximate total pressure of the mix in the absorbing cell in torr

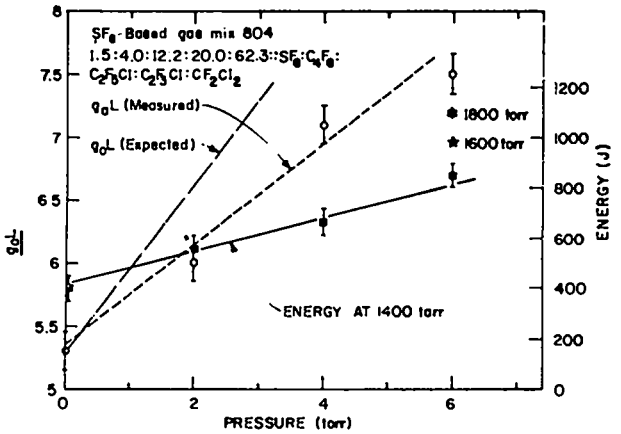

Fig. I-2.
Energy extraction with saturable absorber mixture.

can be derived by doubling $\alpha_o \ell$ for this case. The maximum unconditionally stable gain-length product ($g_o L$) of one pass through the amplifier is given by the dashed curve using the left ordinate scale. In this case $g_o L$ represents gain as measured along the probe laser path and is believed to be about 0.25%/cm below the average on-axis gain of the pumping chamber. The measurements lie close to the expected $\Delta g_o L = \alpha_o \ell$ until the break at $\alpha_o \ell$ = 2. The cause of the reduction in slope above this value is not yet known, but could be because of the onset of a six-pass oscillation mode. It was not possible to pump the amplifier to high enough gains (due to risk of high-voltage overstressing of the pumping chamber) to further investigate the high $g_o L$,high, $\alpha_o \ell$ part of the figure. The solid curve shows the total energy extracted at 1400 torr. The stars indicate the increased energy obtained when the laser gas pressure was raised to 1600 torr and 1800 torr. The 1200 ± 100 J data point represents the achievement of our design goal.

Three methods were used to measure the total output energy: (a) direct absorption into a large calorimeter, (b) absorption of the Fresnel reflection off a NaCl beam splitter into a large calorimeter, and (c) measurement of the energy transmitted by a 17% transmission slit grating, again using a large calorimeter. (c) and (b) were done to avoid the nonlinear region of the large calorimeter above approximately 600 J (i.e., 0.5 J/cm²). A comparison of measurements using all three techniques including the measured calorimeter nonlinearity corrections was used to evaluate the amount of energy extracted. A series of experiments investigating retropulse, gain standoff in the presence of targets, and pulse shapes is still in progress.

Beam Diagnostics (I. J. Bigio, S. Jackson, S. Seagraves, A. Laird). The concepts for the laser beam diagnostics for both the front end and main beams have been established and the necessary components ordered. Figure I-3 shows the front-end diagnostics plan and Table I-I summarizes what is planned for monitoring the main TPA output beams.

High-Voltage Systems (E. L. Jolly, J. Sutton, W. A. Kelly, D. Bernard). All TPA modules have been successfully tested together at 70% of design voltage. Problems associated with reliable electron-beam crowbar gap operation have been circumvented. Recent experience indicates that operation without a crowbar gap does not lead to premature electron gun failure and in fact increases the reliability of gun operation by eliminating the early crowbar fault mode. In view of this, crowbar gaps were removed from all electron-beam pulsers.

To reduce the gain nonuniformity and impedance within the power amplifiers, the output voltage of the electron-beam pulsers has been increased by approximately 20%. There are two reasons for the increased output. The Marx stages within a pulser are now charged to 60 rather than 55 kV, resulting in a 9% increase in output voltage. The internal series resistance of each pulser has also been reduced from 5.0 Ω to 1.5 Ω further increasing the output voltage.

The original anode for the DBM has a flat surface facing the electron gun. An anode with a surface approximately a cylindrical sector (cylindrical axis parallel to optical axis) has been installed on amplifier 4B. The curved surface of this anode is expected to reduce the small-signal gain nonuniformity in the vicinity of the anode. Preliminary small-signal gain measurements confirm that the gain nonuniformity has been reduced compared to that observed during the 4B acceptance tests. Some of the observed reduction is probably due to an increase in electron-beam energy as compared to that used during the acceptance tests. Computer plots of electrostatic fields in the vicinity of the anode indicate that electric fields are not increased outside the discharge area. Thus, the new anode should not be any more prone to electrical breakdown than the original.

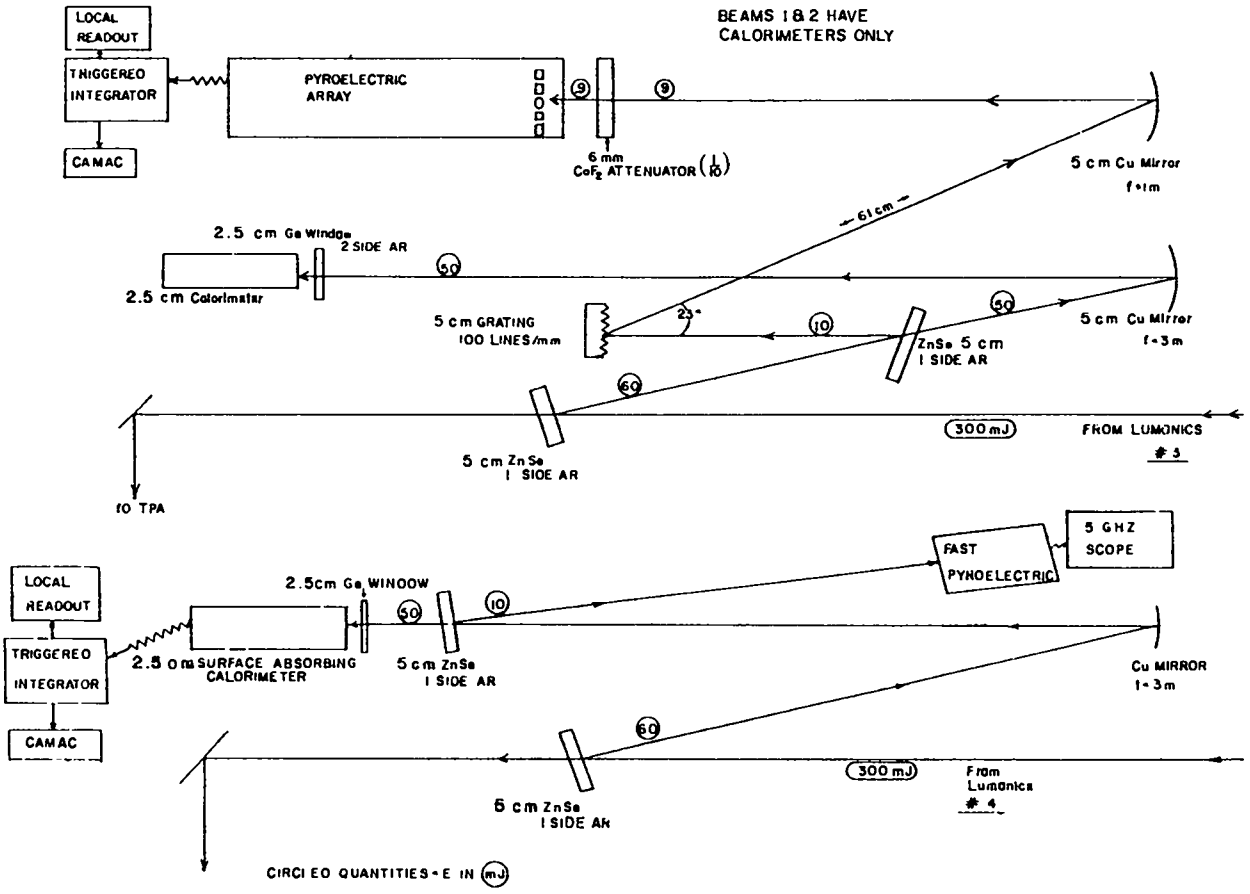

Fig. I-3.
EBS front-end diagnostics plan.

TABLE I-I

MONITORING SEQUENCE FOR MAIN TPA OUTPUT BEAM

1. Measurements to be made are:
   a. Total pulse energy (absolute)—all eight beams.
   b. Ratio of prepulse: main pulse: postpulse energies (relative)—all eight beams.
   c. Spectral line distribution of energy—on any one of the eight beams.
   d. Temporal pulse shape—on any one of the eight beams.
2. System must be flexible enough to add different diagnostic measurements at will. For example: retropulse measurements or focusable energy.
3. System should have local manual control as well as the capability of computer control from "upstairs."
4. System should not introduce noise to the computer.

Controls Systems (E. L. Jolly, M. D. Thompson, J. Sutton, D. A. Remington, L. Sanders, D. Wells, M. F. Ellington, T. Johnson). The EBS Computer system is on schedule. The 96 M byte disk and the 2-branch CAMAC system are now in routine use in EBS operations.

The EBS series of control programs are vastly improved versions of the code DBM. The techniques of overlaying and multitasking are heavily used. The present version has three core resident overlay areas that accommodate the 17 disk resident overlays. Tasking allows slower activities (postshot maintenance and tape operations) to execute in parallel with the operator dialogue program. The whole code runs in 31 K words of memory.

Considerable revision has also been applied to our data storage system. In addition to the fact that the big disk is used as our primary data storage device, the data stored are now more efficiently "packed." Two of the 6-bit digitizer words are now stored in each 16-bit disk word. Also, up to two channels of gain data can be stored along with normal pulser data. This means gain data can now be recalled and reviewed if the operator desires. A separate CAMAC crate has been allotted to handle such laser diagnostic data and allow for increasing requirements. The on-line tape back-up storage system has also been improved. A cyclic system of four data tapes is employed. The computer recognizes that the correct tape is mounted by the operator. With this system the last three to four hundred shots are available from the tapes should something happen to other storage sources.

The target chamber vacuum system controls provide electrical controls to operate all vacuum equipment associated with the target chamber. The control system will be operable from any of three locations and present data at all three locations simultaneously. These locations are the target chamber, the control room, and the computer.

The target insertion device controller will provide electrical controls to transport a target between an air lock outside the target chamber and the center of the target chamber. The controller will also provide capability to control valves and pumps associated with the target. It consists of three parts: a manual control panel, which will allow manipulation of the target insertion device components; a target carrier tracker, which will track target insertion and removal and provide interlock information; and an automatic sequence, which will insert or remove a target upon command.

Pressure monitors have been installed in each gas supply line used for laser gas mixing. These monitors not only provide pressure readouts available in the control room, but also provide pressure switch closures to interlock the mixing station.

All motorized mirror mounts required for the eight-beam segments of the facility have been assembled, installed, and checked out. This work includes the assembly of thirty, 3-in. mounts and five, 4-in. mounts. These are in addition to eighteen, 3-in. mounts that had been assembled previously. Also, eight motor address decoder units have been installed and all cabling has been completed between the beam positioners, address decoders, and the mirror mounts.

Mechanical Systems (G. Zimmermann, D. Ingwerson, B. Maestas, D. Martinez, M. Martinez, J. Valencia, L. Rodriguez, W. Lemons, P. Walsh). All four DBM assembly work is complete. The target chamber vacuum system is installed, mirror mounts are all on hand, and the target insertion device is in place. The EBS hardware is completely assembled and ready for the reduced-power test scheduled for January 1978. Electron-beam foil windows have failed several times recently. All failures were pinhole leaks causing electron beam vacuum degradation. Work is continuing to improve foil-grid gluing methods. It is hoped that window integrity can be improved. A new window changing technique was devised that allows us to make the change without rolling back the pumping chambers, as was previously done. Window removal and installation time has been cut to 3-4 h, in addition to another 3-4 h for re-establishing the vacuum. All triple-pass stands have been strengthened and bolted to the floor. Much improvement in stability has been made.

A hard vacuum test of the target chamber was done in mid-November. After some discovered leaks were fixed, the predicted mid-10^{-7} pressure was reached. Problems have risen with the secondary cryopump compressor necessitating the recall of the vendor's representative to make needed repairs.

The baseline design for the gas saturable absorber system has been completed, and procurement and fabrication of components has started. This includes the gas cells, the mixing station, the pump/fill stations, and a manual control system.

Target Positioning Systems (R. Day, C. Cummings, B. Hansen, T. Tucker).

Room Temperature Target Insertion Mechanism (TIM). The airlock and transfer mechanisms have been installed onto the EBS target chamber. The portion of the TIM inside the target chamber has also been installed. The entire mechanism has been aligned so that one can transfer a target through the gate valve orifice and into the target chamber. (Figure I-4 shows a drawing of the TIM. Figure I-5 shows the airlock mounted to the chamber wall. Figure I-6 shows the transfer mechanism, cart, and target holder inside the target chamber.)

Five target holders have been fabricated and are being assembled. Two alignment sphere holders are being fabricated. A fixture has been fabricated and is being assembled that will allow the targets to be located at the center of the alignment sphere in the target fabrication laboratory. When these parts are completed the TIM will be ready for testing and use in the EBS target chamber.

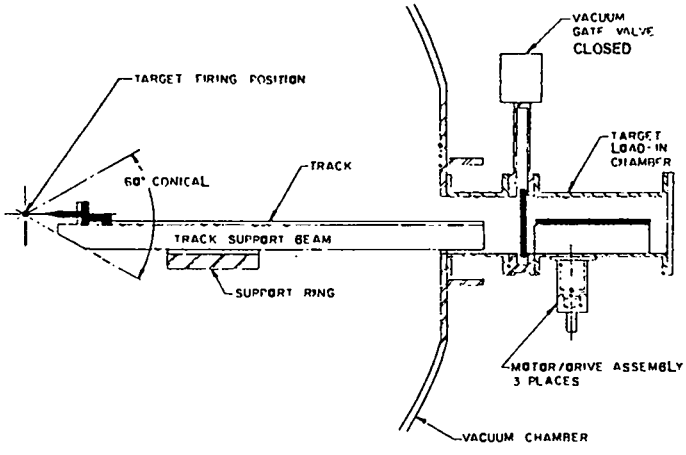

Fig. I-4.
Target insertion mechanism in firing mode.

Fig. I-5.
Target insertion mechanism airlock.

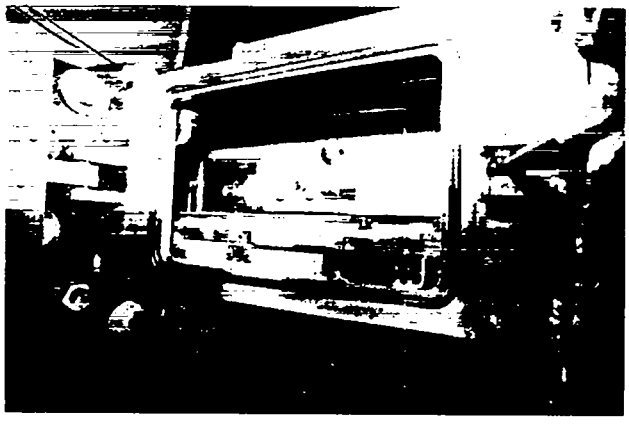

Fig. I-6.
Target insertion transfer mechanism with cart and target holder.

A repeatability test has been performed on the TIM. The test was performed in a thermally controlled room to minimize the effect of thermal gradients in the environment over the duration of the test. The procedure was to back the cart to the end of its track; remove and replace the target holder; and advance the cart until the target holder seats onto the kinematic mount. The position of a 19.05-mm-diam (3/4 in.) alignment sphere mounted on the target holder was sensed by two capacitance gauges and one linear variable differential transformer (LVDT). These gauges were mounted on mutually orthogonal axes.

Two testing samples were taken. The first consisted of 60 runs and the second of 24 runs. The conclusion of the test was that at 99.9% confidence

level, a target will repeat its previous position to within ± 2.5 μm.

Cryogenic Target Insertion Mechanism. The detail design for a cryogenic target insertion mechanism (CTIM) testing fixture is nearly complete.

Optical Systems (I. Liberman, M. Bausman, M. Calcote, J. Handen, J. Murphy, G. Salazar, V. K. Viswanathan).

Target Alignment. As of September 1, 1977, the heart of the EBS target alignment system was a Hartmann/vidicon system similar to the one used in the TBS, but with auxiliary visible tests to ensure that the target and retrosphere were accurately aligned. All cameras, scan converters, monitors and other peripheral electronics have been ordered to accommodate alignment of four beams simultaneously. Eight cameras were to be installed so that with simple electrical switching the second set of four beams can be aligned after the first set is completed. The Hartmann masks and mechanical apparatus for inserting and removing the masks have been designed. An algorithm was developed which showed that from the Hartmann pattern of one shot, the degree of misalignment of the paraboloid and the beam striking the paraboloid can be calculated. Thus, in principle, only one shot is required to correct the misalignment.

The focus and alignment sensitivity of the paraboloids were analytically studied. These analyses also showed that the Hartmann test correctly determines the optimum focus and alignment of the paraboloid for various types of aberrated beams. A scheme to predict the proper way to align the turning mirror and paraboloid based on a given misaligned Hartmann pattern is being studied by the computer. The algorithm has been completed and verification of its accuracy is presently being studied.

Supplementary Target Alignment Aids.

Continuous-wave (cw)-CO_2 Alignment Laser. We determined that a cw-CO_2 laser beam inserted along the same optical paths as the pulsed beam will facilitate alignment. By using a cw laser for alignment the number of shots from the front end will be reduced substantially, thus increasing the mean time between failures. Also, it may be possible to improve the alignment accuracy if the cw laser is truly coincident and provides increased energy on alignment detectors. Finally, the use of a cw-CO_2 laser will simplify the determination of optical quality of the beam at the target. The design of the laser and means to ensure its optical congruence to the pulsed beam have been determined. The equipment is ordered and will be assembled in February.

Alignment Microscope. A means for verifying that the alignment sphere and the target are concentric in the target chamber is required. This is to be accomplished using two orthogonal autocollimating microscopes inside the target chamber having a working distance of about 75 cm. The long working distance will allow the microscope to be permanently fixed to the optical support structure without the need for moving parts. The eyepiece of the system will be outside the target chamber. Both direct visual confirmation as well as TV monitors in the control room will be provided. The system is designed and the components are being purchased. A laboratory mockup has been made using poorer components than the final system. With this system an alignment reproducibility of about 10 μm was observed.

The final goal is a tolerance of 5 μm. In addition to its main function the system will allow a detailed view of the target from two directions to determine its integrity, and will also define the optical center of the target chamber.

Beam Alignment. Installation of the manual beam alignment system is completed and has been checked out at various representative stations. Alignment takes place after the beam is split four ways, then, after the beam is split eight ways, and again after the first pass in the TPA. There are therefore 20 spatial filters that are aligned. Each spatial filter has two alignment points; the beam is first centered on the focusing mirror using a large area position sensor and then centered on the pinhole using a 1 mil niobium quadrant type detector. Thus, there are 40 detectors, each yields four

signals requiring 160 channels of amplifying electronics that are reduced to 80 channels of x and y error information. This information has been calibrated in units of stepping motor-steps on an upstream motorized mirror mount. The electronics required to read the detector information is being built by EG&G and is about 50% completed. Total completion is scheduled for February 1978. The apparatus to close the loop, i.e., automate the procedure, has been developed and is ready to be installed.

Computation Support. The code work needed to satisfactorily model the optical properties of the TBS and EBS has been successfully completed. The computer program FRINGE can in a practical manner convert interferogram photographs into Zernike coefficients. This information is put into the computer program LOTS for modeling the system performance. Whereas no detailed experiments have been done to verify the computational predictions, we have a great deal of confidence in its accuracy.

The FRINGE-LOTS code was used to predict the performance of one beam of the TBS. Good agreement was obtained with the minimal experimental results available.

A similar analysis was performed on one beam of the EBS. Because the 40-cm-diam (16-in.) salt windows to not meet specifications and because the beam passes four times through these windows, the optical performance is poor and shows the necessity of improving the quality of the salt windows. On a high-priority basis we are attempting to find out why the windows meet specifications at the vendor's plant but not at LASL.

II. ANTARES—HIGH-ENERGY GAS LASER FACILITY

The High-Energy Gas Laser Facility (HEGLF) is built around a high-power (100 to 200 TW) short-pulse (0.25 to 1.00 ns) CO_2 laser, Antares, which is being designed to investigate laser fusion phenomena, with the objective of demonstrating scientific breakeven. A prototype module of the laser has been constructed and evaluated in extensive tests.

INTRODUCTION (J. Jansen, T. F. Stratton)

The main thrust of the HEGLF-Antares project was in the area of the prototype power amplifier (PA), the PA design, the optical system design, and facilities construction.

The PA prototype experiments were completed and the results are incorporated into the design of the PA. The large area gridded coaxial gun is now well understood. Uniformity levels of the e-beam current density have been measured and found acceptable. The gas discharge has been well characterized. The code has been refined so that gain levels and cross-sectional distributions can be protected. The cross-sectional gain uniformity has been improved by the introduction of curved anodes and lateral plastic walls. Measurements of parasitic oscillations have been made, which indicate that a double-pass $g_oL = 13$ is achievable, which is commensurate with the baseline design requirements for the Antares PA. Lithium fluoride was proven to be very successful as an antireflective material.

The design of the PA has progressed to the point where hardware drawings for the pressure shell and the e-gun vacuum vessel are ready for review. Both are long-lead procurement items. The dynamic mechanical analysis indicates that feared resonances at low frequencies are no longer a problem. An internal optics support structure is preferred over the previously discussed external support.

The design and analysis of the optical system has reached the point where we now have a workable end-to-end point design. The detailed optical design of the PA is near completion. It includes optical baffles, aperture stops, and beam dumps to reduce parasitic cavity oscillations. It also foresees a saturable gas absorber cell to suppress parasitic PA and PA-target oscillations. Provisions are made for active retropulse isolators, should they become necessary. A new NaCl salt crystal growth technique (Kyropoulis-Czochralski) has shown promise to result in less expensive and more timely salt window delivery than the existing Stockbarger process. Large salt windows have been successfully coated with a NaF antireflection coating.

As regards the HEGLF construction contracts, the construction of the main laser building and its support buildings (Package I), and of the target building (Package II) has begun. The design specifications for the target vacuum system (Package III) have been completed and released to DOE.

PROTOTYPE POWER AMPLIFIER (W. Leland)

Experimental Power Amplifier Results (T. Ganley, G. York, D. Swanson, W. Leland)

Design of the Antares PAs presents engineering problems not previously encountered in LASL's CO_2 Laser Program. The Power Amplifier Prototype Project addressed these problems experimentally.

As reported in LA-6982-PR, we assembled and checked out apparatus required for the experiments. In addition, we performed experiments relating to the mechanical and electrical design of the prototype and verified the mechanical integrity of the inner and outer pressure vessels. More convenient foil structures were tested and withstood the

stresses encountered during operation. All high-voltage power supplies and bushings performed in accordance with expectations.

During the last six months of 1977, we operated the prototype as a completely assembled unit and studied its important performance characteristics in detail. In particular, we operated the gridded cold-cathode gun in cylindrical geometry; identified the voltage-current characteristics of the grid-controlled gun; measured the spatial variation of gun current density; characterized annular gas discharges; studied the discharge behavior of a 28-cm gap, 1800-torr, 1:4::N_2:CO_2 laser gas mixture; measured the spatial variations of discharge current density and of small-signal gain across the discharge aperture for the operating conditions anticipated in the Antares PAs; demonstrated the effectiveness of contoured anodes in leveling the spatial variation of small-signal gain; studied the parasitic-oscillation problems and measured its threshold in folded optical geometry; and characterized the reflection properties of surfaces that are good absorbers of incident 10-μm radiation.

We will discuss in detail the cylindrical gridded cold-cathode gun, the characterization of gas discharges, and the parasitic oscillation studies.

Cylindrical Gridded Cold-Cathode Gun

The gridded cold-cathode gun has been described briefly in LA-6982-PR. The gun cathode consists of 12 emitting blades (1 for each discharge sector) equally spaced on the circumference of a ribbed cylinder. The anode consists of the foils and the foil-support cylinder, all of which are maintained at ground potential. A control grid, resistively coupled to ground, is interposed between the cathode blades and the anode cylinder. By properly choosing the grid resistance we can limit the total emission from the gun to any desired value. Simple theory accurately predicts the operating characteristics of the gun. Predicted performance characteristics are plotted in Fig. II-1. The gun has been operated at voltages from 250 to 500 kV, with grid resistances ranging from 180 to 800 Ω. In all cases, the observed current was within a few percent of the expected value. The gun has been fired over 500 times at full voltage (500 kV) without a single bushing failure and without a breakdown inside the gun chamber.

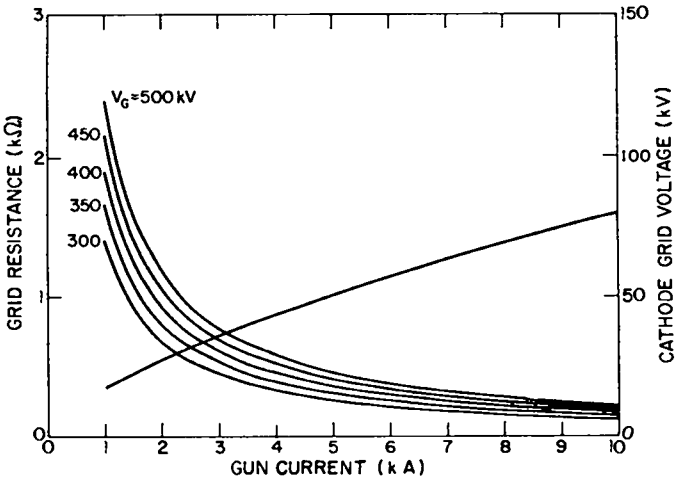

Fig. II-1.
Predicted performance characteristics of prototype Antares cylindrical cold-cathode electron gun.

In extensive experiments we have determined the spatial variation of the primary current density emitted by the electron gun. Small probes were placed outside the foil windows and data were taken for a range of conditions. Typical data taken at three different distances from the foil are shown in Fig. II-2. Data at a fixed distance from the foil for three different values of an externally applied magnetic field are shown in Fig. II-3. The magnetic field is required to simulate the magnetic effects that exist during discharge-current flow. Both scattering and magnetic effects on the spatial variation of the primary current density have been calculated successfully, as shown in Fig. II-4.

Characterization of Gas Discharges

The gas discharges produced in the prototype were 28 cm from anode to cathode, 25 cm wide, and 130 cm long. As shown in Fig. II-5, the sides of the discharge volumes were defined by plastic dividers that restricted the conductivity of the gas to the volume from which optical energy could be extracted. By shaping the discharge in this manner, energy can be more efficiently transferred to the proper gas volume. For instance, with the dividers in place, a desired level of small-signal gain can be created in the discharge volume with 30% less stored

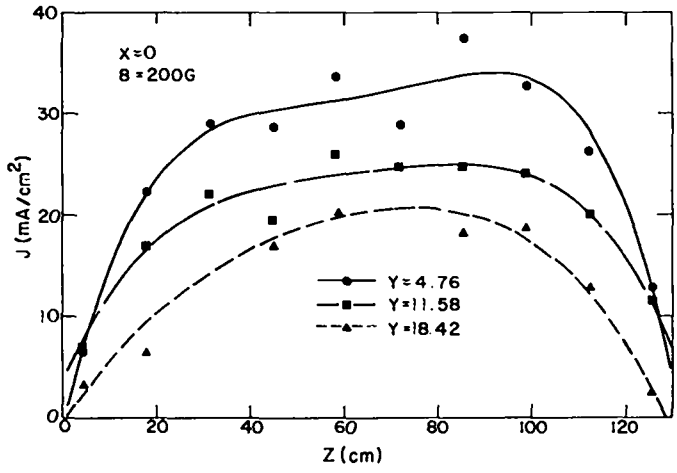

Fig. II-2.
Spatial variation of primary current density emitted by prototype Antares electron gun.

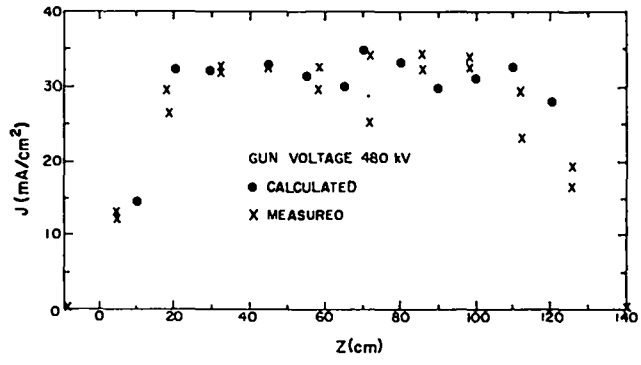

Fig. II-4.
Calculated and measured spatial variations in primary current density emitted by prototype Antares electron gun.

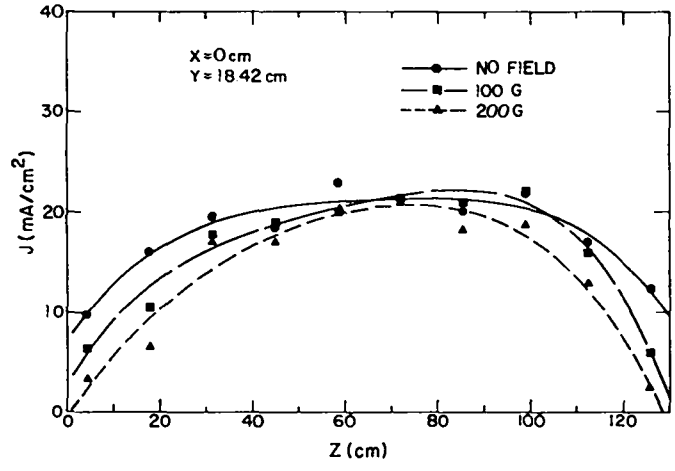

Fig. II-3.
Spatial variation of current density emitted by electron gun for three values of an externally applied magnetic field.

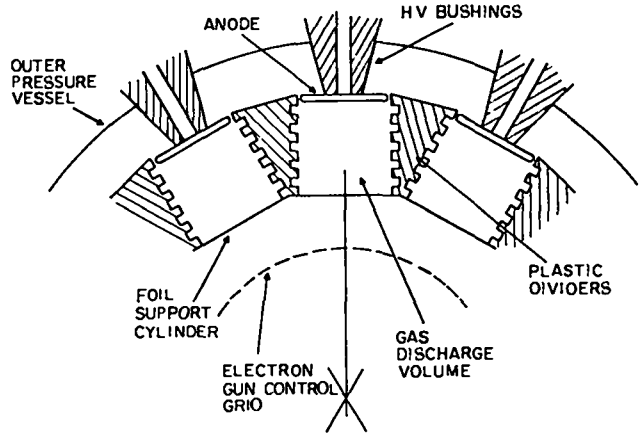

Fig. II-5.
Cross section of gas discharge chambers in prototype Antares power amplifier.

electrical energy than without the dividers. We have operated the discharge with the dividers in place for ~200 shots at full voltage (500 kV) and design current density (7 A/cm²). Arcing has never been observed, either within the gas volume or along the surface of the dividers. No problems have been encountered with the high-voltage bushings, even though the bushings have been subjected to transients of over 800 kV.

The spatial distribution of the discharge current density has been measured by using a segmented anode. Results of one series of measurements as well as calculated distributions are shown in Fig. II-6; agreement is quite good.

We also measured the distribution of small-signal gain over the discharge cross section by using standard techniques. The measured and calculated gain distributions that result from the use of a flat anode are shown in Fig. II-7. Improvements in gain uniformity that result from the use of a curved anode are shown in Fig. II-8. These figures show that, for the

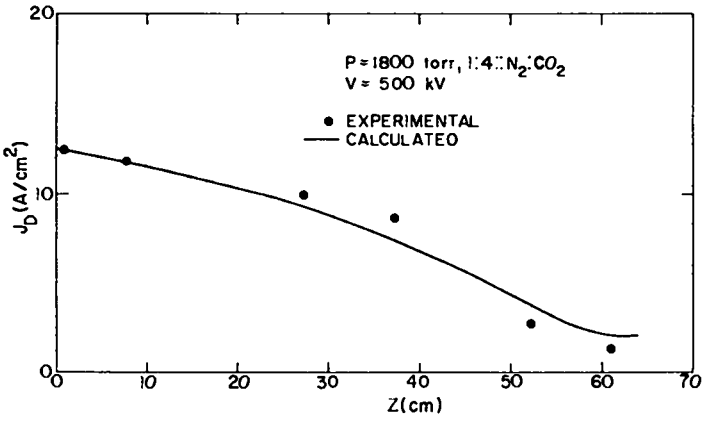

Fig. II-6.
Comparison of calculated and measured discharge-current distribution in prototype Antares power amplifier.

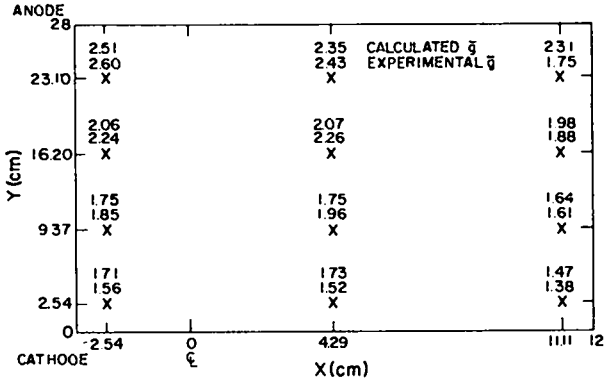

Fig. II-7.
Comparison of calculated and measured gain in prototype Antares power amplifier with flat anode.

discharge operating conditions planned for the Antares PAs, we have attained the expected values of small-signal gain and optical energy storage. Also, it is apparent that a highly uniform gain distribution can be generated across the aperture of these large, high-pressure discharges.

Parasitic Oscillation Studies

The problem of parasitic oscillations within the prototype chamber has been attacked in the following manner.

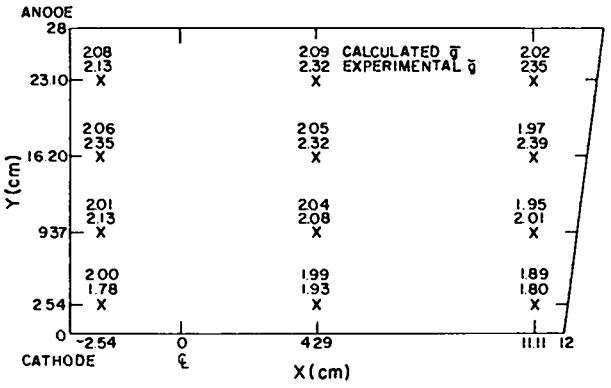

Fig. II-8.
Improved gain uniformity in prototype Antares power amplifier due to the use of a curved anode.

First, we conducted experiments to determine the reflection properties of various low-reflectivity surfaces. These experiments resulted in the selection of two surfaces with significantly lower reflectivity than that of any other surface previously used to suppress parasitics in large CO_2 amplifiers. The surfaces are

- Open-cell polyurethane foam, reflectivity = 0.3%/sr; and
- Flame-sprayed LiF, reflectivity = 0.1%/sr.

Second, we used polyurethane foam to cover the inner walls of the prototype discharge chambers because of the limited time available for performing the prototype experiments. An optical arrangement identical to the setup planned for the Antares PAs resulted in a double-pass gain-length product of 13 in the prototype machine, with no oscillations. Because the Antares PAs will operate at a double-pass gain-length product of only 12, we are confident that problems of parasitic oscillations have been eliminated. Further improvements may be expected if flame-sprayed LiF is used in the Antares PAs.

ANTARES SYSTEM (J. Jansen)

Integrated Optical System (A. Saxman)

Overview. The Antares design and development efforts have addressed the optical-mechanical and end-to-end system performance requirements of the PA and its interfaces with the front end and the

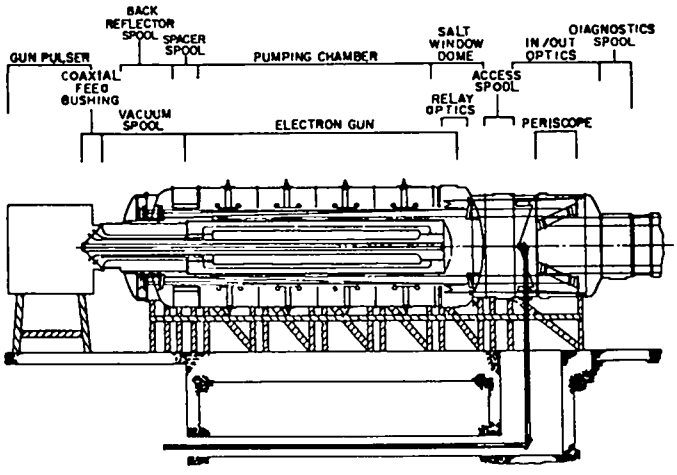

Fig. II-9.
Longitudinal cross section of Antares power amplifier.

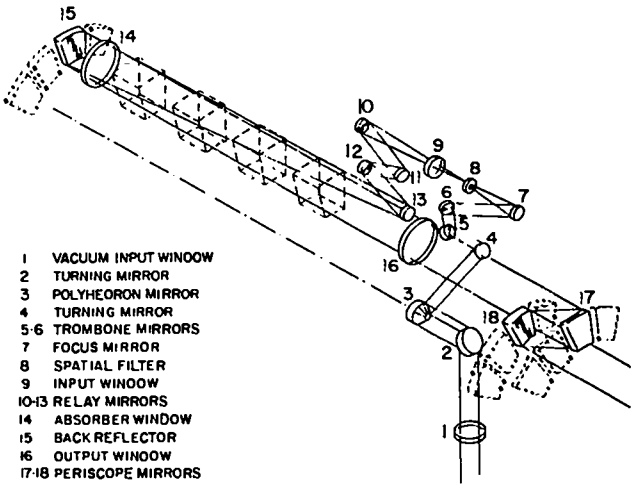

Fig. II-10.
Optical schematic of Antares power amplifier.

target chamber. A new optical "point" design describing the details of all the optical components from the oscillator pulse switchout in the front end to the focusing mirrors in the target chamber has been completed. We have given particular attention to a revised, detailed optical design of the PA that could incorporate a gas saturable absorber cell to enhance its parasitic-oscillation stand-off capabilities (Fig. II-9).

The Antares optical error budget has been updated on the basis of the point design and of current estimates of component quality based on present procurement and manufacturing experience. Encircled energy calculations using wavefront quality parameters derived from the updated error budget have been completed. The resulting predictions of the system's performance for a single sector of a PA indicate a Strehl ratio greater than 0.8 and between 70 to 75% of the transmitted flux within a 300-μm spot diameter. These predictions have been verified by Hughes Research Laboratories under a contract to LASL.

Present energy extraction predictions at Mirror 17 (Fig. II-10) for each PA system show:

	Pulse Width (ns)	
	1	0.25
Energy, kJ	18	9
Power, TW	18	36
Spectral distribution	10.6μm band, 6 lines.	

The interface requirements for the PA and for the front end have been established. The annular input beam at the PA input salt window must have an o.d. of 15 cm and an i.d. of 9 cm. The annular input beam must have the following characteristics:

	PA Output Pulse Width (ns)	
	1.0	0.25
Input energy, J	84.	42.
Input density, J/cm^2	0.72	0.36
Input pulse width, ns	1.5	0.36
Input power, GW	56.	140.
Spectral density	10.6-μm band, 6 lines.	

Front End Optics (J. L. Munroe).

Design. We have prepared a conceptual optical design for the front end, which includes angularly invariant mirror subassemblies and eliminates stable parasitic paths. We have also shown that Fresnel diffraction will not significantly reduce the coupling efficiency between the final driver amplifier and the input optics to the PA.

Code Development. To complete this optical-interface study we have generated two programs: NEARF is a near-field diffraction code that solves the Fresnel diffraction integral for circular and annular beams, whereas EULER analyzes the tilt and

decentration sensitivities of plane-mirror combinations or subassemblies.

Analysis. The particular conclusions resulting from the interface analysis are:

- Beam spillage from diffraction is not a serious loss mechanism.
- No beam aberrations are incurred for reasonable tilt and decenter in the afocal system (from the front end to the PA).

Power Amplifier (K. Jones, W. Sweatt, P. Wolfe, R. Bjurstrom).

Design. A revised optical design for the PA is being detailed (Figs. II-10 and II-11). This new design differs from the one discussed previously in Progress Report LA-6834-PR. The present design reflects new optical design concepts, provisions for retrofits of electro-optical subassemblies, and design provisions for beam alignment subsystems. Specifically, the path-length equalization mechanism, Mirrors 5 and 6 in Fig. II-10, form an angularly invariant subassembly that can incur small angular tilt and decenter deviations, with the result of producing only small decentering errors without inducing pointing or tilt errors on the following mirrors. The decentering errors can be compensated for with slightly oversized mirrors. The spatial filters work with smaller f-number focusing systems.

Relay optics Mirrors 10 through 13 in Fig. II-10, also form an angularly invariant subassembly. The optical beam aberrations induced by the large incident angles on the powered mirrors have been balanced out to less than λ/100. Mirror 13 (Fig. II-10) provides for a region of beam overlap for retropulse isolation. The area ratio of the beam at the input NaCl Window 9, and Mirror 13 (Fig. II-10), is about 3, which allows for additional retropulse damage protection of the NaCl windows.

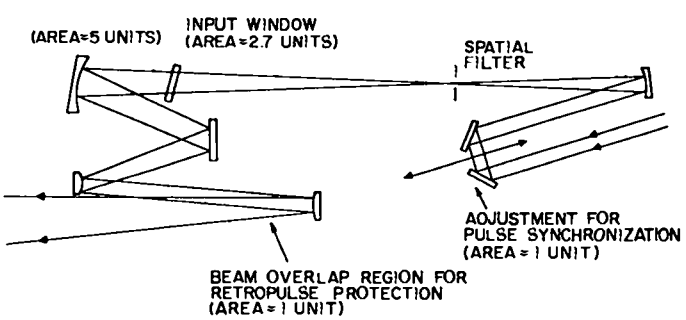

Fig. II-11.
Optical schematic of Antares power amplifier input beam.

A back reflector spool (Fig. II-9) has been added that can be retrofitted with a salt window, Window 14 (Fig. II-10), to form a gas saturable-absorber cell assembly. The primary purpose of the saturable absorber is to provide a means of suppressing target/PA parasitics and secondly to suppress the possibility of certain PA cavity parasitics. The removable spool also allows for easy removal of the electron-gun vacuum vessel.

The periscope mirrors (Mirrors 17 and 18, Fig. II-10), will be assembled as an angularly invariant modular subassembly. The optical spools and domes, which contain all the amplifier optics (Fig. II-9) can be prealigned optically and be positioned and removed independently. Access ports have been designed into all the optical spools for ease of maintenance of the enclosed optical systems (Fig. II-9).

Optical support structures are designed to greatly reduce optical-component movements induced by both static and dynamic loads, thereby easing the automatic beam-alignment requirements. Design provisions have been made for optical baffles, aperture stops, and beam dumps to reduce stray reflections and diffuse scatter, thereby reducing the possibility of parasitic cavity modes. Design provisions have also been made for the possible incorporation of retropulse-active isolators in the relay and the in/out optical sections (Fig. II-9). A diagnostic spool (Fig. II-9) will be incorporated for easy accessibility and subsequent diagnostic measurements of the 12 beams from the periscope optics; and automatic beam-alignment systems from the front end through the PA to the target will be installed.

Code Development. To facilitate the development of the new designs, a number of new codes have been written and others improved. These are: EULER and NEARF, also used in front-end analyses—with the former analyzing tilt and decentration sensitivities of plane mirror combinations, and the latter solving diffraction integrals of circular and annular beams.

ACCOS V has been set up for a three-dimensional representation of the PA and target optics. MINI-ACCOS V is a small and faster version of the ACCOS-V program compiled with the support of the University of Arizona. FRINGE 2, obtained from the University of Arizona Optical Sciences Center for reducing and interpreting interprograms of optical components and assemblies, is used to qualify and quantify all the major optical components of Antares and, in some cases, will be used both by vendors and LASL. Efforts are under way to standardize its use and interpretation.

OVERLAP, the optical breakdown model of inverse bremsstrahlung, has been modified. The modifications consist of introducing an electron-ion recombination electron-loss term and an x-ray generated electron-density term. This code has been applied to the Antares retropulse analysis task.

Finally, NONUN, an energy-extraction rate-equation code, has been developed for examining the combined effects of spatially nonuniform initial gain, input energy density, and first-pass gain depletion on the uniformity of output energy density from the Antares PA. Because of its speed, it has been possible to apply this code to many parametric energy-extraction studies. Selected comparisons with the coherent pulse shape code used in the past have verified the accuracy of the faster code.

Analysis. The following specific conclusions as to the optical performance of the PA have been drawn.

Alignment Sensitivity. No beam aberrations due to reasonable tilt and decentration exist in the afocal system (front end to target chamber). Most sensitive to tilt and decentration is the section between the diverging and collimating mirrors, Mirrors 13 and 15, respectively (Fig. II-10).

Diffraction Analysis. Beam spillover from diffraction is not a serious loss mechanism. The phasing of the individual beams has little impact on encircled energy, and the expected quality of the optical components will result in a very small loss of encircled energy. If the gas saturable absorber is required, the salt window used in the cell must be of the highest quality, because any incurred phase-aberration errors are added coherently to the double-passed beam.

The only significant energy loss mechanisms would be vignetting in the main portion of the optical train if accurate angular alignment is not achieved.

Energy Extraction. Output nonuniformity is almost entirely due to gain nonuniformity; input nonuniformities are masked by saturation, but first-pass gain depletion effects are offset by gain recovery that occurs in the 10-ns elapsed time between passes.

The objective output energy is readily obtained without exceeding optical damage thresholds anywhere in the beam. Tradeoffs between optical input and amplifier gain show ample design margins.

If needed, two alternatives for improving parasitic stability are workable from an energy extraction point of view: (1) operation at increased pressure (reduced gain for equivalent stored energy) and (2) incorporation of a saturable absorber between passes (to decrease gain substantially, while only minimally affecting energy extraction). Figure II-12 demonstrates these principles and also shows the input-gain tradeoffs mentioned above.

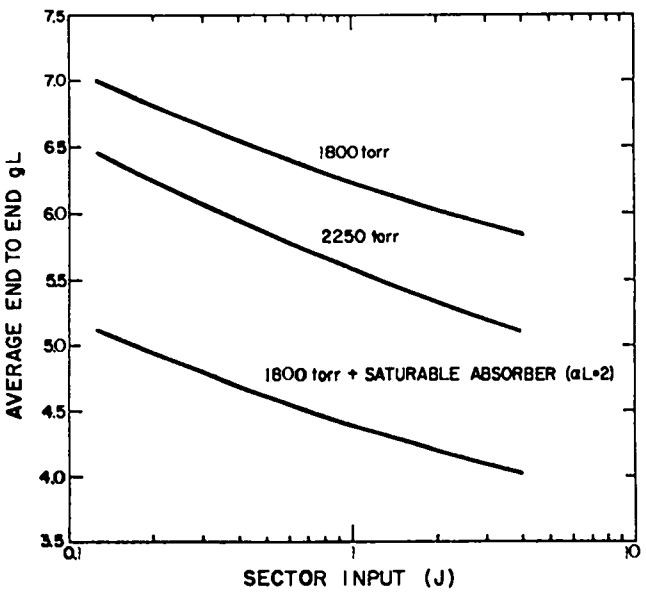

Fig. II-12.
Effect of increased pressure and/or inclusion of a saturable absorber on small-signal gain in Antares power amplifier.

Parasitics. The Antares parasitic analysis results are explained with the use of Fig. II-13. Even in the worst-case analysis, i.e., at a target reflectivity of 100% and with no saturable absorber gas cell, the total accumulated energy density on target is only 1% of that required for target damage. When a gas cell is used with an absorption coefficient of 2, the margin for target protection increases by a factor of 10^4 and the timing is less critical for the pulse extraction with respect to the peak gain point of the PA.

Retropulse Protection. Retropulse analysis for the Antares PA indicates that the maximum energy density of the returning retropulse is incurred at expanding Mirror 13 (Figs. II-10 and II-11). The input salt Window 9 (Figs. II-10 and II-11) is the next vulnerable optical element. The energy density estimated at these two elements is 6.0 and 2.0 J/cm², respectively. These values are below the damage thresholds for copper mirrors and NaCl windows, respectively.

Beam Alignment and Diagnostics. With the completion of the end-to-end optical-system point design and after detailed design of the PA, we are conducting a systematic analysis of alternatives for beam alignment, sampling, and diagnostics. Tradeoffs with respect to the primary and secondary requirements, costs, construction, and integration schedules are being considered.

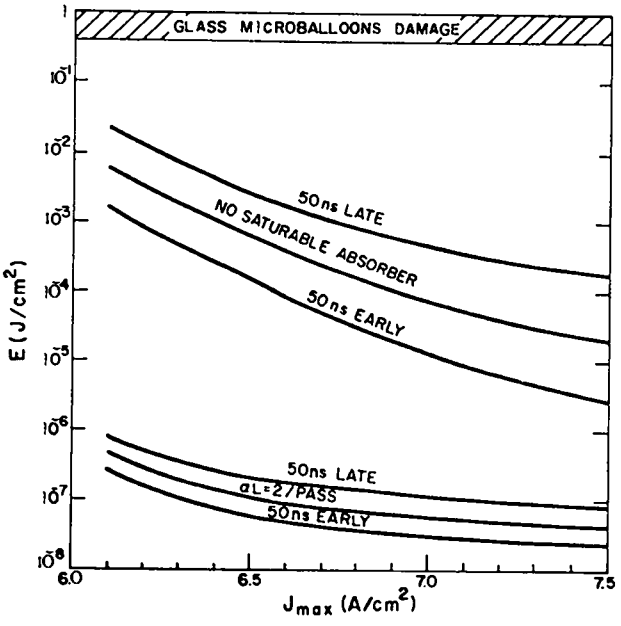

Fig. II-13.
Calculated energy densities of target microballoons due to Antares prepulse parasitics.

Target Chamber Optical System (J. Munroe, W. Sweatt).

Optical Design. The optics for the PA and the target chamber are being designed to minimize the sensitivity to gross motions resulting from the pressurization of the PA and from the evacuation of the beam tubes and target chamber.

A three-dimensional representation of the PA and target optics from the collimator mirror to the target has been set up on ACCOS V. This model is being used to determine accurate mirror sizes and to verify beam sizes.

Diffraction Analysis. Phasing the individual beams has little impact on encircled energy. The main mechanisms of encircled-energy loss are: diffraction by the separations between the sectors, possible vignetting in the target-chamber optics, and aberrations introduced by misalignment of the final focusing parabola.

Beam Alignment. We have completed the calculations describing the effects of pointing errors. Analysis shows that a pointing error of ±4 arcseconds reduces the encircled energy at a 400-μm-diam spot from 82 to 80%.

Outside Contracts (W. H. Reichelt).

Hughes Research Laboratory Study. The first phase of the contract titled "Evaluation of the Optical Design and the Application of Adaptive Optics to the HEGLF System" has been completed. The specific conclusions reached regarding the Antares optical design are mentioned in this semiannual report. The final conclusion is that deformable optics will not be required for the Antares optical train, if the optical components actually installed meet the specifications.

University of Arizona Support. An effort is under way to standardize the use and interpretation of FRINGE 2, which is the primary code for reducing and interpreting interferograms of optical components.

We have begun an analysis and design effort to provide for an integrated, end-to-end optical design of baffles, stops, and contoured apertures that suppresses stray reflections throughout the Antares system.

The Laser Optical Transport System (LOTS) code is being modified to perform diffraction optical transfer function calculations for trapezoidal apertures and fast Fourier transforms of trapezoidal beam profiles.

Y-12 Single-Point Diamond-Turning Activities. After the successful figuring of the EBS parabolic mirrors, the optical turning facility was converted into a separate, environmentally quiet installation that will be used only for the machining of optical components. An additional Moore contouring machine has been procured, which will incorporate all the improvements developed over the past several years, e.g., laser interferometric control. Development work continues in the areas of nondistorting part fixturing, figure improvement through machine-error correction, and linear motor-drive development.

Antares NaCl Window Procurement and Development—Harshaw. The production program at Harshaw Chemical Co. is being defined. Delays in final contract negotiations have demanded a reassessment of the proposed schedule. With the addition of one furnace for crystal growth, we anticipate no problems in meeting the window requirements, the lead item for timely completion of the Antares laser system.

Harshaw Chemical Co. is investigating the Kyropoulis/Czochralski growth technique, an alternative approach to the conventional stockbarger growth process. With this process Harshaw has grown 43-cm-diam by 23-cm-long boules. This process promises to be more cost- and time-effective than the Stockbarger process.

Antireflection Coating of NaCl Windows - OCLI. The Fresnel reflections at window surfaces in Antares have several consequences: (1) energy loss through an uncoated window is ~8%, and (2) the reflections can induce parasitic oscillations, which limit laser performance. Optical Coatings Laboratory, Inc., under contract to LASL, has successfully coated 20- and 40-cm-diam polycrystalline NaCl windows. These single-layer NaF coatings have successfully passed tape and abrasion tests. Damage thresholds measured on these surfaces reveal the importance of surface processing. The latest damage tests on the coated windows indicate a damage threshold of ~6 J/cm^2 for a 1.2-ns pulse. Surface reflectances are on the order of 0.5%. One AR-coated window has been placed in the EBS for prove-in. The success of the program is due in large measure to the combined efforts of Optical Coatings Laboratory and Harshaw Chemical Co. The latter provided the NaCl window and certain processes.

Air Force Weapons Laboratory (AFWL) Support. We are supporting a polishing effort at AFWL. Polishing of alkali-halide windows is of interest both to LASL and to AFWL because both are engaged in large CO_2 laser programs. We have provided an annular lap specifically for the investigation of polishing 16-in.-diam NaCl windows. The lap has been installed at the Development Optical Facility at AFWL. A complete NaCl polishing program is being formulated.

Optical Evaluation Facilities (R. Williamson). The 35.5-cm Zygo interferometer has been installed and is operational. This instrument is extremely valuable in the characterization and evaluation of EBS NaCl windows and mirrors. Both surface characteristics and transmission through the windows are determined. A computer terminal with a platen digitizer has been connected to a computer that contains FRINGE 2 and permits almost immediate interferogram reduction. A 40-cm Davidson collimator is operational in the visible (6328 Å) and at 10.6 μm; it is used in the evaluation of pointing concepts for target acquisition.

Front End System (W. T. Leland)

A design study has been performed for the output stage of the Antares front end. Various alternative

approaches of providing the required six annular beams for Antares PAs were considered.

The selected approach involves the straightforward scheme of selecting an annular output beam from a rectangular amplifier medium. The discharge region will be used as a triple-pass amplifier, thus providing good use of the gain medium. An on-axis Cassegrain telescope system of optics will be installed, which is insensitive to parasitics due to the inclusion of gas saturable absorbers. The annular output-beam configuration requires an output energy of 230 J (for a nanosecond pulse) in a square aperture from which the annular beam is geometrically extracted. Various configurations of gain-medium cross section, length, gain-length product, pressure, and gas mixtures can be used to achieve this performance. The selected parameters (a 15- by 15-cm cross section, a length of 2 m, a gain-length product of 7 for a $1{:}4{::}N_2{:}CO_2$ mixture at 1200 torr) are somewhat arbitrary and, in many instances, chosen to accommodate other considerations such as power supply design and gain uniformity. As a result of calculations relating to gain uniformity and energy extraction, we believe that these design parameters are adequate.

Detailed cost, in-house effort requirements, and performance characteristics have been determined. They were used in a comparison study of alternative solutions, including a detailed in-house design of a suitable module and procurement of commercially available units that could meet our requirements. We decided to procure a suitable amplifier system, power supplies, and controls in total from an outside vendor. A set of specifications based on the above-mentioned studies is being prepared.

Power Amplifier System

Introduction (R. Stine). Consolidation of optical, mechanical, and electrical requirements resulted in complete drawings for the PA. The optical baseline design that defines the optical path through the PA has been completed. Electrical design progressed to the point where mechanical hardware drawings could be completed. Figure II-14 shows the PA configuration. The longitudinal cross section defining the major sections of the PA is shown in Fig. II-9. The collimating back reflector spool incorporates provisions for a gas absorber cell. Next, the spacer spool reflects the design to tie the electron gun tightly to the outer shell. The four pumping-chamber sections follow. The salt-window dome has provisions for mounting the large output salt windows as well as the relay optics. An access spool is mounted between the salt-window dome and the in/out optics section to allow man-access to both the salt-window dome and the input optics.

The in/out optics section contains the beam splitter, as well as provisions for path-length sequalization and spatial filters. The periscope section, to compress the output-beam diameter, makes up the rest of the in/out optics section. A small beam-tube section between the in/out optics and the beam-tube bellows, completes the PA. This section is removable and allows replacement by the separate diagnostics spool, shown in Fig. II-9, for initial PA checkout.

All interfaces for the PA have been defined. Interfacing with the front end is the vacuum input window, located at the bottom of the in/out optics section. At this point, the front-end beam will be annular, 15 cm o.d. by 9 cm i.d. Total input energy will be less than 100 J. The interface at the output of the PA with the target vacuum system will be the flange at the bellows. At this point the beam is annular, with 12 sectors. The beam size will be 1.68 m o.d. and 1.17 m i.d. The energy for a 1-ns output pulse will be 17 kJ.

Interfaces for the control system have also been defined. The control system has three major components: (1) the optical controls, (2) gas and vacuum system controls, and (3) PA monitors.

A preliminary gas and vacuum system design that defines the system requirements has been completed. This design includes a mechanical roughing pump, which is part of the building facility. The vacuum pump for the electron gun is a turbomolecular pump with a rotary-vane backing pump. The system is designed to provide a base pressure of 2×10^{-6} torr and to cope with a maximum leak rate of 5×10^{-7} std atm-cm^3/s. The laser gas system is designed to use dynamic flow controls.

The energy storage system interface for the gas pulser is the high-voltage cable termination at the gas pulser. The interface for the gun pusher is the coaxial feed bushing located between the gun pulser

tank and the electron gun. Performance requirements for both the gas pulser and the gun pulser have been defined.

The optical-system interface consists of four parts: (1) the diagnostic system which includes the diagnostic spool and provisions for measuring small-signal gain, (2) the alignment system with its sensors and readouts; (3) parasitic suppression components including baffles and apertures, antiparasitic coating, and dielectric dividers; and (4) the retropulse protection system.

The Laser-Hall interface includes three items: (1) the support-stand floor loading and connection to the Laser-Hall floor; (2) clearances within the Laser Hall for electron-gun removal, optic-shell removal, high-voltage cable support structures, recessed cable trenches, and door sizes; and (3) alignment bench marks to facilitate the placement of the PAs at their precise locations.

A change order has been submitted to raise the roof of the Laser Hall by ~1 m. This will increase the overhead crane hook height from ~8 m to ~9 m, so that the optics sections can be lifted high enough to clear the other PAs without turning the sections when they are removed for maintenance. The recessed cable trenches alongside each PA have been moved out by ~15 cm to provide clearance for the PA support structure. Several doors within the building have been enlarged to allow the optics shells to be moved from the Optical Evaluation Laboratory and maintenance facility to the Laser-Hall floor without being rotated. Coordinates have been defined to locate the input beam from the front end and to define the hole in the 1-m-thick concrete floor. The optical tunnels from the front end have been moved to line up with the PAs and thus to make it easier to locate the input beam exactly.

The critical PA items in terms of lead time have been defined; these include the pumping-chamber outer shells, the salt-window dome, the back-reflector shell, the electron-gun vacuum vessel, and the coaxial feed bushing. The electron gun is the pacing item because it has to be fully assembled and checked out before being installed in the PA. The plastic coaxial feed bushing is a critical item because a prototype must be fabricated and checked out first.

Optical Design Impact (R. Stine). The impact of the optical design on the PA is discussed below. The longitudinal cross section of the PA is shown in Fig. II-9. The input optical interface will be the vacuum input window at the bottom of the in/out optics section. Provision for a path-length equalizer has been made. The input salt window to the pressurized portion of the PA is an 8-cm-diam window above the main output salt window. The relay optics will provide both beam overlap for retropulse protection as well as beam expansion, which reduces the energy density of the retropulse at the input salt window. A saturable gas absorber cell has been incorporated into the back-reflector design; the cell has provisions for adding salt windows at a later time. The design of the output salt window and of its mounting has been based on EBS experience: two O-rings are used to float the salt window in the metal frame, and the window was tilted upward at ~6° to prevent reflections, which may cause parasitic oscillations, from hitting the anode.

The output optics in the periscope section are being revised to provide maximum beam area. The second periscope requires provisions for remotely controlled tip and tilt, but the first periscope mirror needs only a manual adjustment. Exact mirror locations have been defined by the mechanical mounting requirements, and this information has been incorporated in the optical design. Tip and tilt, as well as movement, have been defined for several mirrors including the back reflector and the second periscope. One or two other mirrors will also require remote control. However, the keystone of the optical design has been the desensitization to movement of as many mirrors as possible. The result is a much simpler control system. Vibration tolerances at each mirror location are being analyzed.

Requirements for access to optical components have been defined resulting in man-access of the in/out section, the diagnostics section, and the salt-window dome. Also, all optical components within the PA pressure vessel are accessible after removal of the electron gun. Hand-access ports have been provided in the in/out section for the spatial filters.

Mechanical Design (G. Ross). The preliminary mechanical layouts for the entire pressure vessel, and final designs and hardware drawings for a number of sections, have been completed. The vessel has four pumping-chamber sections and one spacer section between the pumping-chamber sections and the back reflector spool, as shown in Fig. II-9. The

spacer section acts as a static-load ring to retain the electron gun within the pressure chamber. Provisions for 12 anode penetrations have been made in the pumping-chamber shells; these oversized holes accept any of the bushings for the cables under consideration. The gun-support system has been designed and an experiment defined to test the air bearing concept. The back reflector design has been modified to incorporate the gas-absorber cell. Elliptical heads are used to minimize the stresses in the optical support structure. The salt-window dome drawing has been completed; it shows an elliptical head welded to a cylindrical section. An in/out optics section layout has been completed, which incorporates optical mountings for the input optics as well as for the periscopes. This section also used an elliptical head. A diagnostic section has been designed to fit between the in/out optics and the bellows section.

Detail drawings for the electron-gun vacuum vessel have been completed. The design is based on the PA prototype. Four separate rolled sections, electron-beam welded after machining, are used. A vacuum spool has been added to the rear of the electron gun to provide a vacuum and a pulse-power interface. Provision for electron-gun removal has been made. The design requires that the back-reflector optical section be removed before the gun can be lifted out. Handling fixtures for both the back-reflector section and the electron gun will permit quick, damage-free disassembly and assembly. A development program for electron-beam foil-support structures in which titanium foil is brazed to punched stainless steel backing plates has been completed successfully. This design provides a rip-stop feature and prevents the entire foil from tearing if punctured.

Dynamic Analysis of Antares Facility (W. Miller). The computer model of Antares facility structural dynamics yielded predictions of foundation response. These predictions will be used to obtain the dynamic response of the optical support structure in the vicinity of critical optical structures, e.g., PA, preamplifiers, and target chamber.

Predictions derived from this model have been compared with actual foundation responses for the EBS and other technical facilities. This comparison, which was to substantiate the subseismic soil motion used as input to the facility structural model, revealed that the soil displacement amplitudes used as input to the model in the lateral direction were appropriate, but those in the vertical direction were too high by a factor of 2.

On the basis of this evaluation, we established an envelope of foundation response in the Laser Hall for structural dynamic design analyses of the PA. The envelope provides an upper limit of the floor response that the subseismic and machinery-induced vibrations will not exceed. For example, the foundation response above 25 Hz will be less than 0.025 μm. A structure designed with its fundamental resonant mode above this frequency will limit the dynamic motion of the optical supports to a tolerable level.

Power Amplifier Internal Optical Support Structures (W. Miller). The baseline optical-support-structure design for the PA uses internal supports for the optical structures, as shown in Fig. II-14. This design approach is preferred over an external support arrangement because it facilitates handling of the optics and is less expensive. Much of our initial concern regarding the dynamic behavior of the optical support structures and its effect on the PA assembly has been alleviated through refinements in the design approach and structural analyses.

The optical support structure for the in/out optics section has been studied in detail using SAP IV, a computer code for structural analysis. The results

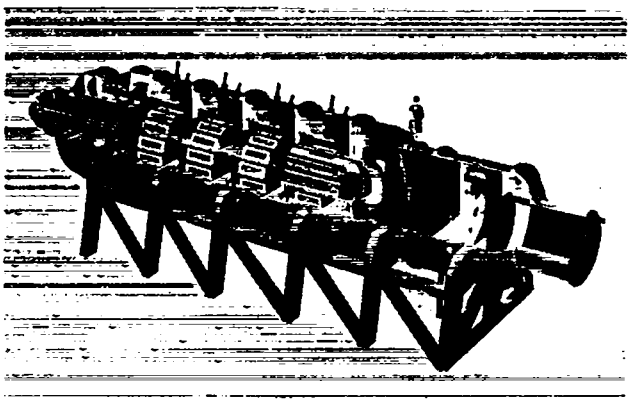

Fig. II-14.
Antares power amplifier configuration.

have been extended to assess the preliminary design arrangements of the other optics housed within the PA. An all-welded structure, bolted to the PA shell, has been selected for the in/out optics section. The structure is composed of two aluminum face plates, each 5 cm thick, separated at a distance of 1.22 m by twelve 2.5-cm-thick aluminum radial webs. The radial webs provide a sandwich construction that resists shear forces. Individual 30-cm-thick honeycomb panel structures were also considered, but costs were prohibitively high.

A finite-element structural model of this optical support design has been used to predict static loads and structural resonant conditions, i.e., frequencies and mode shapes. The model included the external shell and the end closure bulkhead. The results revealed that:

- Optic base-plate distortions that stem from the 1-atm shell pressure load are less than 4 arcseconds;
- The plate structure's lowest mode, i.e., along the PA's longitudinal axis, is above 100 Hz. This value does not include the effect of the mirror masses, which would decrease the fundamental mode somewhat, although not extensively.

Structural deformations due to the static shell pressure load are well within optical alignment tolerances and will not result in vignetting of the beam. If the optical system is aligned before the optics section is evacuated, a small adjustment in the beam steering mirror will be sufficient to correct the beam alignment.

Structural resonance of the lowest mode is higher than our design goal (35 to 50 Hz), which ensures that the dynamic response of the structure is within acceptable bounds. Dynamic motion of the optical mounting surfaces, e.g., beam jitter, cannot be corrected once the system is completely assembled. Therefore, significant design effort was expended to ensure that the dynamic motion will be well below the optical requirements. Preliminary design arrangements of optical support structures have been established for the relay and back-reflector optic sections. Evaluation of these design approaches using finite-element methods has not been completed. However, engineering estimates of their structural stiffness gives us confidence that the design specifications will be met.

Electrical Considerations (R. Lindstrand). Design and analysis of the anode structure and the anode bushings have been completed. A safety factor of 1.7 was provided for these units. The PA pumping-chamber anodes have been analyzed with respect to their high-voltage standoff capabilities. It has been determined that corona rings will be required to prevent electrical breakdown to the amplifier shell walls. The anode design is being reviewed, and a test on the prototype PA is planned to determine whether individual anodes may be interconnected to decrease the number of high-voltage cables required.

Several options for anode bushing design have been considered for the PA including water bushings, oil bushings, solid bushings, and gas bushings. A final decision on the design awaits selection of a high-voltage cable,but all the bushing designs considered are electrically acceptable.

During tests of both the prototype PA and the high-voltage test module, the 138-kVac standard power cables showed a high failure rate. Analysis of the data indicates that these cables will produce an unacceptably high failure rate in the PA. Two alternatives were identified and cable samples have been procured: A dry-cured polyethylene cable rated at 220 kVac that utilizes a different curing process to reduce voids and improve performance; and an oil-impregnated, paper-insulated cable using a high-viscosity impregnant, capable of withstanding very high stresses. The first cable will be tested early in 1978. A test facility is being designed to test several cable lengths simultaneously and to obtain adequate data to establish cable life expectancy.

The electron-gun design remains basically a cylindrical grid-controlled cold-cathode type. A cost analysis was completed, and a capacitively graded gun-support bushing was selected over a straight vacuum bushing. A bushing of essentially the same design has been used successfully in the prototype PA. Tests in the high-voltage test module indicate a voltage safety factor higher than 2 for this design. A 1.37-m-diam coaxial feed bushing will provide the interface between the electron gun and the gun pulser. Computer-assisted electrostatic field analysis indicates a safety factor higher than 5 for this bushing. The bushing will also be tested electrically in conjunction with the gun pulser.

The grid cathode will use a continuously welded stainless-steel grid. This design was used because prototype testing indicated that grid emission could result either from the use of aluminum materials in the grid structure or from joints in the grid structure itself. Tests in the prototype PA and the test vehicle have been completed to determine the spacing from grid to cathode and from grid to anode. The spacings have been minimized while diameters have been maximized to reduce the current-induced magnetic field deflections in the electron beam.

Energy Storage System (K. Riepe)

Overview (K. Riepe). The energy storage system supplies the high-power, high-voltage pulses to the gas discharges and electron guns in the PAs. It consists of 24 gas pulsers and 6 electron-gun pulsers. The gas pulsers are Marx generators, which operate as impedance-matched single-mesh pulse-forming networks (PFN). Each pulser stores 300 kJ at 1.2 MV open circuit voltage, and has a short-circuit current of 400 kA. The gun pulsers are two-mesh PFNs, storing 28 kJ at 1.3 MV open-circuit voltage.

Because of the number of pulsers required, their complexity, and the need for high reliability, prototypes of both pulsers are being built. In addition, development work on high-current capacitors, high-current spark gaps, and solid high-voltage resistors has been performed. The resistors will be used in place of the liquid resistors usually used in Marx generators.

Gas Pulser (K. Riepe). The prototype gas pulser has been assembled. Because the development of 400-kA spark gaps has not been completed, the pulser has spark gaps that are not rated for the pulser full-charge short-circuit current and, because the solid resistors have not been developed, it will have liquid charge and trigger resistors. These will be replaced when development is completed.

The pulser has been operated in air at ±10 kV charge with a short-circuit load to measure the inductance. With the original spacings the inductance was 3.8 μH. Because the goal was 3.0 μH or less, some spacings had to be decreased, which reduced the inductance to 2.9 ± 0.1 μH. The decreased spacing will cause no breakdown problem, the highest field being 40 kV/cm, but it does make assembly more difficult.

The spark-gap self-breakdown voltage at 0 psig is 50 kV. The Marx erected reliably at 20 kV on the gaps (safety factor, 50 kV/20 kV = 2.5). We intend to operate with a safety factor of 2.0 to keep the prefire rate low. It appears that the trigger coupling scheme will allow low-jitter operation at this high safety factor.

Electron-Beam Gun Pulser (G. Allen). The computer model of the electron-beam gun pulser has been refined to include the inductance and capacitance of both the multicoaxial gun feed line and the gun electrode structure (Fig. II-15). In addition, a peaking circuit has been added to the output of the pulser to ensure adequate ignition properties. The model also incorporates the impedance of a space-charge-limited diode impedance between the cathode and the grid. With these new model features, the computed waveforms give a relatively accurate estimate of the actual waveforms. A typical cathode voltage waveform (Fig. II-16) shows the high rate of change of voltage (dV/dt) provided by the peaking circuit and the subsequent slower rise of the pulser.

The ratings of the components chosen for use in the pulser exceed the normal and fault conditions sufficiently so that the expected pulser lifetime is on the order of 100 000 shots.

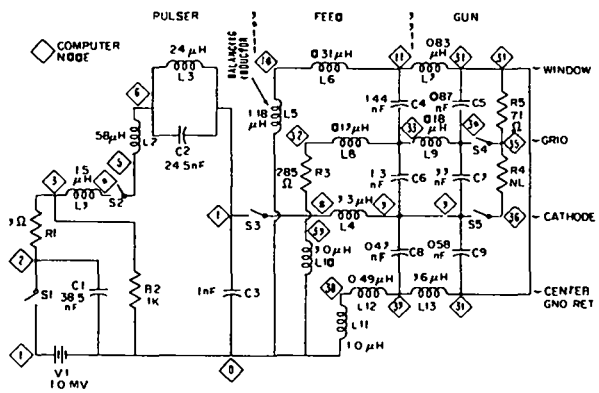

Fig. II-15.
Computer model of gun pulser and electron beam gun.

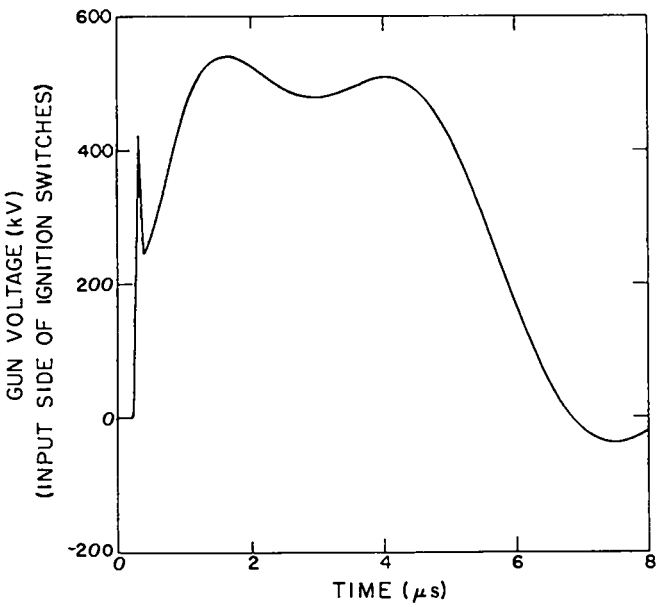

Fig. II-16.
Typical cathode voltage waveform for Antares electron-gun pulser.

A layout of the prototype gun pulser components and a tank design have been completed. All components are on order and the tank is ready for fabrication.

Component Development (J. Bickford). The component development and testing program in support of the energy storage system has concentrated on three areas: high-current capacitors; high-current spark gaps; and high-energy, high-voltage solid resistors.

Capacitor Testing. The peak fault current per capacitor in the gas pulser is 130 kA. We felt that this high current might burn the soldered connections inside the capacitor. Two capacitors, rated at 1.85 μF and 60 kV, manufactured by Maxwell Laboratories, were tested at 200 kA (250 kHz ringing frequency, 85% reversal). One was tested for 4000 shots, the other for 5000 shots. Neither showed significant damage to the internal connections.

Spark Gap Testing. The fault current per spark gap in the gas pulser is 400 kA, with 6 C charge transfer. Spark gaps were purchased from Ion Physics Co., Maxwell Laboratories, and Physics International for qualification against this requirement for 1000 shots. None of the gaps met the requirements, but the following knowledge was gained.

- Acrylic and urethane insulators are too brittle. They fail under the pressure impulse of the discharge. Cast nylon with a 19-mm wall is suitable.
- It is very difficult to make high-current connections to aluminum end-plates.
- Sintered and pressed copper/tungsten electrodes appear to be suitable. Pure molybdenum is not; it flakes off the surface.

Nylon compression rods stretch under the pressure impulse. Stronger rods, such as Permali, are required.

Testing will continue to determine the optimum electrode materials, end-plate materials, and spark-gap diameter.

Resistor Testing. Charge and trigger resistors in Marx generators are usually liquid electrolytes in flexible tubing. These have a tendency to leak. Because of the number of resistors involved in the energy storage system, a more reliable resistor design is required. Calculations have shown that a gap prefire can dump 10 to 15 kJ into the resistor string of a stage. We have tested several solid resistor designs for energy handling ability and voltage holdoff.

The wire-wound resistors tested were rated at 225 W, and had been manufactured by Dale Electronics. They failed at an input of 600 J. The failure is apparently due to the high temperature of the wire affecting the resistor coating.

Two models of carborundum resistors were tested. Model 106-AS, 100-Ω, "pencil-shaped" resistors are solid, 15 cm long, 6.4 mm in diameter, rated at 1900 J. Model 889-AS resistors are hollow, 25 mm o.d., 19 mm i.d., rated at 35 kJ.

A Model-889 resistor failed at 3.6 kJ after soaking in oil for four days. The failure mechanism is apparently vaporization of the oil that has soaked into the resistor material, which causes chipping of the surface of the resistor.

Model-106 resistors were purchased with an epoxy coating to prevent oil from soaking into the resistor material. After soaking in oil for four days, these

units failed after58 shots at 750 J/shot. Dry, unsoaked resistors, tested in air, ran for 300 shots at 2 kJ without failure.

Another sample of 106-AS resistors that had been coated with polyimide high-temperature varnish is being tested.

Target System (V. L. Zeigner)

Focusing System (V. L. Zeigner). The size of all elements in the target focusing system has been reduced, increasing the beam energy density at the focusing mirrors to 3 J/cm^2.

The size was reduced by converging both the individual beam sectors and the beam arrays, each of which consists of 12 sectors. Beam-sector convergence begins at the back reflectors in the PAs; whereas beam convergence starts at the output of the PAs, i.e., at the second element of the periscopes.

The result of this reduction is appreciable: The diameters of focusing mirrors are reduced from 1.68 to 1.32 m; folding mirrors are reduced by essentially the same amount; turning mirrors are reduced by about two-thirds as much. This permits us to reduce the target-chamber diameter from 7.6 to 6.9 m and its length from 6.0 to 5.8 m. The beam tubes between the turning-mirror chambers and the target chamber are reduced from 1.88 to 1.65 m in diameter.

Preliminary calculations have indicated that the natural frequency of the space frame for the focusing system has increased by ~30%, due simply to its smaller size and reduced weight.

Manpower has not been available to begin the actual engineering design of most of the hardware for the focusing system, with the exception of the mirror positioners, as noted below.

Mirror Cells (D. Blevins)

Mirrors. Aluminum alloy 2124, a low-iron, low-silicon, metallurgically cleaner version of 2024 aluminum alloy, has been selected as the most promising material for mirror substrates. From the literature, and from consultations with outside organizations, it offers excellent stability, high yield strengths, and excellent plating characteristics. Its dimensional stability will be verified by tests at Southwest Research Institute. We are procuring an initial process prove-in batch of fourteen 2124 substrates. They will be plated by the plating vendor selected by Y-12, and samples of the plated substrates will be diamond-turned for a final check on plating quality.

Mirror Positioners. All parts for the prototype mirror positioners except the special bearings are on hand or have been shipped. The special bearings are expected by the end of January 1978. Positioners and their actuators will be assembled and checked out in the immediate future.

An improved positioner has been designed and is being drawn up. It uses flexures instead of ball bearings and incorporates a flexure-type level system between the movable face plate and the actuators.

Target Vacuum System (V. L. Zeigner/J. W. Allen). The design specifications for the target vacuum system have been completed and released to DOE in the form of a Request for Proposal (RFP) to be forwarded to the list of potential suppliers. All responses to the RFP are to be in the hands of DOE by 1 March 1978.

Control System (B. G. Strait)

Energy Storage System Controls (D. Call). An energy-storage simulator has been designed and built. It facilitates the development and checkout of the energy storage circuits and software. The simulator charges the capacitor bank to 15 V rather than 550 kV required for Antares.

The controls system configuration has been finalized. The controls for each pulse power system will be housed in a shielded container mounted on the tank of the pulser. It will contain a microcomputer and will interface to the pulser system through fiber-optics. The system will be controlled from the control room through the HP-3000 control computer.

Beam Alignment Controls (D. Gutscher). A beam-centering concept that uses a laser diode and quad detector has been investigated. The concept involves mounting the laser diode with its optics on

the mirror being aligned and placing the quad detector on the support structure close to the next mirror down the beam path. After the mirror has been properly aligned manually, the laser diodes and the quad detector are aligned to produce a null in both axes of the quad detector. Thereafter, the mirror can be returned to the same relative position by aligning the laser diode on the quad detector. The advantage of this concept is the possibility of aligning a mirror independently of the system optics. Therefore, all mirrors can be aligned simultaneously, without requiring a complex alignment algorithm.

Quad detectors and laser diodes have been evaluated for this application.

Antares Grounding Rules (M. Thuot). Design recommendations and grounding rules for the Antares control system have been formulated. The principles and limitations of a practical ground system in a pulse-power environment have been investigated. A ground system for Antares was selected based on consideration of the noise sources, coupling modes, and facility size.

Fiber-Optics Development (M. Thuot). Successful employment of a distributed microcomputer control system for Antares is highly dependent on a well-shielded (electromagnetically) environment for the microcomputers. To ensure shielding integrity, only fiber-optic cables will be permitted to penetrate the shielded rooms or containers (except for power lines).

The fiber-optic development effort centered on defining a complete set of control and monitor fiber-optic interface functions for Antares controls. The following fiber-optic interfaces have been completed: low-error-rate digital communication links between computers; binary fiber-optic power controls for motors and valves; binary fiber-optic status interfaces to monitor switch positions; and analog pulse waveform interfaces for transmitting fast (10 MHz) amplitude-modulated information. Under development are: the voltage-to-frequency converter for transmitting slowly varying analog signals over fiber optics, and the timing and trigger interfaces to transmit reference pulses to controllers that sequence the firing of the laser subsystems.

HP-3000 Computer System (F. McGirt). Several software packages have been completed which enhance the use of the HP-3000 computer. A scrolling editor called SEDIT is operational and will be used in designing man/machine interface software for control terminals. A communications package has been written which will send any printing ASCII message to any terminal. We have begun to evaluate the HP-3000 input/output (I/O) procedures for the terminal multiplexer, multiplexer channel, and selector channel. Detailed understanding of the I/O is required to implement the microcomputer network and the graphics terminals needed for the control functions.

Microcomputer Software Development (W. Seifert). A high-level language from Wintek Corporation has been purchased as a stop-gap measure to support immediate needs in the development of M-6800 microcomputer software. The software package has been evaluated; it includes: PL/W compiler, cross assembler, relocating linker, and a simulator. It will be installed on the HP-3000 computer.

A real-time executive for multitask operation is being developed for the M-6800. The design of the executive is complete; coding and checkout will follow.

PASCAL (J. P. Hong). The study reported in Progress Report LA-6982-PR continued and resulted in the selection of PASCAL as the common high-level computer language. This language has data constructs as well as program flow contructs and, with extensions to facilitate direct bit manipulations, would be well-suited to the development and implementation of controls algorithms. A common language for the HP-3000 and the microprocessors enhances the efficiency of code development. A version of the PASCAL compiler that produces P-Code (code for an imaginary ideal machine) has been obtained for the HP-3000 from LASL's CRAY computer. We have begun to produce a translator that will take P-Code as input and generate as output SPL (HP-3000 language) or assembly instructions for a microprocessor. Progress in this effort included the following: a simple PASCAL P-Code program has been translated and executed; addressing items

in the most recent incarnation of nested dictionaries has been demonstrated; nested calls to functions and procedures have been demonstrated; and all major design concepts for the translator have been tested.

Simulator (J. Gilbert). A simulator has been designed that would act like a microcomputer with its peripheral input/output devices. External device interface specifications are included in any simulation allowing an algorithm developer to write programs and evaluate their performances without the need of hardware. A Software Note details the design and implementation suggestions.

Site and Structures (E. Swickard/J. Allen)

HEGLF Site and Structures. The HEGLF project has two major parts; the Antares laser system and the site/structures construction to accommodate that system. Site and structures are made up of five major buildings, utilities, roads and parking lots, and landscaping. Construction is divided into two packages, I and II.

Construction Package I. Included in this package are the Laser Building, Mechanical Building, Office Building, and Warehouse. The construction contract was awarded to Allen M. Campbell Co. and work started in September 1977. Earthwork and exterior utilities work is on schedule. Two major changes in the original contract are under way: a separate target diagnostics control room is being added and the warehouse design is being modified to provide insulation and heating so that it may be used for mechanical assembly as well as for storage. Completion is scheduled for May 1979.

Construction Package II. The main item in this package is the Target Building; also included is the major part of site landscaping, some access-road widening, upgrade of the area fire-protection water-supply system, and upgrade of the area electrical distribution system. This construction package was awarded in December 1977, also to Allen M. Campbell Co. Completion is scheduled for May 1979.

Optical Evaluation and High-Voltage Laboratories. The construction contract for these two laboratories was awarded to John R. Lairs in December 1977. Completion is scheduled for October 1978.

The Optical Evaluation Laboratory will be used primarily to measure the optical quality of Antares mirrors, NaCl windows, and other optical components. It will also have the capability for limited maintenance of optical items and for small optical system mockups.

The High-Voltage Laboratory will be used in the development and testing of Antares high-voltage components such as pulsers, cable terminations, bushings, and spark gaps. It will also have a capability for maintenance of those components.

III. CO_2 LASER TECHNOLOGY

Each of our CO_2 laser systems described earlier represents a significant advance in the state of the art of reliable CO_2 laser subsystems, components, and diagnostics. The design, construction, and improvement of the systems therefore require basic support of CO_2 technology. Some important areas are: the development of short-pulse multifrequency oscillators, amplifier optimization, development of subsystems for the prevention of system self-oscillation and removal of prepulse energy, improvement of the transverse profile of the amplified laser pulses, and measurements of optical damage thresholds in system components.

GAS ISOLATOR DEVELOPMENT (S. J. Czuchlewski, A. V. Nowak, E. Foley)

Introduction

This was a period of intensive activity in the gas isolator development program, which culminated in the successful deployment of a saturable-absorber isolator in the EBS.

This development was conducted in the following sequence:

1. Identification of gases that absorb in appropriate regions of the CO_2 spectrum, using an ir-spectrometer.
2. Design of broadband multicomponent gas mixes capable of effectively suppressing lasing throughout the CO_2 spectrum. A mockup amplifier was used for testing these mixes.
3. Measurement of the high-intensity, saturated transmission of the proposed mixes in the five 10-μm P-branch lines at which the EBS will operate.
4. Verification that no "holes" exist in the absorption spectra of the mixes by performing very high-resolution diode-laser scans of the transmission spectra.
5. Evaluation of the actual performance of the gas isolators in the EBS.

A detailed discussion of the first 3 stages of this program was presented in LA-6982-PR, where it was indicated that two EBS isolator candidates were ready for performance testing. One of these gas mixtures (No. 630B) was based on SF_6 as the saturable component; the other (No. 628B) was based on FC-152a (CF_2H-CH_3). Results for these as well as a second SF_6-based mixture designated Mix-804 will be discussed in the present report. Table III-I lists the composition of the three gas mixtures.

In a series of experiments, it has been demonstrated that the SF_6-based Mix No. 804 could be used to prevent parasitic oscillations within the TPA of the EBS. In addition, the installation of this isolator enabled the first arm of the EBS to reach design-point operation at 1.2 kJ.

Subsequently, Mix 804 was successfully used in the TBS to deliver 375 ± 41 J/beam on target, a factor-of-2 improvement over the previously measured target energy.

To more fully characterize the physical behavior of the gas isolator, additional high-intensity transmission and absorption recovery-rate measurements were begun. Results obtained to date are described.

EBS Gain Stand-off Measurements

Although the gas mixes can be rapidly and carefully evaluated in the mockup amplifier, the latter cannot exactly simulate the self-lasing characteristics of the TPA for two reasons. First, the laser medium of the TPA is operated at a much

TABLE III-I

COMPOSITION OF GAS ISOLATOR MIXES TESTED IN THE EBS[a]

Mix 630B	Mix 804	Mix 628B
SF_6 = 0.84%	SF_6 = 1.51%	FC-152a = 66.2%
C_4F_6 = 4.0%	C_4F_6 = 4.14%	FC-1113 = 22.2%
FC-115 = 10.0%	FC-115 = 12.2%	FC-115 = 11.6%
FC-1113 = 18.1%	FC-1113 = 19.8%	
FC-12 = 67.1%	FC-12 = 62.4%	

[a]All but Mix 628B depend on SF_6 as the saturable absorber. Mix-628B employs FC-152a (CF_2H-CH_3) for this purpose. Of these, Mix 804 performs most satisfactorily in the EBS. The chemical compositions of the fluorocarbons are FC-12:CF_2Cl_2, FC-115:CF_3-CF_2Cl, and FC-1113:CF_2-CFCl.

higher pressure than that of the mockup TPA amplifier and, hence, the bandwidth of the TPA laser lines (12 GHz) is considerably greater than that of the mockup amplifier (4 GHz). Second, because the mockup is a double-discharge device, whereas the TPA is an E-beam-pumped module, the gain-frequency profiles of the two amplifiers are expected to differ slightly. Consequently, evaluation and "fine-tuning" of the gas isolator mixes in the TPA itself was essential.

In the first phase of these tests the gain standoff capability of the gases was investigated. Electrical problems prevented the TPA module from operating at full gain with the laser gas at its design pressure of 1800 torr. Unless otherwise noted, all data reported here were taken with the laser gas at 1400 torr. Amplifier gain was measured with a cw CO_2 probe laser that traversed a diagonal path, close to the cathode, through the TPA. The gas isolator cell was 75 cm long and located in front of the large turning mirror, so that the laser pulse traversed the cell twice between its second and third passes through the amplifier (Fig. III-1). The self-lasing threshold of the TPA with no saturable absorber was found to correspond to a single-pass gain-length product (g_0L) of 5, measured on the 10-μm P(20) line. This represents a small-signal gain g_o of 0.025 cm^{-1}. Because design point for the system is a g_oL of 8, an isolator with a saturable single-pass, small-signal absorption-length product of 3 was seen to be required.

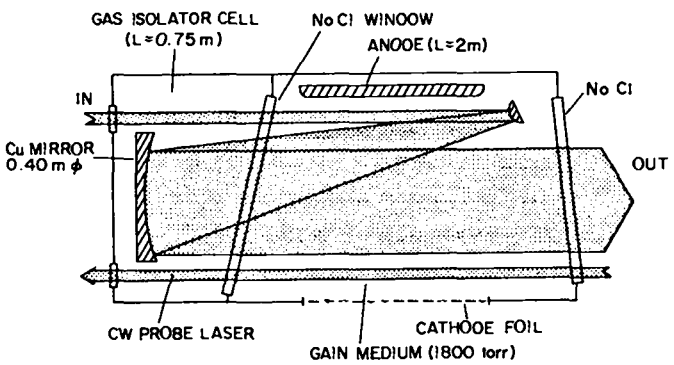

Fig. III-1.
A highly simplified schematic of the EBS triple-pass amplifier. The effective length of the gas isolator cell is determined by the distance (75 cm) between the Cu mirror and the NaCl window, whose tilt is exaggerated in the figure.

Next, the ability of the isolator to effectively provide the needed saturable absorption was determined by observing the increase in the TPA self-lasing threshold (Δg_oL) as a function of gas pressure in the isolator cell. Observed performance of two mixes is shown in Fig. III-2, in which two features are immediately evident. First, the effective increase in g_oL due to either mix is noticeably less than predicted. Second, Δg_oL levels off at a value of ~2, corresponding to a minimum $g_oL \approx 7$ in the TPA

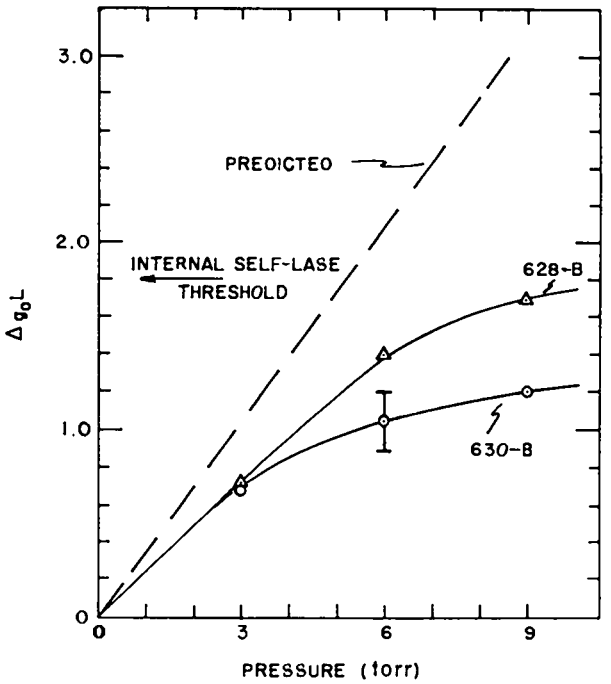

Fig. III-2.
Gain stand-off $\Delta g_o L$ as a function of mix pressure. $\Delta g_o L$ is the increase in the self-lasing threshold that is observed when the gas is added. The horizontal line at $\Delta g_o L$ = 1.8 indicates the gain at which the internal self-lasing mode appeared when the mirror was blocked. This was later eliminated by changing the orientation of the NaCl window at the front of the gas cell.

in this experiment. This behavior indicates the onset of an internal self-lase mode that does not involve the large mirror and hence does not pass through the gas cell. This was caused by reflections from the NaCl window at the front of the gas cell, which was originally tilted at a small angle towards the anode of the TPA. When this window was tilted toward the bottom of the amplifier, this self-lase mode disappeared. Initially, delays between shots permitted the reference self-lase threshold to change significantly. Because of this and the presence of the internal self-lase mode, it is likely that the low-pressure portions of the curves in Fig. III-2 represent the potential stand-off performance of the gases modified by temporary idiosyncrasies of the TPA configuration for these initial tests.

A spectrometer, located at the output of the TPA, enabled us to determine the frequency of the self-lase pulse. For the situation in which the Fig. III-2 data were obtained, lasing always occurred near the 10-μm P(20) line. Because of the spectrometer's low resolution, identification of the lasing frequency was uncertain by ± 2 rotational lines. We could drive the lasing to the 10-μm R-branch by increasing the relative content of SF_6 in the 630B mix. This suggested that the relative gain of the P(20) line, or of an adjacent line, was much stronger than expected for the TPA. Additional stand-off measurements were made with other mixes similar to the 630B mix, except for an enhanced SF_6 concentration, without conclusive results on this point.

Initial EBS Energy Extraction Experiments

In the second phase of these performance tests, the effect of the gas isolators on the output energy of the TPA was investigated. For these measurements, either a Nextel-coated screen or a large Nextel-coated calorimeter was located at the output of the amplifier. The mix (No. 804) employed for these tests was enriched in SF_6 (Table III-I) and immediately provided the desired gain stand-off, although the amount of gas required was again more than was predicted (Fig. III-3). Results of the energy-extraction measurements were highly satisfactory and are presented in Fig. III-3. With 1400 torr of laser gas, 850 J were obtained; on several shots at 1800 torr, energies of 1.2 kJ were observed. The TPA continued to operate at a pumping voltage of only 220 kV instead of its design value of 275 kV.

These measurements showed somewhat more saturation of the gas isolator in the TPA than we would have predicted from mockup experiments. This behavior is believed to be due to a higher-than-expected flux incident on the gas cell, of order 300 mJ/cm^2, or to a radial intensity profile unlike the mockup profile.

Because the gases remain bleached for perhaps a few hundred nanoseconds, it is possible for a self-lase pulse to develop after the passage of the 1-ns main pulse. However, diagnostics with 1-ns resolution showed no evidence of any postlasing, demonstrating that the calorimeter measurements represented useful, short-pulse energies.

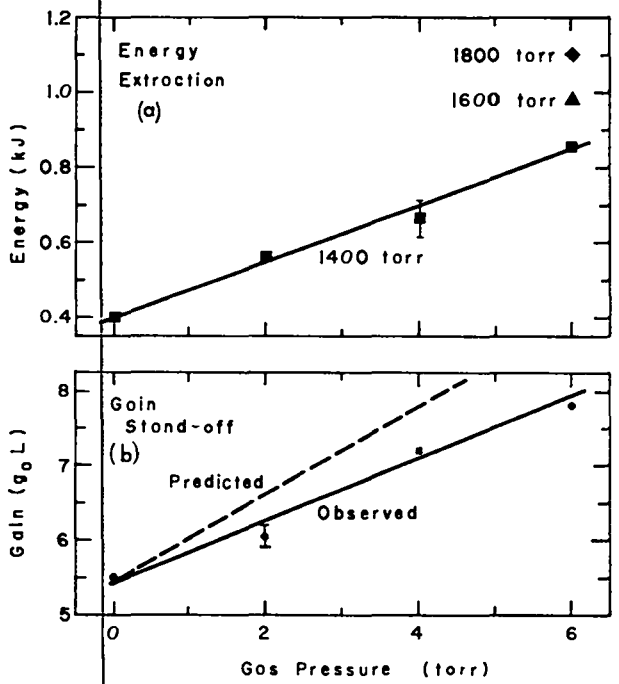

Fig. III-3.
(a) Extracted energy, and (b) Gain stand-off as a function of the pressure of isolator Mix 804. All data are for 1400 torr of laser gas except the two points noted.

TBS Isolation

Following the successful deployment of a broadband gas isolator (Mix 804) in the EBS, a series of tests was initiated to determine whether this isolator could also improve the performance of the TBS. Although the TBS mechanical design does not presently permit installation of a gas cell within the TPA to provide interpass isolation, a 10-cm cell was installed at a less optimum location between the amplifier and the target chamber to decouple the target from the TPA and eliminate self-lasing involving target reflections.

Flat polyethylene targets have presented the most serious self-lasing problem, where on-target energy was previously limited to 187 J/beam when pure SF_6 was used as the isolator. One beam of the TBS was used to compare the effectiveness of Mixes 630B and 804 in suppressing self-lasing with flat targets. Mix 804, which contains twice the concentration of SF_6 included by Mix 630B, was more efficient. It enabled the TBS to deliver 375 ± 41 J/beam on target, a factor-of-2 improvement over the previously measured target energy.

With GMB and gold-coated GMB targets, initial results show that this gas isolator permits extraction of approximately 500 and 400 J/beam, respectively. It should be noted that Mix 804 was not specifically designed for this application and that more efficient mixes could be developed, if required.

Transmission Measurements

To predict the performance of gas isolator Mix 804 in various laser systems, a more complete set of transmission data as a function of both gas pressure and input-pulse intensity was required. These data were obtained in the Gigawatt Test Facility, using a single-line 1.2-ns pulses at the 10-μm P(20) wavelength. Figure III-4 shows the transmission of Mix 804 over a 7-decade range of incident pulse intensity for the approximate cell length and pressures employed in the EBS. Figure III-5 presents similar data for operating conditions that pertain to the TBS. The residual, high-intensity absorption coefficient derived from these data is 9.3 x 10^{-4} cm^{-1} $torr^{-1}$ over a 6 to 85 torr pressure range. The small-signal absorption coefficient obtained from these short-pulse transmission data (α = 8.5 x 10^{-3} cm^{-1} $torr^{-1}$) is in good agreement with that obtained with an ir-spectrometer (α = 9.3 x 10^{-3} cm^{-1} $torr^{-1}$). These observations support the validity of using the spectrometer to determine small-signal

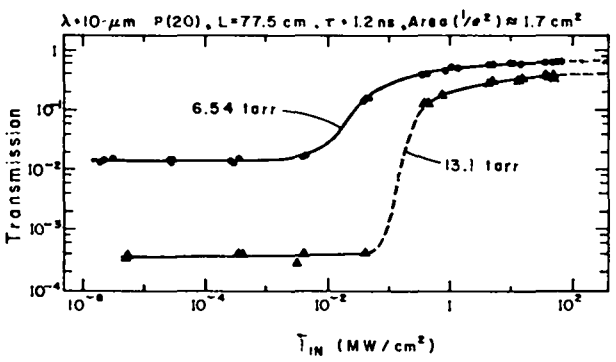

Fig. III-4.
Transmission of Mix 804 vs 10-um P(20) fluence for EBS conditions.

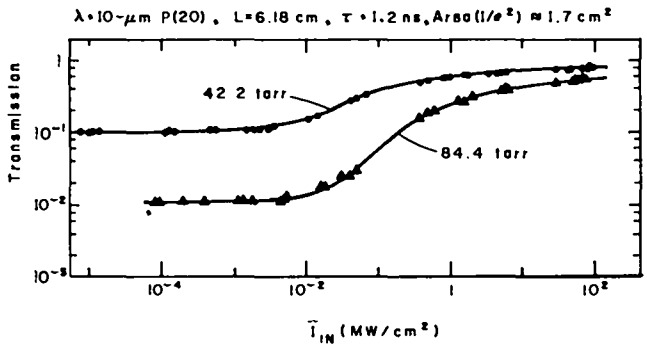

Fig. III-5.
Transmission of Mix 804 vs 10-um P(20) fluence for TBS conditions.

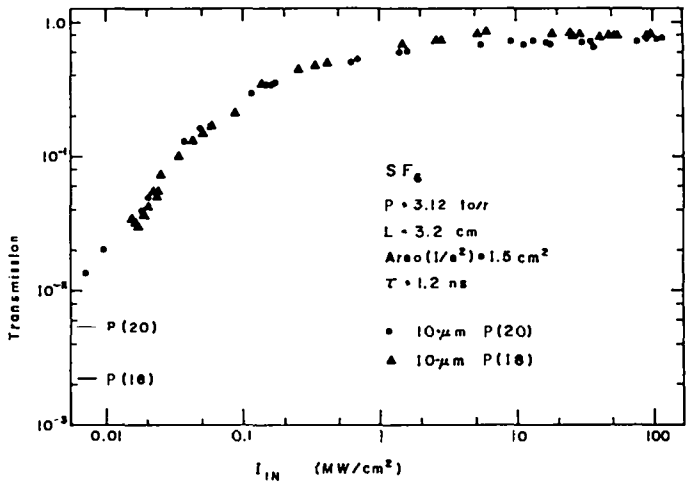

Fig. III-6.
High-intensity transmission of SF_6 at 10-μm P(18) and P(20) as a function of the incident pulse intensity. The small-signal (cw) transmissions are indicated on the left. Note that some bleaching occurs even at the relatively low intensity of 10 kW/cm².

absorption coefficients. A detailed study of pure SF_6 was also undertaken, in which its transmission on each of the P(14) to P(22) 10-μm CO_2 laser lines was measured over several decades of input intensity (Fig. III-6 and III-7).

High-Resolution Spectroscopy

Diode-laser scans of the absorption spectra of various saturable gases were obtained over a range ± 6 GHz relative to line center for the P(12) through P(22) 10-μm CO_2 laser lines, with 3MHz resolution. Although analysis of these data is not complete, preliminary inspection indicates that the absorption coefficients do not differ by more than 30% from the mean values in these regions. Hence, we do not expect to encounter any significant changes in the effectiveness of the gas isolators in transferring them from the 600-torr (4-GHz bandwidth) mockup amplifier to the 1800-torr (12-GHz) TPA.

Saturation Recovery Rates

The dynamic behavior of the gas isolators provides insight into the physics of the saturation process and also provides information relevant to their use in high-power laser systems. Of immediate interest is the time in which the gases recover from the saturated state to again become effective absorbers. If the recovery time is fast enough (≤ 50 ns for the EBS), the isolator would provide protection

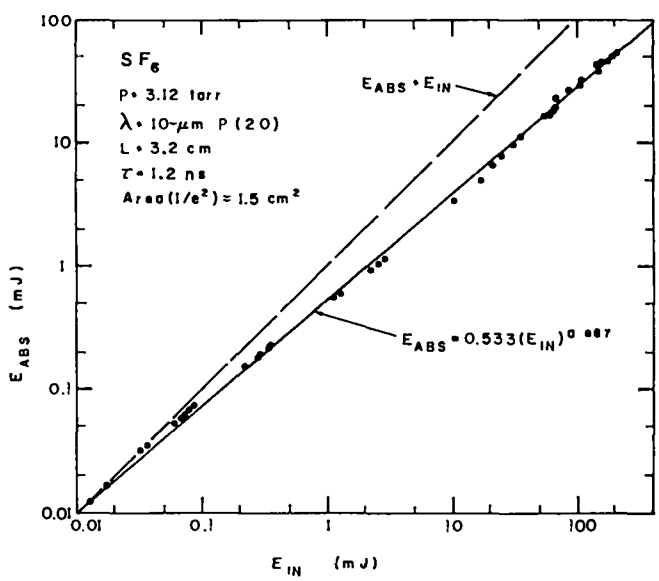

Fig. III-7.
Energy absorbed by SF_6 as a function of the input energy. Note that the data can be fit over several decades by the function given in the figure. The highest absorption shown corresponds to an average absorption of 5.5 photons per molecule.

against postlasing and against damage from the retropulse reflected from the target. Preliminary results on the recovery process in Mix 804 have been obtained, using the well-known infrared double-resonance technique.[1]

In the present experiment the gas to be studied is contained in a 10-cm-long glass cell of 4-cm diameter fitted with NaCl windows. A 1.2-ns pulse tuned to the 10-μm P(20) line saturates the gas. The beam is approximately 8 mm in diameter with a maximum energy of 250 mJ per pulse. A low-power cw probe beam, about half the diameter of the pulsed beam and tuned to the 10-μm P(16) line, intersects the pulsed beam at the center of the glass cell. The angle between beams is about 5°. The cw beam emerging from the cell is passed through a spectrometer and monitored with a SAT Hg-Cd-Te or a liquid-helium-cooled SBRC Hg:Ge detector. The spectrometer isolates the detector from scattered light originating with the 1-ns pulse.

The passage of the 1-ns pulse through the gas bleaches it and causes a sudden increase in the transmission of the cw probe beam. The transmission then decays to its original value. The risetime of the transmission is faster than 4 ns. Its decay has the following characteristics.

1. It first decays to a level slightly higher than the prepulse level in several microseconds. This is followed by a slower decay to the original transmission level in several hundred microseconds.
2. The fast decay (which is the one of interest), appears not to be represented by a single exponential.
3. The decay rate is energy dependent. The change in transmission induced by higher energy pulses decays at a faster rate.
4. For Mix 804 in the range 5 to 20 torr, the fast decay τ approximately obeys the relationship $p\tau = 10$ μs-torr, where p is the pressure of the gas.

Measurements are currently being made to determine the exact energy dependence of the decay rate as well as the pt value. The decay of the transmission will also be monitored at other wavelengths. The decay process when both pump and probe lasers are tuned to the 10-μm P(20) line is of particular interest. Simple saturable-absorbing gases, including binary SF_6 mixtures, fluorocarbon-152a, and dimethyl ether, will also be studied.

Gigawatt Test Facility

The Gigawatt Test Facility (GWTF) was operated in support of a wide variety of investigations. These included:

- gas isolator transmission and recovery times,
- saturable absorption properties of KCl doped with ReO_4^- ions,
- small-signal gain and saturation energy of a commerical, large-aperture (9-cm), double-discharge CO_2 laser, and
- damage threshold effects in AR-coated NaCl windows.

Details on each of these experiments are presented elsewhere in this report. The focusability of the output beam produced by this system was studied, and it was found to be two to four times diffraction limited.

Plans for substantially modifying and upgrading the facility to a 0.6-ns, 10-J system, which will be capable of supporting target diagnostic development, as well as other high-power experiments, are now being implemented. The new system is expected to be operational in the summer of 1978.

SOLID STATE PHYSICS (C. R. Phipps, J. F. Figueira, R. K. Ahrenkiel, S. J. Thomas)

Introduction

A new and promising solid-state saturable absorber involving substitutional dopants in alkali halides is introduced in this report. Preliminary experiments are reported for a doped KCl sample operating on the 10-μm P(28) transition. Peak transmissions of 85-90% were obtained with P(28) intensities above 500 MW cm^{-2} in a 5-cm-long KCl sample whose small-signal transmission was 29%.

Several materials which are being used or considered for use at high intensities in CO_2 laser devices have not been adequately tested for nonlinear optical effects. Examples are intrinsic Ge, which has been suggested as a Faraday rotation medium[2] and certain gas mixtures as well as p-type Ge which have been employed as bleachable absorber isolators. In particular, unexpected beam phase or amplitude modification due to self-focusing or multiphoton absorption are a significant concern if of sufficient magnitude to affect the far-field

brightness of beams intended for target irradiation. During this period, we measured the high-intensity transmission and transmitted far-field brightness of several key materials at 10.6 μm.

The third part of this section reports the progress of an effort to develop Faraday rotation devices using cobalt spinels. This is a problem that is both difficult and promising. The difficulty has been in accurately characterizing the process for making the spinels so that transparent samples are obtained repeatably. We now believe that substantial progress has been made in this area. The promise lies in the very high Verdet coefficient (320 deg cm^{-1}) and good figure of merit, which have been observed in cobalt spinels at 10.6μm.

Finally, we discuss a promising means of synchronizing infrared and visible laser beams with very low jitter relative to laser-fusion plasma events. This technique employs thermomagnetic switching in a cobalt-spinel visible-wavelength Faraday rotation film. Initial experiments, reported here, have been very encouraging.

Nonlinear Optical Properties of Substitutional Dopants in Alkali Halides

The use of solid-state saturable absorbers for laser isolation has been demonstrated on the EBS. In these experiments, large gallium-doped Ge slabs were used as the nonlinear absorber. Although these tests successfully demonstrated the concepts involved, the practical problem of optical damage to the Ge prevented use of this device at powers higher than ~400 MW/cm^2. We have extended this concept to other solids exhibiting nonlinear absorption that are more damage resistant than germanium. We report primarily results on the saturation properties of absorbing centers in KCl when irradiated with intense pulses of CO_2 radiation. Saturation intensities in the range of 5 - 20 MW/cm^2 are observed with transmissions approaching 100% above 500 MW/cm^2.

When negative ionic complexes with tetrahedral symmetry are doped into alkali-halide host lattices, they can replace a halogen anion and introduce an internal vibrational mode which is ir-active in the 10μm region. Upon irradiation with intense photon fluxes (~100 MW/cm^2), this absorption can saturate with an efficiency which depends upon the nature of the lattice-ion coupling. This doping technique has the advantage that both the frequency of the absorption band and its strength can be controlled by the proper choice of dopant material, amount of doping, and host material.

To demonstrate this effect, samples of KCl doped with 0.3% $KReO_4$ and 1% KBr were grown by the Czochralski method at the Cornell Crystal Growth Facility. Measurements of the small-signal transmission were made using a CO_2 laser spectrophotometer. The samples had a narrow absorption band centered on the P(28) line of the 10-μm CO_2 laser branch with a linewidth of 2 cm^{-1} at room temperature as shown in Fig. III-8. Off-resonance transmission was limited by scattering and Fresnel reflection to 94%. The measured transmission at P(28) was 29% for the 5-cm-long sample.

The large-signal transmission properties of these samples were then measured using two CO_2 oscillator/amplifier systems tuned to the P(28), 10-μm line. First, pulses of 1.9-ns duration were passed through the sample and the input and output energy were measured with disk calorimeters. The irradiating beam was arranged to provide a uniform spatial distribution. Time distributions were Gaussian with FWHM of 1.9 ns. With this arrangement, the transmission as a function of power was

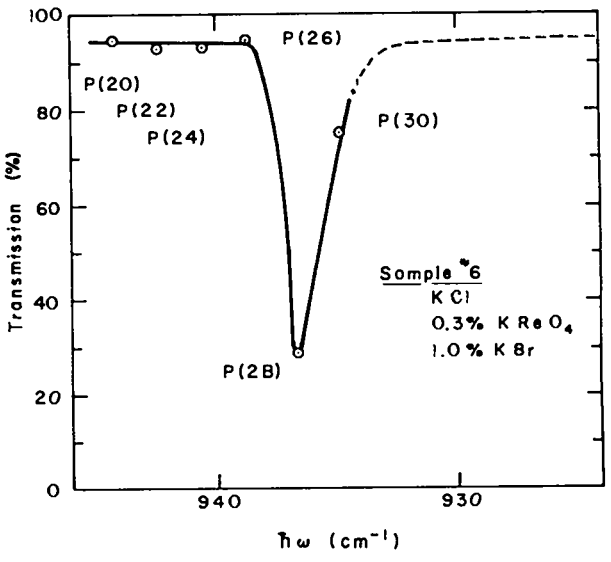

Fig. III-8.
Absorption spectrum of doped alkali halide sample.

measured at room temperature. Figure III-9 shows some typical results of these measurements. At input powers of 1 MW/cm², the sample transmission begins to saturate and reaches full transmission for input powers in excess of 100 MW/cm². At low powers, the transmission can be fit with a simple Frantz-Nodvik[5] saturation model with a saturation parameter E_s of 5 mJ/cm². However, at high powers, the experimental results deviate from this simple model, with the effective saturation parameter approaching 20 mJ/cm².

Using a second laser system producing 1.0-ns pulses of P(28) radiation and using a high-speed detection system (100 ps risetime), time resolved transmission measurements of the KCl sample were made. From the asymmetry of the transmitted pulses, we deduce that the decay time (T_1) is of the same order as the pulse duration, 1 ns. This lifetime is many orders of magnitude smaller than typical excited-state lifetimes of gas molecules (~1 ms·torr), but orders of magnitude larger than the H^- center local-mode excited-state in CaF_2 (~11 ps). We can conclude, therefore, that the internal vibrational modes of the ReO_4^- complex are only weakly coupled to the KCl phonons. By changing this lattice coupling the effective saturation parameter will vary, so that tailoring of the dynamic-optical properties of this material is possible.

In conclusion, we have demonstrated that it is possible to construct a solid-state isolator based on substitutional dopants in alkali-halide host lattices.

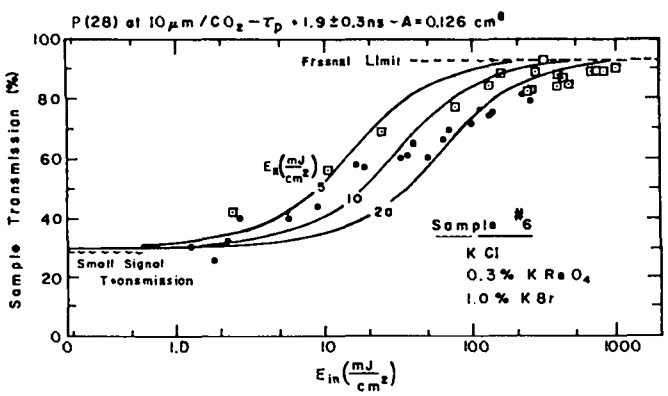

Fig. III-9.
Transmission vs 10-um P(28) fluence for doped alkali-halide sample.

These devices can be potentially useful as target isolators in compact laser systems (i.e., the EBS) or as intersystem isolators in the EBS or Antares. More work will be done to demonstrate their application to the CO_2 systems.

High-Intensity Beam Propagation in CO_2 Laser Isolator Materials

We set up two types of experiments to observe whole-beam self-focusing or defocusing effects sufficient to cause degradation of the focusable intensity in a well-characterized, 2-ns, 10.6-μm test signal after transmission through 3 different isolator materials. These were p-type (gallium-doped) germanium, intrinsic germanium, and a gas mixture similar to that used to isolate the EBS. Intensity-length products up to 35 GW cm^{-1} were employed.

The arrangement of the initial experiment (Fig. III-10) was intended to reveal simple self-focusing. Here, an effectively parabolic radial intensity profile was employed to generate an approximately lenslike intensity-dependent phase delay in the sample, assuming only that the sample refractive index is modified in a single-valued fashion by intensity, $n(I) = n_0 + \Delta n(I)$.

When a Gaussian-profile beam is apertured at 70% of peak intensity the radial intensity gradient of the remaining central portion is essentially that of a parabolic profile (Fig. III-10). At the same time, this apertured portion will have a far-field distribution given closely by the Airy pattern of the iris*. If such a distribution is focused by a lens of focal length f, the on-axis intensity variation a distance z from the focal plane is given by[6]

$$\frac{I(0,z)}{I_0} = \frac{4f^2}{z^2} \sin^2\left[\frac{\pi r_0^2 z}{2f(f-z)\lambda}\right]$$

$$\approx \left[F\left(\frac{\sin Y}{Y}\right) \cdot \right]^2 \text{ for small } z. \qquad \text{(III-1)}$$

*To obtain a quantitative estimate of the magnitude of nonlinear effects in a bleachable absorber, it is important that such effects are observed when the sample is essentially bleached, so that a reasonably uniform intensity is obtained in the region studied. It is also helpful if the radial profile in the region studied varies only slightly. This is a second reason why the arrangement described here was used to study the saturable materials.

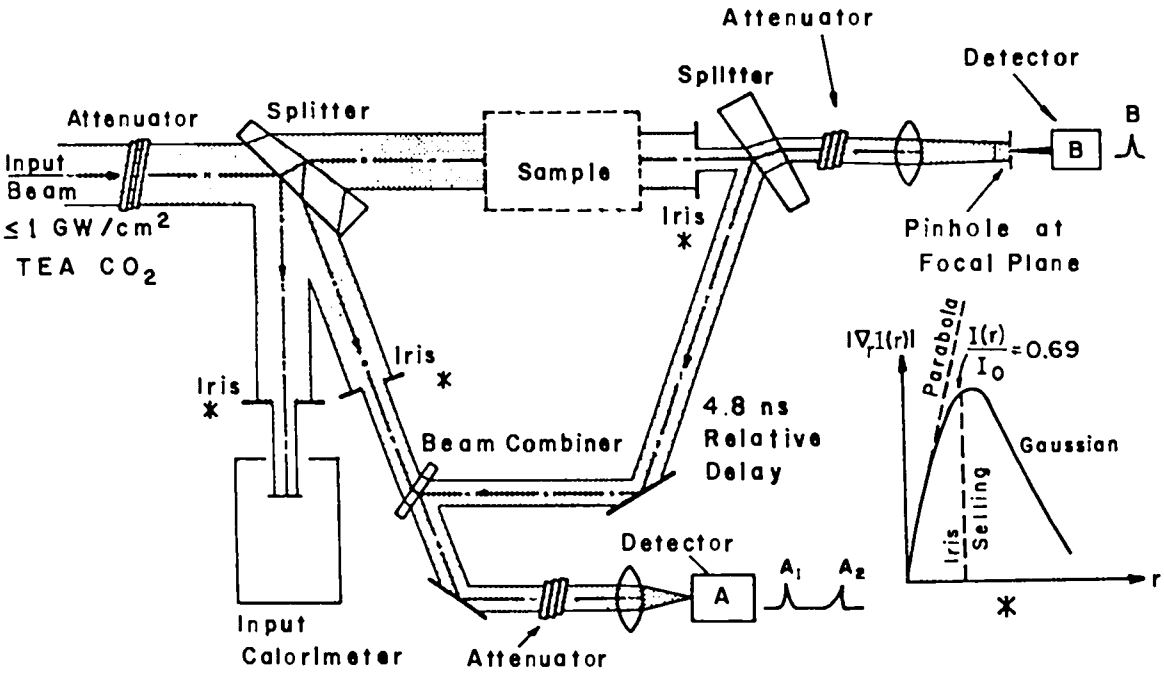

Fig. III-10.

Experimental setup for studying self-focusing properties of various materials at 10.6 μm. An effectively parabolic illumination profile was used by appropriately aperturing the beam after transmission through the sample under test. This is illustrated in the inset, where the size of the iris is shown on a plot of the beam radial intensity gradient. The signal ratio B/A_2 gives transmitted beam brightness, while A_2/A_1 gives sample transmission. Detector A was deliberately set up to give an accurate beam intensity reference signal independent of the forward solid angle occupied by the transmitted beam, up to 100 times the undisturbed beam solid angle. Detector B, on the other hand, was set up to sample only the central portion of the far field distribution of the transmitted beam.

In Eq. (III-1), $Y = (Fz/2f\lambda)$, while $F = (\pi r_o^2/f\lambda)$; F^2 is the beam intensity concentration factor at the focal plane, I_o is the intensity at the iris and r_o its radius.

The behavior of the illuminated sample may be approximated by that of a variable focal-length thin lens operating in conjunction with the fixed lens to move the focal plane during the laser pulse. Within the validity range of this approximation, an exact relationship based on Eq. (III-1) was developed that permitted combining the observed dynamics of the on-axis, focal-plane intensity with the intensity in the sample to give $\Delta n(I)$.

If $\Delta n(I) = n_2 I$, the combination of parameters in our experiment would give a minimum resolvable n_2,

$$n_{2min} = \left[0.3 \frac{\lambda\sqrt{\delta}}{I_o L} \right] \text{ GW}^{-1} \text{ cm}^2 , \quad \text{(III-2)}$$

where the quantity δ is the fractional decrease observable in far-field brightness for a sample of length L illuminated by intensity I_o. In practice, the scatter of the B-signal was found to be such that the minimum resolvable fraction δ_{min} was 15%. This limited our sensitivity to $n_{2\,min} = (6 \times 10^{-4}/I_oL)$ GW^{-1} cm² or $(7 \times 10^{-11}/I_oL)$ esu, where in either case the intensity-length product I_oL is expressed in $GWcm^{-1}$ units.

Results for the isolator gas mixture are reproduced in Fig. III-11. Here, with I_oL = 35 GWcm^{-1} at the maximum intensity available, the absence of brightness loss means that the n_2 coefficient was less than 1.7 x 10^{-5} GW^{-1} cm^2 or 2 x 10^{-12} esu. For these measurements, the laser spectrum was allowed to vary from essentially single-line (P-20, 10-μm branch) to "multiline" (predominantly P-18 and -20) with negligible effect on the results. "Brightness" is normalized to that obtained with no sample in the test region which was, in turn, very nearly diffraction-limited in our setup. Peak transmission shows no unexpected behavior. The composition of the gas sample was chosen to be as close as possible to the parameters used in the isolator cell for the EBS.

The second sample studied was p-type, gallium-doped germanium with a 10.6-μm small-signal absorption-length product α_oL = 4.25. Sample length was 7.67 cm, corresponding to a doped hole density $N_p \approx 7.5 \times 10^{14}$ cm^{-3}. The results presented in Fig. III-12 show no brightness changes up to the Ge optical damage threshold, within our ± 15% experimental error. Interestingly, although optical damage to the sample occurred at I_o = 0.38 GW cm^{-2}, the brightness for this shot did not degrade, while transmission dropped substantially. The transmission values obtained show no abnormal deviation from the calculated model (solid line) until the damage intensity is reached. Because the maximum $\int I_o dL$ obtainable here was about 2.0 GW cm^{-1}, we can only say that n_2 in this p-type Ge sample was less than about 3 x 10^{-4} GW^{-1} cm^2 or 3 x 10^{-11} esu.

Figure III-13 shows very different results that were obtained with the third sample, a room-temperature intrinsic germanium boule 14.9 cm in length. Beginning at I_oL values of about 0.7 GW

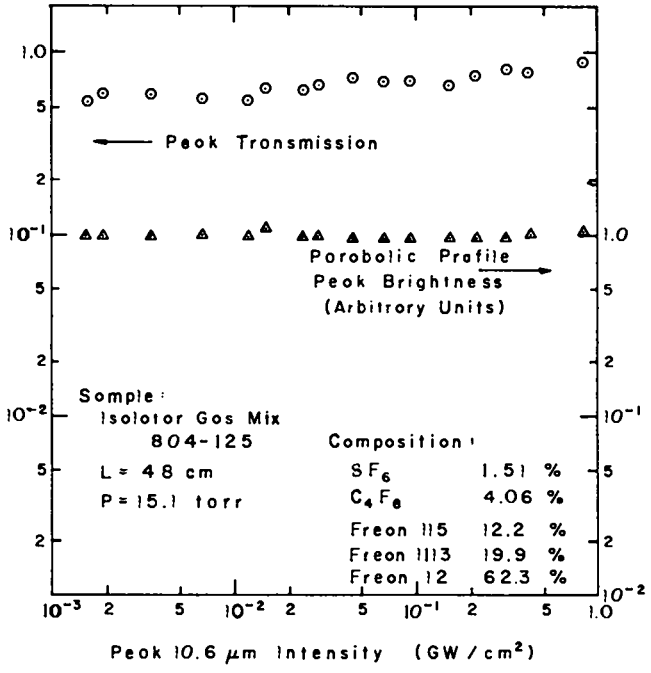

Fig. III-11.
Peak transmission and peak transmitted brightness vs 10.6-μm input intensity for gas Mix 804, obtained with the Fig. III-10 setup. Length, composition, and pressure are similar to parameters used in the EBS isolator.

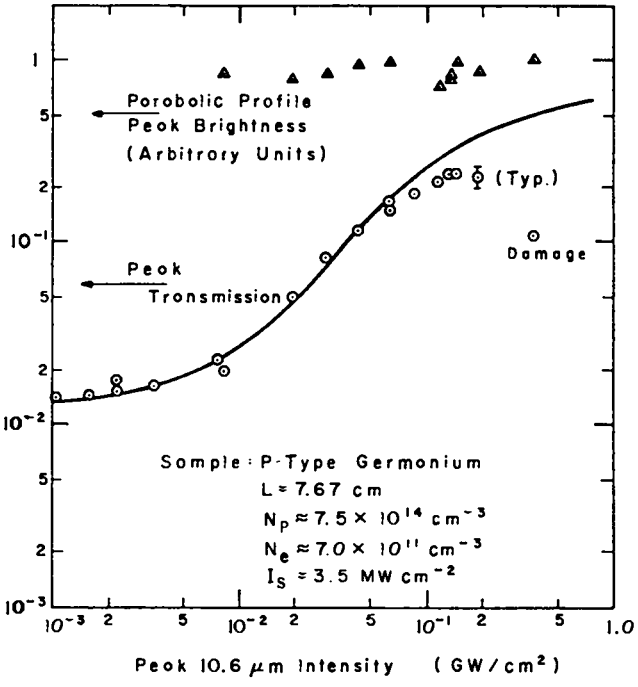

Fig. III-12.
Peak transmission and peak transmitted brightness vs 10.6-μm input intensity for p-type Ge. Path length, average absorption length product ($\alpha_oL \approx 4.25$) and average doping level ($\rho \approx 4.5$ Ω·cm) are similar to those used in the Ge isolator for the EBS; the Ge pieces used are corners removed during manufacture on the first such isolator. The Fig. III-10 setup was used.

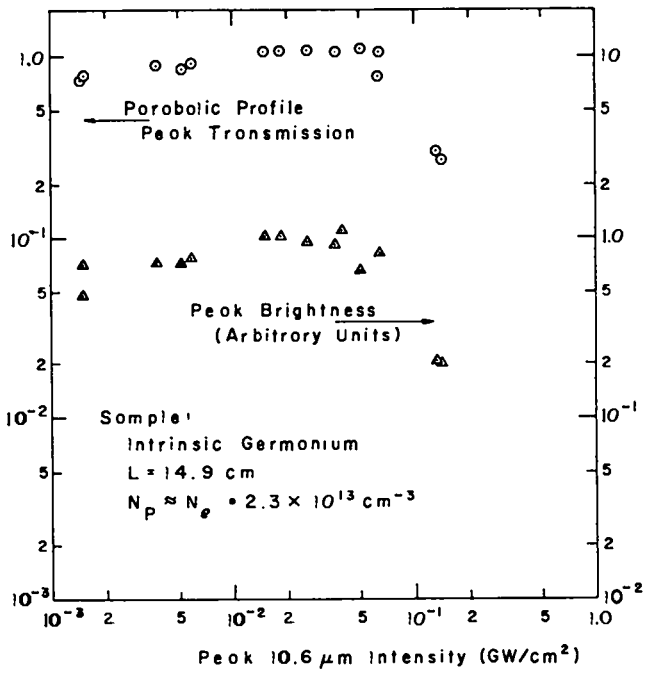

Fig. III-13.
Peak transmission and peak transmitted brightness vs 10.6-μm input intensity for intrinsic Ge. The sample diameter was 5 cm, and its length was 15 cm, to enhance observed effects that were expected to scale with the product of intensity and sample length.

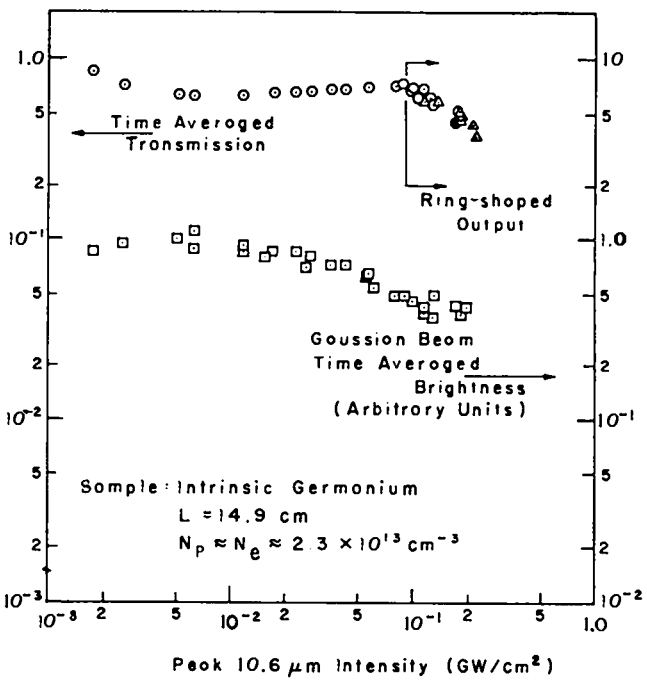

Fig. III-14.
Time-and-space-averaged transmission and transmitted brightness of intrinsic Ge sample, using Fig. III-10 setup. Sample was identical to that used to obtain the Fig. III-13 results.

cm^{-1}, definite degradation of the transmitted brightness is noted, and at slightly higher intensities, a loss of transmission also. At these intensities, an ir-vidicon camera showed a rapid but reversible change of the beam radial intensity profile at the output end of the Ge boule from Gaussian to a ring-shaped distribution with a central minimum.

To study these phenomena with better resolution and less chance of error due to the limited collection solid angle of the transmitted beam reference detector, the experiment was modified to measure time-average transmission and brightness. With the new setup, the collection solid angle for the transmission calorimeter was about 10 times greater than that of the undisturbed illumination beam. The brightness sensor was a pyroelectric device with microjoule sensitivity and good accuracy.

Figure III-14 shows time-averaged measurements made on the same intrinsic Ge sample. Brightness degradation is seen to begin at $I_oL = 0.3$ GW cm^{-1} while transmission begins decreasing at about 4 times this level. Data points on both plots were obtained with increasing as well as decreasing intensity, demonstrating reversibility of the phenomena. To determine that the transmission calorimeter was indeed collecting all the transmitted beam sample, the experiment was repeated with a factor-of-2 change in the collection solid angle. The additional data points that were obtained in the high-intensity portion of the transmission curve are shown as triangles in Fig. III-14 and demonstrate the absence of any such effect.

Identical measurements on other intrinsic Ge pieces of various lengths (all at room temperature) showed that the threshold for these features scales directly with I_oL.

At this point, it is possible to come to the following conclusions regarding this work.

- Neither the gas isolator nor the p-type Ge isolator should show any nonlinear optical effects which would interfere with their use in the EBS.
- The gas isolator in particular has a very comfortable safety factor in this regard.
- Intrinsic germanium exhibits very strong intensity-dependent beam phase and amplitude distortions when used at moderate 10.6-μm intensity-length products. Measurements taken to date do not indicate that these effects are mainly related to nonlinear refractive index. Instead, they would seem to indicate formation of a high density of volume-distributed free carriers that first refract and then absorb the beam as optical intensity increases. These effects in Ge have also been observed in the 2.6- to 4.0-μm range by Wenzel.[7] They would appear to have a significant impact on the use of thick intrinsic Ge samples in high-power 10-μm work, and particularly on interband Faraday rotators.

Work is continuing to determine the sensitivity of the threshold for these effects to the initial free carrier density, and to isolate the physical processes involved sufficiently to permit accurate modeling.

Development of Cobalt Spinels for Faraday Rotation Devices

The program has initially focused on the development of a particularly promising material for this purpose, $CoCr_2S_4$. The development effort has attempted to improve and characterize the fabrication process reported by Kodak workers,[8] and has identified a number of key factors in the production of transparent material.

The fabrication process consists of the preparation of microcrystalline powders of $CoCr_2S_4$ and hot-pressing at 1023 K to 1173 K under high pressure. Pearlman et al[9] indicated that small excesses of chromium are not detrimental to sample transparency, but that a stoichiometric composition is optimum. Our results have not been consistent with the Pearlman results. Attempts to fabricate samples by the published techniques have not produced transparent samples.

A number of troublesome defects have been identified and means have been developed to correct them. The desired transparency appears to be dependent upon three important features.

Powder Morphology. The synthesis of a powder that consists of agglomerates of submicron particles is essential in the elimination of oxide impurities. Such powders undergo a more complete transition to the spinel phase during the intermediate reaction given by

$$Co(OH) + Cr_2(OH)_2 \xrightarrow{H_2S} CoCr_2S_4 + H_2O \quad . \qquad \text{(III-3)}$$

Larger dense particles several microns or more in cross section do not efficiently convert to spinel. Pressings from such powder show hard extrinsic "phase islands" under metallographic examination. Microprobe analysis of such phases indicates a sizable oxygen concentration. X-ray diffraction studies of both powders and polycrystals indicate the probable presence of Cr_2O_3 in these "islands".

We have learned to control the morphology of our starting hyroxides by changing the rate of addition to hydrazine in the hydroxide synthesis. Here

$$(X)\ C_rO_3 + (y)\ CoCl_2 \xrightarrow{\text{Hydrazine}} Co(OH) + Cr_2(OH)_2 + \text{by products.} \qquad \text{(III-4)}$$

Rapid addition of hydrazine results in submicron hydroxides, but with subsequent cobalt loss. Slow addition results in the large,dense particle that cannot be completely converted to spinel. An intermediate rate has been found that produces particles of desired morphology and insignificant cobalt loss.

Elimination of Excess Chromium and Obtaining Exact Stoichiometry. The correlation of x-ray diffraction studies and metallographic microscopy techniques has shown that Cr_2S_3 is formed as a spurious phase. The concentration of this phase is apparently related to excess chromium in the starting hydroxide. Infrared spectroscopy has shown that Cr_2S_3 in a KBr matrix has very strong absorption bands in the 9- to 30-μm wavelength range. Hence, chromium excess must be avoided. A cobalt spinel powder has recently beem made with an ideal Cr/Co ratio of 2.00.

Polycrystal Densification. Polycrystal densification requires experimentation with the pressing temperature and pressure. We have found that every powder preparation has a different pressing characteristic. Porosity is also a source of optical loss. Further experiments are under way.

In conclusion, we have found that powder morphology, chromium excess, and hot-pressing techniques are key factors in the sample preparation process. With this knowledge, we believe that transparent samples can be made in the near future.

Faraday Switch For the Synchronization of CO_2 and Visible Laser Beams

For CO_2 laser fusion experiments, a scheme for synchronizing a visible-wavelength diagnostic signal with the CO_2 pulse would be useful.

One means of accomplishing this synchronization is by thermomagnetic switching of a visible wavelength Faraday rotator by the CO_2 laser pulse. Thermomagnetic switching occurs when the absorption of 10.6-μm radiation heats the visible rotator above its Curie temperature and large-amplitude lattice vibrations destroy the spin-exchange order. Thin film materials with very large Verdet coefficients are required for fast switching of the visible signal.

A large, visible-wavelength Faraday effect has been reported for certain cobalt spinels.[10] Thermomagnetic writing experiments on MnBi films with 250 ps mode-locked pulses indicated that switching occurs in times much less than the laser pulse width.[11]

We used thermomagnetic switching for the Faraday effect in the spinel $Fe_{1.2}Co_{0.8}Rh\ O_4$ to rapidly switch a helium:neon laser beam (6328Å) either on or off during illumination by a ns-duration CO_2 laser signal.

The thin film sample employed (~ 5000Å) was supplied by William Maisch of the Naval Research Laboratory. Faraday rotation in this material is about 4 degrees at 6328Å and the Curie temperature $T_C \approx 350K$.[12] The thin magnetic-oxide film was placed in the center of a small air-core solenoid which drove the film into magnetic saturation ($H_{sat} \cong 7KOe$). A 1.6-ns CO_2 pulse was generated at the maximum of the pulsed magnetic field and was coincident on the sample surface with a polarized, 50-MW helium neon beam.

In Fig. III-15a, a polarizer placed in front of a fast photomultiplier was set to extinguish the red beam in the absence of the magnetic field. Here the photocurrent produced by the red beam rises as the magnetic field turns on a Faraday rotation of the film.

In Fig. III-15b, a CO_2 pulse (1.6-ns FWHM) is incident on the film and the transmitted intensity drops abruptly to zero. The total energy here is about 150 mJ/cm² and the peak power is about 90 MW/cm². By using a 3 mm aperture to produce a uniform spatial profile, the switching threshold of the magnetic film was found to be 15 to 30 mJ/cm².

To date, the red beam switching time has been found to be 2 ns or less. We believe the film

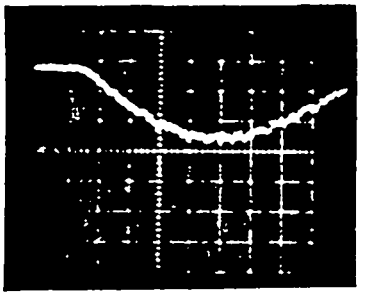

(a) Signal produced by Faraday rotation of thin magnetic film without CO_2 laser pulse at sweep speed of 2 μs/div.

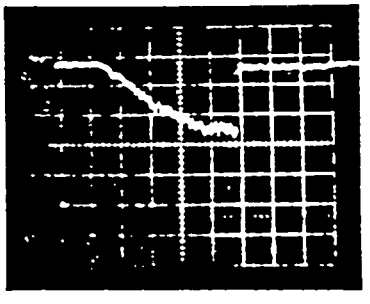

(b)Signal truncated by thermomagnetic switching by CO_2 pulse. This switching time was separately observed to be less than 2 ns.

Fig. III-15.
Performance of Faraday switch.

switching mechanism involves direct absorption by lattice modes. In this case, magnetic disorder is predicted to occur in several vibrational periods, i.e., in the ps range. Further measurements will determine the actual switching time.

The red signal was also switched on by nulling the transmitted beam with the magnetic field turned on. Therefore, two such devices may be used in series to generate a pulse of desired width. Alternatively, one may generate red beam short pulses directly from a signal such as shown in Fig. III-15b by reflection from a Fabry-Perot interferometer.[13] This arrangement also permits setting the second polarizer at 45° to the incident polarization, thereby greatly increasing the switched intensity. Results for this experiment together with characterization of switch performance will be reported at a later date.

CO_2 LASER PHYSICS (B. J. Feldman, R. H. Fisher)

Introduction

An Nd:glass mode-locked laser pulse was synchronized successfully with a gain-switched oscillator to permit laser interferometry on CO_2 laser-produced plasmas with subpicosecond resolution.

Two 3-cm-aperture, 1800-torr double-discharge CO_2 laser amplifiers built for LASL by the Westinghouse Electric Company were successfully operated and partially characterized. Measured transverse gain uniformity was within 10%, bearing out computer predictions based on electrode and preionizer geometry.

A Lumonics Research Ltd. model 600A, 10-cm-aperture double-discharge laser amplifier was also characterized. Gain and saturation data were obtained for a 80:5:15::He:N_2:CO_2 laser mixture. Saturation data could not be fit by a single Frantz-Nodvik curve.

The temperature dependence of CO_2 line broadening was studied using laser diode spectroscopy. The results indicate that the CO_2 - CO_2 pressure-broadening collisional cross-section is independent of temperature in the range of operation of CO_2 laser systems.

We describe the achievement of MW-level lasing on the $(0, 0°, 2) \rightarrow [(1, 0°, 1), (0, 2°, 1)]_{I,II}$ sequence bands and on the $(0, 1^1, 1) \rightarrow [(1, 1^1, 0, (0, 3^1, 0)]_I$ hot band of CO_2 at 1800-torr pressure using the Westinghouse laser. The sequence-band lines are interspersed between the conventional 9- and 10-μm CO_2 laser lines, whereas the hotband lines are near 11-μm wavelength.

We present calculations of short-pulse amplification in a large CO_2 laser amplifier and discuss the problem of parasitic oscillations in our laser systems.

Synchronization of Nd:Glass and CO_2 Laser Pulses (R. L. Carman, N. Clabo, F. E. Wittman)

The synchronization of a Nd:glass, mode-locked laser pulse to a gain-switched oscillator output was accomplished, making possible subpicosecond-resolution laser interferometry on CO_2 laser-produced plasmas.[14,15]

The problem of synchronizing a mode-locked Nd:glass laser to a gain-switched CO_2 source has two components: (1) How to synchronize the laser output envelopes, and (2) how to synchronize the two individual pulses. We chose an all-electronic technique because of its general applicability. Also, because any optical element added to the Nd:glass cavity would drastically degrade the diffraction-limited performances as well as the ultrashot pulse width, we let the laser run normally, and dictate the timing for the CO_2 laser. Therefore, we resorted to Pockels-cell pulse-clipping techniques to produce the ~1-ns CO_2 pulse.

Gain-switched CO_2 oscillators readily produce ~200-ns pulses of excellent mode quality, while the Nd:glass pulse train envelope is much longer than 1 μs. We thus must synchronize the two envelopes to a jitter of ~500 ns. Despite the normal jitter in the passively mode-locked Nd:glass laser output of 10 to 20 μs, much smaller jitters can be obtained by a change in the flashlamp driver circuit. Because the lifetime for the upper state of Nd is T_1 ~300 μs, a flashlamp pump of 300 μs duration base-to-base width is very efficient in producing the inversion. If the pump energy is reduced to achieve ~90% of the required Nd inversion, no lasing occurs. We now apply a second flashlamp pump of ~1-μs duration containing the remaining ~10% of the pump energy required to make the Nd lase. As a result, the overall

jitter is reduced to ~500 ns, the Nd pulse envelope build-up time.

A single pulse is then selected as follows: the CO_2 output is split and a portion used to trigger a krytron circuit via a photodiode to select two Nd:glass pulses. The first of these returns to the CO_2 laser to trigger a second circuit, activating the CO_2 Pockels-cell pulse clipper. The second Nd pulse is used for our experiment. Splitting of the two Nd:glass pulses is accomplished by a second Pockels cell, driven by the electrical pulse from the first Nd:glass laser Pockels cell, but cable-delayed by 10 ns, the inter-pulse spacing. Jitter in the Nd:glass Pockels-cell electrical-pulse generator is inconsequential as long as the jitter is low enough to guarantee good transmission of the single mode-locked laser pulse. However, jitter in the electronics used to drive the CO_2 pulse clipper appears as jitter in the synchronized pulses. Whereas a Mylar spark gap[18] has been demonstrated to possess < 30 ps jitter when driven with a ~30-ps Nd:Yag laser at ≤ 5 ps, damage to the anode occurs simultaneously with triggering. A Fabry-Perot etalon could increase the duration of the Nd:glass pulse used to trigger the CO_2 pulse-clipper, but we are exploring krytron and avalanche transistor circuits, which show promise of < 100 ps jitter.

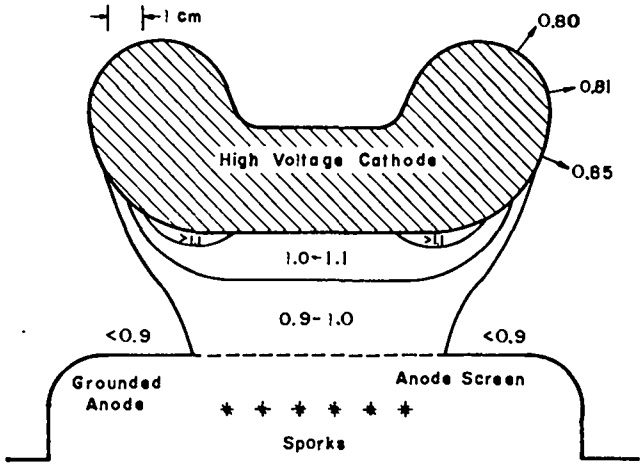

Fig. III-16.
A cross-section drawing of the interior of the Westinghouse laser amplifier, showing location of the preionizers and calculated plots of the electric field within the discharge gap.

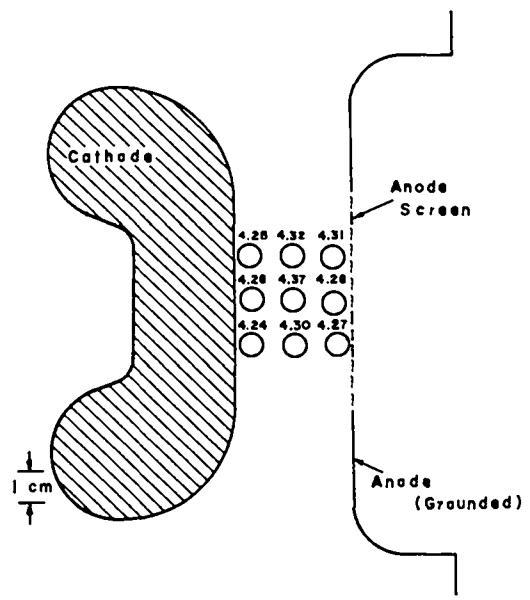

Fig. III-17.
Measured P(20), 10.6-μm gain coefficients (%/cm) along several longitudinal paths located as shown within the gain volume of the Westinghouse laser amplifier.

Performance Evaluation of an 1800-torr Large Aperture Double Discharge CO_2 Laser Amplifier (B. J. Feldman, R. H. Fisher)

We report on the successful operation of a pair of 1800-torr, 3- by 3-cm optical-aperture, 1.5-liter double-discharge CO_2 laser amplifiers. These devices were designed and constructed by the Westinghouse Electric Co., under contract with LASL, to provide 300 J/ℓ electrical input for high energy storage subnanosecond pulse preamplifiers in the LASL CO_2 laser-fusion program. They represent a significant advancement in the state of the art of CO_2 amplifier technology.

A cross-section of the electrode profile, showing the position of the preionizer sparks, and computer contour plots of the electric field within the gap are shown in Fig. III-16. The active discharge volume of each amplifier is 154 by 3.5 by 5.0 cm. Computer evaluation of the electrode and preionizer geometry indicated good gain uniformity over a 3- by 3-cm optical aperture. Small-signal gain measurements taken on the system bear out the computer predictions. The small signal gain of an 80:10:10::He:N_2:CO_2 mix with 10 ppm tripropylamine measured across the discharge aperture is shown in Fig. III-17.

Transverse gain uniformity was better than 10% with an average gain-length of about 4.3 per amplifier stage. Shot-to-shot gain variation was less than 5%. Reliable operation was limited to about 20 shots (at 1 shot every 15 s) before arcing degraded performance. The provision of slow gas flow in the system is expected to solve this problem. The amplifier system described here compares favorably with similar-volume, e-beam-sustained, high-pressure amplifiers in terms of simplicity of design and repair, reliability of performance, uniformity of discharge, and gain risetimes.

Gain and Saturation Data on Lumonics 600A Amplifier (B. J. Feldman, R. H. Fisher)

The Lumonics 600A series CO_2 laser amplifier is a 64 cm^2 aperture, 50-cm-long, 1-atm double-discharge system that is under consideration for the GWTF upgrade and also as a possible front-end component for the Antares system. To evaluate and quantify the performance of the amplifier, we probed the gain and measured the short-pulse energy extraction efficiency of the device. The gas mix employed was 80:5:15::He:N_2:CO_2. At 45 kV operating voltage, greater than 99% of the test shots were free of electrical arcs.

Under these conditions, we obtained the following small-signal gains:

Line	$g_o(cm^{-1})$
10 μm P(30)	0.025
10 μm P(20)	0.035
10 μm P(18)	0.034
10 μm P(10)	0.026
09 μm P(20)	0.027

Shot-to-shot gain variation was less than 2%.

Short-pulse (1.2-ns) amplification studies were performed for the 10-μm P(20), 10-μm(18), and 9-μm P(20) lines. Some results are plotted in Fig. III-18 and III-19. Superimposed on these graphs are plots of the Frantz-Nodvik expression[8] that relate energy fluence to gain,

$$(1 - e^{E_{out}/E_{sat}}) = (1 - e^{E_{in}/E_{sat}})\, e^{g_o L} \qquad \text{(III-5)}$$

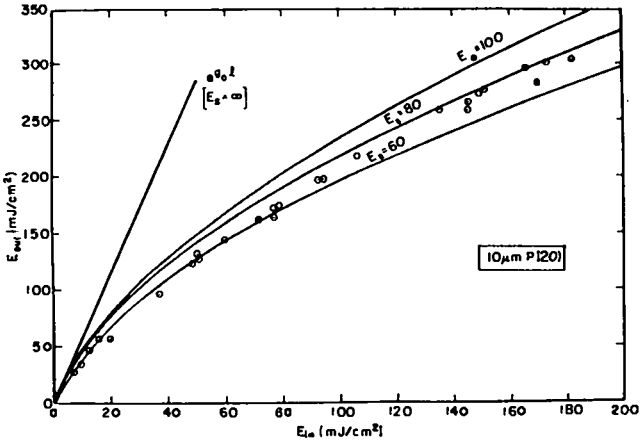

Fig. III-18.
Measured gain saturation for Lumonics amplifier for 10-μm P(20) signal, with solid lines showing Frantz-Nodvik fits using various saturation parameters.

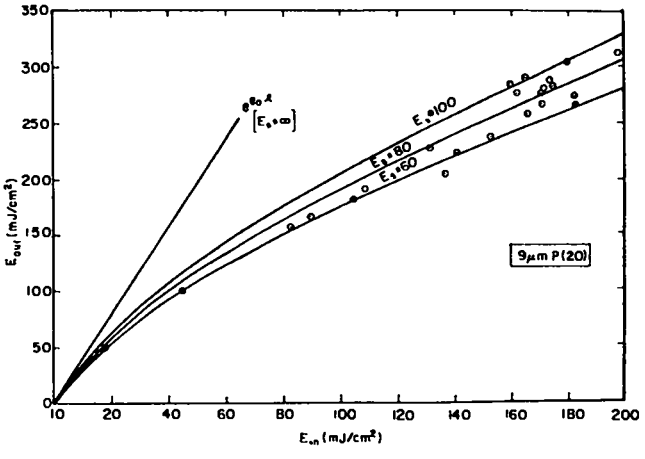

Fig. III-19.
Measured gain saturation for Lumonics amplifier for 9-μm P(20) signal, with solid lines showing Frantz-Nodvik fits using various saturation parameters.

for values of E_{sat} = 60, 80, and 100 mJ/cm^2.

A single Frantz-Nodvik curve does not match the data well at both the high and low energy input values. It is expected that an improved fit will be obtained from computer-generated density matrix calculations currently in progress.

Temperature Dependence of CO_2 Line Broadening (B. J. Feldman, R. H. Fisher)

In the design of large CO_2 laser systems for laser fusion experiments, knowledge of the temperature dependence of the gain lineshape is essential for optimum operation. We have studied the profile of 10-μm absorption in heated CO_2 using the LASL tunable laser diode spectroscopy facility. A weak 10-μm laser beam from a $Pb_{1-x}Sn_xTe$ homostructure diode laser was passed through a 50-cm cell of CO_2 whose pressure and temperature were variable over a wide range. The wavelength of the narrow-band diode source was tuned over the 10.6-μm P-branch CO_2 transitions. The transmission of the cell vs wavelength was monitored with a liquid-helium-cooled Cu-doped germanium detector, and plotted on an xy recorder. Computer reduction of the data yielded FWHM linewidths as a function of CO_2 gas pressure and temperature.

Results of this analysis are shown in Fig. III-20. In Fig. III-20a, we plot the natural logarithm of the observed FWHM linewidth, $\Delta\nu$, vs the log of the temperature, for a gas pressure of 300 torr. Figure 20b shows similar curves for a 500-torr gas pressure. In both cases a linewidth slope of $-1/2$ best fits the experimental data. From this observation the temperature dependence of the CO_2 - CO_2 collision cross-section is readily obtained by noting that

$$\sigma \propto \frac{\Delta\nu}{n\langle v\rangle} , \qquad \text{(III-6)}$$

where n is the CO_2 gas density at constant pressure and volume (inversely proportional to the temperature T), and $\langle v\rangle$ is the mean velocity between CO_2 molecules, proportional to $T^{1/2}$. Consequently,

$$\sigma \propto \Delta\nu\, T^{\frac{1}{2}} . \qquad \text{(III-7)}$$

Now, with our observation that

$$\Delta\nu \propto T^{-\frac{1}{2}} , \qquad \text{(III-8)}$$

we find σ, the collision cross-section to be temperature independent. This parameter is important because the energy storage of a CO_2 laser system can be related to the measured gain only by a precise

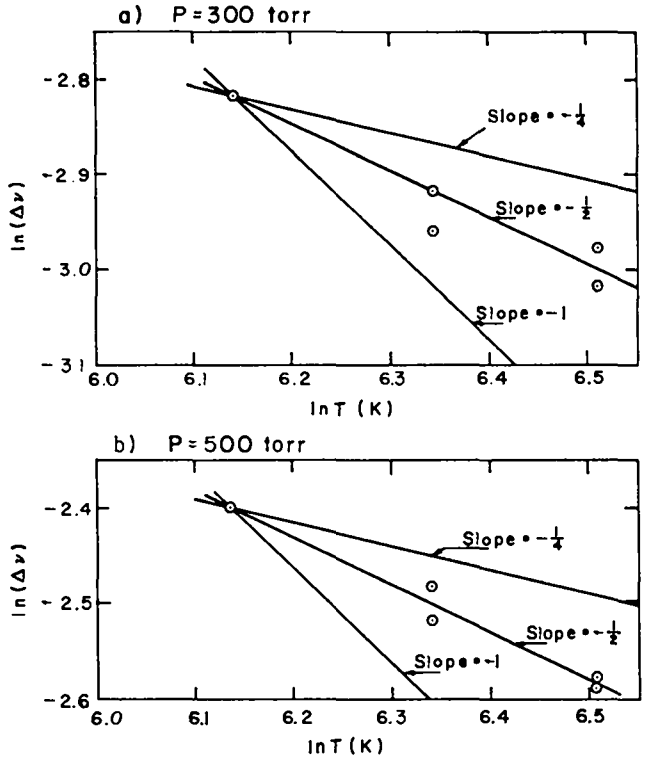

Fig. III-20.
Natural logarithm of the FWHM linewidth of 10.6-μm P-branch CO_2 transitions vs lnT(K) for (a) 300 torr pressure and (b) 500 torr. These results were obtained by tuning a weak 10-μm signal from a narrow bandwidth homostructure diode laser through the transition studied, using a 50-cm cell of heated CO_2.

knowledge of the temperature- and pressure-dependence of the linewidth.

Further studies on He and N_2 broadening of CO_2 are currently in progress, to shed further light on the temperature dependence of CO_2 line broadening in actual laser systems.

Intense Sequence-Band and Hot-Band Lasing in 3-atm CO_2 Double Discharge (B. J. Feldman, R. H. Fisher)

We report megawatt lasing on the (0, 0°, 2) → [(1, 0°, 1), 0, 2°, 1)]$_{I,II}$ sequence bands[17] and on the (0, 1^1, 1) → [(1, 1^1, 0), (0, 3^1, 0)]$_I$ hot band[18] of a 3-atm double-discharge CO_2 device.

In our experiments, we employed the Westinghouse 1800-torr 110-kV double-discharge

device described above. Its active gain length was 154 cm, and the aperture diameter 3.5 cm. Using a low-pressure probe laser, we measured gains in the high-pressure system for several conventional, sequence-band, and hot-band transitions as functions of gas mix and applied voltage. From this information, we obtained vibrational temperatures of the CO_2 ν_3 asymmetric stretch mode and of the ν_2 bending mode. The ν_3 vibrational temperatures were as high as 3000K.

To obtain the sequence-band lasing we set up an optical cavity consisting of a 100-line/mm, 10-μm blaze grating in Littrow configuration and an 80% reflective output coupler with a 20-m radius of curvature.[19] The cavity contained the 1800-torr double-discharge medium, a heated (400K) CO_2 cell 2.4 m long, and a 1-m-long longitudinal discharge in a low pressure CO_2 gas mix. The hot CO_2 suppressed conventional lasing.[20] The low-pressure discharge, when repetitively pulsed,[20] aided cavity alignment and, when pulsed ~200 μsec before the high-pressure discharge, allowed us to obtain a single-mode, temporally smooth output pulse[21] on many sequence-band lines. Output pulses, 250 mJ in 80 ns, were obtained with a 80:10:10::He:N_2:CO_2 laser mix at 1800 torr. Figure III-21 shows an oscillogram of a temporally smooth sequence-band pulse and a densitometer trace corresponding to burn spots taken one at a time at the exit plane of 3/4-m grating spectrometer.

To obtain high-pressure hot-band lasing, a similar system was set up except that the hot CO_2 cell was replaced by a 1-cm-long cell of room-temperature SF_6 and the cavity grating was tuned to 11 μm. The addition of a few torr of SF_6 in the cell eliminated spurious 10-μm lasing from diffuse grating scatter and allowed us to obtain temporally smooth single-line, 200 mJ hot-band lasing on each of seven lines. Pulse lengths were approximately 100 ns. Optimum gas mix at 1800 torr was 78:11:11::He:N_2:CO_2 at an applied voltage of 120 kV.

The hot-band and sequence-band lasers can be fired synchronously and are being used to explore vibrational kinetics and saturation processes in high-pressure CO_2 laser amplifiers.

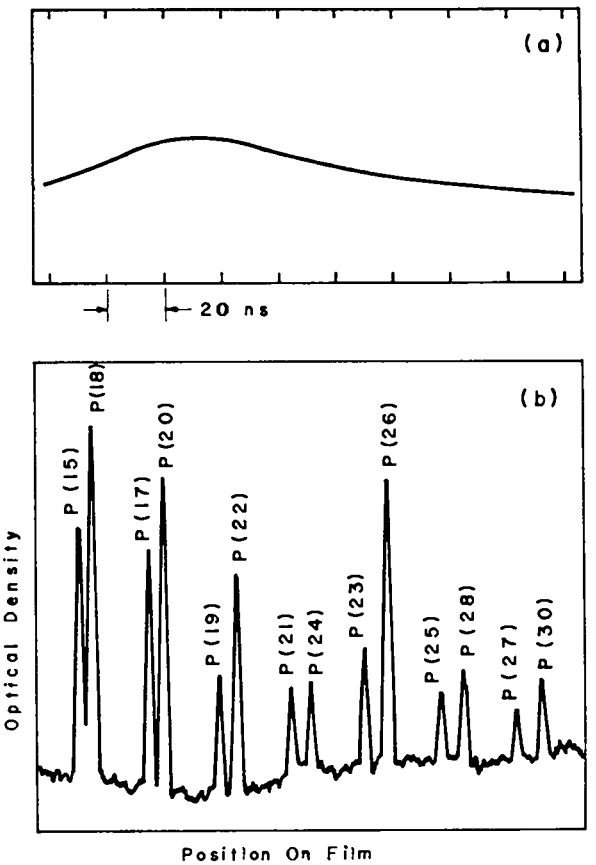

Fig. III-21.
Output of sequence-band laser: (a) Oscillogram of a single-line pulse with the low-pressure and high-pressure discharges properly timed. (b) Densitometer trace corresponding to burn spots taken in the exit focal lane of a grating spectrometer. Conventional lasing lines were taken for reference. Burns were taken one line at a time. The odd numbers identify sequence-band lines.

Modeling of Primary Electron Beams in CO_2 Amplifiers (J. Comly)

General. A series of Monte Carlo electron-transport codes was reported previously[22] for use in modeling the behavior of high-energy, "primary"

electron beams in CO_2 discharge amplifier systems. Basically, the codes consider the effects of beam scattering and energy loss due to background materials, as well as the forces as a result of the electromagnetic fields present in the discharge. These codes have been upgraded to provide more features and greater flexibility in two areas:

- the basic electron-transport structure (i.e., cylindrical or rectangular geometry, with variations in 1, 2, or 3 dimensions; spatially complex material shapes and field components; and structured "primary" beam distributions); and,
- problem-dependent coding (i.e., computations and diagnostics, tailored to a particular problem).

The computations below pertaining to Antares prototype currents were of particular significance, because the corresponding experiments provided the first direct verification of our primary electron transport calculations in these systems.

Prototype Discharge Modeling. As a first step in calculating the gain distribution, the transport codes were designed to calculate the source of ionization within the discharge regions. A 2-dimensional, rectangular-geometry transport code, DEP2DXY, has been designed to interface directly with the code[23] that computes discharge currents, and to use general forms for the electromagnetic fields. By iterating these codes, a self-consistent solution can be found; however, in practice, a single iteration, using a quadratic fit to the magnetic field strength, has proven adequate.

The results of such a self-consistent calculation are given in Fig. III-22, which shows a contour plot of the ionization density for the Antares prototype discharge under operating conditions: the 440-keV primary electrons pass through a 2-mil titanium foil, at x=0.0, into the discharge region which contains a 0:1:4::He:N_2:CO_2 mixture at 1800 torr and a discharge field of 17 kV/cm. In the Antares geometry, the discharge tends to pinch along the z direction (the optical beam path), as shown in the figure by contours at the maximum ionization position (+), and at the 90-, 70-, 40-, and 10-% levels. The data from Fig. III-22, and a similar computation transverse to the optical beam direction (where magnetic fields can be neglected), were used in obtaining the discharge currents and gain values indicated as theoretical in Figs. II-6 and II-7 in Sec. II.

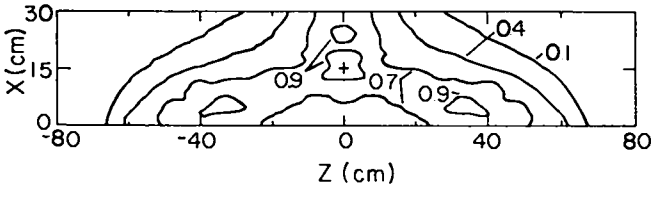

Fig. III-22.
Predicted ionization density in Antares prototype power amplifier discharge region.

Prototype Primary Current Distributions. A cylindrical electron-transport code SCTDEP has been modified to model the experiments that measured the primary currents inside the prototype chamber. The components of the model are shown schematically in Fig. III-23; the transport was three-dimensional, with absorbing boundaries in r and z,

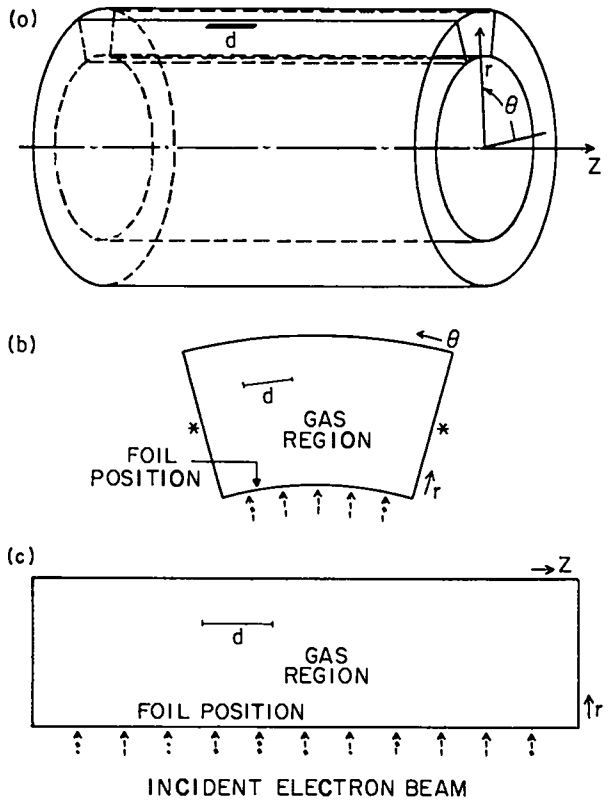

Fig. III-23.
Schematic of geometry treated by code SCTDEP; (a) perspective views, (b) and (c) cross sections of a sector region.

and reflecting boundaries in θ (these latter boundaries, marked * in the figure, simulate the effects of the adjacent sectors); the primary beam impinged uniformly over the area shown in (θ,z), onto the 2-mil titanium foil at r_{min}; magnetic fields were present in the gas region, which contained air at 580 torr.

The object marked d represents a typical detector window, used to record the electron current passing through it; at several values of r, the gas region was covered in (θ,z) with a grid of such detectors. In the experiments, a 0.8-mil titanium foil covered the detectors; Fig. III-24 shows the transmission of such a foil as a function of electron energy and incidence angle. These data, which were calculated by a Monte Carlo preprocessor code, were used by SCTDEP as a detector-response function. Some predicted currents are shown in Fig. II-4 in Sec. II.

Design Optimization. Because the discharge-modeling procedures described above have proven relatively accurate in reproducing the measured gain distributions for several of our CO_2 amplifiers, we feel confident in using these codes to design new laser systems and to upgrade those presently operating. Of the many approaches being considered toward optimizing these complex systems, that of gain engineering uses most fully the abilities of the codes at modeling structurally detailed objects; in this case, the goal is to produce a more uniform gain distribution through simple changes in structures making up the discharge chamber (i.e., primarily changes in the foil, anode, or other boundaries). These computations are in progress; of course, more fundamental changes (alternative gas mixtures, for example) are also being studied.

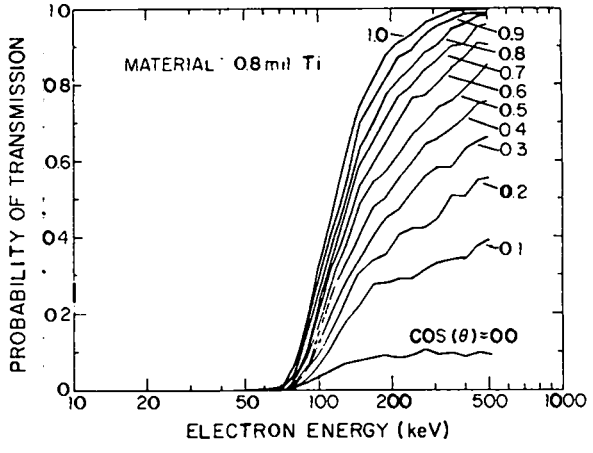

Fig. III-24.
Transmission probabilities for a 0.8-mil titanium foil; the curves are labeled with the cosine of the incidence angle.

Other Applications. In addition to modeling our CO_2 lasers, these codes have been successfully applied to several other laser devices, both at LASL and elsewhere. Also, we have used these codes to investigate aspects of high-energy electron transport as it applies to laser fusion target behavior. Fig. III-25 shows the penetration of a 30-keV, one-dimensional Maxwellian electron source into glass; such curves are useful, not only for target design, but also for judging the accuracy of electron transport in codes such as LASNEX.

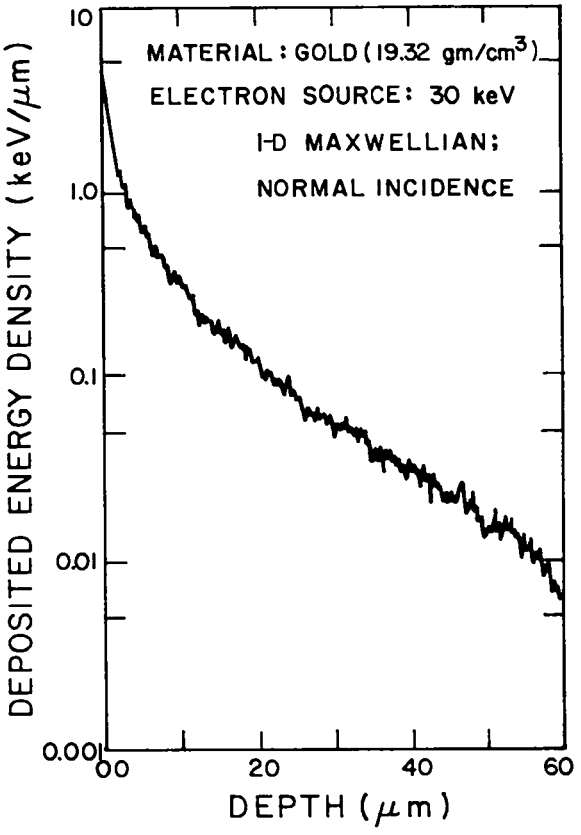

Fig. III-25.
Energy deposition resulting from an electron source at a temperature of 30 keV incident onto glass.

Calculations of Short-Pulse Amplification in a Large CO_2 Laser Amplifier (H. C. Volkin and J. F. Hafer)

Results of calculations and comparison with the experimental data for nanosecond pulses amplified in the LASL TBS are reported here. Modeling of such amplifier systems to predict pulse shape and energy is important for choosing operating parameters to obtain various performance regimes, for designing future systems, and for the possible need to fashion pulse shapes to laser fusion requirements.

The computations are based on the traveling wave description that takes into account (1) the coherence of the medium polarization and (2) the rotational relaxation in upper and lower vibrational levels, as the various lines comprising the pulses interact.[24] For each line P(J) in the pulse, the pulse propagation code numerically integrates the set of coupled equations

$$\frac{1}{c}\frac{\partial E_J}{\partial t} + \frac{\partial E_J}{\partial z} = -P_J ,$$

$$\frac{\partial P_J}{\partial t} + \frac{1}{T_2} P_J = -\frac{1}{2T_2} n_J \sigma_J E_J ,$$

and

$$\frac{\partial n_J}{\partial t} + \frac{1}{T_1}(n_J - n_J^0) = 8 P_J E_J . \qquad \text{(III-9)}$$

The pulse component corresponding to the P(J) transition has its carrier frequency at line center J, with intensity I_J (z,t) (w/cm^2), electromagnetic field envelope $E_J = (I_J/2h\nu_J)^{1/2}$, polarization envelope ρ_J, stimulated emission cross section σ_J, and rotational population inversion density for the transition n_J.

The second term in the third equation characterizes the thermalization of rotational energy within a vibrational level by a single time constant T_1, which is assumed to be the same for both the upper and lower vibrational levels. The rotational Boltzmann distribution $Z_{J-1}(T)$ within the upper vibrational level is postulated to equal $Z_J(T)$ for the lower level, so that the equilibrium inversion is $n_J^0 = Z_J(N^U - N^L)$, where N^U (N^1) is the population density in the upper (lower) vibrational level. This form of the rotational relaxation term is obtained from the so-called reservoir model of the process, where the energy transfer collision probability into any given rotational level is assumed to be independent of the initial rotational level. To follow the time variation of the vibrational populations, the computation uses the dependent equations

$$\frac{d}{dt} N^U = 4 \sum_{J=0}^{\infty} P_J E_J ,$$

$$\frac{d}{dt} N^{L10} = -4 \sum_{J10} P_J E_J ,$$

and

$$\frac{d}{dt} N^{L9} = -4 \sum_{J10} P_J E_J , \qquad \text{(III-10)}$$

with the last two summations extended only over those lines in the 10-μm band and 9-μm band, respectively, that are contained in the pulse.

The transition dipole dephasing time T_2, the rotational thermalization time T_1, and the stimulated emission cross sections for the temperature and pressure in the gas mix used are calculated from measured reference values. In multiple passes, the vibrational-level populations distributed along the amplifier length after traversal of the pulse are stored and then used to determine the vibrational populations encountered by the beam on the next passage through the medium.

The triple pass optical layout in each half of the LASL TBS amplifier is illustrated schematically in Fig. III-26. In all cases the gas mix is

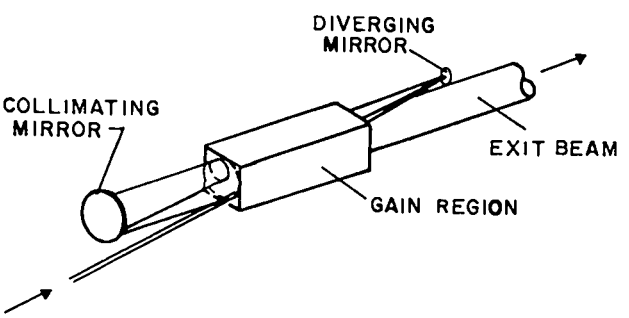

Fig. III-26.
Schematic of triple-pass optical system in amplifier module of Two-Beam System.

$He:N_2:CO_2::3:0.25:1$ at fill pressure and temperature of 2000 torr and 300 K, respectively. Beam dimensions are listed in Table III-II. An estimated 3% reflection loss at each mirror was included. A kinetics calculation of the e-beam controlled discharge at a typical gain value gave the temperature in the 200-cm gain section as 330 K. The same coherent traveling-wave equations are employed to calculate the propagation through the cold absorbing gas of the amplifier. All the pulses presented here are single-line P(20), for which the rotational relaxation model is very accurate.

The leading and trailing halves of a measured input pulse[25] are fitted separately by polynomial curves, and these are used as input for the pulse propagation computations. For one case, Fig. III-27 shows the measured input and output pulses together with the output pulse calculated using the gain value that gives the measured output energy. Table III-III compares measured and calculated values of total energy and leading-edge risetime for five cases. The measured output pulse[25] in Fig. III-27 includes the effects of 70-ps instrument response time, but this effect has been removed from the measured risetimes given in Table III-III. The agreement is seen to be excellent, well within the experimental uncertainties of the measured quantities. We note a small systematic discrepancy in gain values. This is probably a result of the variation in the initial gain across the aperture. The beam path for measuring small-signal gain differs from that of the main beam, hence the measured gain value may differ systematically from the value representative of the amplified beam.

TABLE III-II

BEAM DIMENSIONAL FOR TRIPLE-PASS TBS AMPLIFIER

Pass	Beam Diameter	Path Length (cm) in Gas		
		Cold	Hot	Cold
1	2 cm, uniform	191	200	150
2	17:1 expansion	150	200	150
3	34 cm, uniform	150	200	408

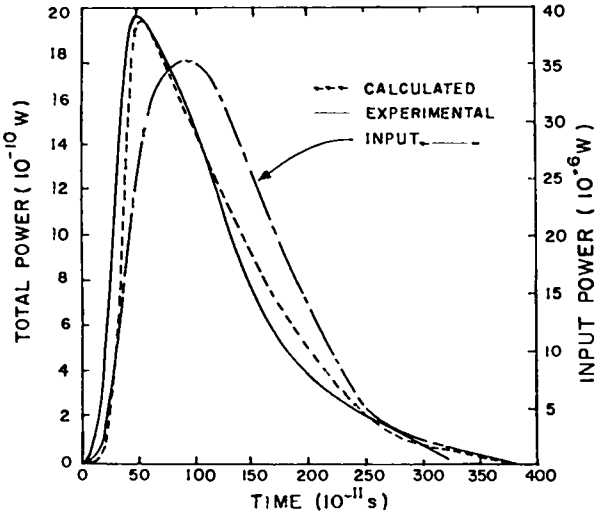

Fig. III-27.
Comparison of measured and calculated output pulses together with the output pulse calculated by using the gain value that gives the measured output energy.

TABLE III-III

MEASURED AND CALCULATED TOTAL ENERGY AND LEADING EDGE RISETIMES FOR TRIPLE-PASS TBS AMPLIFIER

Exp. Input Energy (mJ)	Gain (%/cm)		Output Energy (J)		Output 10-90% Risetime (ps)	
	Expt.	Calc.	Expt.	Calc.	Expt.	Calc.
80.0	1.91	1.84	242	241	237	200
		1.91		279		190
53.0	1.94	1.91	272	274	345	420
		1.94		292		410
39.5	1.86	1.85	221	219	280	320
		1.86		225		310
42.9	1.95	1.88	242	240	415	450
		1.95		282		460
50.0	1.89	1.84	230	232	410	430
		1.89		261		420

Parasitics

Parasitics in the EBS (C. J. Elliott)

The primary problem is that of establishing the static gain threshold for parasitic oscillations. The dynamics of the problem, which determine the extent to which the static thresholds may be exceeded, will be described in a subsequent progress report. All parasitic target modes involve light which is necessarily well-collimated. To reach the target, light must make at least one pass through the laser medium and cannot originate more than 0.5 cm outside the 18-cm-diam radius of the beam at the large recollimating mirror located at the end of the amplifier module. Some of the light that returns from the target may fall near the edge of this recollimating mirror as indicated in Fig. III-28a; this light is responsible for the two-pass oscillation. The majority of light, however, is reflected by the recollimating mirror, makes another pass through the gain medium, and strikes in the vicinity of the small turning mirror as indicated in Fig. III-28b by the number 2. The light falling beyond the edge of this small mirror is responsible for the first of two four-pass modes. The second four-pass mode involves light that was reflected from the turning mirror, but which failed to pass through the spatial filter hole. This light strikes the wall as indicated in Fig. III-28b. The light that did pass through the spatial filter hole is involved in the six-pass mode. In this case (see Fig. III-28c) the light is reflected by the entrance window to the amplifier module, whose surface has an effective nonspecular reflection coefficient of 10^{-4} to 10^{-5}/sr. Although very weak, this mode dominates because of its very high gain.

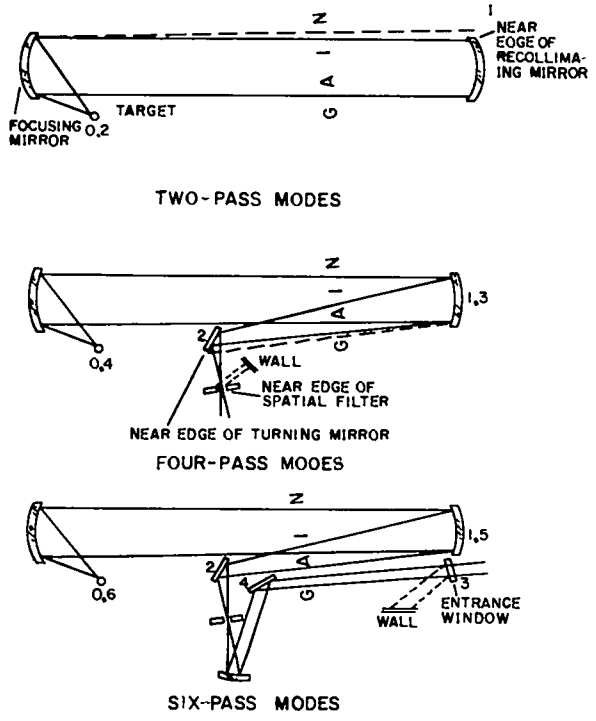

Fig. III-28.
Schematic of modes in the EBS. The mode path can be traced by following the numbers starting at 0.

The target may scatter the impinging light in two ways: either specularly, giving a single ray; or nonspecularly, giving a pencil of rays. All small targets will scatter some light by diffraction, but such scatter can be lumped together with nonspecular reflections in our analysis. In general, specular parasitic oscillations occur at a lower oscillation threshold than the corresponding nonspecular mode. On the other hand, specular modes may be suppressed completely by deliberate lateral target misalignment on the order of 30 to 50 μm. In this case, the six-pass threshold is raised (at $\alpha\ell = 3$) from a gain-length product of 6.5 to the nonspecular value of 7.0.

In estimating parasitic oscillation thresholds, we have assumed the reflection coefficients shown in Table III-IV. In addition, scatter from the surface of the spatial filter fixture is assumed to be specular, with R_{SF} equal unit. At a target diameter of 400 μm the results are only weakly dependent on diameter.

TABLE III-IV

ASSUMED REFLECTION COEFFICIENTS

	Reflection Coefficient (sr^{-1})	
	Nonspecular	**Specular**
Target	$\rho_T = 0.01$	$R_T = 0.1$
Nextel	$\rho_N = 0.01$	0
Salt	$\rho_S = 10^{-6}$*	$R_S = 0.08$*

*With the SF_6 cell, these values should be twice as large unless AR coatings are used.

The results of our theory may be expressed in the form

$$F \exp (6\, g_o \ell_g - 4\, \alpha \ell_\alpha) = 1 \quad , \qquad \text{six pass}$$

$$F \exp (4\, g_o \ell_g - 4\, \alpha \ell_\alpha) = 1 \quad , \qquad \text{four pass} \tag{III-11}$$

where F is the return fraction listed in Table III-V, with subscripts S and NS for specular and nonspecular modes, respectively. The $4\alpha\ell_\alpha$ term is a result of the saturable absorber that is passed four times in either the four- or the six-pass mode (twice on the way out, twice on the way back). The saturable absorber is assumed to be located in front of the large recollimating mirror.

Table III-V gives an expression F_S and F_{NS} for each of the modes, which are defined in terms of reflection coefficients listed in Table III-IV and of solid angles, also given in Table III-V. The quantity appearing under the formula is the estimated F-value and the number in parenthesis is the corresponding value of $g_o\ell_g$ when α is assumed to be zero. The last two entries in Table III-V are the values of $g_o\ell_\alpha$ for $\alpha\ell_\alpha = 3$.

It is seen that the lowest oscillation threshold occuring with $\alpha\ell = 3$ is 6.5, which occurs in a six-pass mode. This mode involves an effective diffuse reflection from the entrance window and a nonspecular reflection from inside the amplifier module. One can raise this threshold by employing antireflection coatings. At only slightly higher threshold is the four-pass spatial-filter mode which occurs when the spatial filter is painted black or when diffraction off of the edge of the spatial filter is appreciable.

TABLE III-V

STATIC THRESHOLD FOR 400-μm TARGET MODES

		$\Delta\Omega_1$	$\Delta\Omega_2$	$\Delta\Omega$	F_{NS}	F_S	($\alpha\ell$=3) Non-specular $g_o\ell_g$	($\alpha\ell$=3) Specular $g_o\ell_g$
6-pass	Entrance Window	0.13	1.3×10^{-6}	3×10^{-7}	$(\rho_T\Delta\Omega_1)(\rho_S\Delta\Omega_2)$ $1{:}7 \times 10^{-14}$(5:2)	$R_T(\rho_S\Delta\Omega)$ 3×10^{-13}(4:8)	7.2*	6.8*
	Inside DBM	0.13	1.3×10^{-6}	3×10^{-7}	$(\rho_T\Delta\Omega_1)(R_S^2\rho_N\Delta\Omega_2)$ $1{:}1 \times 10^{-13}$(5:0)	$R_T(R_S^2\rho_N\Delta\Omega)$ $1{:}9 \times 10^{-12}$(4:5)	7.0*	6.5*
4-pass	Near Turning Mirror	2×10^{-3}	3×10^{-6}	5×10^{-10}	$(\rho_T\Delta\Omega_1)(\rho_N\Delta\Omega_2)$ 6×10^{-13}(7:0)	$R_T(\rho_N\Delta\Omega)$ 5×10^{-13}(7:1)	10.0	10.1
	Spatial Filter Fixture	0.13	3×10^{-6}	10^{-7}	$(\rho_T\Delta\Omega_1)(\rho_N\Delta\Omega_2 R_{SF})$ 4×10^{-10}(5:4)	$R_T(\rho_N\Delta\Omega R_{SF})$ 10^{-10}(5:8)	8.4	8.8
	Blocked Spatial Filter	0.13	2×10^{-3}	6×10^{-6}	$(\rho_T\Delta\Omega_1)(\rho_N\Delta\Omega_2)$ 3×10^{-8}(4:3)	$R_T(\rho_N\Delta\Omega)$ 6×10^{-8}(4:2)	7.3	7.2
2-pass					Insignificant			

*With SF_6 operation, these values should be reduced by 0.1 due to the two pieces of salt near the entrance window (i.e., R_S and ρ_S should be two times as large as in Table III-IV).

Parasitics in Antares (C. J. Elliott and J. C. Goldstein). Calculations show that parasitic oscillations will not damage targets in the Antares system. It had been previously suspected that the fast-rising gains and large distances between target and power amplifier in Antares would minimize the parasitic oscillation problem. Detailed calculations now verify that the parasitic loading of targets is insufficient by far for their destruction before the laser pulse arrives. A parasitic oscillation involves the optical coupling between the target and an internal surface of the amplifier. For feedback to occur, the spontaneously emitting light must travel from the amplifier to the target and back, but before many of these trips take place, the gain is raised and the energy is extracted. This effect requires microsecond pumping times, which are technically feasible for electron-beam-pumped CO_2 lasers, but not for glass or YAG systems. In the Antares system the round-trip time is ~0.4 μs, and as much as 0.8 μs (half the pumping time) is available during which the gain can be raised above the static oscillation threshold without penalty.

The complicated laser optical system is modeled below. Figure III-29 shows a cavity consisting of a gain region (modeled as alternating gain and loss regions) and of two mirrors with return fractions RF_t at the target and RF_p inside the power amplifier. The return fractions are computed from knowledge of the optics. In a simple example of diffuse surfaces at the target and inside the power amplifier, we have

$$RF = \rho\Delta\Omega, \qquad \text{(III-12)}$$

where ρ is the reflection coefficient per steradian and $\Delta\Omega$ is the maximum solid angle subtended by the opposing surface and limited by the optical stops (field stop) of the system.

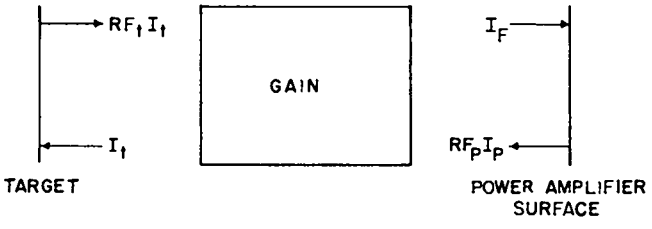

Fig. III-29.
Model of laser optical system.

Accurate estimates return fractions from the target end of the system have been a matter of discussion for some time. To avoid these uncertainties, we have concentrated on the worst case of 100% reflection from the target.

The return fraction within the power amplifier is chosen on the basis of both theoretical expectations and experience with the EBS. There, six-pass and four-pass modes were found to be most worrisome. In Antares, six-pass modes do not exist; we therefore consider the most important four-pass mode, which occurs off of the spatial-filter holder (see Fig. I-3 in Sec. I.) Although spatial filters will certainly be improved, we assume that the spatial filter is a planar aperture coated with a black paint having a reflectance of ρ = 1%/sr. In this case the full solid angle of the collimating mirror, as viewed from the spatial-filter hole, will return light to the target. Assuming a beam area of 850 cm^2 and a collimating-mirror focal length of 1000 cm, we have a solid angle of 8.5 10^{-4}/sr and a return fraction $\rho\Delta\Omega$, of 8.5 10^{-6}.

If light of intensity I_t impinges upon the target, an interesting $RF_t \cdot I_t$ is returned toward the gain region. In Antares, two passes of gain occur so that the intensity of light incident on the power amplifier surface is

$$I_p = I_t\ RF_t\ \exp(2g_o\ell). \qquad \text{(III-13)}$$

The gain coefficient g_o and the intensity must be evaluated at a time different from that of I_p, due to the finite transit time. Ignoring these time-dependent effects, after the return pass, we have

$$I'_t = I_t\ \exp(4g_o\ell)\ RF_p\ RF_t\ . \qquad \text{(III-14)}$$

Thus, any intensity within the cavity will die out unless

$$\exp(4g_o\ell)\ RF_p\ RF_t \geq 1, \qquad \text{(III-15)}$$

which defines the static threshold $(g_o\ell)_t$ as

$$(g_o\ell)_t = -\frac{1}{4}\ell n(RF_p\ RF_t)\ . \qquad \text{(III-16)}$$

If there were a loss $\alpha\ell$ in the system, $(g_o\ell)_t$ would be $[(g_o-\alpha)\ell]_t$. Were the gain independent of time or even slowly rising, this would define the threshold

$(g_o\ell)_t$ above which the intensity would become very large and damage the target.

The gain is not independent of time, and as soon as the threshold is exceeded there is an appreciable amount of radiation within the cavity due to spontaneous emission. The total spontaneous emission from a length $d\ell$ ending up on the target is

$$\frac{\Delta\Omega_t}{4\pi} \exp(g_o\ell) \left[A\hbar\omega\, S_\ell N_u d\ell\right] . \qquad \text{(III-17)}$$

The term in brackets is the total spontaneous emission power emitted by length $d\ell$ and area S_ℓ by upper-state density N_u, which has a lifetime A^{-1} and emits quanta of energy $\hbar\omega$; the $\exp(g_o\ell)$ term describes the gain of those quanta; and the term $\Delta\Omega_t/4\Pi$ is the fraction that ends up on the target. Because the solid angle-area product $\Delta\Omega_t S_\ell$ is an invariant through the system, this description is appropriate even for the expansion pass. The solid angle $\Delta\Omega_t$ itself is proportional to the target area S_T by

$$\Delta\Omega_t = S_T/f_t^2 \quad , \qquad \text{(III-18)}$$

where f_t is the focal length of the focusing mirror. We may, thus, arrive at the intensity on target by integrating over the amplifier length and dividing by target area giving

$$I_T(\text{spon}) = \frac{1}{4\pi f_t^2} \frac{\exp(g_o\ell)-1}{g_o} \left[A\hbar\omega\, S_\ell N_u\right] \quad . \qquad \text{(III-19)}$$

This spontaneous emission and its subsequent amplification have been described in great detail in a number of codes, the results of which are reported below.

The gain curves we used were computed and based upon a model of the electrical network with a time dependent resistive discharge. The peak discharge current density J_{max} describes the shape of the gain curve and is a convenient parameter to use because the discharge pinching constraint is expressed as $J_{max} < 6.6$ A/cm². As shown in Fig. III-30, when J_{max} is increased, the gain builds up faster and the parasitic loading of the target decreases. The target loading plotted is given for one of the six beams.

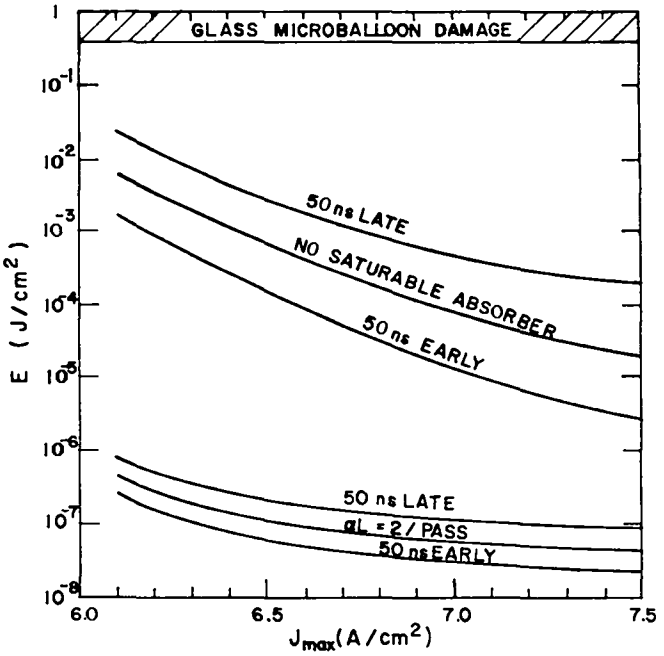

Fig. III-30.
Target loading due to parasitic oscillations.

The upper set of three curves plot the condition for a case with no saturable absorber. The middle curves apply when the oscillator pulse arrives at the intended extraction gain; the lower curve is for a pulse 50 ns early, and the upper, for a pulse 50 ns late. Evidently a saturable absorber is not required in the system.

If for unforeseen reasons the target is damaged at a substantially lower loading than 0.4 J/cm² or if the feedback due to the spatial filter were higher than assumed, saturable absorbers will reduce the target loading even further. The effect of a saturable absorber with an $\alpha\ell$ of 2 per pass is shown by the lower set of curves. Four additional orders of magnitude are added to the margin of safety.

Our calculations assumed that only a single laser line was involved and that all radiation was emitted at line center where the gain is highest. In fact, the target loading is only one-third of that indicated by these calculations. Detailed studies show a ten-fold reduction due to line-width effects and a three-fold increase due to multiple lines, for a net factor-of-3 decrease.

In summary, target parasitics, which presently limit the performance of the EBS, are not predicted

to be a severe problem in Antares. In the event of unforeseen contingencies, saturable absorbers could be used to control these oscillations.

OSCILLATOR DEVELOPMENT (E. J. McLellan, R. F. Harrison, E. E. Bergmann)

Introduction

A TEA CO_2 oscillator with minor modifications has been used to produce single 400-mJ pulses with 170-ps risetime and 650-ps duration. These pulses have multiline spectral content.

Variable pulse-width generation in the 0.15- to 1.15-ns range has been demonstrated using 50-ohm electro-optic switches; CdTe crystals with apertures as large as 1.5 cm have been used to produce these subnanosecond pulses with high reliability and contrast ratio.

Compact, High-Power Oscillator

The TEA CO_2 oscillators presently in use at LASL produce multiline, temporally smooth laser pulses with ~0.5 J in a 100-ns FWHM pulse. To obtain subnanosecond pulses, an electro-optical switch is used to chop out a 0.15-ns to 1.15-ns segment of the longer pulse with a peak power of 1 - 10 MW. Upper limits on pulse energy are established by the optical damage level of AR-coating on the CdTe E-O switch crystals. Previously, tests showed this damage level to be 500 MW/cm^2 for a 1.0-ns pulse, but only 20 - 50 MW/cm^2 for a 100-ns pulse.

A more efficient design for a short pulse generation system would increase the peak power of the input pulse to the E-O switch while sufficiently reducing its time duration to prevent coating damage. A system has been designed to meet this objective with an energy extinction ratio $\geq 10^6$. This is a minimum requirement for present front-end designs.

This system is illustrated in Fig. III-31. Two E-O switches are used to slice a 1-ns-duration segment from the gain-switched pulse in a conventional manner. This slice is then reinjected to make four passes through the oscillator gain medium and finally sent through 3 additional E-O switches. These act to improve contrast ratio and can be used to select pulse widths down to 0.15 ns.

A pressure regulation system has been added to hold the oscillator main discharge at 760 ± 0.1-torr pressure. By varying the pressure in the cavity, the cavity optical length can be pressure-tuned with a resolution of ~0.1 μm.

Figure III-32 shows the 400-mJ pulse produced by the four-pass system when a 1.15-ns pulse is switched out of the 200-mJ oscillator pulse and reinjected. Little change is seen in the pulse risetime (170 ps) but the pulse is shortened to 650 ps due to the heavy saturation during the four-pass amplification. Measured pulse energy variation is ± 5%. In fact, the oscillator medium is so heavily saturated during the four-pass amplification that output energy is highly reproducible even when the initial switched-out pulse energy varies by factors of 3. Background energy after the four passes is 30 mJ, mainly due to the oscillator path diffraction coupling into the four-pass amplifier path. A spatial filter at the output eliminates the coupled background energy, reducing the background to the value determined by the E-O switchout extinction ratio and reducing the pulse energy to 325 mJ. Additional switchout crystals can be used after the four passes to provide isolation and to increase the energy extinction ratio to the required value for any amplifier system. Line content and amplitude of the pulses vary, but a typical pulse energy spectrum is composed of 5% P(22), 10% P(16), 25% P(18) and 55% P(20), all in the 10-μm band. A Q-switch is being installed in the oscillator path to increase the line reproducibility and the number of lines and to make the energy on each line equal. Optical quality of the pulse appears good and tests are under way to determine its Strehl ratio.

Variable Pulse-Width Generation Methods

Inertial confinement fusion using laser drivers requires efficient, high-power, high-contrast pulses of ir radiation. The CO_2 laser drivers used are typically high-gain devices that require careful control of input pulse risetime, pulse durations, and prepulse background from a master oscillator. To meet this requirement, a system has been developed that is capable of generating CO_2 laser pulses with full

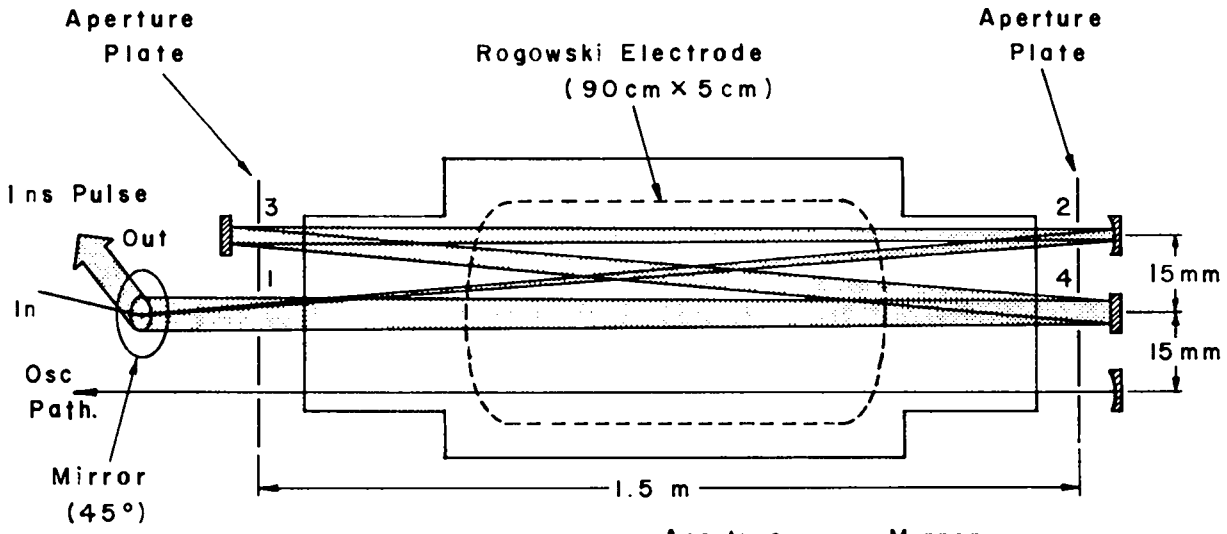

	Aperture (dia-mm)	Mirror (rad-m)
1	15	∞
2	10	5
3	8	∞
4	12	∞

Fig. III-31.

Schematic diagram of the compact, high-power subnanosecond pulse generation system. Two electro-optic switches (not shown) are used to slice a 1-ns duration section from the signal labeled "osc. out," which is then reinjected through the partial reflector shown for four additional passes in the oscillator gain medium. The amplified output pulse is sent through additional electro-optical switches (not shown) to improve contrast ratio.

width at half maximum in the range 0.15 to 1.15 ns, and risetime as short as 0.1 ns.

The basic building block of this system is a 50-Ω CdTe Pockels cell with 95% voltage transmission and an electrical bandwidth > 1 GHz. The high-voltage transmission and wide bandwidth allow series stacking of the cells to produce variable width, high-contrast-ratio, subnanosecond-duration CO_2 laser pulses. Two of the 10-mm-aperture cells with 1.5 GHz electrical bandwidth were used in series to generate variable-width pulses of CO_2 radiation. The first cell was placed between crossed polarizers and transmitted CO_2 radiation only when voltage was applied. The second cell was placed between polarizers that were aligned parallel and blocked CO_2 radiation when voltage was applied. Timing of the two cells is determined by the difference between the optical transit time for the CO_2 radiation and the transit time for the high-voltage pulse between cells. CO_2 pulse width was varied by changing the optical path length between cells while maintaining fixed electrical length in the interconnecting cable. As the optical path became shorter, the pulse width was decreased, by 33 ps/cm.

The output from this double Pockels cell system was monitored with a commercial pyroelectric detector and displayed on a LASL 5-GHz oscilloscope. Detection system risetime was 100 ps with a point spread function of 140 ps. The change in the pulse shape with decreasing optical path length is shown in Fig. III-33a through Fig. III-33d. Further decreases in the optical path beyond a point determined by the initial CO_2 pulse risetime do not further decrease the pulse width. In a systems application, one or more additional cells would be used to increase the contrast ratio and eliminate the post-pulse transmission shown in the figures.

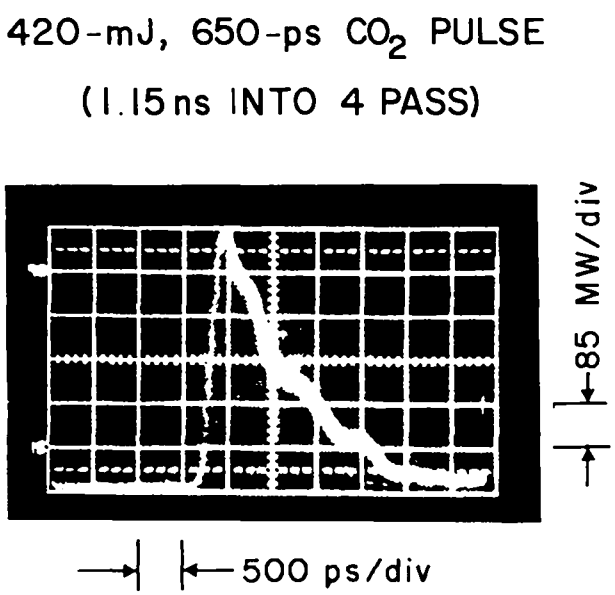

Fig. III-32.
Output power vs time for the compact, four-pass oscillator system described in text for 1.15 ns reinjected pulse width.

Multiwavelength Pulse-Shaped CO_2 Oscillator (R. L. Carman, N. Clabo, H. Lane)

The feasibility of replacing TEA CO_2 oscillators with several low-pressure stabilized CO_2 oscillators that are line-selectable has been examined. By controlling both the specific line content and their relative amplitudes, the requirements for efficient subnanosecond energy extraction, and for pulse shaping of several nanosecond-duration pulses might be satisfied.

Multiple low-pressure CO_2 oscillators for pulse generation in CO_2 fusion systems must satisfy several criteria. First, we must demonstrate highly reproducible outputs for any P-or R-branch line in at least the 10-μm band, if not also in the 9-μm band. Using an Invar cavity and a 1:1:1 mix of $He:CO_2:N_2$ at a pressure of 15 torr, we have successfully demonstrated very stable pulsed outputs of ~100 watts at P-20 with little change in peak power as we scan from P-10 to P-30 in the 10-μm band. R-branch outputs show a similar stability. The final mirror cavity now being fabricated will house 6 independent oscillators, each with a PZT-translator feedback stabilization system.

A second requirement for successful deployment of the low-pressure pulse generator is that it deliver an output intensity comparable to that of a TEA CO_2 oscillator with comparable amplitude stability and a reproducible spectrum. In this connection, we have examined the possibility of amplifying the low-pressure CO_2 oscillator outputs, after beam synthesis by an ir grating, in low-pressure CO_2 amplifiers. To be successful, we first had to develop the capability of producing gains in low-pressure devices comparable to that of a TEA medium.

We note that the use of a TEA medium for this purpose is not desirable because we are adding more gain to the overall system and unnecessarily enhancing its ability to amplify retropulses. By using a low pressure device, we can amplify a 100-ns portion of the 100-μs, low-pressure oscillator output without significantly enhancing the time-integrated system gain.

At an electric field-vs-pressure ratio (E/p) of ~10 to 15 V/cm·torr and ~1 cm in diameter, a uniform, well-stabilized plasma is established continuously in a $CO_2:N_2:He$ mixture, which efficiently stores energy in the CO_2 (00°1) level at total pressures of 1 to 20 torr. Attempts to increase the density-diameter product leads to unstable discharges and/or to less efficient discharge coupling to the CO_2 (00°1) level. By pulsing the electrical system, more current can be introduced without corresponding detrimental gas heating, increasing the optical output.

The krytron Marx bank, constructed for this purpose had a measured risetime of ~1 ns 60 kV output and a 50 Ω load. Two such banks are used to drive the anodes at each end of a 1-m-long, of 1.6-cm diam CO_2, laser tube. The cathode at the center of the tube was grounded. Pulsed electric fields of 1200 V/cm were thus available. The electron avalanche is sufficiently fast that current in the tube starts to flow in < 500 ns with a risetime of ~100 ns for a $CO_2:N_e:He$ fill of ~4 torr. Increasing total pressure reduces both the delay and the risetime. The current pulse duration is less than 2 μs, but, even at 4-torr pressure, maximum laser output did not occur until ~100 μs later, even in N_2-free discharges. Further, we find that the only role of the He in this connection was to facilitate plasma initiation. Addition of N_2 did not alter the observed time intervals by more than 20%, but did substantially increase the laser energy output. This is to be expected

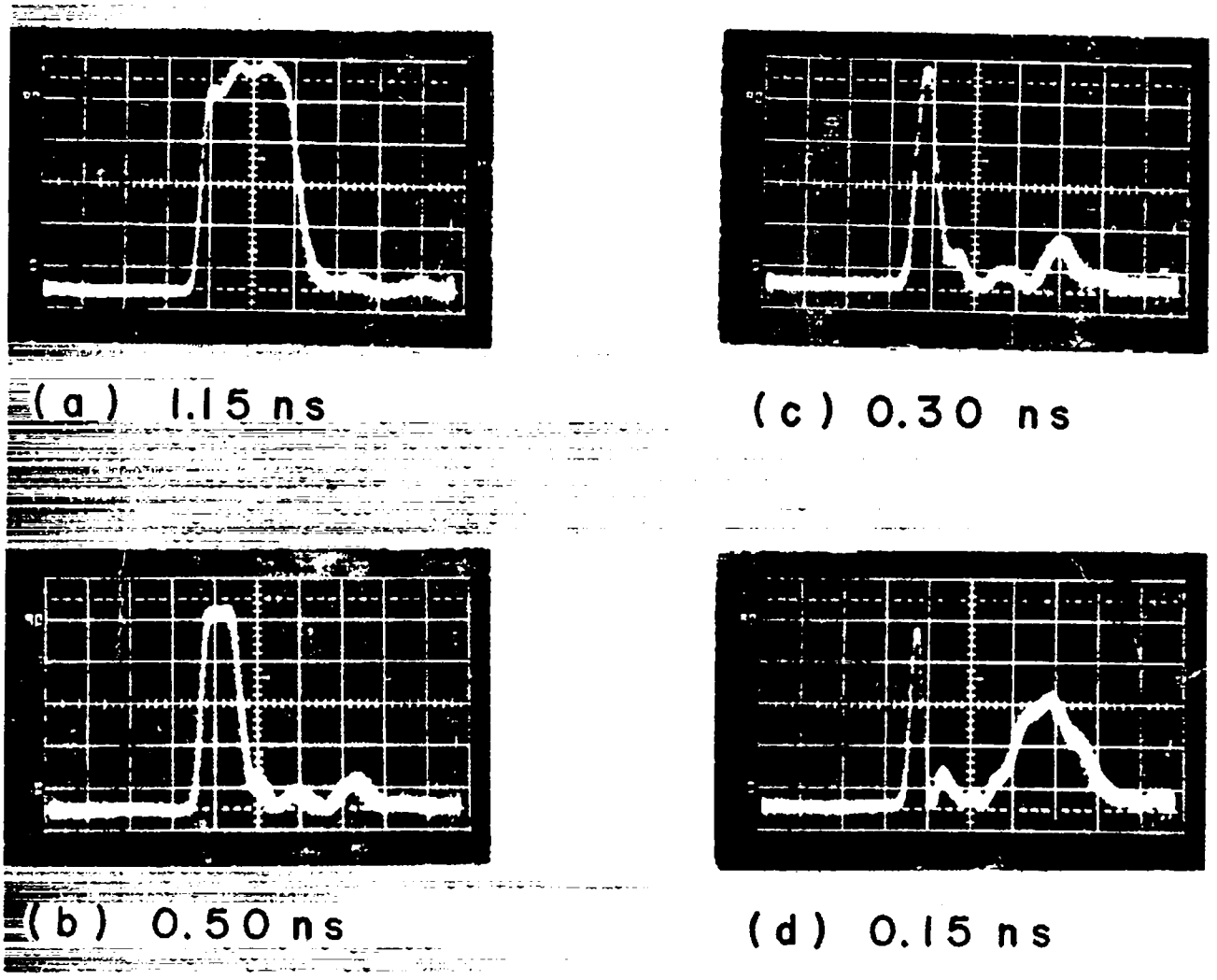

Fig. III-33.
Photographs (a) - (d) show continuously variable pulsewidth at 10.6 μm generated by consecutively reducing the optical path length between the two Pockels cells used in the system described in the text.

because the electron-resonance excitation of vibrations has a broader energy width in N_2 than in CO_2. The origin of the long delay appears to be connected with the large number of collisions required to thermalize the very highly excited CO_2 (00°n) vibrational manifold.

For higher density-diameter products, a steady field of ~200 V/cm is superimposed. The voltage level adjusted to be just below discharge conditions, and helps stabilize the discharge, greatly improving its reproducibility. For the highest density-diameter products we used, the voltage was used to establish a small "simmer" discharge current. Its effect was to lower the initial impedance of the tube, making it easier to achieve the desired pulsed-plasma conditions. At higher pressure, the small gas heating induced by this procedure is negligible.

The optical properties of 0.8-, 1.6-, 3.2-, and 7.5-cm-diam tubes with fill pressures between 1 and 60 torr have been studied for an oscillator/amplifier system of this design. We found that a 1:1 CO_2:N_2 partial pressure was optimum, whereas the optimum He:CO_2 pressure ratio varied from 1:1 to 3:1,

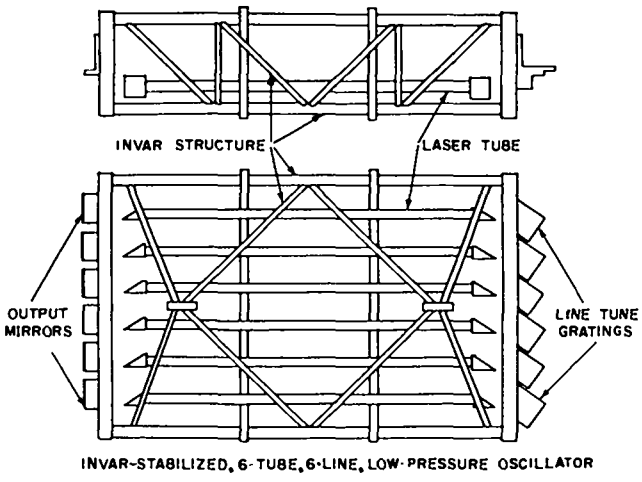

Fig. III-34.
Illustration of the layout of the 6-tube, low-pressure, CO_2 pulse generator capable of reproducible 6-line outputs. Note each is grating-tunable and has active PZT amplitude stabilization.

depending on total pressure and tube diameter. Optical gain rose in ~50 to 100 μs, whereas the fall was dictated by vibrational to translational decay processes, as well as by optical pulse saturation. Peak gains in excess of 2.5%/cm at repetition rates of > 1 pps were obtained. A detailed parameter study of the effects of varying voltage, capacitance, ballast resistance, pressure mix, and tube size was also performed.

We are presently procuring an Invar-stabilized, 6-tube, 6-line low-pressure oscillator, illustrated in Fig. III-34; a GaAs 100-ns pulse clipper; and a 2-m double-pass, low-pressure CO_2 amplifier. We believe this system will produce greater than 100-kW peak power in ~100 ns.

OPTICAL DAMAGE STUDIES (B. E. Newnam, D. E. Gill)

Introduction

A continuing program of damage research at 10.6 μm is conducted in support of the LASL CO_2 effort. One major program (AR coatings on Ge) was concluded while a second (AR coatings on NaCl) is continuing. Several smaller efforts are also reported.

Damage Resistance of (AR-Coated Germanium Surfaces

Gallium-doped germanium was developed at LASL for possible use as a saturable absorber in the final amplifiers of the EBS because laser damage has been previously observed at operating intensities, a careful evaluation of the state of the art of AR-coated Ge for 10.6 μs was performed.[25]

Antireflection coatings comprising fourteen coating designs using eight film materials were obtained from nine coating manufacturers. Polycrystalline, p-doped Ge substrates polished by one vendor were supplied to each. Substrates polished by a second vendor were also supplied for comparison. Additionally, single-crystal, Ge, p-doped and undoped, and undoped polycrystalline Ge were coated by one vendor to evaluate the effect of crystal structure and doping.

This study produced a number of results, which are briefly summarized. Damage thresholds were measured with 1.2-ns pulses on bare and coated surfaces by single-shot (1-on-1) and multishot (N-on-1) irradiation of a site. Only front surface damage was observed. With few exceptions, the thresholds for coated surfaces were centered at 0.49 ± 0.03 J/cm². Bare Ge had a threshold ranging from 0.65 to 0.70 J/cm². No significant differences due to substrate polish, crystallinity or doping level were evident, and multiple-shot conditioning resulted in the same threshold as for single-shot tests. From an analysis of standing-wave electric fields, damage of AR-coated Ge appeared to be limited by the surface properties of Ge. Measurements at both 1.2 and 70 ns indicated that the threshold of both coated and uncoated Ge increases as the square root of the pulse-width, i.e., $E_D(J/cm^2) \sim \tau^{1/2}$.

Use of Mylar Films to Prevent Damage to NaCl Windows

Retropulse energy incident on the input NaCl window (uncoated, 4-in. diameter) of LASL's eight-beam CO_2 amplifier has caused damage. To circumvent this problem without resorting to extensive amplifier redesign, a thin Mylar film (Dupont polyethylene terephthalate) was conceived as a sacrificial shield when placed in front of the window.

Experience with Mylar films at LASL has shown that at breakdown a sufficient number ($\sim 10^{19}/cm^3$) of free electrons are generated in a plasma to terminate transmission of a CO_2 laser beam by absorption and scattering. Because breakdown of Mylar occurs at a lower fluence than does NaCl, we measured the amount of protection provided by a thin 1/4-mil Mylar film. Kapton (polyimide) films were also tried.

For practical application in LASL's amplifiers, the films could not attenuate much of the primary, forward-going CO_2 pulses. Therefore, transmittance measurements of several thicknesses of Mylar and Kapton were performed both with coherent CO_2 pulses (P(20) line at 10.59 μm) and with an ir spectrophotometer. From these measurements the refractive index and absorption coefficient of Mylar were determined to be 1.2 ± 0.1 and $\sim 130\ cm^{-1}$ at 10.6 μm. The respective values for Kapton were 1.5 ± 0.1 and $\sim 300\ cm^{-1}$. Thus, only 1/4-mil Mylar had an acceptable transmission of 90%. The incident energy densities at the threshold of rear-surface damage of the uncoated Polytran NaCl window for single 1.15-ns, 10.59-μm pulses are given in Table III-VI. With the Mylar films in place, the fluences listed are actually the quantities which would have reached the NaCl window in the absence of the films. In other words, at the damage threshold for each test, the same fluence, 5.8 J/cm² (or 4.7 GW/cm²) reached the sample. Thus, a single, 1/4-mil Mylar film provided 2.2 times protection and two films afforded greater than 2.3 times protection. (Actually, we could not muster enough laser intensity to damage the NaCl window when protected by two films.) We observed, however, that contamination of the front surface of the NaCl window occurred with a film as close as 4 mm. This would probably have caused front surface damage if irradiated a second time. Further, the damage threshold (hole blown in the film) of the 1/4-mil Mylar was approximately 2.5 J/cm² or 2 GW/cm² for a single 1.15-ns pulse.

TABLE III-VI

INCIDENT ENERGY DENSITY AT THRESHOLD OF REAR SURFACE DAMAGE OF UNCOATED POLYTRAN NaCl

Condition	Energy Density (J/cm²)	Protection by Films
1. No Mylar protection	5.8	-----
2. With 1/4-mil Mylar film 6 cm in front of substrate	12.8	2.2 X
3. Same as 2 but with 2nd 1/4-mil Mylar film 4 mm in front of substrate	>13.2	>2.3 X

AR Coatings on NaCl

LASL has a contract with OCLI to develop better AR coatings for NaCl windows, for use with the EBS and Antares. OCLI sends samples to LASL for damage testing and then uses the results of our measurements to determine the next approach. At the beginning of this period, typical damage thresholds for AR-coated NaCl were 3 to 4 J/cm² for a 1.2-ns FWHM, 10.6-μm laser pulse. (A complete description of the damage test facility and procedure is available in Ref. 19.) Thresholds have shown continuous improvement over the period. The last and best sample measured had thresholds at three locations on the sample of 5.3, 6.1, and 6.9 J/cm², with a range of $\pm$ 1.0 J/cm². Note that this sample was 8 in. in diameter, indicating the vendor's ability to handle larger sizes. In the future some samples as large as 16 in. in diameter will be produced and tested.

Two samples were subjected to a humidity test. The samples were soaked for 24 h in 30-50% humidity. The thresholds were reduced by 7% in one sample and 13% in the other.

Metal Mirrors

The damage thresholds of four metallic mirrors have been measured. These mirrors are to be used in the diagnostic section of the EBS. The thresholds in Table III-VII were obtained using 1.15-ns 10.6-μs laser pulses.

TABLE III-VII

DAMAGE THRESHOLDS FOR FOUR METALLIC MIRRORS

Mirrors	Thresholds (J/cm^2)
Electroless Au on electroless Ni and Al	1.15
PTR-Ag on Pyrex (1800 Å thick Ag, overcoated with 350 Å ThF_4)	1.35
PTR-Au on Pyrex (1800 Å thick Au, no overcoat)	1.07 – 1.67
PTR-Al on Pyrex (1000 Å thick Al, overcoated with 450 Å MgF_2)	1.03

Note: The gold had a very large range from point to point on the surface. The damage thresholds of all of these samples could probably be raised by requiring thicker layers of metal. This will be tried in the future.

REFERENCES

1. J. Steinfeld, J. Chem. Phys. **52**, 5421 (1970).
2. C. R. Phipps, Jr. and S. J. Thomas, J. Appl. Phys. **47**, 204 (1976).
3. S. J. Czuchlewski, A. V. Nowak, and E. Foley, Optics Letters, to be published.
4. C. R. Phipps, Jr., and S. J. Thomas, Optics Letters, 1, 93 (1977).
5. L. M. Frantz and J. S. Nodvik, J. Appl. Phys. **34**, 2346 (1963).
6. M. Born and E. Wolf, *Principles of Optics* (Pergamon Press, New York, 1959).
7. R. G. Wenzel, G. P. Arnold, and N. R. Greiner, Appl. Optics **12**, 2245 (1973).
8. E. Carnall, Jr., D. Pearlman, T. J. Coburn, F. Moser, and T. W. Martin, Mat. Res. Bull. **7**, 1361 (1972).
9. D. Pearlman, E. Carnall, Jr., and T. W. Martin, J. Solid State Chem. 1, 138 (1973).
10. R. K. Ahrenkiel and J. Coburn, IEEE Trans. on Mag. **11**, 1103 (1975).
11. H. Haskal, E. Bernal, and D. Chen, Appl. Optics **13**, 886 (1974).
12. G. Prinz, Naval Research Laboratory, personal communication, 1977.
13. R. Fisher and B. J. Feldman, Optics Letters **161** (1977).
14. J. Reintjes, R. L. Carman, and F. Shimizu, Phys. Rev. **A8**, 1486 (1973); J. Reintjes, thesis, Harvard University (1971).
15. E. B. Treacy, IEEE J. Quantum Electron **QE-5**, 454 (1969); E. B. Treach, Phys. Letters, **A28**, 34 (1968).
16. H. D. Sutphin, R. F. Benjamin, A. J. Lieber, and C. B. Webb, "Low Jitter Laser Triggered Spark Gap Using a Thin Solid Dielectric," Los Alamos Scientific Laboratory internal report (1975).
17. J. Reid and K. Siemsen, Appl. Phys. Lett. **29**, 250 (1976).
18. J. A. Howe and R. A. MacFarlane, J. Mol. Spectrosc. **19**, 224 (1966); B. Hartmann and B. Kleman, Can. J. Phys. **44**, 1609 (1966).

19. P. Lavigne, J. L. Lachambre, and G. Otis "Sequence-Band Emission in a 1-atm Amplifier," presented at the 1977 Annual OSA Meeting, Toronto, Canada, Oct. 13, 1977.

20. J. Reid and K. Siemsen, J. Appl. Phys. 48, 2712 (1977).

21. A. Gondhalekar, N. R. Heckenberg, and E. Holzhauer, IEEE J. Quantum Electron, **QE-11**, 103 (1975).

22. D. B. Henderson, "Electron Transport in Gas Discharge Lasers," Los Alamos Scientific Laboratory report LA-5154-MS (April 1973).

23. E. Stark and F. Skoberne, "Laser-Fusion Program, October 1-December 31, 1976" Los Alamos Scientific Laboratory report LA-6834-PR (October 1977), pp. 14-15.

24. B. J. Feldman, "Multiline Short Pulse Amplification and Compression in High Gain CO_2 Laser Amplifiers," Opt. Commun. 14 (May 1975), pp. 13-16.

25. P. C. Goldstone and J. McLeod, Los Alamos Scientific Laboratory, personal communication.

26. B. E. Newnam and D. H. Gill, "Damage Resistance of AR-coated Germanium Surfaces for Nanosecond, CO_2 Laser Pulses," presented at the Ninth Symposium on Materials for High Power Lasers, NBS, Boulder, Colorado, October 4-6, 1977.

IV. LASER FUSION EXPERIMENT, TARGET DESIGN, THEORY, AND MILITARY APPLICATION

In an integrated program of theory, target experiments, and target design, we are establishing a fundamental understanding of laser-target interactions, particularly of the relevant plasma physics and hydrodynamics. Both the experimental and the theoretical efforts have concentrated on studying the wavelength-dependence of laser-plasma interactions. The close coupling of theory and experiment has made it possible to eliminate theories that are not supported by experiment. In general, basic studies of laser-plasma interactions have shown that the design difficulties associated with long wavelengths are less severe than believed earlier, and that breakeven target designs are attainable even in the presence of a hot-electron spectrum. These results have given us new confidence that significant yield can be obtained from more efficient, less expensive CO_2 lasers.

TARGET EXPERIMENTS

Introduction

Having successfully completed the first major milestone of the experimental program - to demonstrate the use of high-power CO_2 laser radiation to burn DT fuel in spherical targets - we developed a simple physical model that describes the features of the targets. A common parameterization of the model allows a direct comparison between 1.06-μm-driven and 10.6-μm-driven targets. Essentially identical behavior of the targets is observed with the two wave-lengths.

Emphasis was given to experimentally testing computations of electron transport and x-ray generation performed with the design code LASNEX. This area was chosen as the next portion of LASNEX that was likely to display the greatest inaccuracy. Furthermore, accurate transport calculations are essential to the design of future laser fusion targets. A variety of diagnostics were employed in experiments that yield x-ray continuum spectral information in the 30-eV to 2.5-keV range, high-resolution characteristic x-ray line spectra in the 0.75 keV to 1.3 keV and 1.8 keV to 2.2 keV regions, temporal resolution of the lowest energy portion of the spectrum, and spatial resolution of both continuum and line emission. X-ray imaging techniques were employed that yielded two-dimensional emission information for various portions of the x-ray spectrum and three-dimensional reconstructions for broadband emission. Spectral line shape fitting of "seed" impurities in the fuel of spherical targets yielded densities in agreement with spatially resolved line and two-dimensional imaging methods. The agreement among these measurements proves that the fuel in CO_2-driven spherical targets remains confined inside the shell pusher until peak compression.

The effects of CO_2 laser light prepulses were examined in detail. Bulk heating of spherical glass shells was dominant. It could be concluded that prepulsing in our Two Beam laser spherical-shell experiments did not cause fuel escape before compression of the fuel. This conclusion is in agreement with spatially resolved x-ray measurements.

Electron preheat reduction using low-density conduction paths for the elimination of suprathermal electrons has been, and continues to be, an active

area of research, as is verification of the momentum impulse imparted to a target by escaping low-energy ions.

The energy loss attributable to fast (accelerated) ions has been accurately determined to be less than 10% for CH_2 and Be targets. This value is in agreement with calculations that take into account the exponential velocity dependence of the fast ions, the determination of "hot" electron temperature solely by the field geometry in the absorption region, and the necessity for the absorbed laser flux to be carried away by electrons. This fast-ion loss fraction is expected to be laser wavelength-independent.

A thorough study of the absorption of 10.6-μm laser light by targets of various shapes was completed. Accurate measurements of unabsorbed (scattered) laser light indicated absorptions nearly identical to those measured at a wavelength of 1.06-μm.

Simple Model for Exploding Pusher Targets (D. Giovanielli). Analytic models that describe physical phenomena are preferable to numerical solutions if the analytic models can be derived while still preserving the essential physics. A limited understanding of which physical processes are dominant clouds our judgment of the validity of a given model. As data become available, the model can be used to predict the outcome of individual experiments and, more importantly, the dependence of derived quantities on input parameters.

Models have been presented[1] to explain the results of laser-driven spherical exploding-pusher experiments - the only spherical experiments that have been successful to date. Sufficient data now exist over a range of target and laser parameters to allow comparison to the models and to lend confidence to the ability of the models to predict behavior in new parameter regimes. A model is presented below, which is, perhaps, the simplest conceptually of those presented thus far, and appears to fit the available data at least as well as other models.

Model Assumptions. The following assumptions were made.

1. All the absorbed laser energy, minus the fast ion and radiative losses, goes to heating the target shell and fuel mass.
2. The energy is carried throughout the target instantaneously by energetic electrons whose ranges are large compared to target areal mass-densities.
3. The fuel and pusher material are in thermal equilibrium at peak compression.
4. Half of the shell mass explodes outward and half explodes inward pushing the fuel mass in front of it.
5. The inner half of the shell distributes itself with uniform density from the initial sphere radius to the compressed radius.
6. The shell collapse velocity is the sound speed

$$C_s \approx \sqrt{\frac{Z_s}{A_s}\frac{T}{M_p}}$$

7. The fuel density is uniform throughout the core.
8. The fusion reaction time is twice the time it takes for the compressed fuel to expand such that the fuel ion density decreases by a factor of $\sqrt{2}$.
9. The fuel expansion is isothermal and occurs with a velocity equal to the sound speed in the fuel.
10. The D-T reaction rate is given by the Gamow formula.
11. Uniform heating of the target is assumed and no hydrodynamic instabilities are considered.
12. Shock heating is not included.

Definitions. To simplify the later discussions, a table of the symbols used in the analysis is included here:

β - laser light absorption fraction (typically 0.25)[2]

ε_l - fast ion and radiative loss fraction (typically 0.25)[3]

$E_L(t)$ - laser energy input up to time t

t_b - time of peak compression, referenced to start of laser pulse.

E_s, E_f - useful energy in shell, fuel at time t_b

E_u = $E_s + E_f$

M_s, M_f = mass of shell, fuel

M = $M_s + M_f$

ε = E_u/M - useful specific energy

M_p - one atomic mass unit

T_s, T_f - temperature of shell, fuel (energy units)

A_s, A_f - average atomic weights of shell, fuel

Z_s, Z_f - average ionic charge of shell, fuel

ρ_s, ρ_f - initial material density of shell, fuel

N_{i_S}, N_{i_f} - number of ions in shell, fuel

n_{i_S}, n_{i_f} - ion density in shell, fuel at $t = t_b$

r_1 - original shell radius (center of shell)

Δr_1 - original shell wall thickness

r_o - collapsed fuel radius

δt - reaction duration time

δr - fuel radius increase in time $\delta t/2$

Derivation of Expression for Yield. From assumptions 1 and 2

$$E_u = \beta (1-\varepsilon_l) E_L(t_b) = \frac{3}{2}\left[N_{i_S}(1+Z_s)T_s + N_{i_F}(1+Z_f)T_f\right]. \quad \text{(IV-1)}$$

Solving for T_s.

$$T_s = \frac{2}{3}\frac{E_u}{M}\frac{A_s}{1+Z_s} = M_p \frac{1+\frac{M_f}{M_s}}{1+\frac{M_f}{M_s}\frac{A_s(1+Z_f)}{A_f(1+Z_s)}\frac{T_f}{T_s}}. \quad \text{(IV-2)}$$

From assumption 3, $T_s = T_f$ and

$$T_f = \frac{2}{3}\varepsilon\frac{A_s}{1+Z_s}M_p \frac{1+\frac{M_f}{M_s}}{1+\frac{M_f}{M_s}\frac{A_s}{A_f}\frac{(1+Z_f)}{(1+Z_s)}}. \quad \text{(IV-3)}$$

Using assumption 3 and the fact that at peak compression the fuel and pusher pressures are equal (i.e., momentum is conserved),

$$(1+Z_f)n_{i_f} = (1+Z_s)n_{i_s} \quad (t = t_b). \quad \text{(IV-4)}$$

Then, from assumptions 4 and 5,

$$n_{i_s} = \frac{1}{2}\frac{N_{i_s}}{4\pi r_1^2}\frac{3r_1^2\Delta r_1}{r_1^3-r_o^3} = \frac{3}{8\pi}\frac{M_s}{A_s M_p}\frac{1}{r_1^3-r_o^3}. \quad \text{(IV-5)}$$

From assumption 7

$$n_{i_f} = \frac{3}{4\pi}\frac{M_f}{A_f M_p}\frac{1}{r_o^3}. \quad \text{(IV-6)}$$

Combining Eqs. (IV-4), (IV-5), and (IV-6) we obtain the collapsed fuel radius r_o in terms of the target parameters,

$$r_o = \left(1+\frac{1}{2}\frac{1+Z_s}{1+Z_f}\frac{A_f}{A_s}\frac{M_s}{M_f}\right)^{-1/3} r_1. \quad \text{(IV-7)}$$

We see that for a given material shell density ρ_s and a given initial gaseous fuel fill pressure ($\rho_f = \rho_o P$),

$$r_o = \left(1+\frac{3}{2}\frac{1+Z_s}{1+Z_f}\frac{A_f}{A_s}\frac{\rho_s}{\rho_f}\frac{\Delta r_1}{r_1}\right)^{-1/3} r_1. \quad \text{(IV-8)}$$

For the special case given by $\rho_s/\rho_f = 10^4/P(\text{atm})$, $A_f = 2.5$, $A_s = 20$, $Z_s = 10$, $Z_f = 1$,

$$r_o \approx \left(1+\frac{10^4}{P(\text{atm})}\frac{\Delta r_1}{r_1}\right)^{-1/3} r_1. \quad \text{(IV-9)}$$

The collapse time t_b is obtained from Eqs. (IV-3) and (IV-7) and assumption 6,

$$t_b = \frac{r_1 - r_o}{C_s} \quad . \tag{IV-10}$$

The time during which fusion reactions take place is, using assumptions 8 and 9,

$$\delta t = \frac{2\delta r}{\sqrt{\frac{Z_f}{A_f}\frac{T_f}{M_p}}} \tag{IV-11}$$

where δr is obtained, under assumption 8, from

$$\left(\frac{r_o + \delta r}{r_o}\right)^3 = \sqrt{2} \tag{III-12}$$

or

$$\delta r = r_o(2^{1/6} - 1) = 0.1225\ r_o \ . \tag{IV-13}$$

The volume within which reactions are assumed to take place is taken as the average of the minimum compressed volume and the volume at which point n_{i_f} drops by $\sqrt{2}$,

$$V = \frac{1}{2}\frac{4}{3}\pi r_o^3(1 + \sqrt{2}) = 5.06\ r_o^3 \quad . \tag{IV-14}$$

The fusion yield from the target is obtained from the formula

$$Y = n_{i_f}^{\ 2}\ V\ \delta t\ \overline{\sigma v} \quad . \tag{IV-15}$$

The average emission volume, V, is given by Eq. (IV-14); the burn duration is given by Eq. (IV-11), using Eqs. (IV-13) and (IV-8). The value of $n_{i_f}^2$ is taken as the peak value (at minimum fuel radius), and $\overline{\sigma v}$ is evaluated at the temperature of the fuel at peak compression.

Combining equations (IV-14), (IV-11), (IV-13), (IV-8), (IV-6) and the Gamow formula for the DT reaction rate[4] yields

$$Y = 5.3 \times 10^{28}\ \frac{r_1^4 \rho_f^2}{Z_f^{1/2} A_f^{3/2}}$$

$$\left[1 + \frac{3}{2}\left(\frac{1+Z_s}{1+Z_f}\right)\frac{A_f}{A_s}\frac{\rho_s}{\rho_f}\frac{\Delta r_1}{r_1}\right]^{2/3} \frac{\exp\left(\frac{-19.94}{T_f^{1/3}}\right)}{T_f^{7/6}} \ , \tag{IV-16}$$

where T_f is in keV, length in cm and initial densities in g/cm³. In the case of moderate aspect ratios (less than 300) and an initial fuel density-to-shell density ratio less than 10^{-3}, the second term in the parentheses in Eq. (IV-16) dominates and

$$Y = 6.9 \times 10^{28}\left[\left(\frac{1+Z_s}{1+Z_f}\right)\frac{1}{A_s}\right]^{2/3}$$

$$\frac{1}{Z_f^{1/2} A_f^{5/6}}\ r_1^{10/3} \Delta r_1^{2/3}\ \rho_f^{4/3} \rho_s^{2/3}\ \frac{\exp\left(\frac{-19.94}{T_f^{1/3}}\right)}{T_f^{7/6}} \ . \tag{IV-17}$$

For a DT fuel, $Z_f = 1$, $A_f = 2.5$. The ratio $(1 + Z_s)/A_s$ for any pusher material is approximately 0.5, which leaves,

$$Y \cong 1.3 \times 10^{28}\ r_1^{10/3} \Delta r_1^{2/3} \rho_f^{4/3} \rho_s^{2/3}\ \frac{\exp\left(\frac{-19.94}{T_f^{1/3}}\right)}{T_f^{7/6}} \tag{IV-18}$$

if

$$\frac{\rho_s}{\rho_f} >> \frac{r_1}{\Delta r_1} \ . \tag{IV-19}$$

Thus, we see that the target parameters--wall thickness, radius, and D-T fill pressure--each have an important effect on the fusion yield, and the outputs from various targets cannot be compared without taking account of the target parameters, as well as the laser parameters such as total energy, pulse risetime, and peak power. From Eq. (IV-18) we

see that a natural yield parameter to consider is the normalized yield Y* where

$$Y^* = Y \times \left[\left(\frac{r^*}{r_1} \right)^{10/3} \left(\frac{\Delta r^*}{\Delta r_1} \right)^{2/3} \left(\frac{\rho_f^*}{\rho_f} \right)^{4/3} \left(\frac{\rho_s^*}{\rho_s} \right)^{2/3} \right] \tag{IV-20}$$

and r^*, Δr^*, ρ_f^*, ρ_s^* are convenient normalization values for initial radius and wall thickness and initial fuel and shell-mass densities. A convenient separation of parameters then occurs if T_f depends only on the laser parameters, but not (or only weakly) on the initial target parameters.

If condition (IV-19) is satisfied then

$$\frac{M_f}{M_s} = \frac{1}{3} \frac{\rho_f}{\rho_s} \frac{r_1}{\Delta r_1} \ll 1 , \tag{IV-21}$$

and Eq. (IV-3), for the fuel temperature during burn becomes

$$T_f \cong \frac{2}{3} \frac{A_s M_p}{1+Z_s} \mathcal{E} \tag{IV-22}$$

or

$$T_f(\text{keV}) \approx \frac{7 A_s}{1+Z_s} \mathcal{E} \ (\text{J/ng}). \tag{IV-23}$$

Unfortunately, $\mathcal{E}$, the useful specific energy, or the useful absorbed energy per unit target mass depends both on the laser parameters and the target parameters. Because $\mathcal{E}$ is the absorbed laser energy per unit target mass minus fast-ion and radiative losses integrated up to peak compression time t_b, the target dimensions and initial densities must enter,

$$\mathcal{E} = \beta (1-\mathcal{E}_i) \frac{E_L(t_b)}{M} . \tag{IV-24}$$

For a triangular temporal profile to the laser pulse, which rises linearly from zero to peak power in time τ_1 and falls linearly back to zero in time τ_2, the base to base temporal width is $\tau_1 + \tau_2$ and the FWHM is $1/2\ (\tau_1 + \tau_2)$. If the peak power is P_o, then the total energy in the laser pulse striking the target is $E_o = 0.5 \times P_o \times (\tau_1 + \tau_2)$ and

$$E_L(t) = \begin{cases} \dfrac{E_o t^2}{\tau_1(\tau_1+\tau_2)} , & 0 < t < \tau_1 \\ \dfrac{2E_o}{\tau_2(\tau_1+\tau_2)} \left[(\tau_1+\tau_2)\left(t - \dfrac{\tau_1}{2}\right) - \dfrac{t^2}{2} \right], & \tau_1 < t < \tau_1 + \tau_2 \\ E_o , & t > \tau_1 + \tau_2 . \end{cases} \tag{IV-25}$$

$\mathcal{E}$ must be found by iteration; the useful energy needed to cause the inner half of the shell to move into radius r_o at time t_b must be equal to the useful laser energy available up to that time. For cases such that conditions (IV-19) and (IV-21) are satisfied then we can use Eqs. (IV-8), (IV-10), and (IV-22) to get the approximate expression

$$t_b = 1.22 \left[1 - \left(\frac{\rho_f}{\rho_s} \frac{r_1}{\Delta r_1} \right)^{1/3} \right] r_1 \Big/ \sqrt{\frac{Z_s}{1+Z_s} \mathcal{E}} \tag{IV-26}$$

Because $\mathcal{E}$ is derivable from observed quantities for each target then various experiments can be compared on a curve of normalized yield vs useful specific energy. Alternatively, normalized yield may be graphed against fuel temperature (easily derivable from $\mathcal{E}$).

Figure IV-1 shows normalized neutron yield vs useful specific energy for a number of experiments. The experiments were performed with a CO_2 laser whose parameters were

$150 < E_o < 600$J,
$160 < \tau_1 < 500$ ps, and
$0.11 < p_o < 0.44$ TW.

The ranges of target parameters covered in these experiments were

$45 < r_1 < 105\ \mu$m,
$0.6 < \Delta r_1 < 1.4\ \mu$m,
$0.18 < \rho_f < 7.2$ mg/cm^3, and
$\rho_s = 2.4$ g/cm^3.

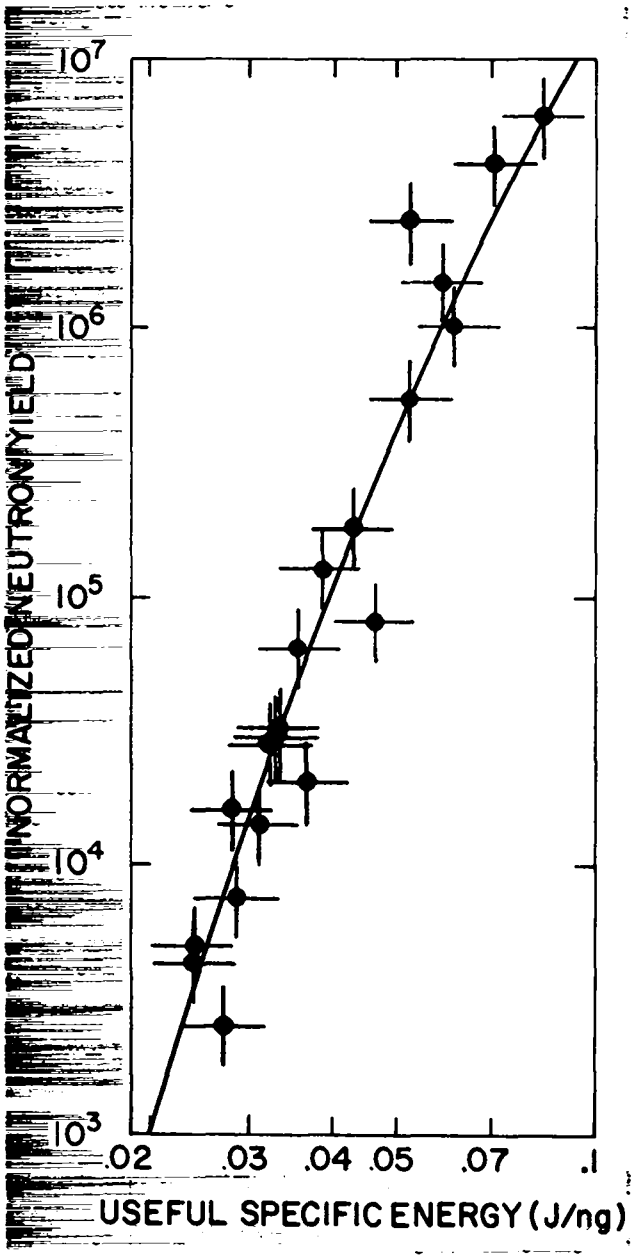

Fig. IV-1.
Normalized neutron yield vs useful specific energy for exploding-pusher targets. Normalized yield is defined by Eq. (IV-18) with $r^* = 100\ \mu m$, $\Delta r^* = 1.0\ \mu m$, $\rho_f^* = 0.2\ mg/cm^3$, $\rho_s^* = 2.4\ gm/cm^3$. *Results of experiments using a* CO_2 *laser (black) and a Nd:glass laser (red) are shown. The Nd: glass laser data are taken from Ref. 1 (Storm et al.).*

The agreement between the simple model and experiment is generally within experimental accuracy. Experiments quoted in Ref. 1 (Storm et al) have also been calculated with this model and the measured yield was calculated within the quoted experimental uncertainties. Some of these are indicated in Fig. IV-1.

The possibilities of predicting the scaling of yield with various target and laser parameters, and of optimizing target designs (with respect to yield) for given laser parameters, are the real advantages of an analytic model. At least we would hope to be able to outline the region of parameter space to be investigated by a more complete, and complicated calculation.

Figures IV-2, IV-3, and IV-4 show the predicted variation of yield with initial target radius, wall thickness, and DT fill pressure, respectively, other parameters being held fixed. For these cases a single temporal profile was assumed for the laser pulse. In Fig. IV-5 the variation of optimum DT fill pressure with laser pulse risetime is shown. In this case a shell radius of 200 μm was assumed with a wall thickness of 1 μm.

Figure IV-6 shows the results of reoptimizing the target parameters at each peak laser power for two laser-pulse temporal shapes. The wall thickness was constrained to be greater than 1000 Å. It is clear that breakeven (fusion energy equal to laser pulse energy) is not feasible with exploding-pusher targets and typically shaped laser pulses. In fact, other laser pulse shapes also do not give breakeven results, even for rather unrealistic shapes.

Figure IV-7 shows the variation of yield with peak laser power for several physically realizable target geometries and pulse shapes.

X-Ray Continuum Spectra (D. B. vanHulsteyn, P. Lee, K. B. Mitchell, and P. D. Rockett). The spatial and temporal characteristics of sub-keV x rays have been measured with x-ray diodes (XRD). A simple schematic of a typical XRD is presented in Fig. IV-8. X rays incident upon a cathode produce electrons that are accelerated to an

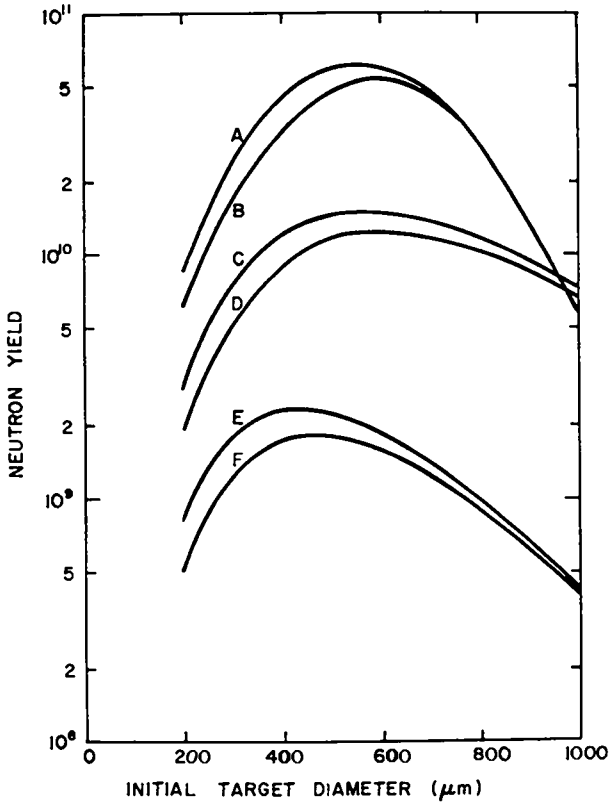

Fig. IV-2.
Yield vs glass microballoon initial diameter for different laser parameters. Initial wall thickness was 1.0 μm and DT gas fill pressure was 10 atm. The fraction of incident laser light absorbed was taken as 0.2. Triangular temporal laser pulse shapes were used with risetime τ_1, fall time τ_2, peak power P_o, and total energy E_o. A: τ_1 = 0.2 ns, τ_2 = 0.3 ns, P_o = 20 TW, E_o = 5 kJ; B: $\tau_1 = \tau_2$ = 0.25 ns, P_o = 20 TW, E_o = 5 kJ; C: τ_1 = 0.2 ns, τ_2 = 1.8 ns, P_o = 10 TW, E_o = 10 kJ; D: τ_1 = 0.25 ns, τ_2 = 1.75 ns, P_o = 10 TW, E_o = 10 kJ; E: τ_1 = 0.2 ns, τ_2 = 1.8 ns, P_o = 5 TW, E_o = 5 kJ; F: τ_1 = 0.25 ns, τ_2 = 1.75 ns, P_o = 5 TW, E_o = 5 kJ; F: τ_1 = 0.25 ns, τ_2 = 1.75 ns, P_o = 5 TW, E_o = 5 kJ. The initial target radius for optimum yield in these cases is between 200 μm and 325 μm, with a rather weak dependence (less than factor of 2) variation in yield over this range of radii.

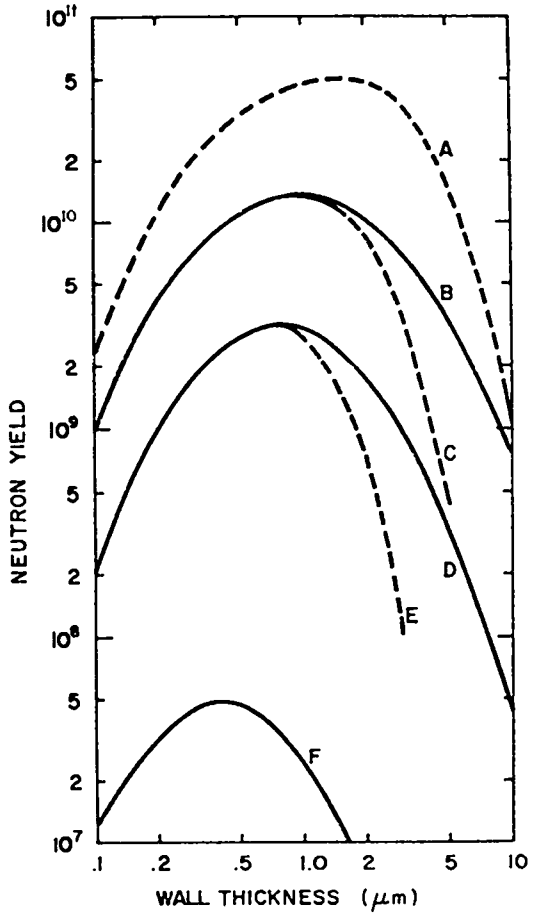

Fig. IV-3.
Neutron yield as a function of glass microballoon wall thickness for several laser triangular temporal pulse shapes, peak laser powers, and initial target radii. The fraction of incident laser energy absorbed was 0.25. A: τ_1 = 0.25 ns, τ_2 = 0.25 ns, E_o = 5 kJ, P_o = 20 TW, r_1 = 200 μm, initial DT fill pressure of 13 atm; B: τ_1 = 0.25 ns, τ_2 = 1.75 ns, E_o = 10 kJ, P_o = 10 TW, r_1 = 200 μm, fill pressure = 10 atm; C: τ_1 = 0.25 ns, τ_2 = 0.25 ns, E_o = 2.5 kJ, P_o = 10 TW, r_1 = 200 μm, fill pressure = 10 atm; D: τ_1 = 0.25 ns, τ_2 = 1.75 ns, E_o = 5 kJ, P_o = 5 TW, r_1 = 200 μm, fill pressure = 10 at m; E: τ_1 = 0.25 ns τ_2 = 0.25 ns, E_o = 1.25 kJ, P_o = 5 TW, r_1 = 200 μm, fill pressure = 10 atm; F: τ_1 = 0.25 ns, τ_2 = 1.75 ns, E_o = 1.0 kJ; P_o = 1 TW, r_1 = 150 μm, fill pressure = 7 atm.

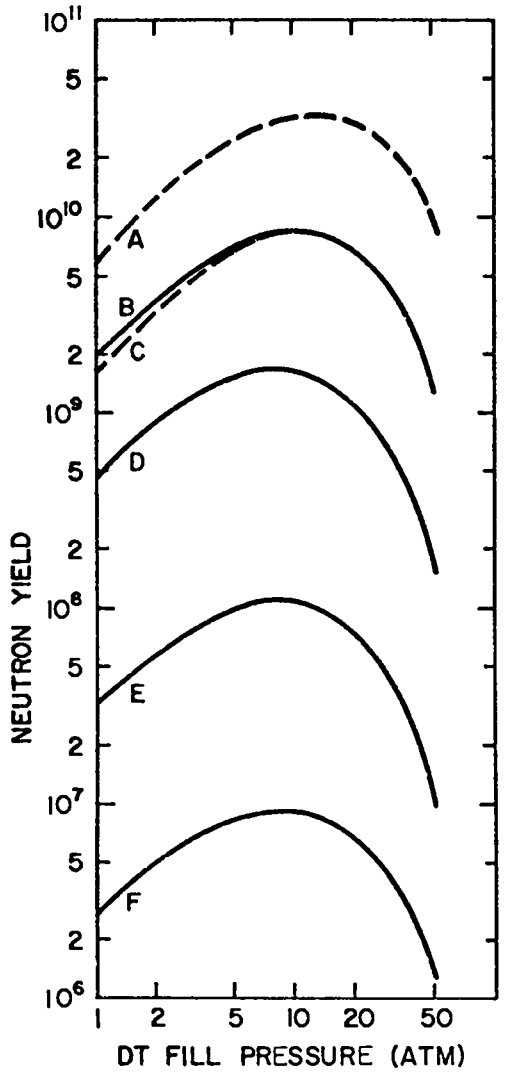

Fig. IV-4.

Neutron yield as a function of initial DT-fill pressure in a glass microballoon. The wall thickness was chosen as $\Delta r_1 = 1.0$ μm, and the zero-to-peak power risetime (τ_1) of the laser temporal pulse was taken as 0.25 ns in all cases. The solid curves are for a peak power to zero fall time (τ_2) of 1.75 ns, while for the dashed curves $\tau_2 = 0.25$ ns. A: $r_1 = 200$ μm, $E_o = 5$ kJ, $P_o = 20$ TW; B: $r_1 = 200$ μm, $E_o = 10$ kJ, $P_o = 10$ TW; C: $r_1 = 200$ μm, $E_o = 2.5$ kJ, $P_o = 10$ TW; D: $r_1 = 200$ μm, $E_o = 5$ kJ, $P_o = 5$ TW; E: $r_1 = 150$ μm, $E_o = 2$ kJ, $P_o =$ TW; F: $r_1 = 100$ μm, $E_o = 1$ kJ, $P_o = 1$ TW.

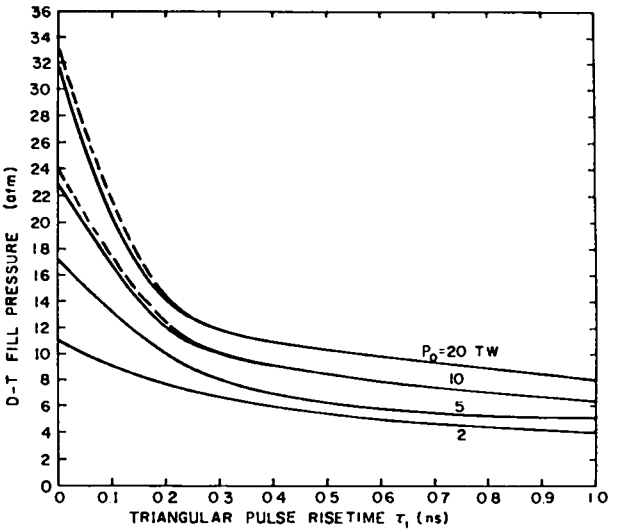

Fig. IV-5.

Initial DT gas fill pressure (50% each by number with no impurities) for maximum yield versus triangular laser pulse risetime. The initial glass microballoon radius was 200 μm and initial wall thickness 1.0 μm. Solid curves are for a 1.0-ns FWHM laser pulse; dashed curves are for a 0.25-ns FWHM pulse. Peak laser powers are indicated for the four powers considered. The absorption fraction for the laser light was assumed to be 0.25.

anode, the resultant current being displayed on a 5-GHz oscilloscope. The response of an Al cathode with various filters is shown in Fig. IV-9. 5000 Å Al filters have responses at 30 eV and 800 eV. The responses of 39-mg/cm² Formvar are at 160 eV and 800 eV while those of 272-mg/cm² Kimfoil are near 270 eV and 800 eV.

The risetime of an XRD depends on the electron time of flight from the cathode to the anode as shown in Fig. IV-10. The risetime is directly proportional to $V^{-1/2}$ where V is the detector bias. A decrease of the anode-cathode spacing of 1.8 shortened the risetime by the same amount. Figure IV-11 shows an x-ray pulse in the 270-eV region taken with a Kimfoil-filtered XRD. The time scale here is 100 ps/div; 1.06-μm Nd:laser light with a pulse of 30 ps FWHM was focused onto an Al target. The risetime of our fast XRD plus the 5-GHz oscilloscope

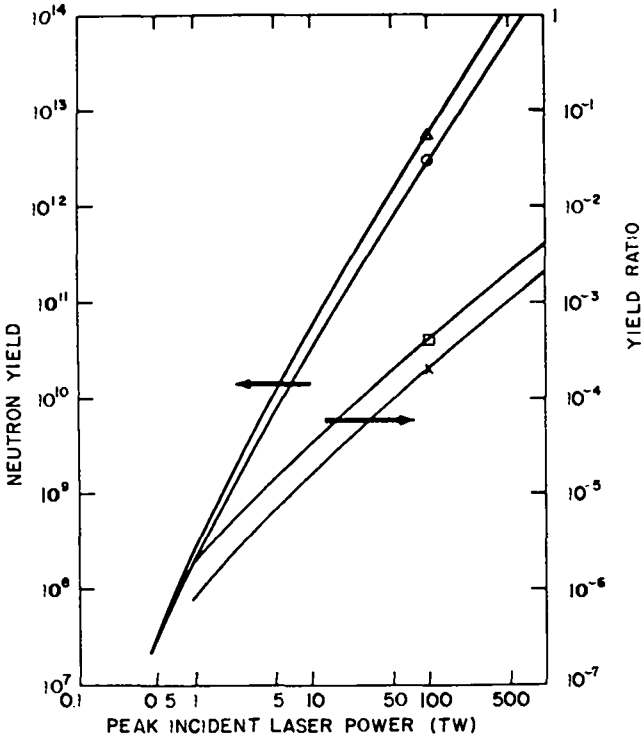

Fig. IV-6.
Neutron yield and yield ratio (fusion energy output divided by laser energy incident) for optimized exploding-pusher targets. Triangular temporal laser pulse shapes were used with a base-to-peak power time of 0.25 ns. Two fall times were used leading to full widths at half maxima of 1.0 and 0.25 ns. Δ: neutron yields vs peak laser power for 1.0-ns FWHM laser pulses. ○ : neutron yields vs peak laser power for 0.25-ns FWHM pulses. □: yield ratio for 0.25-ns FWHM pulse. X: yield ratio for 1.0-ns FWHM pulses. The optimized exploding-pusher fusion yield is seen to scale approximately as the square of the peak laser power. For these optimization calculations the DT gas filled glass microballoon was constrained to have a wall thickness greater than 0.1 μm; 25% of the laser energy was assumed to be absorbed by the target.

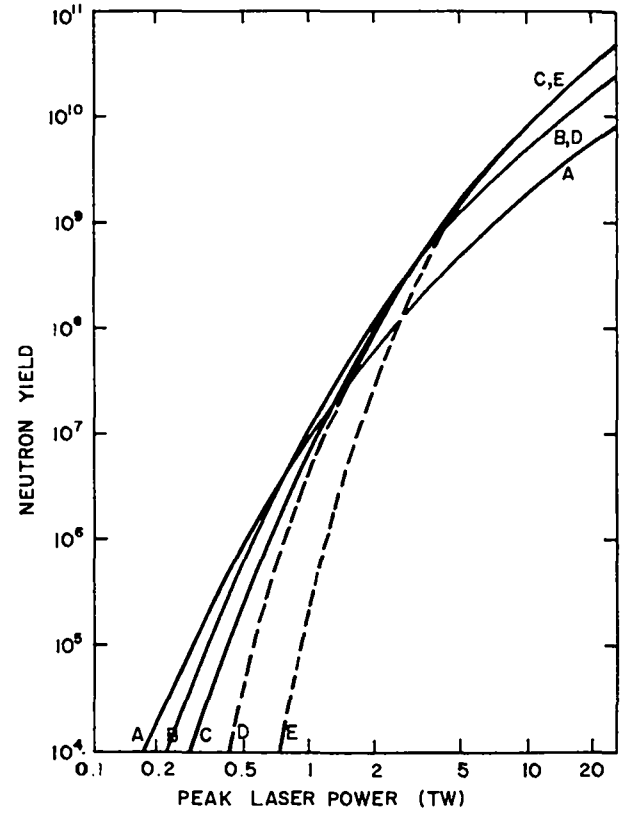

Fig. IV-7.
Neutron yield as a function of peak incident laser power. Triangular temporal laser pulses were assumed with a base-to-peak power time (τ_1) of 0.25 ns. Solid curves assume a peak power to zero fall time (τ_2) of 1.75 ns; dashed curves assume a fall time of 0.25 ns. The laser light absorption fraction was taken to be 0.2. Initial DT fill pressure was taken as 10 atm for all cases and the initial wall thickness of the glass microballoon was taken to be Δr_1 = 1.0 μm. A: r_1 = 150 μm; B, D: r_1 = 150 μm; C,E: r_1 = 200 μm.

is 90 ps with a similar value for the fall time. The interesting thing to note is that the x-ray pulse lasts for another 200 ps. This is due to the finite lifetime of the plasma. So, with a very short laser pulse the sub-keV x rays do not follow the laser pulse.

For our CO_2 laser where the light pulse at FWHM is 1.2 ns the sub-keV x rays can track the laser pulse as illustrated in Fig. IV-12. One beam of the two-beam CO_2 laser was focused onto an Fe target. The time scale here is 1 ns/div. Here a deformed CO_2 light pulse was chosen to illustrate the tracking feature. Note that as the x-ray energy is decreased the XRD signal hangs on for progressively longer times. The break seems to occur at 100 eV. Above this energy the x-ray pulse follows the laser pulse reasonably well, and below 100 eV this is not the

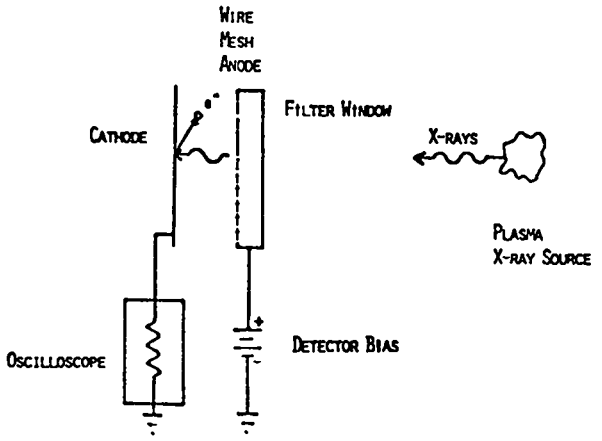

Fig. IV-8.
Schematic of typical x-ray diode (XRD).

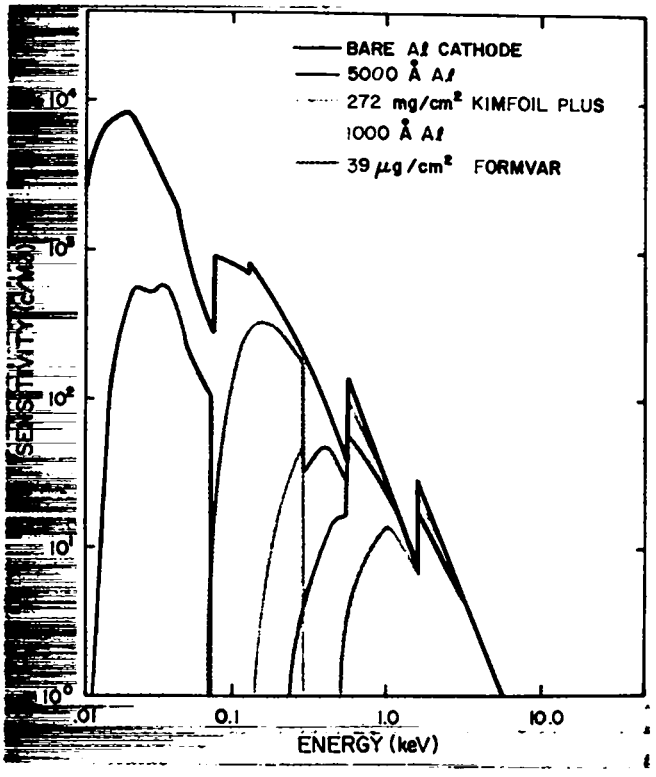

Fig. IV-9.
Response of XRD cathode with various filters.

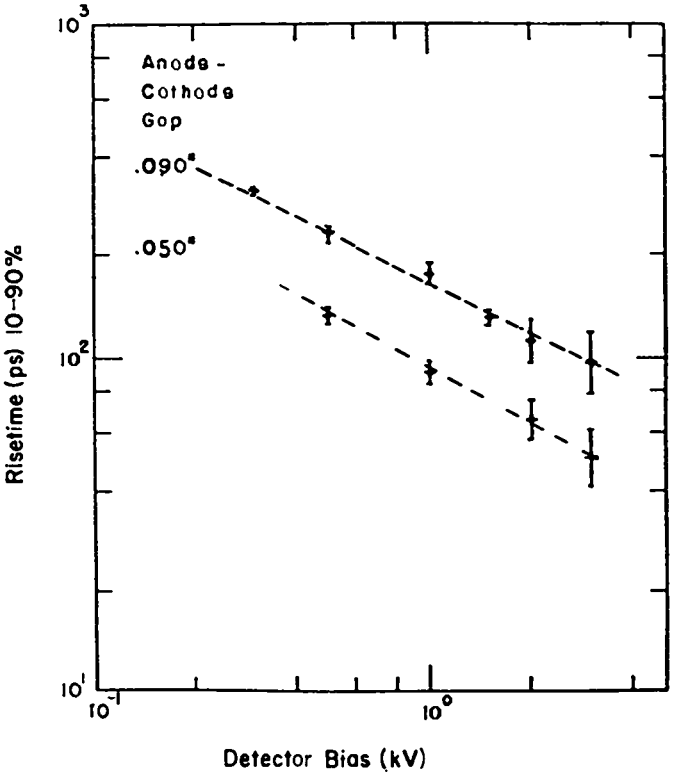

Fig. IV-10.
Risetime of an XRD as a function of anode-cathode tracking.

case. Figure IV-13 shows a similar trend for an Al target and the time scale here is 1/2 ns/div.

A grazing-incidence grating spectrograph, which covered the range from 50 eV to 400 eV, was borrowed from the Naval Research Laboratory. Figure IV-14 shows an Al spectrum. The Al spectrum was obtained with a fine wire stretched across the entrance slit. The interesting feature here is that below 100 eV the line radiation passes right through the shadow of the wire and is emitted from a physically larger source than the harder x rays. The implication here is that the life of the softer x rays is longer than the harder ones. This is consistent with the XRD results.

The dependence of x-ray yield on the atomic number was measured for a wide range of elements. Figure IV-15 gives the x-ray intensity vs atomic number for different x-ray energies. The x-ray output has a very weak Z-dependence for energies above 0.5 keV. There could be some shell structure dependence on Z, but these effects are within the experimental error.

The x-ray conversion efficiency for energies from 30 eV to 2.5 keV, as a function of atomic number, is shown in Fig. IV-16. The conversion efficiency jumped from 0.2% for Be to 0.9% for elements above Ni. The emission of x-rays is assumed to be isotropic.

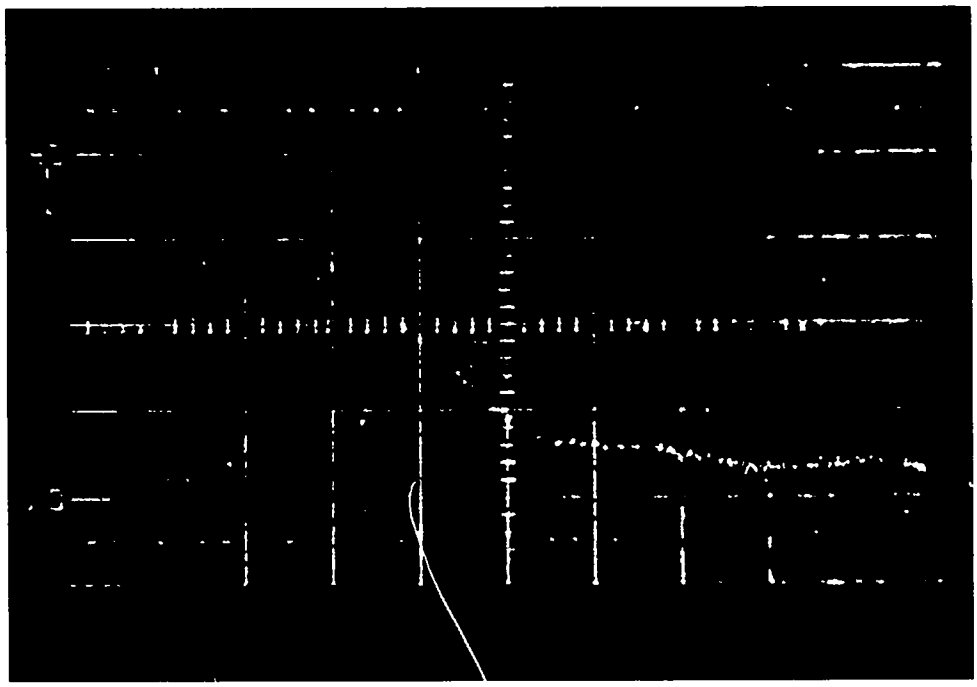

Fig. IV-11.
X-ray pulse in 270-eV region taken with Kimfoil filtered XRD.

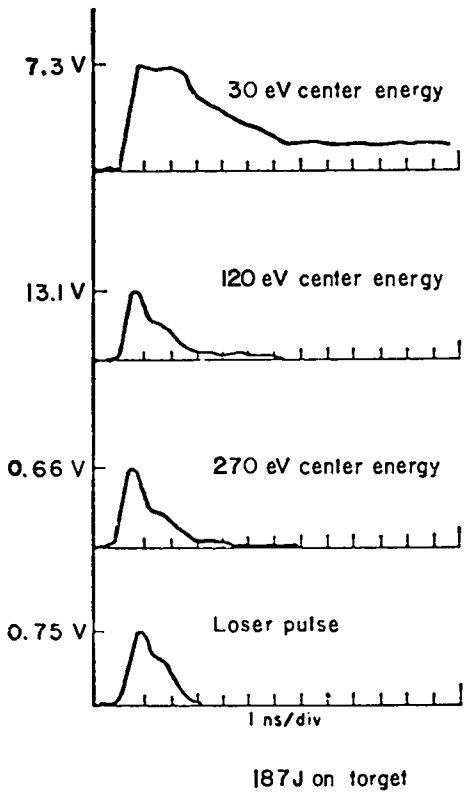

Fig. IV-12.
XRD tracking of CO_2 laser pulses by sub-keV x rays. Iron foil target.

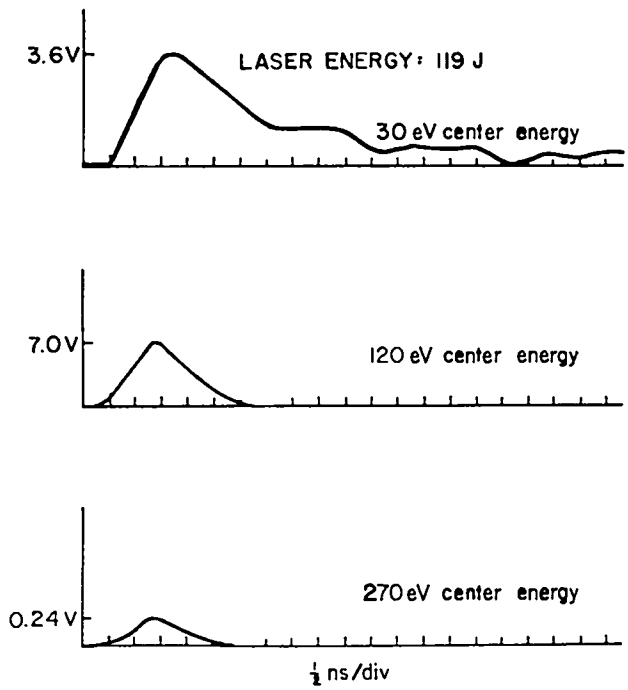

Fig. IV-13.
XRD tracking of CO_2 laser pulses by sub-keV x rays. Aluminum target.

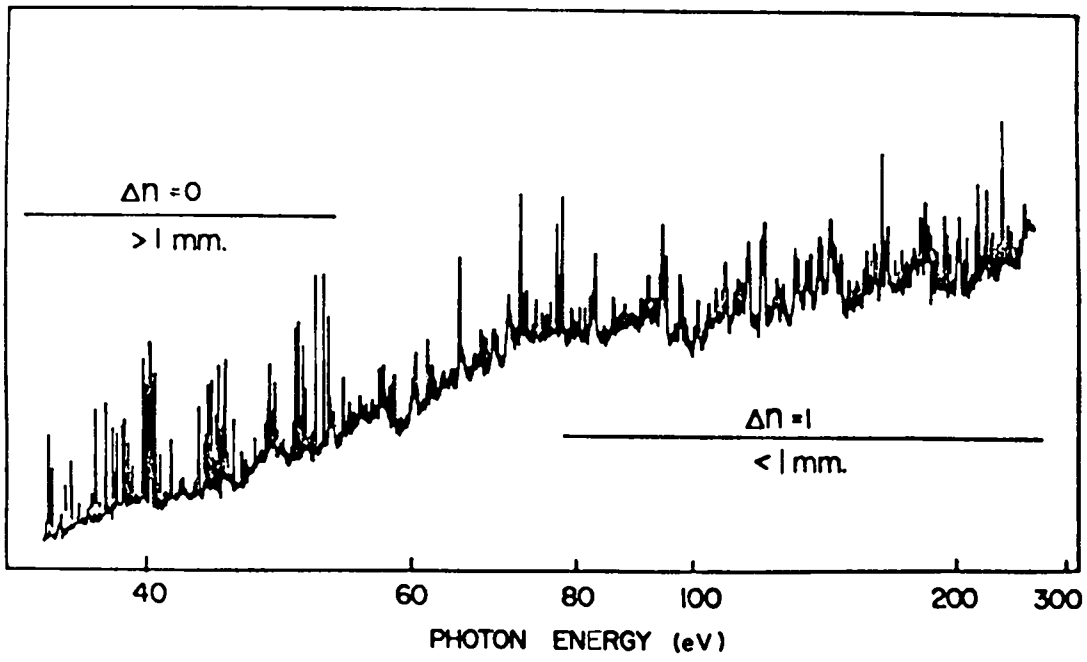

Fig. IV-14.
Aluminum tracking obtained with grazing-incidence grating spectrograph.

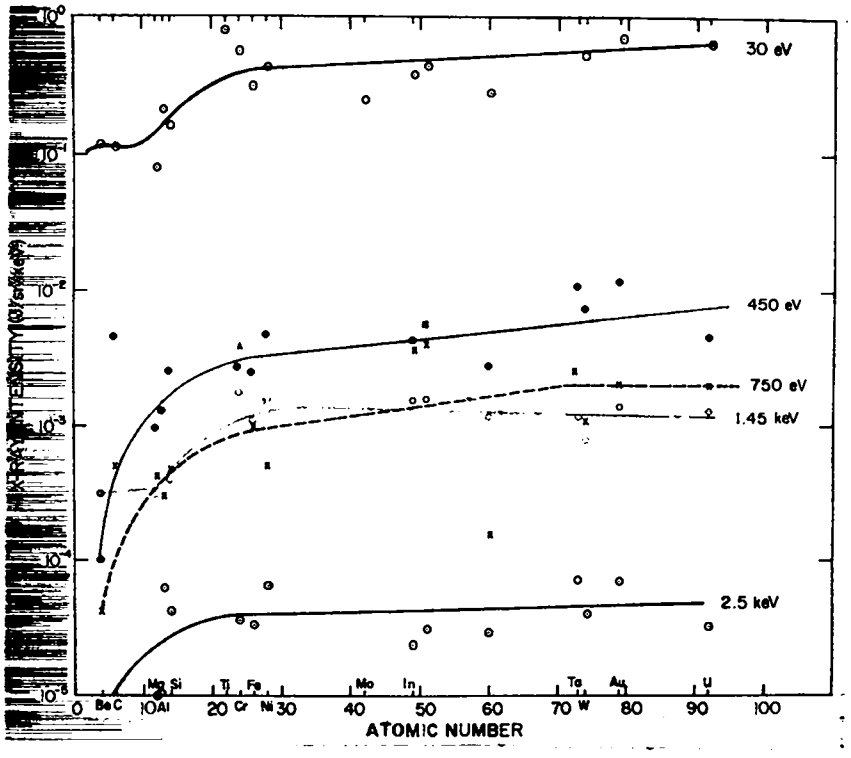

Fig. IV-15.
X-ray yield normalized to 100 J laser energy as a function of atomic number for a wide variety of elements.

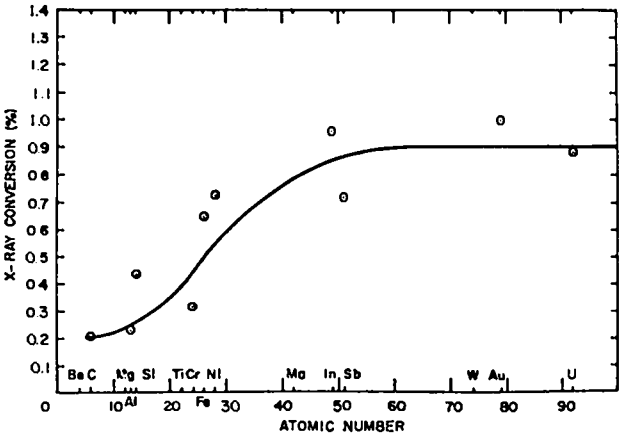

Fig. IV-16.
X-ray conversion efficiency for energies ranging from 30 eV to 2.5 KeV at a function of atomic number for various elements.

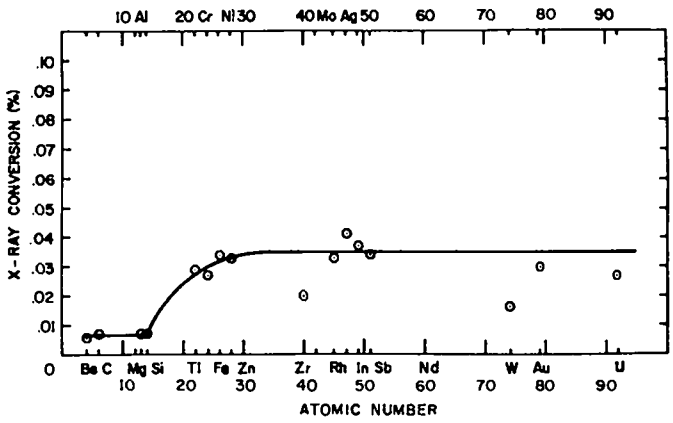

Fig. IV-17.
X-ray conversion efficiency for energies ranging from 1.0 to 2.5 keV for a variety of elements.

The x-ray conversion efficiency from 1 keV to 2.5 keV is shown in Fig. IV-17. The average conversion efficiency in this range is 0.03%.

Figure IV-18 shows the x-ray spectrum for a Ni microballoon. The first three data points are from the time-integrated XRD measurements and the rest of the points are from the filter-foil detectors. The open circles are from computer simulation runs of LASNEX. The fit is reasonably good. The peak of the spectrum indicates a temperature of 50 eV and the slope suggests a 400 eV temperature. These are typical gray-body emission characteristics.

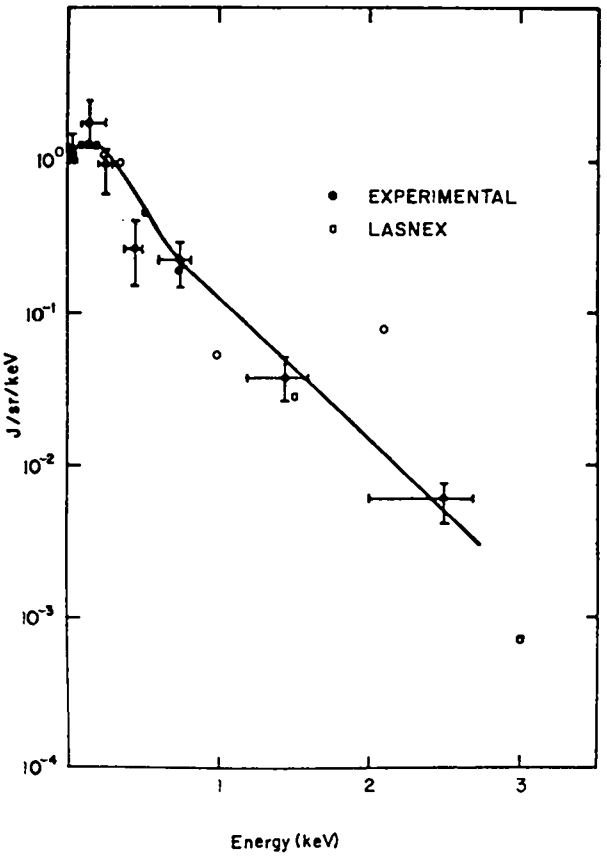

Fig. IV-18.
X-ray spectrum of nickel microballoon.

While the use of XRDs is not new, the design of fast XRDs is a recent development. XRDs are well-suited for laser fusion work and other experiments where x rays are generated in a short pulse.

Two- and Three-Dimensional X-Ray Imaging (D. B. vanHulsteyn and P. Lee). A pinhole camera was used during the Z-scan x-ray conversion experimental series to obtain an estimate of the area over which the laser energy was deposited. This information, in conjunction with the x-ray emission data obtained from XRDs and spectrometers, made it possible to determine the efficiency of x-ray energy production.

X-ray images obtained in a series of shots on gold microspheres, flat targets, and thin gold triangles, showed the manner in which the energy is deposited. In Fig. IV-19, for example, the irradiation of the gold sphere illustrates how the incident beams

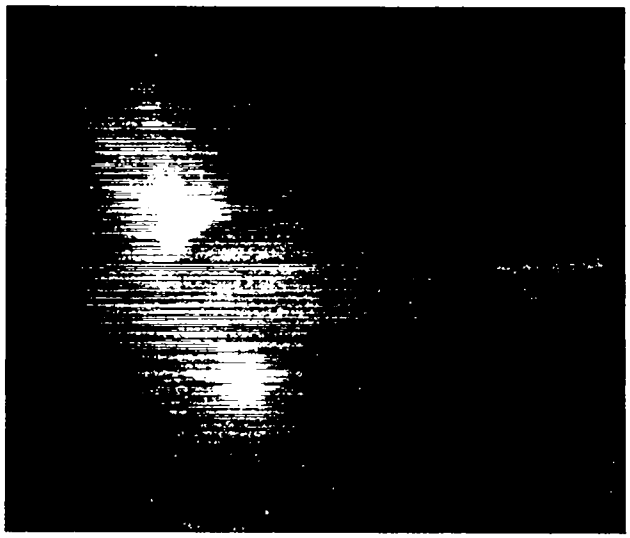

Fig. IV-19.
Irradiation of gold sphere.

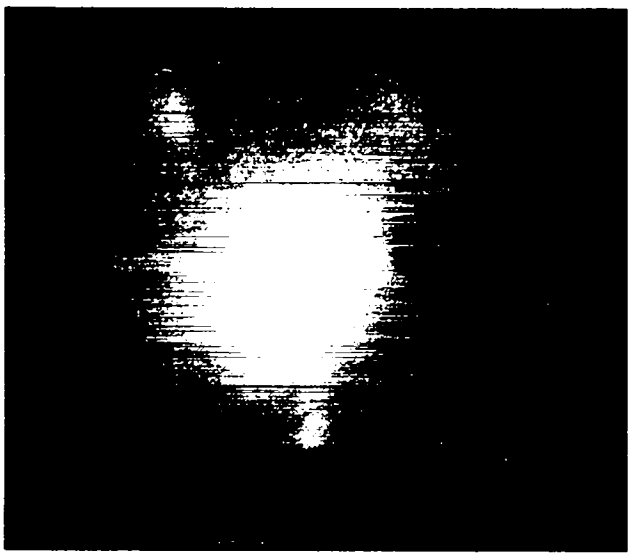

Fig. IV-20.
Irradiation of glass microballoon.

hit. An interesting comparison can be made with the more familiar glass sphere in Fig. IV-20 showing that the conduction around the glass sphere is more pronounced. The difference in behavior is attributed to the fact that the gold spheres, having walls 13 μm thick as opposed to the 1-μm thickness of glass are 200 times as massive. The hot electrons produced by

Fig. IV-21.
X-ray image of gold triangle.

the laser irradiation heat the gold to only 30 eV compared with the temperature of 300 eV for the glass microspheres. As a result, the x rays which can penetrate the 0.5-mil beryllium light filters on the pinhole cameras are greatly reduced in the case of the gold. Furthermore, we see local heating of the sphere in the region of the laser focal spot, indicating slow energy flow away from that region.

In Fig. IV-21 the x-ray image of a gold triangle is shown and compared with a photograph of the target before irradiation. A key feature here is the illumination of the 5-μm glass fibers, indicating pronounced conduction along these supports. A similar effect is evident in Fig. IV-20, where the glass stalk is seen to glow very strongly. The heating of these structures indicates a loss mechanism which may reduce the efficiency of x-ray production.

In addition to conventional x-ray pinhole photographs, progress was made in several related areas, three of which involve either computer analysis of the images or computer design of the camera. These advances include:

1. A program developed by C. Cox and J. Frussel to provide a two-dimensional densitometer analysis of an image. This is important where filtered techniques are used on the pinholes to pass x rays in preselected energy bands. As an example, Fig. IV-22 shows the computer reconstruction of the images produced when 20-μm pinholes were filtered with thin layers of aluminum and magnesium (IV-22a and IV-22b, respectively). Since the materials are

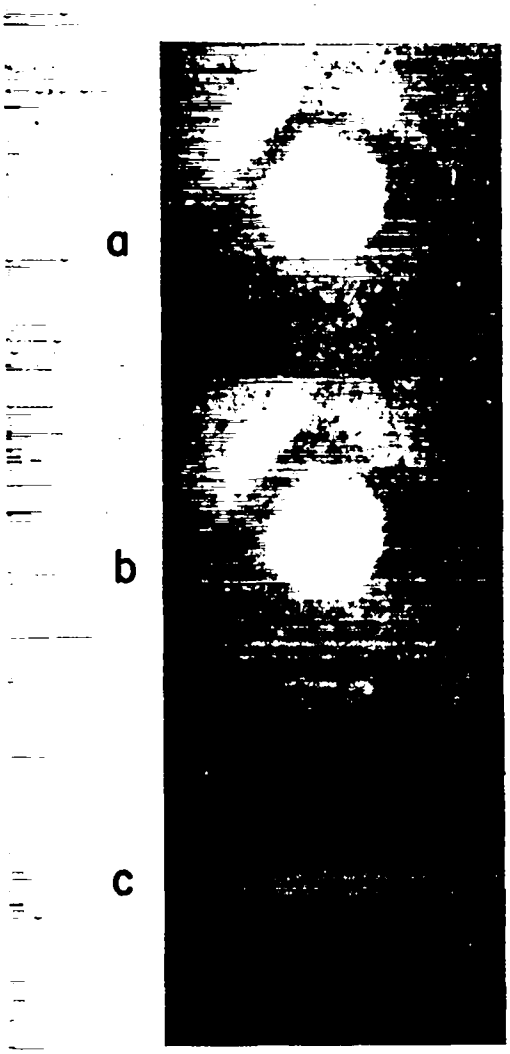

Fig. IV-22.
Computer reconstruction of filtered 20-μm pinhole images.

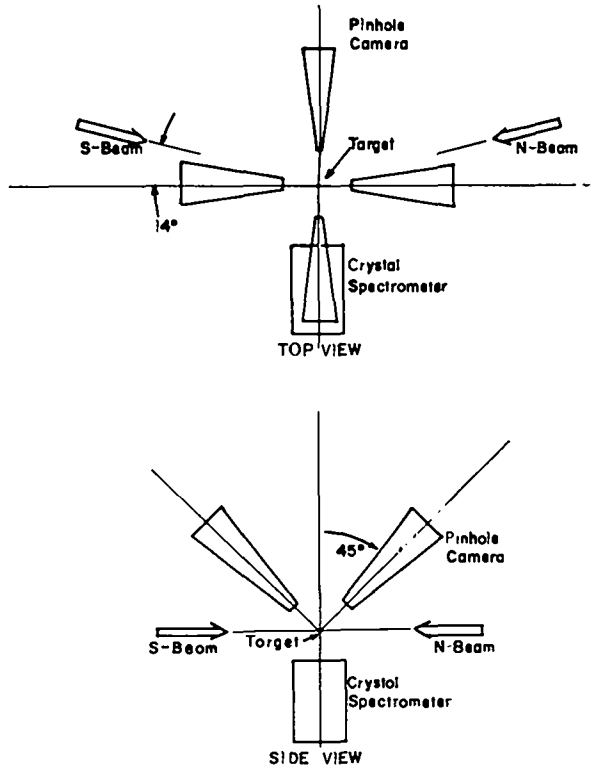

Fig. IV-23.
Pinhole camera arrangement.

matched Ross filter pairs, the difference in the images is due to the x rays between the Al and Mg K-edges. Thus, by subtracting the two images point-by-point, the photograph in Fig. IV-22c is obtained. This tells us where the 1.32-1.56 keV x rays originate. Also, because the target in this case was known to be glass (SiO_2), there is little, if any, line radiation in this band. Hence, by assuming the energy dependence to be of the form exp(-E/kT) and by folding in the filter and film responses, the temperature can be estimated. Preliminary results indicate kT to be of the order of 300 eV in the regions of strong emission.

In addition to these K-edge filters, a set of M-edge filters using W, Os, Ir, Re, Pt, and Au have been fabricated and measured. The results indicate that the filters are quite well matched and can be used to analyze the lines produced by silicon. This is a very difficult experiment, which will be performed within the next two months. The data obtained can be used in conjunction with the x-ray spectrographs to analyze the origin of the various spectral lines.

2. A technique has been devised for reconstructing a three-dimensional image based upon data obtained from four two-dimensional views. With the pinhole cameras arranged as shown in Fig. IV-23, photographs from a number of shots were obtained, one set of which is presented in Fig. IV-24. The central region, which appears in some views to have a hot spot in the middle, is actually shaped somewhat like a tomato. The apparent hot spot was shown to be nothing more than an illuminated region on the far side of the compressed

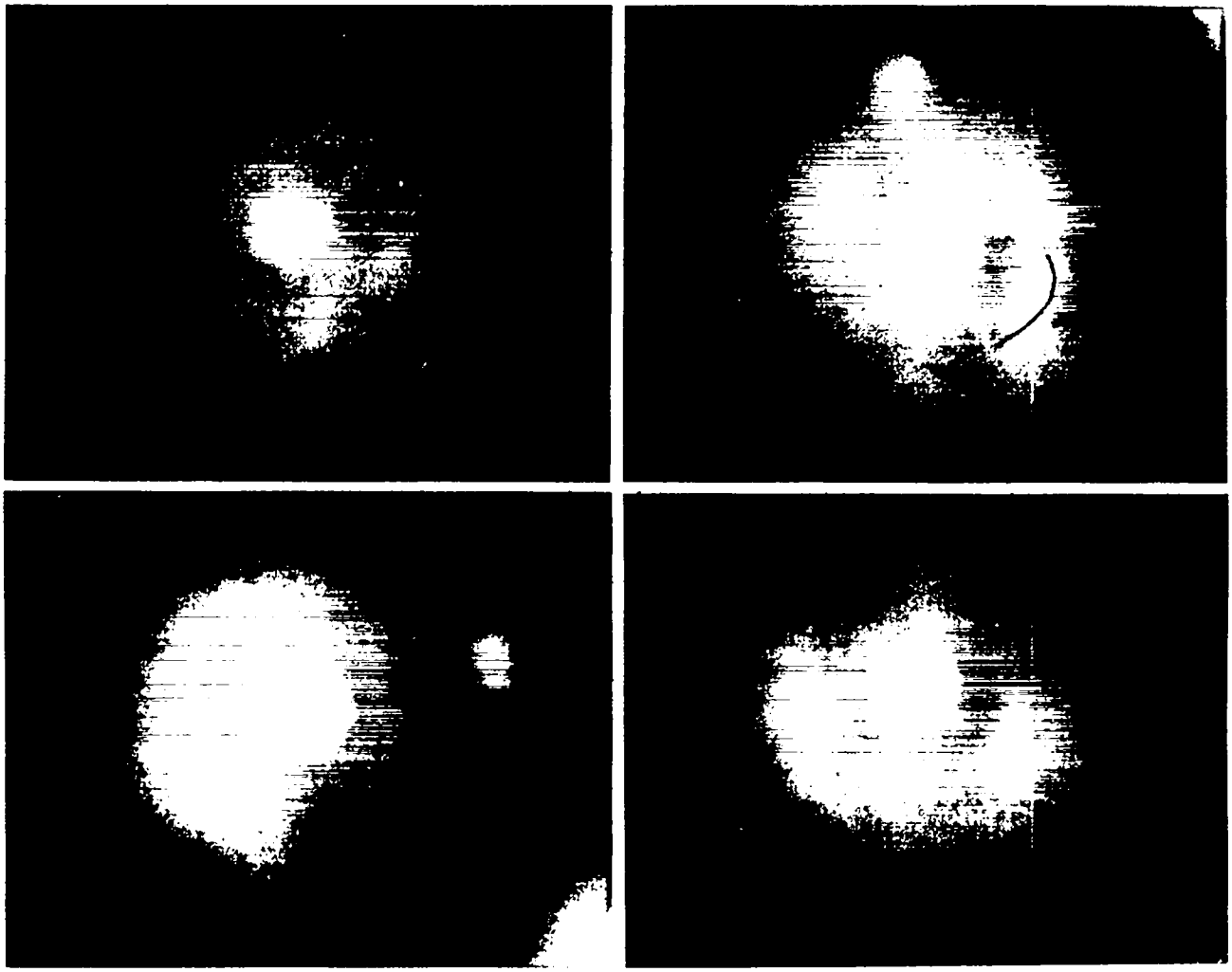

Fig. IV-24.
Set of pinhole-camera photographs of various illuminated targets.

surface. This finding is auspicious, because this sphere was filled with a 10-atm DT/neon mixture. The absence of a hot core indicates that the glass pusher did not breakup during the compression phase. The minimum average radius observed agrees with predictions.

3. A camera was developed which uses an array of square pinholes to enhance the image intensity and the signal-to-noise ratio over single pinhole cameras. The arrangement of these 1-mil apertures was based upon a computer analysis of an array which minimized the noise in the photograph due to cross-talk produced in de-convoluting the photograph. This de-convolution is necessary because there are approximately 40 000 pinhole images partially superposed on adjacent images.

The pattern of pinholes, dubbed a uniformly redundant array, is shown in Fig. IV-25. The array, manufactured commercially, has been fabricated and shipped to LASL. The camera has been designed and is under construction. It should be ready for installation in the TBS by the middle of March 1978.

4. A prototype backlighting camera has been built and is ready for preliminary testing. The device consists of a platform for supporting a target

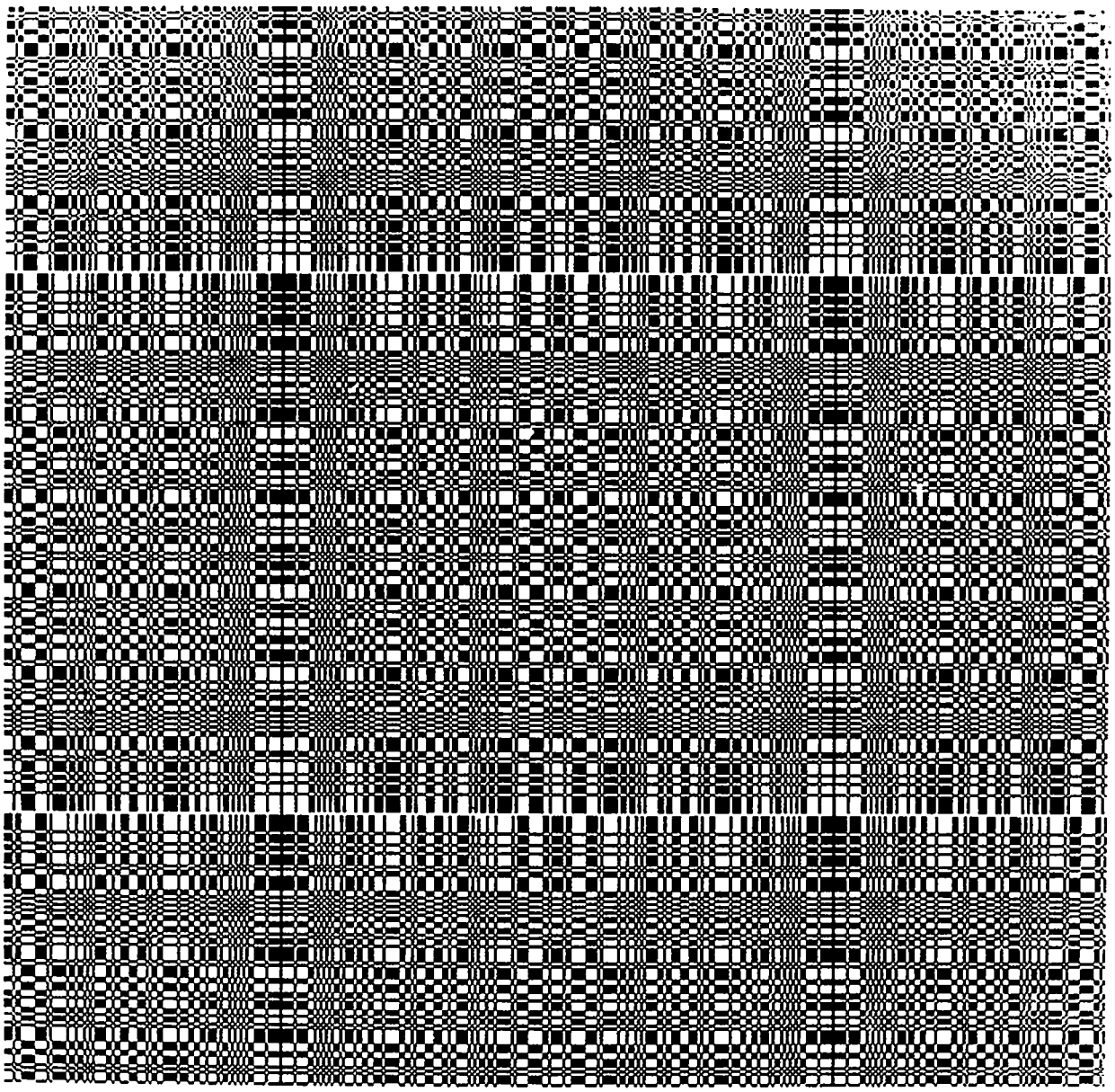

Fig. IV-25.
Uniformly redundant array of pinholes to enhance image intensity and signal-to-noise ratio of cameras.

and an x-ray source for producing a shadow of the target. The imaging is produced by a slit-and-crystal combination, much like a conventional spectrograph. Spatial resolution will be obtained in both the spectral and transverse directions. The transverse imaging is provided by the slits, while the spectral imaging is afforded by the angular width of the source. This angle, which combines the crystal rocking curve and source broadening, dictates the spatial resolution along the direction of dispersion. This, in effect, leads us to a crystal such as EDDT, which has a high resolving power. Because the camera contains a worm-gear drive for rotating the crystal to 6-arc-minute accuracy, the camera can be

tuned to any desired spectral line. The image is then obtained on a piece of rotatable film located at the appropriate angle with respect to the crystal. In this manner, perpendicular and parallel magnifications can be made equal, which preserves the image shape.

Two additional features are worth noting. First, the main function of the crystal is to eliminate x rays produced by the target itself. This concept offers a distinct advantage over the backlighting scheme for which no selective filtering technique is available. Second, the spatial resolution along the dispersion axis can be improved by using either parallel-bore collimators or Soller slits. The camera was designed with this option in mind.

10-μm Compression Experiments with Neon-Filled Glass Microspheres (G. H. McCall and K. B. Mitchell)

Experiments were conducted to demonstrate compression induced from the interaction of 10-μm laser light on exploding pusher targets. The targets were glass microspheres filled with 1 to 10 atm of DT with 10% by volume of neon gas. Targets were irradiated with our TBS. Laser energy varied from 200 to 500 J per beam in a pulse of 1.2 ns FWHM.

Compression of the fuel was determined from space-resolved x-ray spectra of the neon gas. Spectral measurements of the plasma in the region from 9.7 Å to 14.7 Å were made containing a flat thallium-acid-phthalate (TAP) crystal. Spatial resolution of the source was obtained by having a slit or slits perpendicular to the dispersion direction. The spatial magnification of the spectrograph was 3.05 times.

Figure IV-26 shows a space-resolved x-ray spectrogram from a glass microsphere target filled with DT and 10% neon at 10 atm. This spectrogram was taken with the spectrograph slit 65 μm wide. The glass microsphere was 180 μm in diameter and had a wall thickness of 1.1 μm. Spectral features on the spectrogram are identified as neon and sodium lines in the first order and silicon lines in the second order. The silicon and sodium lines, configuration ($1s2p\text{-}1s^2$) He-like, have a spatial extent when referred to the source of about 180 μm, the diameter

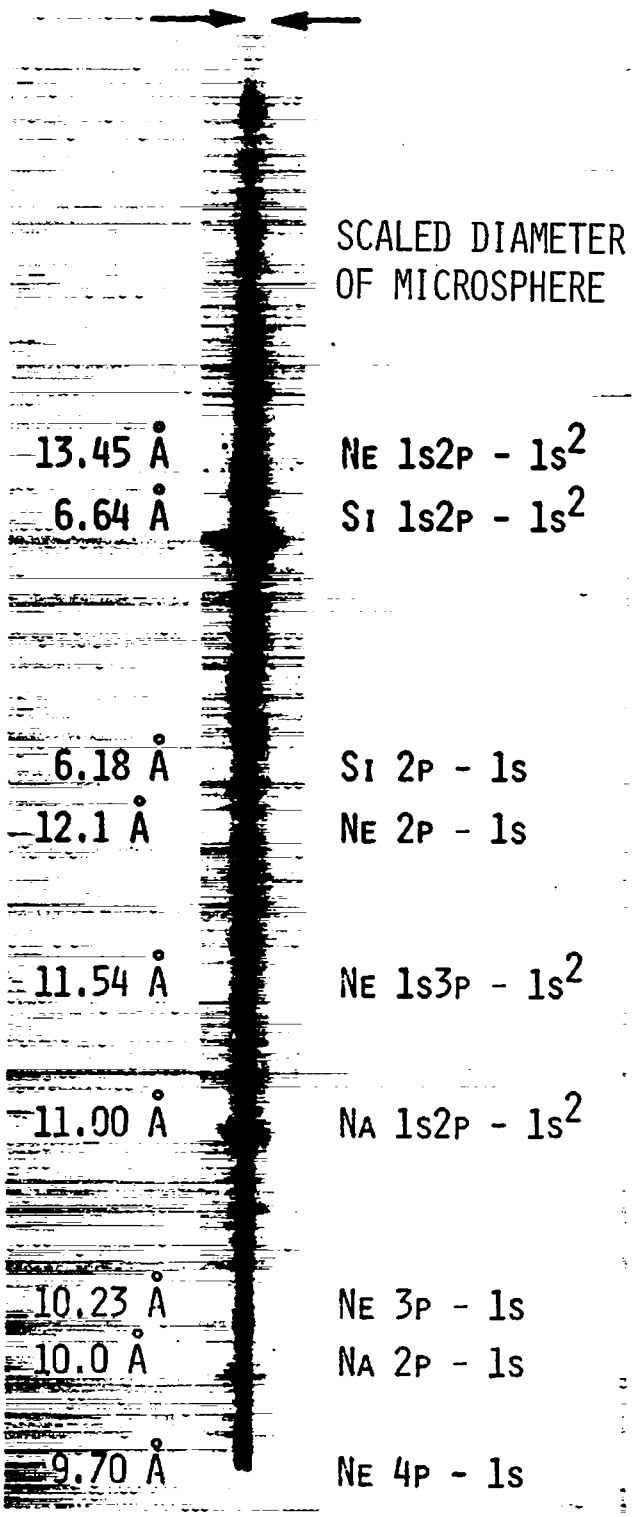

Fig. IV-26.
Spectrogram of plasma from DT, neon-filled glass microsphere target.

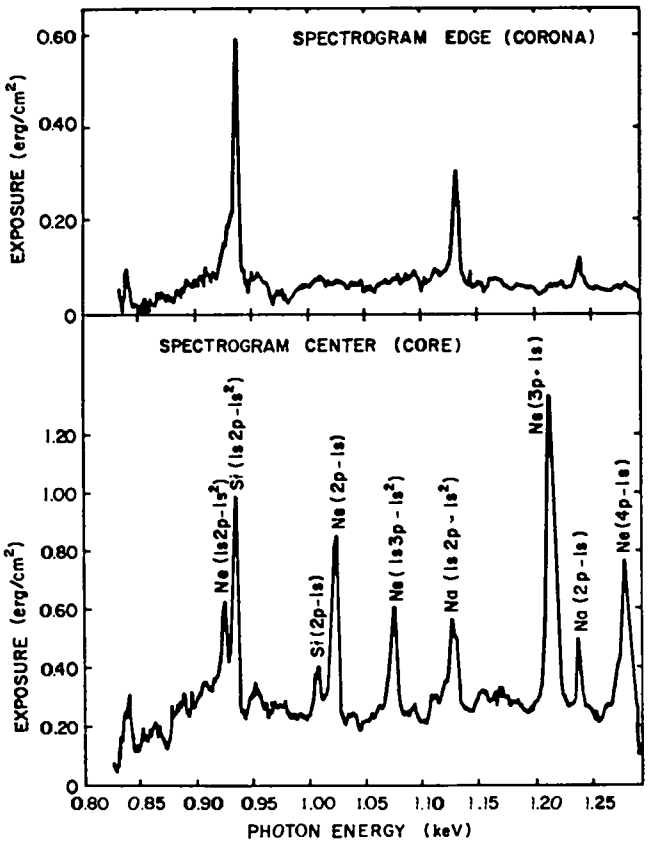

Fig. IV-27.
Scans from an x-ray spectrogram (shot 0081) produced from 545 J of 10-μm laser light on a 180-μm - diameter glass microsphere target filled with 9 atm DT and 1 atm neon.

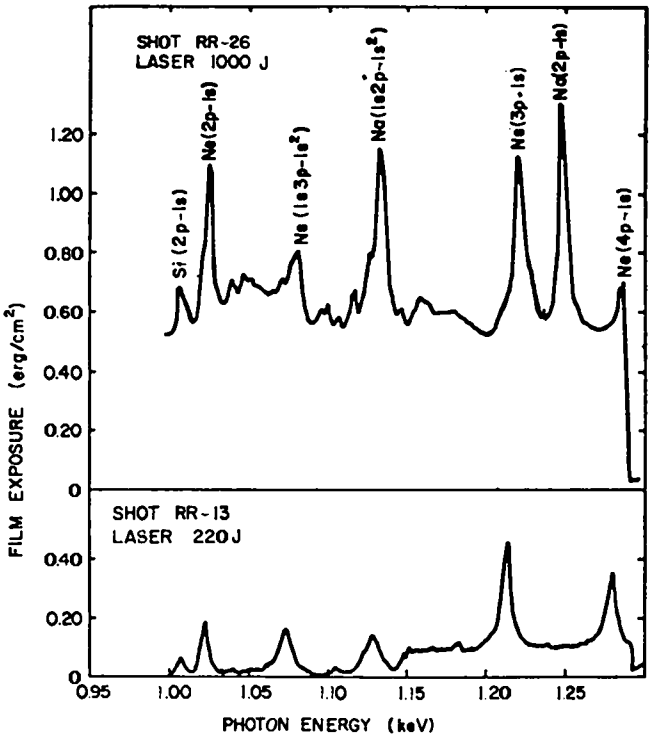

Fig. IV-28.
X-ray spectra from neon-filled glass microspheres irradiated with laser energies of 220 J and 1 KJ.

of the microsphere. All of the neon lines are in the center of the spectrogram with a spatial extent of 45 μm at the source. The spatial extent of the neon lines is direct, unambiguous evidence of compression.

The spatial differences can be seen more clearly from densitometer scans shown in Fig. IV-27. The lower trace is a scan through the center of the spectrogram, or the core of the plasma. The upper trace is at the edge of the spectrogram, or the corona of the plasma. The He-like lines of sodium and silicon dominate in the corona of the source. The He-like line of silicon, and the neon lines, are present only in the core. Also, the continuum is dominant in the core. The core is, therefore, hotter than the corona where the laser light interacts with the glass microsphere.

Quantitative temperature determination from line ratios is difficult because self-absorption of the lines or opacity of the source is unknown. However, temperature estimates from space-resolved spectrograms can be very instructive. The ratio of the intensity of the Na(2p-1s) line to that of the Na(1s2p-1s²) line shows that the core is nearly 100 eV hotter than the corona. The exploding silicon pusher is not in thermal equilibrium with the neon. The silicon lines in the core are mostly He-like. An estimate of the gas temperature, from the neon lines, is from 350 eV to 400 eV. There are striking differences in x-ray emission from these plasmas with an increase in absorbed laser energy. This can be seen by comparing Fig. IV-28a, shot RR-26 (1 kJ, 500 J per beam) with Fig. IV-28b, shot RR-13, a single-beam 220-J shot on a neon-filled glass microsphere. The continuum

(free-free radiation) in this region of the spectrum has increased by a factor of 20 for an increase of a factor of 5 in laser energy. The intensity ratio Na(2p-1s)/Na(1s2p-1s^2) has increased by a factor of 10 for the same increase in laser energy, but the intensity of the neon lines has increased very little. The neon becomes more fully stripped as the temperature increases. Self-absorption effects are now being studied from careful line-broadening measurements. More accurate temperature estimates can be made when the self-absorption of lines is better know.

The unfolding of the spatial distribution of the compressed core from a spatial scan of the spectrum is complicated by the fact that the slit width is approximately equal to or greater than the source diameter. Although the same diameter can, in principle, be determined by measuring the width of the image, the presence of continuum radiation and noise make it difficult to determine the width of the image at the baseline with suitable accuracy. It was decided, therefore, to fit the entire trace with physically meaningful analytic functions in an attempt to obtain information on both diameter and asymmetry.

The spectrometer characteristics are as follows:

Crystal	TAP
Film	Kodak RAR 2490
Magnification	3
Slit widths	24 μm and 58 μm
Lines observed:	Ne: 2p - 1s, 3p - 1s, 4p - 1s
	Si: 1s2p - 1s^2 in 2nd order
	Other Si and Na lines.

The neon lines were observed with a signal-to-noise ratio of ~5 to 10 using the 24-μm slit. A reduction in slit width would probably degrade the signal-to-noise ratio such that little improvement in precision would be obtained.

The films were read using the a Joyce-Loebl scanning microdensitometer. A densitometer slit width of ~5 μm, referred to the source, was used. The densitometer provided digital data directly to a Data General NOVA-840 computer for analysis. The use of the NOVA placed a limit on the complexity of the analysis, but it was adequate for this purpose. This system has the advantage of an interactive graphic

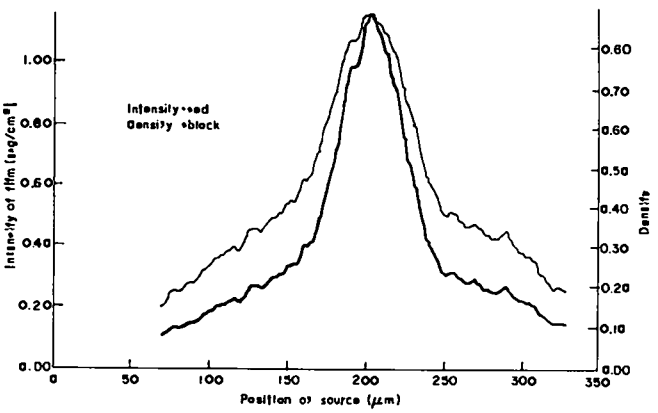

Fig. IV-29.
Film density and intensity as a function of distance from source.

system, and a number of useful spectrometer analysis programs had been written earlier.

Film has a number of advantages as a recording medium, but linearity is not one of them. Fortunately, the sensitivity of Kodak RAR 2490 film has been measured by Benjamin, Lyons, and Day[6] as a function of wavelength. The parameters that they determined were used to convert optical density to exposure in erg/cm^2. Linear interpolation was used to determine the film for energies between those at which measurements were made. Figure IV-29 shows the film density and intensity (exposure) as a function of distance referred to the source for the neon 3p - 1s transition in shot RR-26. A qualitative difference is apparent. All analyses were done using intensity—not density.

The model used as a guide for unfolding the effect of the slit requires some discussion. It is not correct to describe the spectrometer as a slit camera. In the limit of a perfect crystal and zero-width lines, it is a pinhole camera with a magnification of three in the spatial direction, and an ideal collimator wavelength direction is blurred by the crystal rocking curve and line broadening, but it is not true that each source point forms a line of infinite extent in the direction parallel to the slit. Because of the imaging in the wavelength direction and the noise in the data, it was decided that a cylindrical model of the source was adequate. Diffraction effects were neglected.

A point source forms a line image at the film with a width w(M+1) where w is the slit width and M is the magnification. Referred to the source, this width is w(1+1/M), and it can be seen that resolution is improved if $M \gg 1$, but other experimental constraints make it impractical to satisfy this condition. A unit point source which images at a point x_f of the film produces an image described by

$$R_f(x) = \begin{cases} 0 & x - x_f > w(M+1)_2 \\ \frac{1}{w(M+1)} & x_f - \frac{w(M+1)}{2} < x < x_f + \frac{w(M+1)}{2} \end{cases} \qquad \text{(IV-27)}$$

Referring all coordinates to the source and defining

$$\delta = w(1+1/M)/2, \qquad \text{(IV-28)}$$

the response to a source S(x), can be written as

$$I(x) = \int_{-\infty}^{\infty} S(t)R(x-t)dt. \qquad \text{(IV-29)}$$

Using IV-27

$$I(x) = \frac{1}{2\delta} \int_{x-\delta}^{x+\delta} S(t)dt. \qquad \text{(IV-30)}$$

In principle, S(t) can be determined by differentiating (IV-30) to obtain

$$2\delta \frac{dI}{dx} = S(x+\delta) - S(x-\delta), \qquad \text{(IV-31)}$$

Because S(x) is bounded, it can be determined by iterating (IV-19) if the derivative can be calculated from the data. In addition to the noise resulting from differentiating rather noisy data, the iterative process increases or decreases the noise by a factor of $\sqrt{N}$, where N is the number of intervals over which the iteration is performed. An attempt was made to do a piecewise linear fit to the data to determine dI/dx, but the use of (IV-31) produced results that were too noisy to be of value. Therefore, an attempt was made at a least-squares fit to (IV-30). It was observed that, for a uniformly emitting, optically thin cylinder, the intensity at a surface outside the cylinder is proportional to the length of a chord in the direction of the line of view. For a cylinder of radius R, the length of a chord normal to the axis to a distance x from the center is given by

$$L(x) = 2R\left(1 - \frac{x^2}{R_2}\right)^{1/2}. \qquad \text{(IV-32)}$$

To allow for asymmetry in the source, the fitting function was chosen as

$$S(x) = \sum_{i=0}^{N} C_i \left(\frac{x}{R}\right)^i \left(1 - \frac{x^2}{R^2}\right)^{1/2} \quad \text{for } |x| < R, \qquad \text{(IV-33)}$$

and

$$S(x) = 0 \text{ for } |x| > R.$$

Defining

$$F_i(x) = \frac{1}{2\delta} \int_{x-\delta}^{x+\delta} \left(\frac{t}{R}\right)^i \left(1 - \frac{t^2}{R^2}\right)^{1/2} dt, \qquad \text{(IV-34)}$$

a function that can be determined analytically, a least-squares fit can be made to the data points (x_j, $I_{j,}$) in the usual way. For N+1 parameters, the set of linear equation

$$R \sum_{i=0}^{N} C_i \sum_{j=1}^{K} F_1(x_j)\, F_\ell(x_j) = \sum_{j=1}^{K} I_j F_\ell(x_j) \qquad \text{(IV-35)}$$

is obtained with $\ell = 0, 1, \ldots, N$.

These equations were solved for various values of N, using approximately 500 data points for two shots on the TBS(RR-11 and RR-26). RR-26 produced a large continuum background, so a point-by-point subtraction of the continuum was made by scanning the continuum near the line of interest. The 3p-1s line was used for most of the analysis. Fits to the 4p-1s line showed no difference in source size, but did show a difference in shape. The difference was not taken seriously because of noise in the data.

In general, this method appears to work well for determining the source extent and the presence of asymmetry. The accuracy which source details can be determined, however, depends on the signal-to-noise ratio of the data. For the TBS shots, noise is the limiting factor. Shot RR-11 appears to have produced a source region with a radius of $36 \pm 2\ \mu$m, and RR-26 produced a source region with a radius of $25 \pm 2\ \mu$m.

Figures IV-30 33 show the spatial distribution of the source of x rays (Ne 3p-1s transiton) in the compressed core of a glass microballoon filled with DT and 10% Ne.

Figure IV-30 shows the fit to data from Shot RR-11 obtained when a spherical source distribution was assumed. The figure shows the data, the source function, and the fit to the data obtained from Eq. (IV-29). Figure IV-31 shows the fit to the same data obtained when the spherical source was perturbed by a third-order polynomial. The sensitivity of the fit to the source radius for data from shot RR-26 is exhibited in Figs. IV-32, IV-33 and IV-34, where the continuum contribution was subtracted from the line scan. The source radii used for these figures were 20 μm, 25 μm, and 30 μm, respectively. It can be seen that a 5-μm change in the assumed radius produced fits which were obviously worse than those for an assumed radius of 25 μm.

Spectral Line Shape Determinations of Peak Fuel Densities (P. Lee, D. B. vanHulsteyn, K. B. Mitchell, and P. D. Rockett)

An independent measurement of target compression can be obtained from the Stark-broadening of the observed neon lines. Figure IV-34 shows the neon L_β line and the best fit from calculations of Keppel and Griem.[6] The electron density for this particular shot is 1.9×10^{22} /cm^3. Their theory is fairly accurate in the wings of the distribution where most of the contribution is due to quasi-static ion broadening. Near the center, electron motion and ion motion become important and the theory is not as accurate. The inaccuracy of the Stark-broadening method, aside from the fact that the microfields are not well known at high densities, is due to the noise on the lines.

A comparison of the spatial measurement of compression vs the Stark-broadening measurement is shown in Table IV-I. Three shots at comparable gas pressure but different laser power are presented. Note that the measurements of neon density from the two methods agree well within experimental errors. The volume compression is relatively independent of laser power. This agrees with the exploding-pusher model of target compression. Only a fraction of the laser pulse is used to explode the glass shell.

Prepulse Damage Study (R. F. Benjamin and G. T. Schappert)

Prepulse laser energy that damages the target will give spurious experimental results. We studied this problem experimentally by measuring the damage threshold and by studying the damage mechanism. The results are discussed below following a brief review of the sources of prepulse energy. The experimental results served three functions.

1. The upper limit for acceptable laser prepulse energy was established.

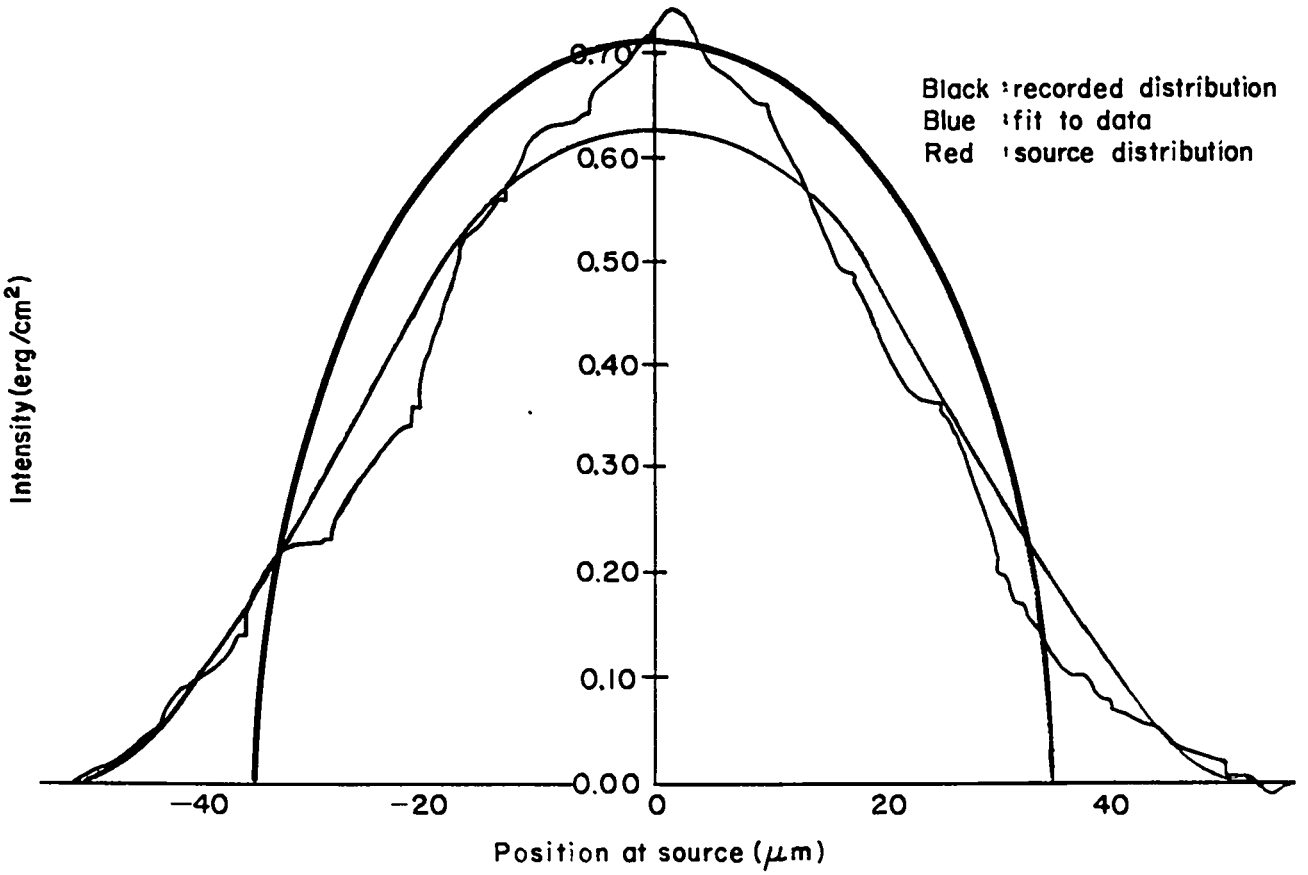

Fig. IV-30.
Spatial distribution of Ne 3p-1s x-ray source with analytical fit assuming spherical source distribution.

2. Improved target design to permit higher prepulse energy was suggested.
3. A precise technique for measuring beam-on-target alignment accuracy was developed.

Prepulse energy on target may be due to (1) amplified spontaneous emission (ASE), (2) self-oscillation, (3) feed-through, or (4) onset. While damage due to "onset" occurs temporally too near the main pulse to cause fuel loss (although it may change the target's absorption properties), the other three mechanisms certainly can cause target break-up and fuel loss before the main pulse arrives.

We simulated these conditions for the purpose of measuring the damage threshold by a single switched-out pulse from a mode-locked train of pulses. The beam, having a pulsewidth of about 1.5 ns FWHM, was propagated through the SBS and focused onto targets using the same optics employed in high-power laser experiments. We attenuated the beam with SF_6 gas and CaF_2 filters.

We determined damage in four ways. Postshot analysis involved (1) visual inspection and (2) fuel assay (when there was no hole), whereas *in situ* techniques included visual observation of (3) a flash and (4) a change in a visible beam's scatter from the target. These diagnostics were consistent except within several microjoules of threshold where postshot analysis revealed a small hole even though we saw no *in situ* flash or change in visible beam scatter. Figure IV-35 shows a typical damage hole in a GMB target.

The experimental results are:

1. The damage threshold is about 30 μJ for a 1.5-ns pulse of 10.6-μm wavelength incident on a GMB (nominally 200-μm diameter, 1-μm-thick wall) having a 10-atm DT fill.

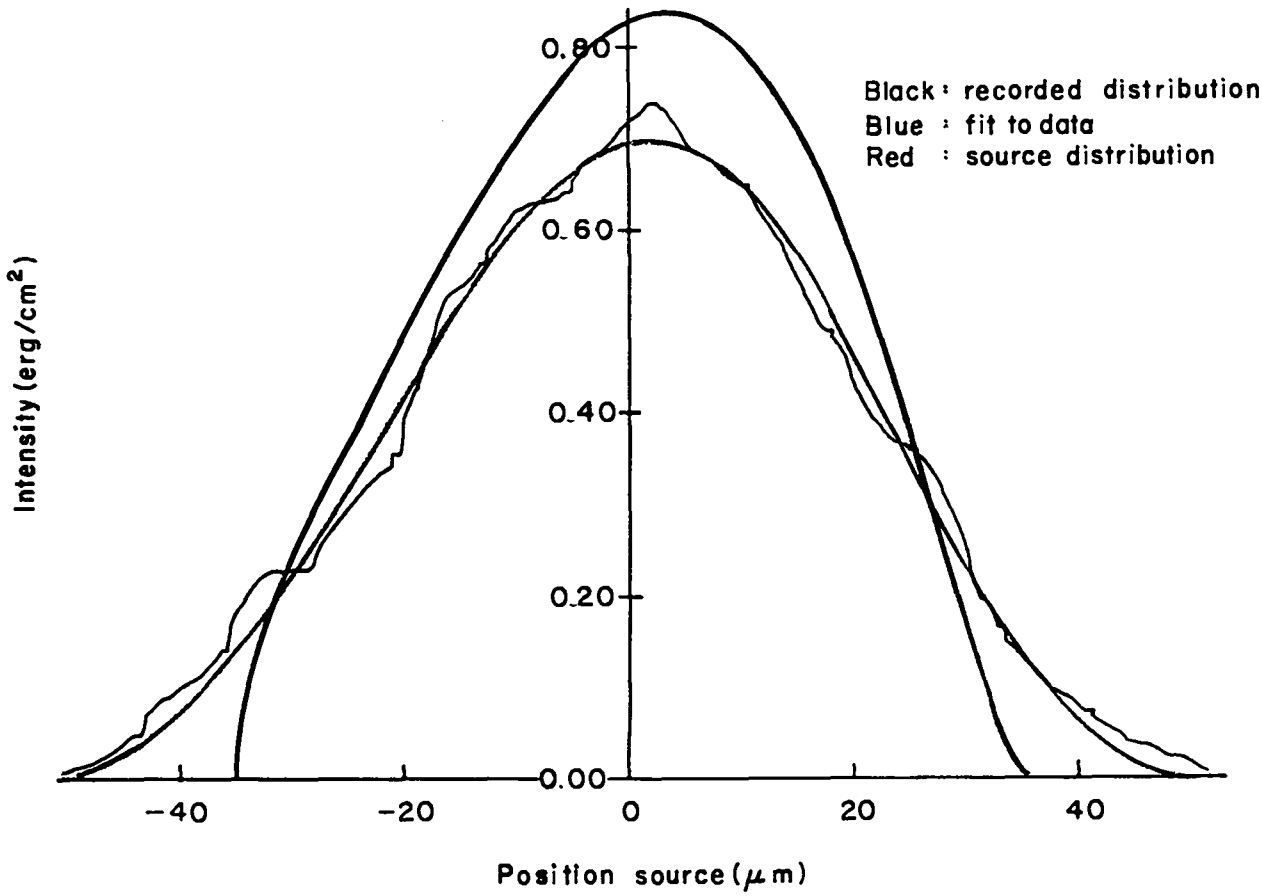

Fig. IV-31.
Spatial distribution as in Fig. IV-30 with assumed spherical source perturbed by a third-order polynomial.

2. The damage mechanism appears to be localized softening of the glass followed by perforation of the wall due to the internal gas pressure. This is depicted in Fig. IV-36.
3. The GMB damage consists of a fairly round hole. Near damage threshold we observed no shattered GMBs.
4. Damage thresholds for metal-coated (gold or copper) microballoons are at least several times as great as for GMBs.
5. Only one hole was drilled in each target. Even shots at several times the damage energy did not puncture the GMBs rear wall.

We believe that the 30-μJ damage threshold is applicable to the prepulse sources listed above. Targets with reflective coatings have considerably higher damage thresholds, but they also increase the likelihood of self-oscillation. Further experiments are required to determine the type of reflective coatings that offers the optimum trade-off between prepulse damage and propensity for self-oscillation.

Electron Preheat Reduction (T. H. Tan)

We have demonstrated previously the effectiveness of vacuum insulation in minimizing electron preheating.[7] We have also demonstrated that the supporting glass fibers used in connecting, infinite, flat, vacuum-insulated targets, if kept to reasonable dimensions (~2-μm diameter), will not be heated enough to destroy their insulation quality. Recently, we have begun an investigation of another possible scheme to reduce electron preheating of a

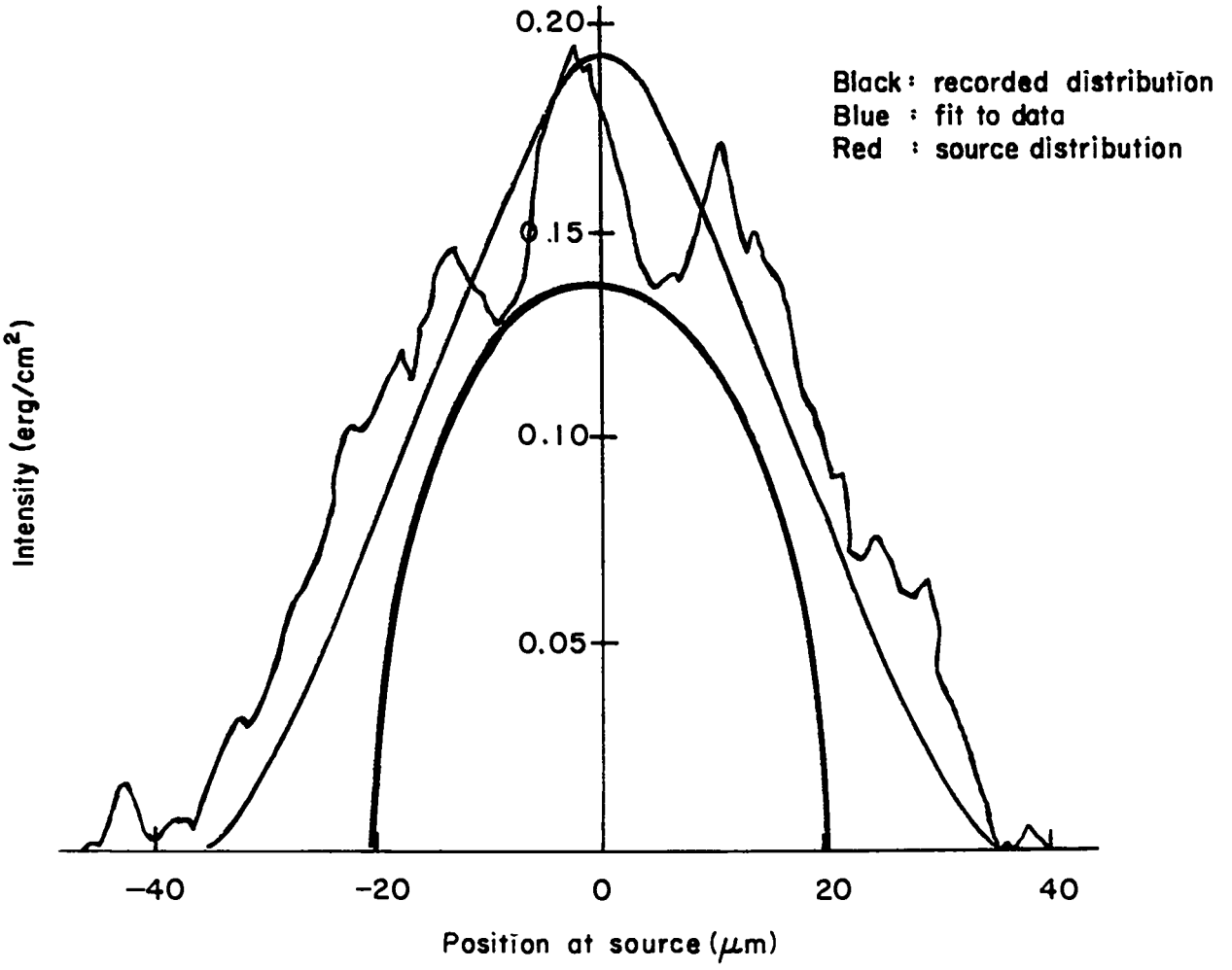

Fig. IV-32.
Spatial distribution of the Ne 3p-1s x-ray source with continuum contribution subtracted from line scan. Analytical fit assumes spherical source distribution of 20 μm.

laser fusion target. The purpose of the experiment is to determine the effect of a low-pressure gas background (~few torr) on the plasma expansion. In the presence of the low-pressure gas, the faster component of the expanding hot electrons may ionize the gas and create a conducting path to bleed out the fastest of the electrons from the main body of the plasma. The consequence of this would be a drastic drop in the accelerating potential for the ions. If this phenomenon occurs, it may be used to reduce the number of hot electrons penetrating the target interior.

To study this problem, experiments using the SBS have been carried out to measure the fast ions emitted from the front and the rear surfaces of 1000-Å plastic foil illuminated by a CO_2 laser beam at a power level of ~2 x 10^{13} W/cm². The background gas pressure was varied from 1 x 10^{-6} torr to 1 torr in air. The results are shown in Fig. IV-37. We know that the fastest ion component for a plastic target consists almost entirely of hydrogen ions. Therefore, for convenience, the data plotted show kinetic energy vs the amount of mass through which the hydrogen ions have to travel before reaching the detector. The mass here in mg/cm² is the product of the gas pressure times the distance of each detector from the target. For comparison, the range-energy curves are plotted for both the front- and the rear-emitted

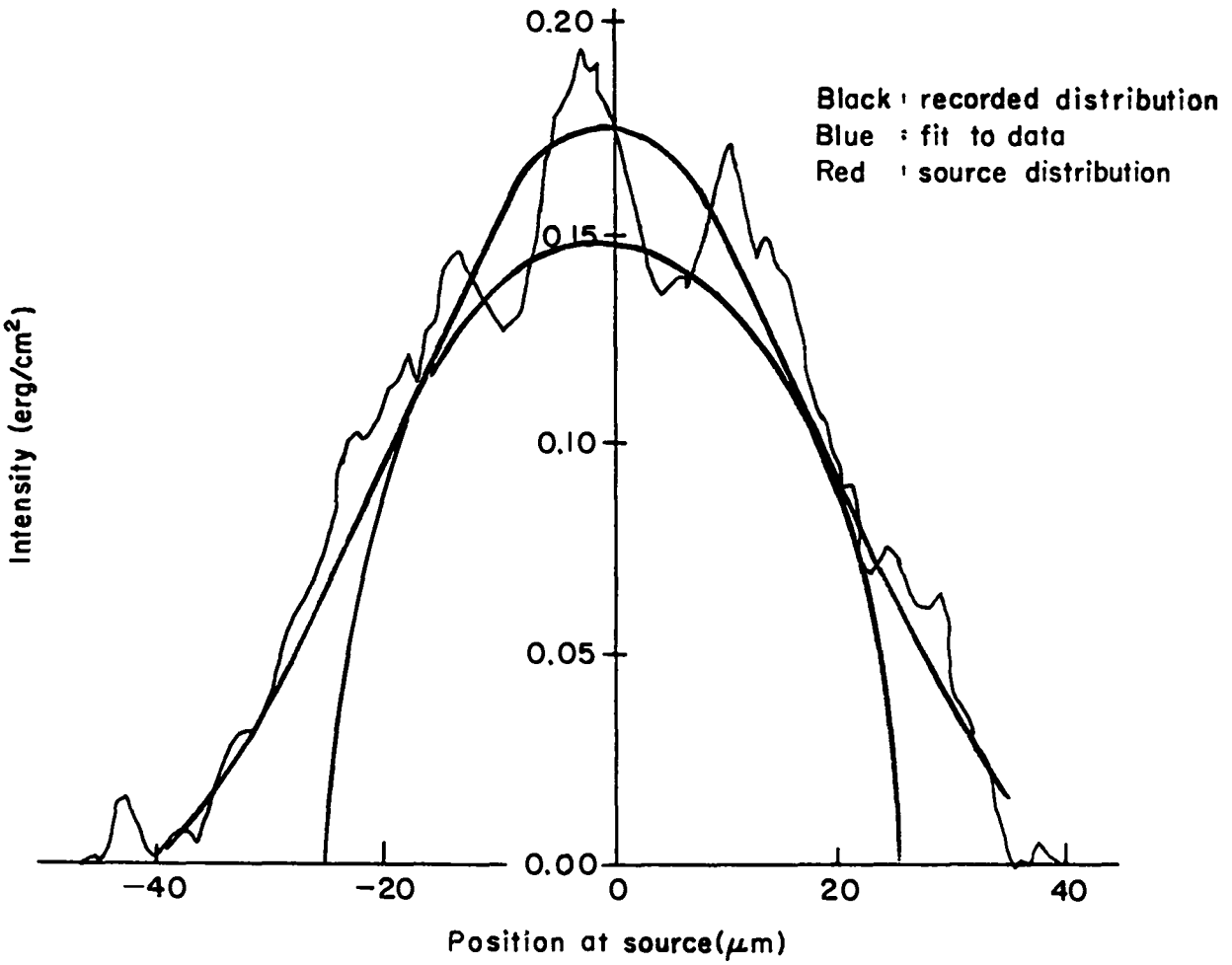

Fig. IV-33.
Spatial distribution as in Fig. IV-32. Analytical fit assumes spherical source of 25 μm.

hydrogen ions. The departure of the front-emitted ions from the range-energy curve implies that (a) the presence of the background gas reduces the fast-ion velocity slightly; (b) this may have resulted because of pre-ionization of the gas immediately in front of the target by the incident laser beam and the soft x rays from the plasma; (c) the effect is not large enough to affect those electrons moving toward the target interior, as can be seen by the data points of the rear-emitted ions at higher gas pressure. Note that the effect here is very similar to a typical target shot when a low-level precursor is present in the laser beam.

When we look at the data points for the rear-emitted ions, they fall very well along the range-energy curve. The absence of any electron "bleeding" effect in the rear-emitted ions due to the presence of the gas may be the result of insufficient ionization, since no direct illumination by the laser occurs on the back surface. This is probably the reason why a small-diameter fiber does not short out the vacuum in the double-foil experiment.

We have also measured the electron spectrum at $P \sim 10^{-6}$ torr and at $P \sim 10^{-1}$ torr. The spectrum at 10^{-6} torr is very similar to those reported previously when incident laser energy is properly taken into account. At 10^{-1} torr, however, the spectrum shows no high-energy components. Careful consideration shows that most electrons in the 100-keV region or

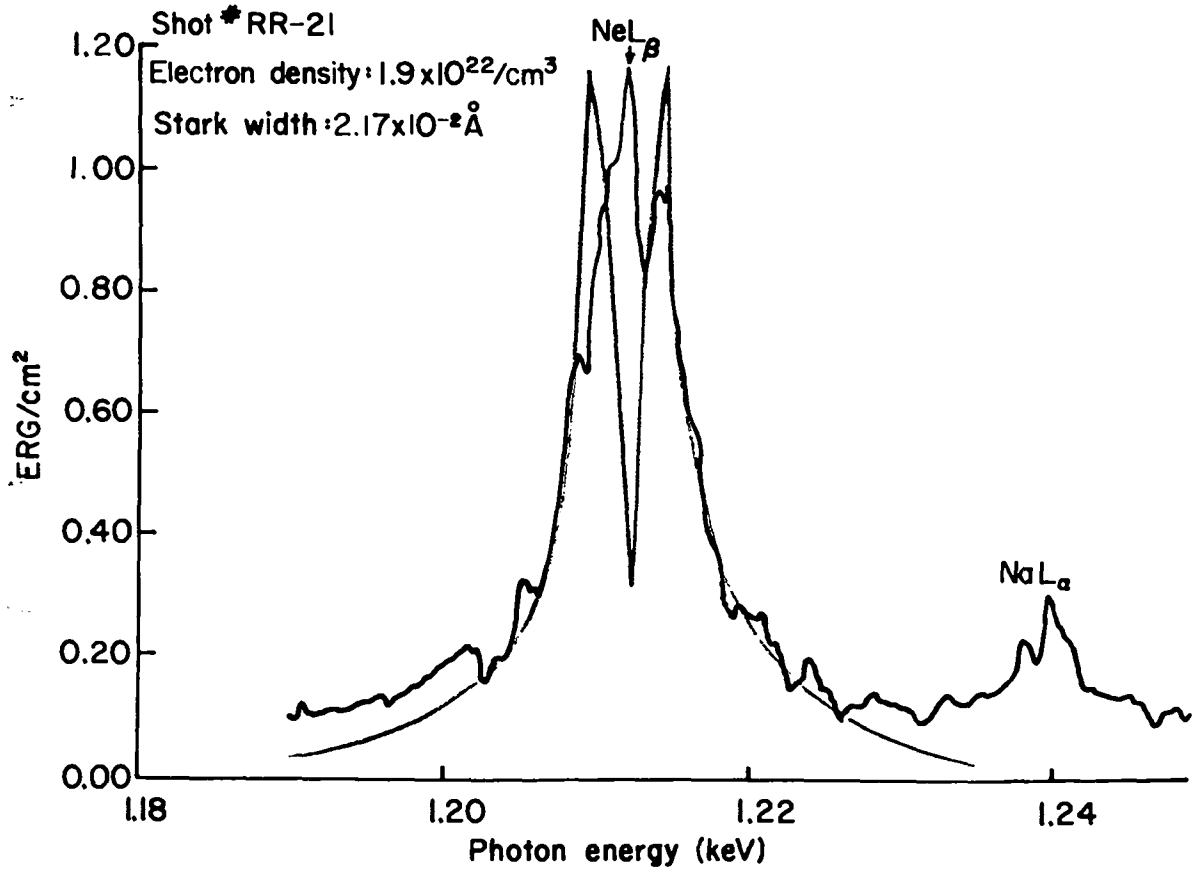

Fig. IV-34.
Neon L_β line from Stark-broadening determination.

TABLE IV-I

NEON DENSITY MEASUREMENTS USING COMPRESSED-SOURCE SIZE DETERMINATIONS COMPARED TO STARK-BROADENING MEASUREMENTS

Shot #	Target Fill DT + Ne	Laser Power (W)	Initial Diam. (μm)	Final Diam. (μm)	Neon Density Volume Measurement (cm^{-3})	Neon Density Stark (cm^{-3})	Volume Compression, Stark
RR-11	8 atm	3.24×10^{11}	189	68	4.2×10^{20}	5.8×10^{20}	30
RR-21	8 atm	4.52×10^{11}	185	56	7.1×10^{20}	9.5×10^{20}	48
RR-26	7 atm	8.22×10^{11}	181	50	8.1×10^{20}	7.9×10^{20}	46

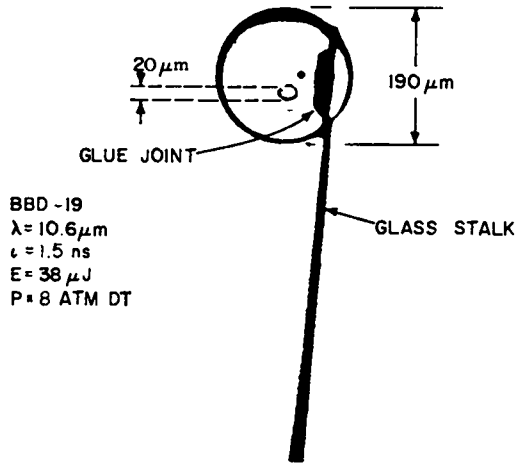

Fig. IV-35.
Typical damaged glass microballoon.

Fig. IV-36.
Localized softening of glass microballoon.

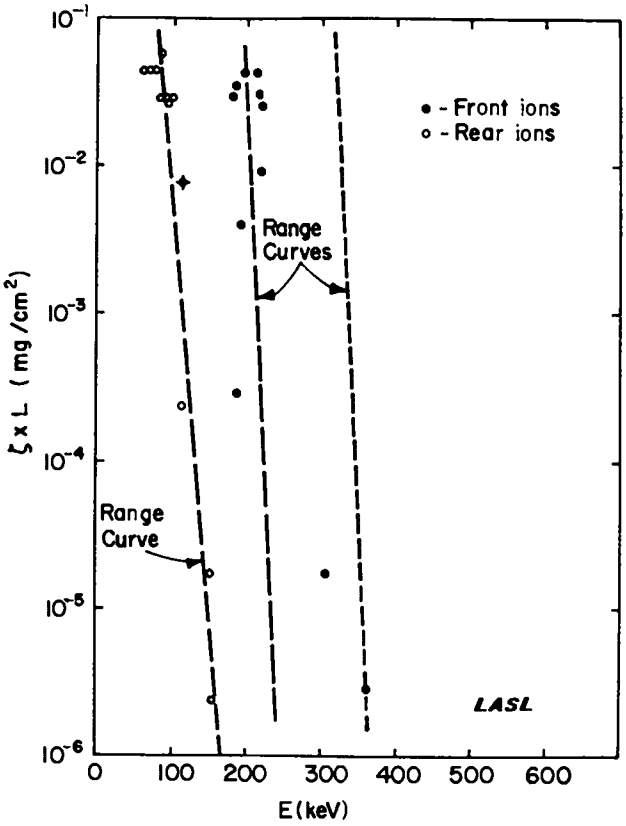

Fig. IV-37.
Fast ions emitted from front and rear surfaces of 1000-Å plastic foil illuminated by CO_2 laser beam.

below will suffer multiple scatterings before reaching the slit of the spectrometer.

One must bear in mind the fact that we are operating here in the regime of 10^{13} W/cm². The situation may be very different at higher intensities. In fact, when the effect of gas pressure is no longer a strong factor in the dE/dx loss of the ions, an isothermal expansion model predicts a logarithmic behavior for the maximum ion velocity as a function of the gas pressure. Similar measurements will be carried out at the TBS.

Ion Impulse Measurements (A. W. Ehler and J. P. Carpenter)

The TBS was used for these experiments with 250 J per beam and 1-ns pulse length. The laser energy was focused by f/2.5, off-axis, parabolic mirrors onto DT-filled GMB targets (mass $\simeq 2 \times 10^{-7}$ g) mounted on a thin glass stalk.

A multipurpose calorimeter was used with selective filters to measure the angular distribution of laser-plasma reaction products. The basic calorimeter consists of 25-μm chromel-constantan wires. We used a configuration of two calorimeters that allowed differential measurements of reaction products at a given observation angle relative to the target. Various filters were used on one side of the calorimeter in an attempt to make it selectively sensitive to electrons, fast ions, x rays, or 10-μm radiation. The unfiltered element is sensitive to all reaction products.

Charge collectors were mounted at various angles around the vacuum tank to obtain spatial distribution and energy, and an estimate of the number of fast and slow ions. A ballistic pendulum of Be 6.5 cm^2 (1 sq. in.) area and 25 μm thick was hung 25 cm from the target by 2 Mo wires 25 μm in diameter and 60 cm long.

Measurements are not complete, so that an accurate assessment of mass, momentum, and energy balance is not yet possible. In the following discussion of experimental results, the absorbed laser energy is assumed to be converted mainly into ion energy. This assumption seems reasonable, but can be verified only with more detailed measurements.

One calorimeter was covered with 76 μm of polyethylene to stop the ions but to transmit the 10.6-μm radiation. (The polyethylene also transmits high-energy electrons, x rays, and visible ir radiation, all of which have been neglected here.) The other calorimeter was open to collect both ions and CO_2 radiation. Measurements indicated that about one/third of the laser energy was absorbed. This agrees with other, independent measurements.

For some measurements, one side of the calorimeter was covered with a 5000-Å Ni foil which stops the 10.6-μm radiation and low-energy ions, but transmits ions with energy above 50 keV. These measurements indicated that less than half the ion energy was in fast ions.

There are about 2×10^{18} atoms in the GMB target. If 380-J laser energy is incident on target and one-third of that is absorbed and converted into ion energy, then the average energy per ion is about 40 keV. The charge collector data shows almost negligible ion energy below 1 keV.

The ballistic pendulum gave an anomalously high value of ion momentum. It is possible that an electrostatic force may produce the pendulum motion. Several mechanisms could produce a charge on the pendulum. However, a positive and negative potential of 300 V was applied to the pendulum with no effect. Effort is continuing to resolve the momentum discrepancy.

If one can measure (1) ion momentum (pendulum), (2) ion energy (thermocouple) (3) target mass, (4) total energy, (5) spatial distribution of ions (charge collector) and (6) an approximate value for the absorbed laser energy, then the number, mass, and velocity of the ions can easily be determined with redundancy.

Thomson Parabola Measurement of Fast-Ion Spectra and Population of Ion-Charge States (F. Young)

The Thomson Parabola ion analyzer[8] has been used with a cellulose nitrate track detector to measure the spectra and energy content of the fast-ion distribution in laser-produced plasmas.

Typical single-shot velocity distributions of high-energy ions from CO_2 laser irradiation of CH_2 and beryllium planar targets are shown in Figs. IV-38 and IV-39, respectively. The experimental conditions for the laser-target-detector system are listed in Table IV-II.

Using the isothermal expansion model[9], the H^+ velocity distribution in Fig. IV-38 gives an electron temperature of ~94 keV, which is characteristic of light ion acceleration in a heavy ion plasma. The measured proton peak at velocity $\sim 10^9$ cm/s was predicted by Crow et al. [9] An estimate for the electron temperature for the carbon ions noted in Fig. IV-38 is given approximately by

$$t_e = 10\frac{A}{Z}\ \text{keV}, \qquad \text{(IV-36)}$$

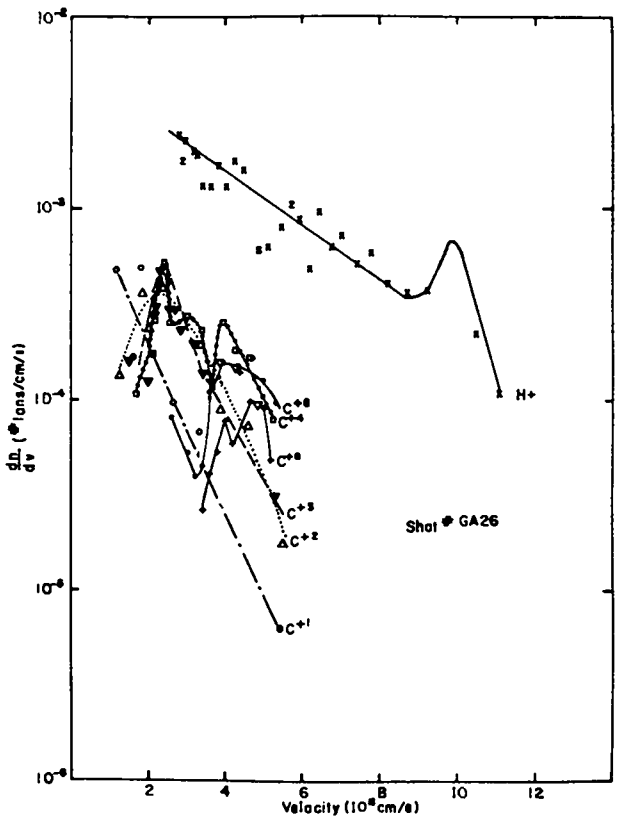

Fig. IV-38.
dN/dv (ions/cm/s) vs ion velocity for CH_2 plasma.

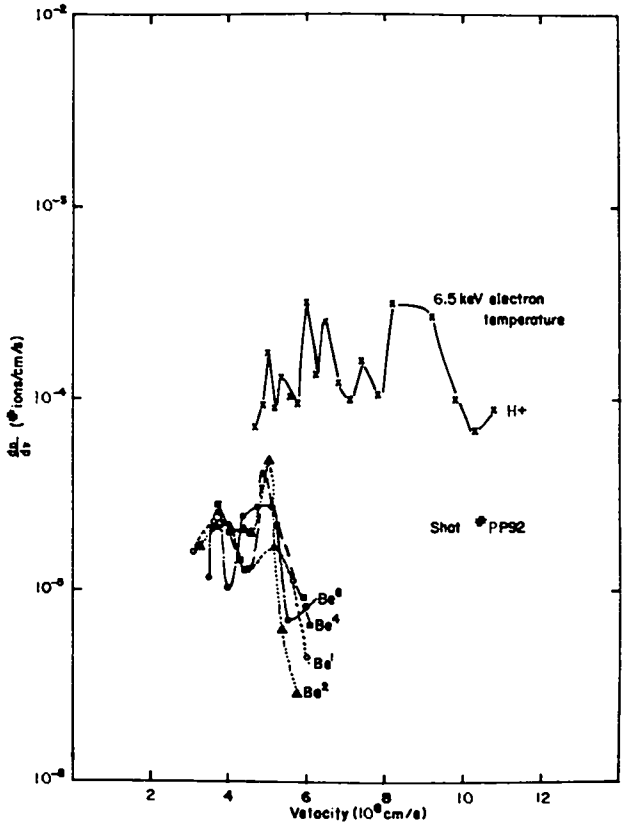

Fig. IV-39.
dN/dv (ions/cm/s) vs ion velocity for Be plasma.

where A is the ion mass number and Z is the ionization state.

The fast component of both the H^+ and the beryllium ion velocity distribution in Fig. IV-39 gives an electron temperature of ~6.5 keV. Note, however, that in this case the detector viewed the side of the planar beryllium target which was not illuminated by the laser.

Maximum and minimum ion kinetic energies measured from the CH_2 and beryllium plasmas are tabulated in Table IV-III. Also, for ion velocities greater than 10^8 cm/s, the partitioning of absorbed laser energy per ion type is tabulated.

The ion energies listed in Table IV-III have been corrected for effects from the target-to-detector geometry and angular distribution of ions, which are emitted from the target.

Figure IV-40 was used to estimate the correction for the angular distribution of ions. In this figure the function

$$f = \frac{1}{(n+1)\cos^n\theta} \qquad \text{(IV-37)}$$

is plotted as a function of n and θ, where n characterizes the shape of the distribution and θ is the angle between the detector axis and the target normal. The function f is a measure of the difference between an isotropic distribution for the emitted ions to that of an anisotropic distribution such as the $\cos^n\theta$ function. For our experimental conditions, f is a constant to within 6% or less for $4 \leq n \leq 11$ and θ ~29°.

Note in Fig. IV-38 that all carbon ions are accelerated to the same velocity of ~5.5 x 10^8 cm/s. Furthermore, in Fig. IV-39 all the beryllium ions are accelerated to an asymptotic velocity of ~3 x 10^8 cm/s.

At carbon ion velocities greater than ~10^8 cm/s, ~8% of the absorbed laser energy was partitioned into the production and heating of CH_2 plasma ions.

TABLE IV-II

EXPERIMENTAL CONDITIONS OF LASER/TARGET/DETECTOR SYSTEM USED IN THOMSON PARABOLA MEASUREMENTS

	Shot GA26 50-μm-thick CH_2 foil	Shot PP92 12.7-μm-thick Be foil
Incident Laser Energy, J	North – 245	North – 0
Laser Pulse Width, ns	~1.0	~1.0
Absorbed Laser Energy, J	123.	26.
Detector Axis to Target Normal Angle, deg	29.2	29.2
Target-to-Analyzer Entrance aperture Distance, cm	135.	135.
Analyzer Entrance Aperture Width, cm	0.02	0.01
Analyzer Magnetic Field, g	385.	385.
Analyzer Electric Field, V/cm	960.	960.

TABLE IV-III

KINETIC ENERGIES MEASURED FROM CH_2 AND Be PLASMAS TOGETHER WITH ION SPECIES PRODUCED AT VARIOUS LEVELS OF ABSORBED ENERGY

Ion Type	E_{min}(keV)	E_{max}(keV)	Total Ion Energy (J)
H^+	41.2	0644	3.38 ± .27
C^{+1}	89.7	1860	0.52 ± .04
C^{+2}	94.2	1850	1.0 ± .08
C^{+3}	138.	1790	2.3 ± .19
C^{+4}	184.	1750	1.15 ± .09
C^{+5}	422.	1750	0.84 ± .07
C^{+6}	752.	1710	0.50 ± .04
		Total	9.68 ± .78
H^+	113.	0591	1.33 ± .11
Be^{+1}	451.	1691	17 ± .02
Be^{+2}	507.	1570	27 ± .02
Be^{+3}	563.	1650	31 ± .03
Be^{+4}	639.	1720	32 ± .03
		Total	2.39 ± 0.19

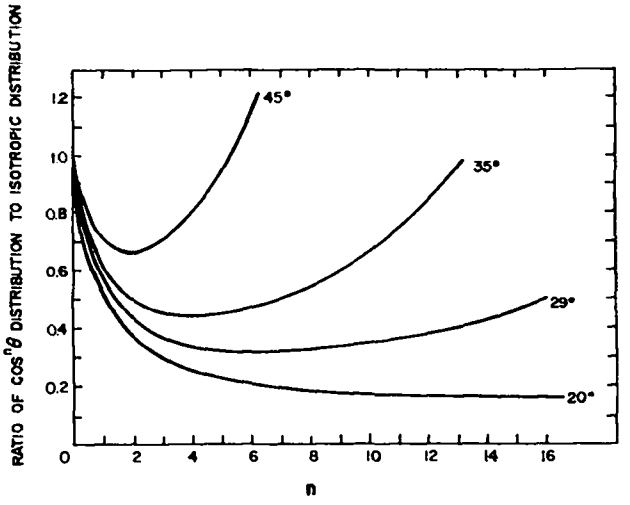

Fig. IV-40.
The function $1/[(n+1)\cos^n\theta]$ is plotted as a function of n for θ = 20°, 29°, 35°, 45°, where θ is measured from planar target normal.

Furthermore, at beryllium ion velocities greater than ~3 x 18^8 cm/s, ~3.6% of the absorbed laser energy was used to produce and heat the beryllium plasma ions.

The total loss of absorbed laser energy into the production and heating of plasma ions consists of a slow and fast-ion loss component. We have measured the fast-ion loss component. In order to estimate the contribution from the slow-ion loss component we have used the following expression,

$$\beta = \frac{\int_{V_{min}}^{\infty} V^2 e^{-V/C_s} dV}{\int_0^{\infty} V^2 e^{-V/C_s} dV} = \frac{1}{2}\left[\delta^2+2(1+\delta)\right]e^{-\delta}, \quad \text{(IV-38)}$$

where $\delta = V_{min}/C_s$, V_{min} is the minimum ion velocity detected by the cellulose nitrate film, C_s is ion sound speed, and β is the fraction of the ions in an isothermal distribution, which could be detected by the cellulose nitrate film. In our experiments δ ~1.23 and $1/\beta$ is ~1.15, which indicates that 15% of the total ion flux was not measured. If this correction for the slow ion loss is included, then, for all ion velocities, ~9% and ~4.2% of the absorbed laser energy was used to produce and heat the CH_2 and beryllium plasma, respectively. These results on the partitioning of absorbed laser energy into ion heating are lower than previously suspected.

To test the experimental results, consider the following simple calculation that estimates the amount of absorbed laser energy deposited into ion heating and acceleration.

Using the isothermal expansion model the ion flux, ϕ_I, can be expressed as

$$C_s = \left(\frac{Z}{A}\frac{T_H}{m_p}\right)^{1/2}, \quad \text{(IV-39)}$$

where n_o is the initial ion density, M is the ion mass, and the ion sound speed C_s can be written as

$$\phi_i = 3\, n_o M C_s^3, \quad \text{(IV-40)}$$

where,again, A is ion mass number and Z is the ion atomic number; m_p is the proton mass, and T_H is the hot-electron temperature. It can be further shown that, for a Maxwellian electron distribution, the initial ion density, n_o, can be derived from the 'hot' electron flux; that is,

$$n_o \sim \frac{\alpha \phi_\lambda}{Z T_H^{3/2}}, \quad \text{(IV-41)}$$

where δ is the fraction of laser flux ϕ_λ absorbed. Inserting Eqs. (IV-40) and (IV-41) into Eq. (IV-39) gives

$$\phi_i \sim 0.09\left(\frac{Z}{A}\right)^{1/2} \alpha \phi_\lambda, \quad \text{(IV-42)}$$

which states that an upper limit for the portion of absorbed laser energy used for ion heating and acceleration is ~9%. This calculated result is in agreement with our experimental results.

Absorption Measurements - 10.6-μm CO_2 Laser Light (V. Cottles, D. Giovanielli, L. White and A. Williams)

Computer simulations of laser-fusion target neutron yields indicate that the fraction of laser-light energy absorbed by the target has a significant

effect on the degree of thermonuclear burn achieved. Cranfill,[10] using LASNEX, and Giovanielli, ("Simple Model for Exploding Pusher Targets," Sec. IV) have shown that the neutron yield varies as the absorption to between the second and third power. Because of this strong scaling, it is imperative that the absorbed fraction of laser energy be known to a high degree of accuracy. Existing semianalytical treatments are all based on recently obtained data and may not predict absorption values accurately outside of the parameter space of the base data. The computer time and computer capability available to us do not permit more reliable simulation studies (e.g., PCI, WAVE, etc.). We have, however, completed absorption measurements on a number of target geometries to obtain real values for use in model calculations. We can, thus, avoid having to scan absorption as an unknown parameter. The results of many of these measurements were reported by Cottles and Giovanielli,[11] and by Cottles.[12]

The absorption measurements were made at the LASL SBS. The target type studied first was a massive slab representing a half-space of material to the focused, incident laser beam. A mirror collection scheme described by Van Kessel, et al.,[13] was used to make the measurements using a total-light-balance method. A schematic of the system is shown in Fig. IV-41. Calorimeters were used to monitor the incident laser energy and the laser energy scattered back thru the focusing optics. A 2 π elliptical mirror collected the side-scattered light which was measured with a calorimeter. The thick target did not transmit any of the laser energy; thus all of the available scattering space was monitored. The absorbed fraction is defined as the energy fraction not collected by the scattered-light collection optics. The parameters for the laser pulse used in the studies, described earlier by Kohler and Weiss,[14] was a 1.6-ns (FWHM), 10.6-μm laser pulse with energy between 0.1 and 100 J and a focal spot size of ~80 μm.

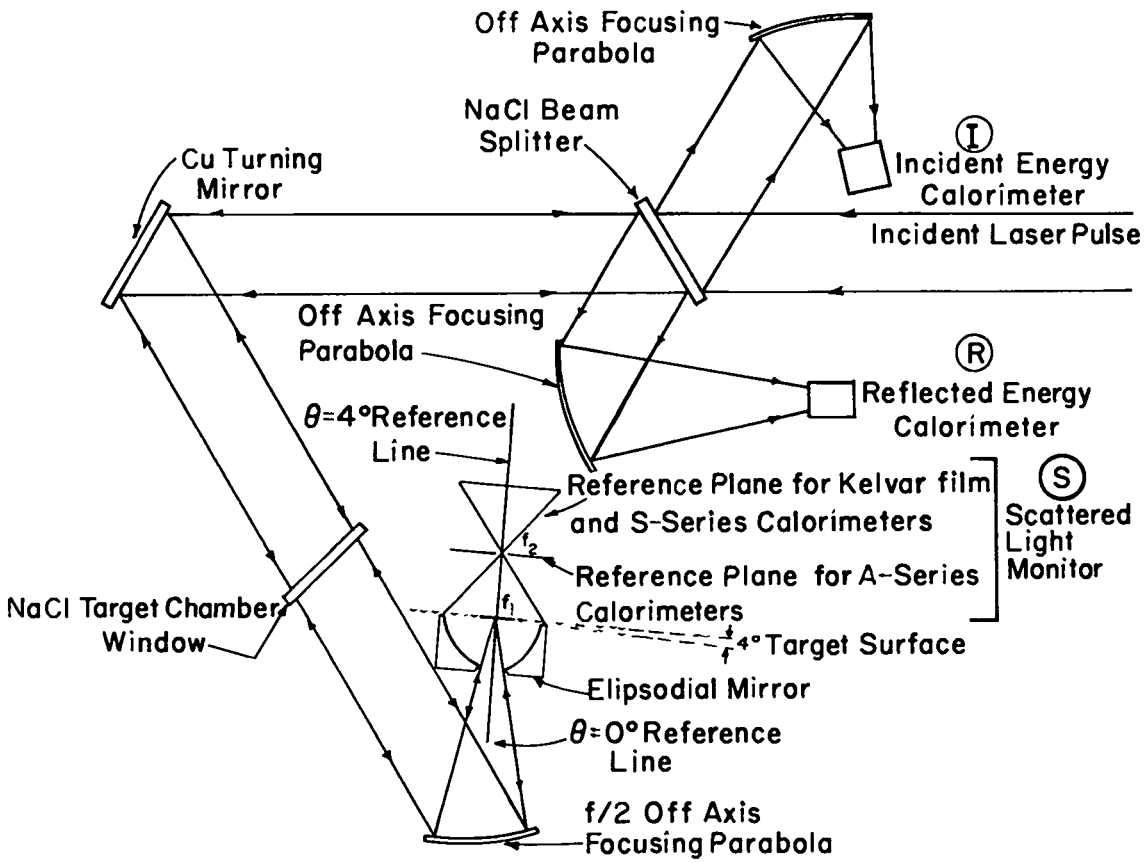

Fig. IV-41.
Light collection scheme using 2π elliptical mirror.

The calorimeters used to monitor the incident energy, and the energy reflected back through the focusing optics, were both Scientech 4-in.disk units (Fig. IV-42a). They were operated at an incident flux level that assured a linear response. Before measuring the energy scattered into the ellipsoidal mirror, we compared calorimeters of different design by placing them behind the focus of the off-axis parabola where the beam diameter was 3 in. The 4-in. Scientech calorimeter was found to be nonlinear above ~10 J. We, therefore, used this calorimeter behind the second focus of the ellipsoid to measure incident energies < 20 J.

A calorimeter of inverse Knudsen-cell design developed at LASL (Fig. IV-42b) gave a linear response, but the thermocouple junction burned out at ~20 J. We used a less sensitive calorimeter of this type (Fig. IV-42c) at the focus of the ellipsoid to record incident energies > 20 J.

Figure IV-43 shows the values measured for the reflected and backscattered light obtained for 150-μm-thick CH_2 slabs mounted on a 2-mm-thick Al backing disk attached to a 2-mm glass rod. Energy on target varied from 0.3 to 80 J and flux densities from $\sim 10^{12}$ to $\sim 3 \times 10^{14}$ W/cm^2. The scattered light intensities showed constant values of 7% for the light reflected back through the focusing optics and 48% for the light-scattered into the elliptical mirror. If one uses these results in an energy balance, the absorption, as shown in Fig. IV-44, is $45 \pm 7\%$ and is essentially independent of the incident flux density. Identical results were obtained when the 150-μm CH_2 foil was replaced with a 50-μm Au foil. This implies that the Z of the target material has no strong influence over absorption. Figure IV-45 shows the angular distribution of the light scattered into the elliptical mirror as measured by placing a sheet of uv-sensitized, Type 100 Kalvar film 5.9 cm behind the second focus of the ellipse. The polarization of the incident pulse is such that the electric vector is vertical. The unexposed circle in the center is a fiducial generated by the entrance aperture in the ellipse; the unexposed line is caused by the 2-mm target support rod. The threshold of the film for 10-μm light is $\sim$ 1 J/cm^2. In this case, a 50-J pulse was incident on the target. If one defines the incident beam to be along the z-axis, the azimuthal angle to be the angle between the E vector and a vector in the plane of the film, then there appears to be no strong azimuthal dependence for the scattered light. The slight elongation along the axis perpendicular to the E-vector is believed to be an artifact of the focal-spot shape that was observed to have a similar structure and orientation. The area of the film where threshold was exceeded was $\sim$ 10.5 cm^2, indicating that more than 10 J of the $\sim$ 25 J scattered into the mirror was within a cone having a half-angle of 28°. This is consistent with strong forward-peaking of the reflected/scattered light as opposed to a simple cosine distribution.

For spherical targets, we designed a different type of mirror collection system to allow $\sim 4\pi$ collection of the scattered light. This system is shown in Fig. IV-46. A prolate ellipsoid was cut in half by a plane containing the semimajor axis. One of the halves was rotated about a focus, keeping the cut in the bisecting plane. Detectors with a large acceptance angle were placed at the two exposed "half" foci and the target was placed at the other focus. The two detectors collect all the light scattered over a solid angle of 4π except for the light scattered back into the focusing optics. Figure IV-47 shows the system undergoing alignment tests. A light beam reflects off a small mirror at the target focus, scatters off the ellipsoidal mirror, and strikes a ground glass plate to show where the collector should be located.

Figure IV-48 shows scattering results obtained with microspheres of SiO_2, Ni, and Au-coated Ni, and with a 600-μm diameter CH_2 disk 37 μm thick. The absorption does not scale strongly with the radius and is essentially unaffected by the atomic number of the target. Forward scattering (i.e., the energy that gets past the target) scales with size as expected, but the total backscatter is essentially constant.

A target support stalk was placed in the target chamber and the laser was fired at a spot corresponding to the center of a 75-μm-diam ball. A small amount of absorption was measured, indicating that expanding plasma blow-off from the stalk may be interacting with the main pulse peak power. This would not be a serious problem for pulses $\leq$ 100 ps as the blow-off would not have time to move into the region of interaction.

Figure IV-49 shows the effect of moving the focus away from the center of the microballoon. The forward and backward scattered light is strongly affected, and the absorption peaks when the focus is near the center of the microballoon.

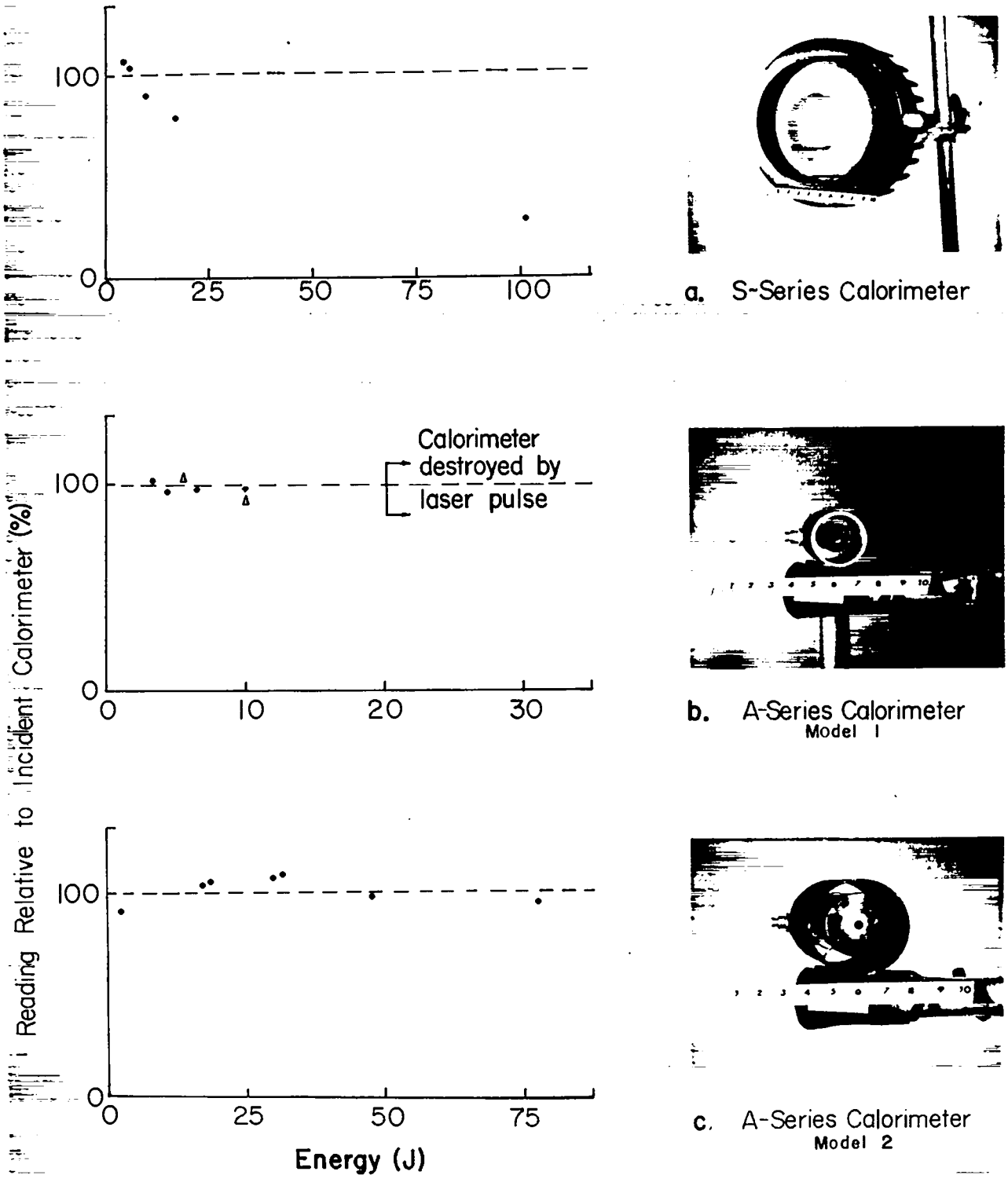

Fig. IV-42.
Calorimeters used to measure incident and scattered energy and data showing relative linearity of response to laser pulse.

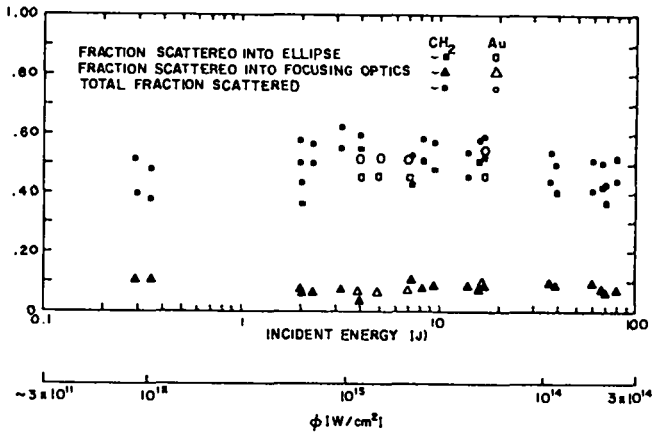

Fig. IV-43.
Values measured for the reflected and backscattered light obtained for 150-μm-thick CH_2 slabs mounted on a 2-mm-thick Al backing disk attached to a 2-mm glass rod.

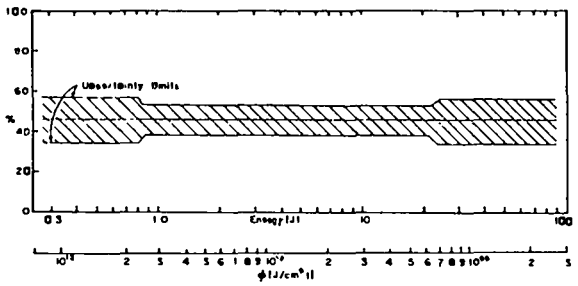

Fig. IV-44.
Energy balance showing that absorption is essentially independent of incident flux density.

All our results to date lead to important conclusions regarding target design, for 10.6-μm laser light.

1. The absorption of semi-infinite slabs is 45 ± 7% and is independent of irradiance above 10^{12} W/cm² at normal incidence.
2. The absorption of finite slabs is 34 ± 5% at normal incidence.
3. The absorption of spherical targets is 25 ± 5% and is not sensitive to radius.
4. The fraction of absorbed energy for a particular irradiation geometry is independent of the atomic number of the target.

These values of absorption are too large to be explained by inverse bremstrahlung alone, or by

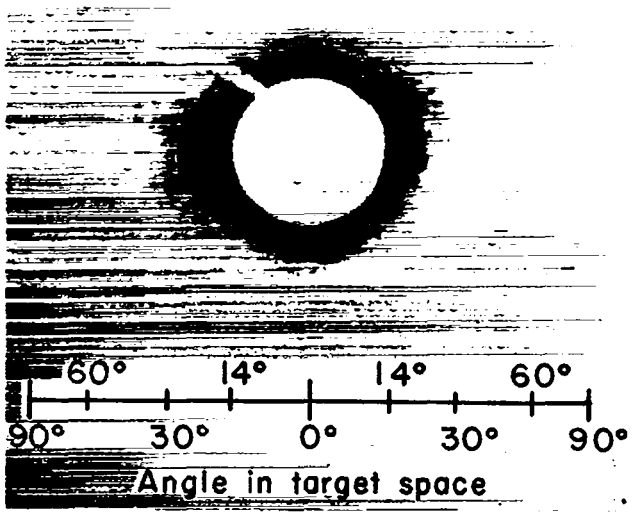

Fig. IV-45.
Angular distribution of light scattered into elliptical mirror.

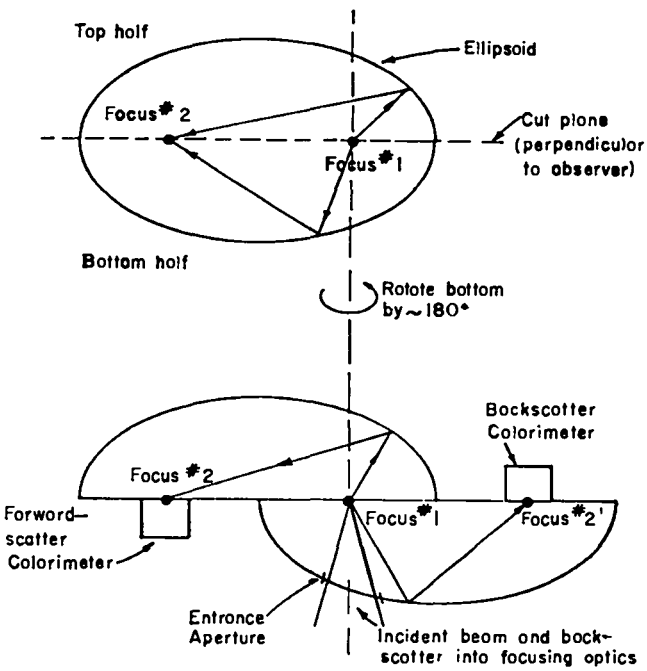

Fig. IV-46.
Spheroidal mirror collector for scattered light.

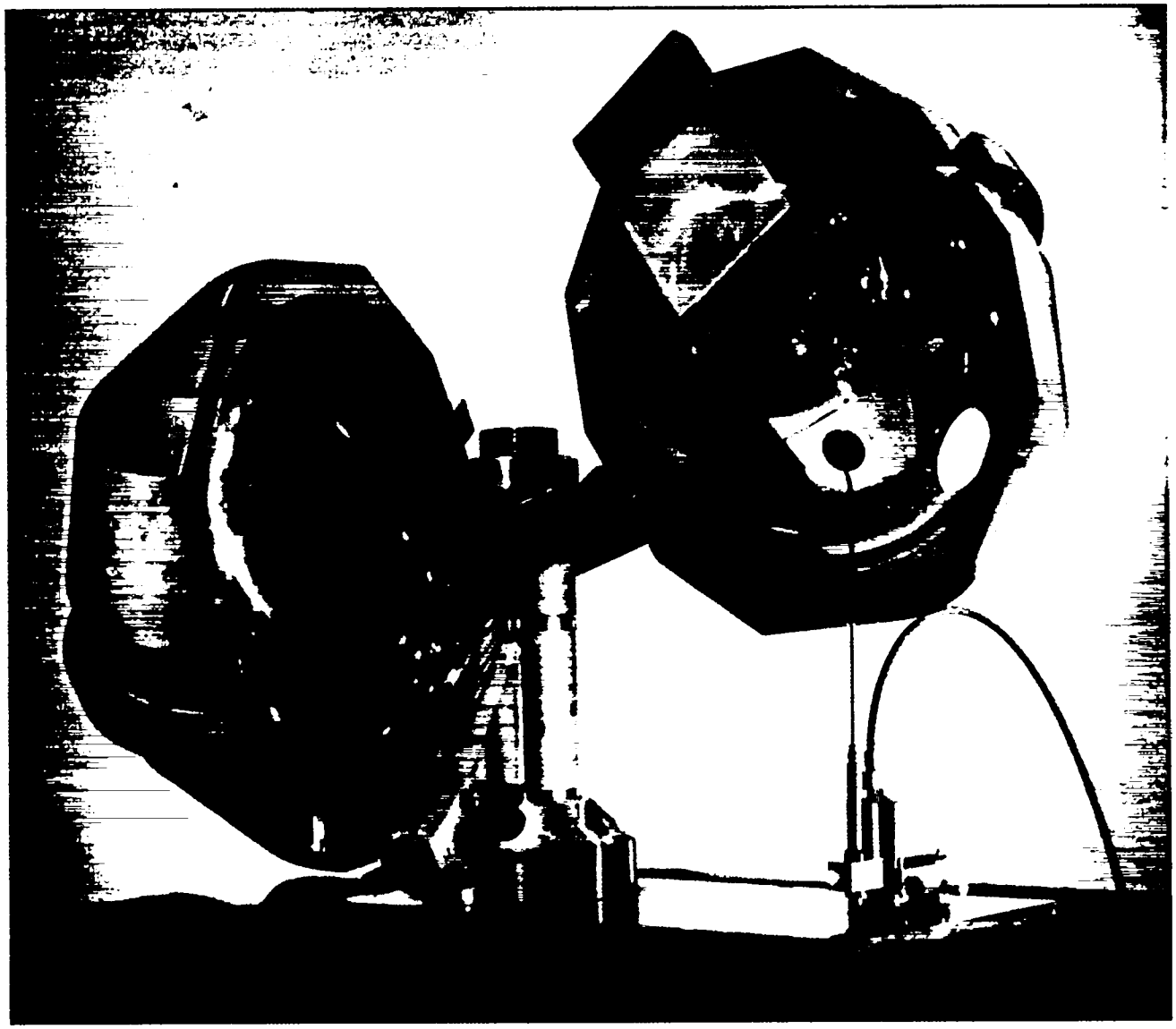

Fig. IV-47.
Ellipsoid mirror collector for scattered light.

parametric instabilities, and tend to corroborate theories that propose a resonant absorption mechanism.

We have begun experiments to look for the resonance absorption signature as reported for 1-μm laser pulses.[16-17] We propose to measure the absorption of finite slabs as a function of the angle of incidence of the laser pulse for S-and P-polarized light. Prolate ellipsoid collection optics are currently being fabricated to allow temporally resolved scattering measurements using the higher power levels of the TBS. We also hope to study the absorption of highly structured targets and make transmission studies using very thin films.

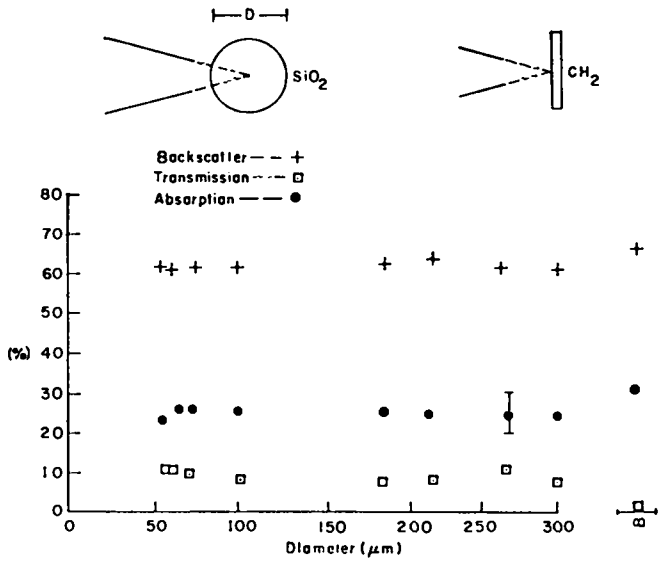

Fig. IV-48.
Data from scattering experiments using microspheres of SiO_2, NI, and Au-coated Ni and a 600-μm diameter CH_2 disk showing that absorption is essentially independent of target radius and atomic number.

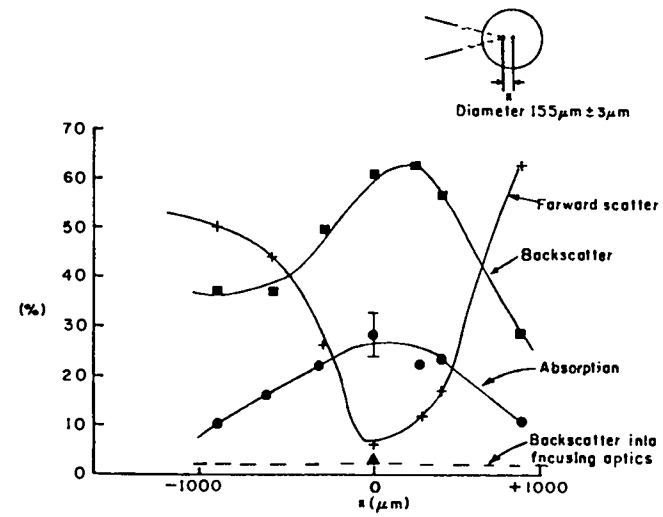

Fig. IV-49.
Data showing effect on absorption of laser focus moving away from center of microballoon.

TARGET DESIGN

Introduction

Target designs for the soon-to-be-completed EBS have been generated with the LASNEX code modified by us to better model the physics. In addition to Sirius targets, which are exploding pusher GMBs with yields of 10^8 to 10^{10} neutrons, we have emphasized high-compression targets designed to attain 20 times liquid-DT density. The major problem is the design of a target whose compression can be verified experimentally. Work has also proceeded on other pellets such as the double-shell exploding-pusher design. This target uses a thin outer shell, which explodes isothermally by suprathermal-electron heating and achieves a high degree of symmetry. The stability of these LASNEX designs will soon be evaluated quantitatively by the code DOC, which will postprocess LASNEX output.

A major difficulty in some of our designs was the sensitivity to the improper hot-electron energy deposition encountered in LASNEX. Work is proceeding to remedy this problem and to make LASNEX a more standard code that will run faster and cheaper on the CRAY-1 supercomputer.

High-Density Target Design (W. P. Gula)

One of the goals of the laser fusion program is to develop a pellet that implodes ablatively instead of explosively. In an exploding-pusher type pellet the containing shell is relatively thin and so it is heated uniformly by the laser pulse. Thus, it explodes both outwardly and inwardly and compresses and heats the fuel it contains (see Fig. IV-50). In an ablative implosion, the containing shell is relatively thick. Thus, the laser heats only the outer layers of this shell. This ablates off these layers and drives the inner layers inward just as heated rocket fuel drives a rocket (see Fig. IV-51).

In the ablatively driven implosion, the fuel remains relatively cold during the initial stages of the implosion because the thick shell shields it from

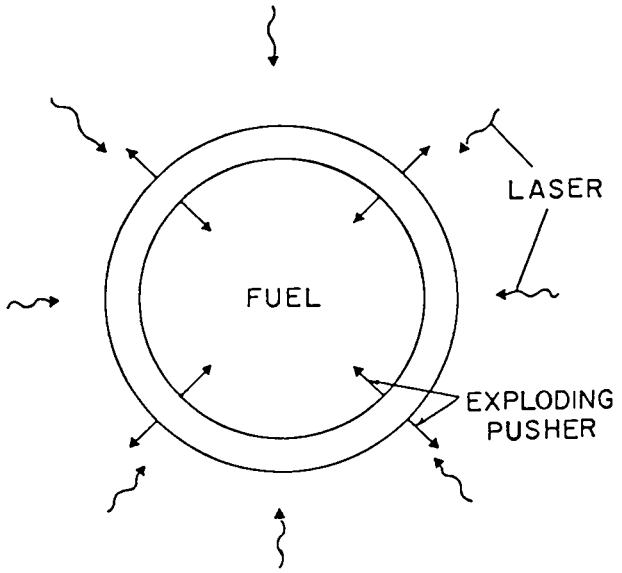

Fig. IV-50.
Exploding pusher target.

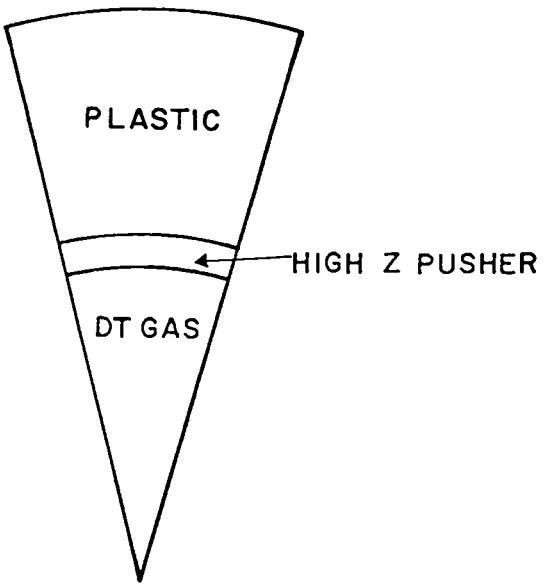

Fig. IV-52.
Plastic high-Z pusher target.

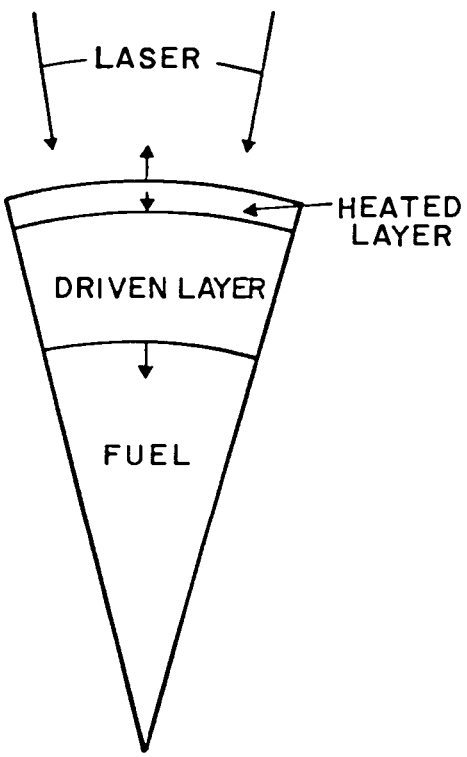

Fig. IV-51.
Ablatively driven target.

the hot electrons generated in the laser absorption region. One result of this preheat shielding is that much higher final fuel densities can be obtained than in the exploding-pusher case. This fact gives us a means of showing that an ablative implosion has been achieved, i.e., if we can prove that we have obtained a high DT fuel density such as 20 times liquid density, then we can be reasonably sure that an ablative implosion has taken place.

We have calculated a basic target design by using the computer code LASNEX. This basic target (see Fig. IV-52) is a sphere consisting of (1) a central core of DT fuel at 100-200 atm pressure with a radius of 100-200 μm, (2) a high-Z (e.g., nickel, molybdenum, or tungsten) pusher 1-5 μm thick, and (3) 50-200 μm of plastic. The laser pulse was assumed to be characteristic of the EBS.

The fuel region is at a relatively high pressure and large radius so that the final compressed radius will not be so small that it will be difficult to measure.

The high-Z layer is also a high-density layer that acts as an intact pusher for the fuel. It is also a final shield of the fuel from hot electrons and photons.

The plastic layer is the ablator. Because of its high-density radius (ρr), it shields the fuel from the hot electrons and to some extent from the photons. Its large outer radius also reduces the energy per unit area of the laser falling on the pellet and thus reduces the temperature of the hot electrons. Its thickness should also guarantee that the high-Z

layer stays compressed. This is necessary if a backlighting procedure is used to measure the outer radius of the high-Z layer to get an upper bound on the radius of the fuel.

In addition to the three materials of the pellet indicated above, there are others that are there for fabrication reasons. Specifically, the material next to the fuel region is glass, because these targets are fabricated by starting with a GMB. These materials have been included in the LASNEX calculations.

The general behavior of the targets is that they absorb useful energy from the laser for the entire pulse length of, e.g., 1-3 ns. Because of the larger amount of material between the fuel and the laser, the fuel is shielded from hot-electron and x-ray preheat and thus stays cold with relatively little back pressure. It also stays cold because the acceleration of the pusher is slow and gentle so that large shock waves are not formed in the fuel. Thus, the fuel is compressed to fairly high density while it is still cold and because it is still cold. At the same time it is heated to about 300-500 eV and should produce on the order of 10^8 neutrons. The process is very slow compared to the exploding-pusher targets. The peak compression occurs from 4-5 ns after the start of the laser pulse.

There are a number of uncertainties in the calculation. In particular the amount of hot-electron shielding needed is known only very generally from the calculations both because the code is known to have errors in its calculations of electron range and scattering and because the actual hot-electron spectrum generated by the CO_2 laser is not known very well experimentally. Despite these uncertainties, we feel that a target of the type described above will produce a density of over 20 times liquid density at peak compression for any reasonable laser pulse expected from the EBS. The most difficult part of the experiment will be making a direct measurement of this high density.

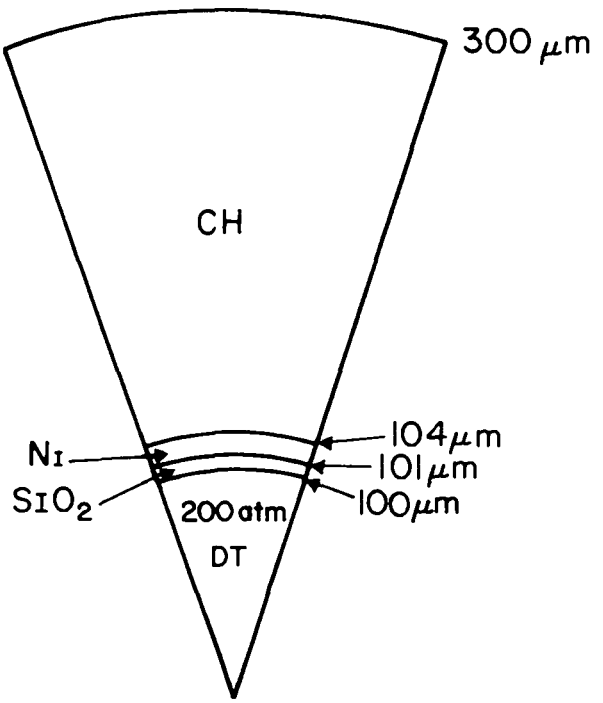

Fig. IV-53.
EBS high-compression target.

High-Compression Target Implosion Scenario (R. Kopp)

To illustrate the sequence of events during the implosion of an ablatively driven target to high densities, consider the specific target configuration shown in Fig. IV-53. This target was tailored for use on the EBS. It consists of (1) a glass microshell, 200 μm in diameter and 1 μm thick, containing a fuel region of DT gas at a pressure of 200 atm; (2) a 3-μm nickel high-Z pusher, which provides some shielding of the fuel from preheat, but more importantly acts to contain the fuel inertially during its compressed state, thereby optimizing conditions during the interval when thermonuclear (TN) burn occurs; and (3) an outer plastic shell, which provides the bulk of preheat shielding and acts, as described previously, to diffuse the incident laser illumination over a large area, thereby diminishing the energy and range of the suprathermal electrons generated at the critical density surface.

The specific choice of parameters characterizing this target was made through a lengthy process of "tuning" a target of the generic type outlined above for optimum performance. This depends, among other things, upon the exact temporal shape of the laser pulse to be employed. The pulse shape used in the present design is shown by the solid line in Fig. IV-54, viz., a triangular pulse with 200-ps risetime, total duration 1.2 ns, and total energy of 5 kJ (0.625 kJ/beam of the EBS), giving a peak power of 8.33 TW. This corresponds to a conservative assumption about the output of the EBS (dashed profile in Fig.

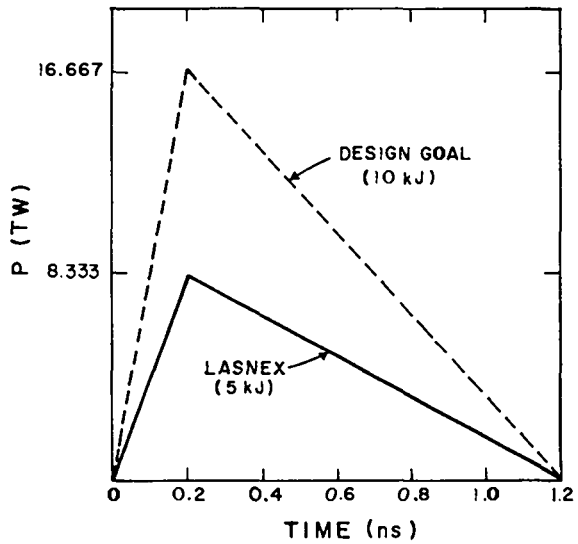

Fig. IV-54.
EBS laser time profile.

IV-54). It is assumed that the incident laser energy is distributed uniformly over the target surface, and that 20% of this energy is absorbed.

The ensuing implosion can be regarded as occurring in three well-defined phases: (I) a preheat phase, (II) a shock-heating phase, and (III) a final phase of adiabatic compression to the desired high density and temperature for significant neutron yield. Each of these phases is identified by the dominant physical process characterizing it, as described in the following:

I. Preheat — During the laser pulse copious fluxes of suprathermal electrons and x-rays generated near the critical density layer at the target surface penetrate the target interior. Subsequent thermalization of the energy transported thereby leads to nonadiabatic heating of the pusher and fuel. This target preheat, which must be carefully controlled, is important for two reasons: (1) Together with the shock-heating of Phase II, fuel preheat establishes the adiabat along which the final compression to high DT-density will occur. Excessive preheat prevents high densities from ever being achieved, because the ablation pressure for a given laser pulse cannot be made arbitrarily large. On the other hand, some preheat is required to ensure that temperatures in the compressed core are high enough (i.e., 300 eV or more) to produce significant TN-burn (at least 10^5n). For a 200 atm target, preheat should not raise the fuel temperature to more than about 5 eV at the end of the laser pulse. (2) Preheat of the high-Z pusher leads to a considerable expansion, or thickening, of this shell before its major hydrodynamic acceleration takes place. This greatly reduces the initially large aspect ratio of the pusher and makes it less susceptible to Rayleigh-Taylor instabilities as it subsequently accelerates inward. As a result of this expansion, a weak pressure wave is launched into the fuel region, which gives rise to an initial adiabatic compression of the fuel to densities of 0.1 - 0.2 g/cm^3.

II. Shock Heating — The rapid laser heating of the ablator generates a strong shock, which propagates into the target interior on a hydrodynamic time scale. Spherical convergence of this shock at, and reflection from, the center of the fuel region occurs at about 4 ns after laser turn-on, and this further compresses (by a factor of 20 to 30 over the initial density) and heats the fuel nonadiabatically, and it sets the pusher in motion for Phase III.

III. Adiabatic Compression — In this last phase of the implosion, the inertia imparted to the pusher by the shock and subsequent ablation pressure, is used to compress the fuel more-or-less adiabatically to its final high-density state, where it is inertially confined by the pusher during TN-burn.

Figure IV-55 shows a plot of the average fuel density as a function of time, for the target illustrated in Fig. IV-53, as calculated by the laser fusion code LASNEX. The maximum density achieved is just over 14 g/cm^3, or 80 x liquid density, and occurs 4.5 ns after the laser is turned on. The neutron yield for this target is predicted at 5 x 10^6. Although the latter quantity is uncertain by perhaps an order of magnitude, the *time of yield* should coincide with maximum compression; thus, the relative slowness of these ablatively driven targets may make a measurement of the time delay between laser turn-on and neutron yield the most useful and reliable diagnostic technique for this type of target.

Conventional diagnostic techniques for exploding-pusher targets encounter severe difficulties when applied to these first-generation ablatively driven targets. Pinhole imagery of soft x-ray emission is virtually useless, for example, because (1) the pusher

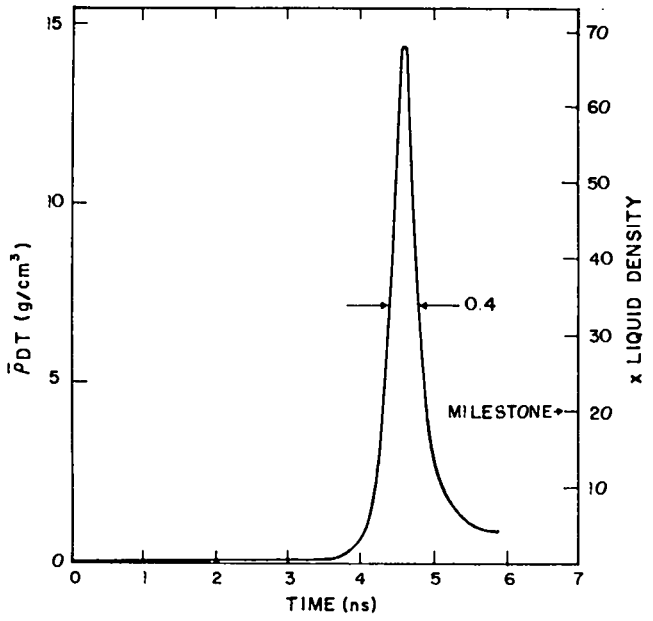

Fig. IV-55.
Average fuel density as a function of time for target shown in Fig. IV-53.

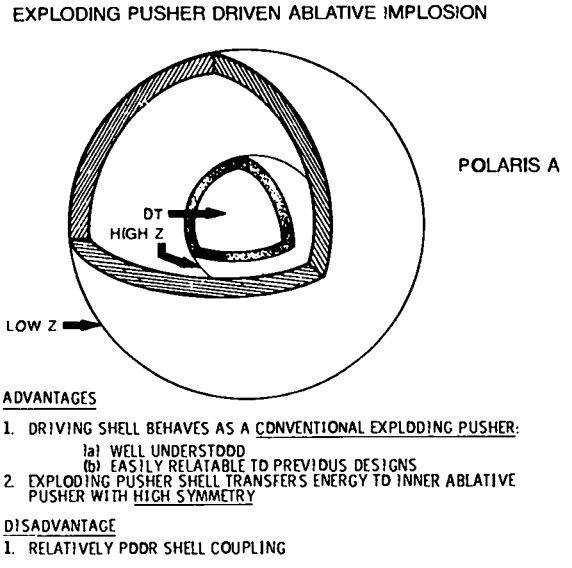

Fig. IV-56.
Double shell exploding pusher target.

and ablator never get hot enough to emit a detectable x-ray flux, and (2) the high-Z pusher, which is necessary to ensure an efficient implosion, is opaque to x rays generated in the fuel region. A technique for backlighting the target by a short x-ray pulse timed for maximum compression would be useful here, by making possible a direct measurement of the minimum pusher radius (22 μm for the target described above), and is currently under consideration.

DOUBLE-SHELL TARGET DESIGNS FOR LASL EBS (J. M. Kindel and M. A. Stroscio)

Double-Shell Exploding Pusher (DSEP)

Figure IV-56 depicts a two-shell laser-driven target[18-21] with the outer shell in the exploding pusher mode.[22-25] This type of target has been previously discussed in Ref. 22; thus, this report is intended to expand on the basic idea and to present a specific target design for LASL's EBS. The basic motivation for studying this design comes from the observation that laser-driven exploding-pusher shells implode with a high degree of symmetry as a result of their isothermal character. Associated with this advantage is the obvious disadvantage that the exploding pusher shell couples poorly to the inner shell, which is to be driven by electron conduction. We consider (1) the advantage of this target by comparing one- and two-dimensional LASNEX[26,27] simulations and (2) the disadvantage (poor coupling) by actually calculating the performance of the proposed target. It is concluded that in the laser energy range of interest the disadvantage is not particularly great — especially when symmetry problems inherent in velocity-multiplying, ablatively driven targets are taken into account.

Further comparison of the proposed target with exploding-pusher and conventional double-shell targets is given in Fig. IV-57. In addition to the symmetry advantage discussed above it is found that specific designs of the DSEP target are

1. relatively insensitive to the fill pressure between the exploding pusher and electron-driven shells for low gas densities,
2. relatively insensitive to 50% variations in the superthermal electron temperature,

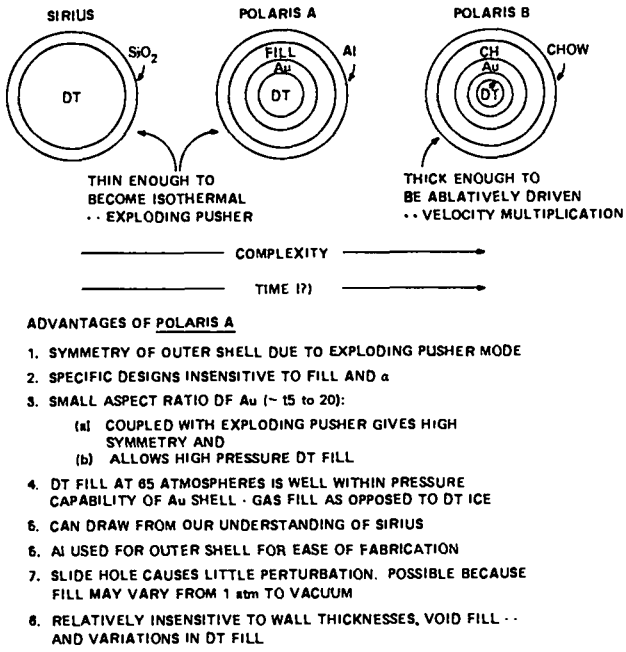

Fig. IV-57.
Comparison of (1) exploding pusher, (2) double-shell exploding pusher, and (3) conventional double-shell laser fusion targets.

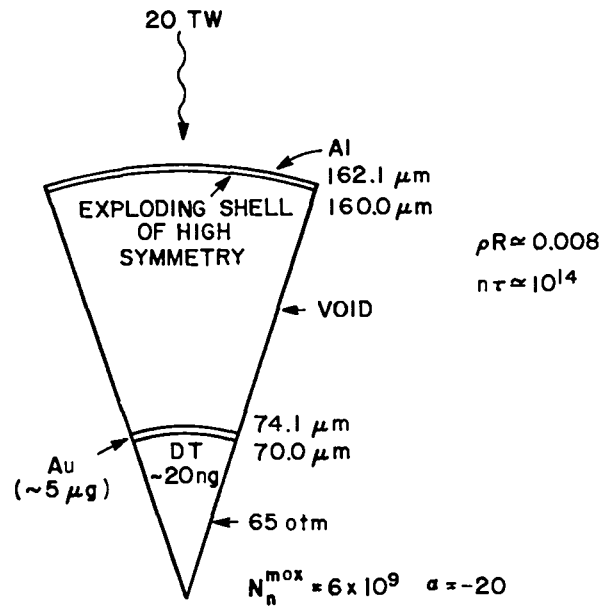

Fig. IV-58.
A typical DSEP design.

3. amenable to small-aspect ratio inner, ablatively driven shells, and
4. can be optimized for relatively low DT gas fills near 75 atm.

Several of the advantages are clearly related to the high symmetry inherent in the DSEP target. Finally, we add that the relative insensitivity of the design to various parameters and two-dimensional effects implies that this target is probably (1) relatively easy to construct and (2) accurately predicted by the present numerical simulations.

A specific DSEP target design is shown in Fig. IV-58. For a laser pulse that rises linearly to 20 TW in 200 ps and falls linearly to 0 TW at 0.8 ns, a maximum neutron yield of approximately 6 x 10^9 is calculated with the suprathermal electron parameters, alpha,[28] taken as −20. In addition, a ρr of 0.008 g/cm^2 and an $n\tau$ of approximately 10^{14} are achieved. These parameters are not observed to be strongly influenced by varying alpha between 8 and 30. In obtaining this result (and all results herein) it is assumed that suprathermal electrons are reflected at the sheath until the void is filled. The insensitivity of this design to alpha is inherent in the exploding pusher scheme.

The number of neutrons, N_n, produced by a similar DSEP target is found to scale with greater than the third power of P_L, the peak laser power. This behavior is displayed in Fig. IV-59 for a design operating at 20 TW similar to that in Fig. IV-58, but with an Al wall thickness of 1.3 μm and an Au wall thickness of 4.1 μm. In Fig. IV-59, a separate design, optimized for 10 TW, is seen to give similar neutron yields. This 10-TW design has a gold thickness, an Al thickness, and a DT fill of 3.2 μm, 1.5 μm, and 75 atm, respectively.

The general behavior of the DSEP target for a design similar to that in Fig. IV-58 with a peak power of 20 TW is summarized in Fig. IV-60, IV-61, IV-62. Figure IV-60 depicts the radius of the Au-DT interface as a function of time with the instantaneous implosion velocity given at two specific times. Figure IV-61 illustrates the average ion, electron, and radiation temperatures in the DT gas as a function of time. Finally, Fig. IV-62 represents

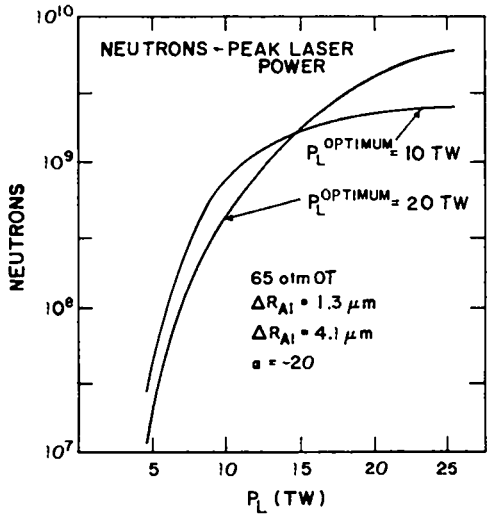

Fig. IV-59.
Neutron yield as a function of peak laser power for targets optimized at 10 TW and 20 TW.

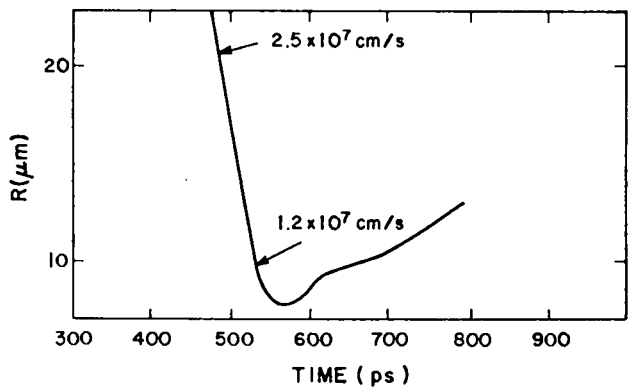

Fig. IV-60.
Radius of gold-DT interface as a function of time.

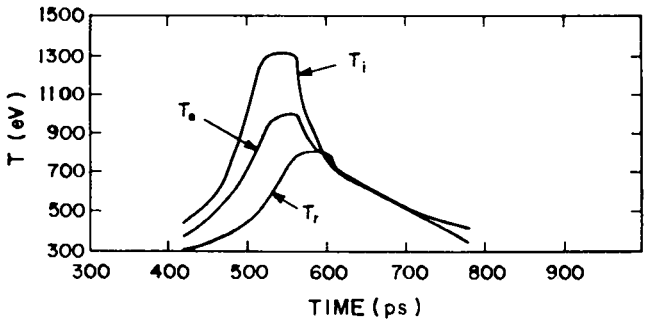

Fig. IV-61.
Average ion, electron and radiation temperatures in the DT gas as a function of time.

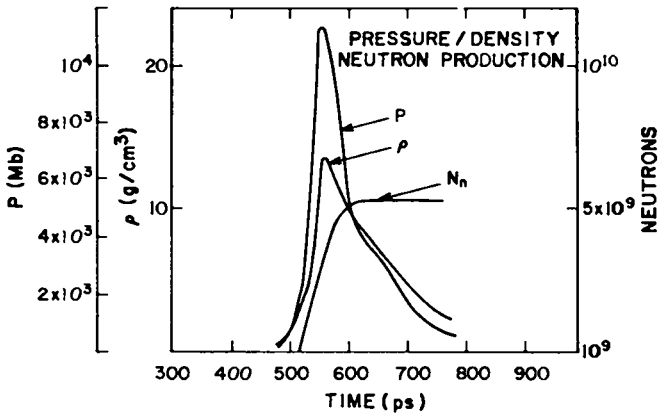

Fig. IV-62.
Time histories of the DT gas pressure, density, and neutron production.

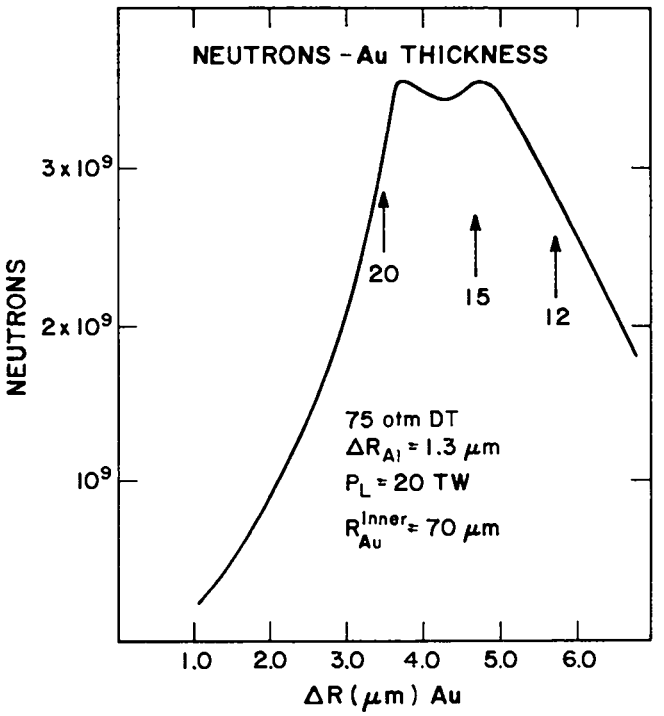

Fig. IV-63.
Neutron yield as a function of gold shell thickness.

the time history of the DT pressure P, the average DT density ρ, and the neutron production.

The insensitivity of the DSEP target to wall thickness of the pusher shell is illustrated in Fig. IV-63. The one-dimensional LASNEX simulations

presented in these figures indicate that large variations in material thicknesses have only minor influence on neutron production. This is in definite contrast to the conventional double-shell targets, which usually are very finely tuned with regard to wall thicknesses. In addition, Fig. IV-63 illustrates that the shell (ablative shell) thickness may be varied to give aspect ratios from 12 to 25 without causing large fluctuations in the neutron yield. In Fig. IV-63, the three arrows indicate the thickness corresponding to aspect ratios of 12, 15, and 20.

In addition to the small aspect ratios needed in the DSEP targets, LASNEX simulations indicate that the two-dimensional effects do not seriously degrade the neutron yield. In fact, two-dimensional LASNEX simulations predict reductions in neutron production by only a factor of 0.3 for a 10-to-1 pole-to-equator illumination asymmetry. In many standard, double-shell velocity multiplying targets a 10-to-1 illumination asymmetry is sufficient to drastically reduce the neutron yield.[29]

Finally, we note that the absorption values for CO_2 laser light used in this study were taken to be the plane slab values[30,31] because the focal spot for the EBS is predicted to be smaller than the 320-μm diameter of the DSEP target discussed above. The absorption fraction has been taken as 40%; however, variation from 30% to 50% indicate only a factor of 5 change in the neutron yield.

In summary, the basic idea incorporated in the target design of Ref. 21 has been applied to a specific target design for the EBS. It is found that the DSEP design is predicted by LASNEX simulations to yield approximately 5 x 10^8 neutrons and to achieve densities in excess of 70 times solid DT density. Furthermore, the design is relatively insensitive to various design parameters and two-dimensional effects associated with laser illumination asymmetry.

Low Fuel-Mass Design

The primary reasons for studying a POLARIS design with a low fuel mass are to achieve high fuel density and large fractional burn-up of the fuel. In optimizing a design with the above goals in mind, it is necessary to evaluate the effects of

1. Preheat by suprathermal electrons and photons,
2. Target sensitivity to laser illumination symmetry,
3. Sensitivity of target to changing material radii,
4. Varying cushion mass to target performance,
5. Varying the fuel mass, and
6. Replacing a DT ice layer with a DT gas, and changing the laser power.

It is found that the suprathermal electron preheat is a major factor in the design. Specifically, a high-Z outer pusher leads to more scattering of suprathermal electrons and then less preheat. In addition, high-Z materials are necessary for preventing photon preheat. On the other hand, high-Z materials are usually accompanied with high densities. Thus, in an attempt to maintain small aspect ratios and high-Z materials, the total mass of the shell in question becomes too large. These considerations lead one to an outer pusher of a low-Z material with a high-Z impurity. In the designs discussed herein this material is CHOW. By atom percent its composition is 32.3% carbon (C), 64.6% hydrogen (H), 2.2% oxygen (O) and 0.88% tungsten (W).

Figure IV-64 depicts a double-shell velocity-multiplying target with a low fuel mass (2.7 ng) and an

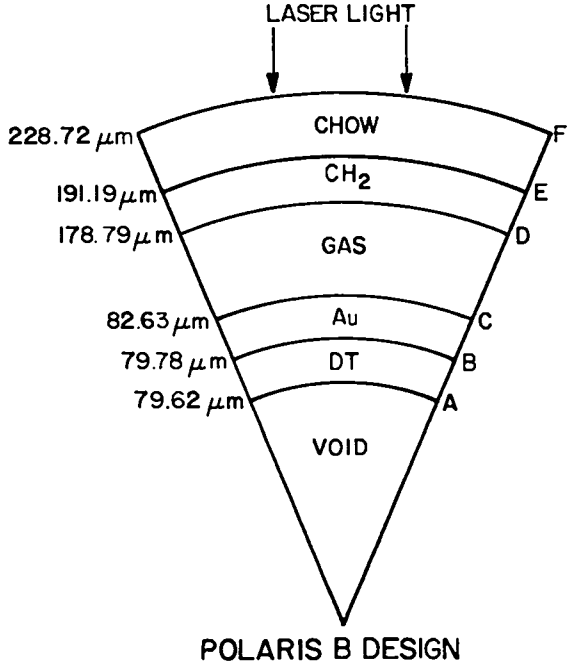

Fig. IV-64.
A typical double shell, velocity multiplying design with a low fuel mass.

outer pusher of CHOW. For this design a factor-of-3 variation in the cushion mass has less than a 10% effect on the neutron yield. Replacing the layer of DT ice by DT gas and filling the entire inner volume indicates the peak ion temperature and neutron yield are reduced by approximately 20%. In contrast the peak density is reduced by about a factor of 3 upon replacing DT ice with DT gas.

The design in Fig. IV-64 is matched to a laser pulse which rises linearly from 0 TW to 10 TW in 200 ps and then falls linearly to 0 TW at 1 ns. In addition, we have (1) used the hot-electron formulation of Ref. 28 and (2) taken the coefficient alpha to be 20. For these conditions, the target of Fig. IV-64 achieves a peak density of ~30 g/cm^3 (150 times solid density), a peak ion temperature in the DT fuel to 620 keV, and a neutron yield of 2 x 10^7. These values are obtained without finely tuning the target and it is therefore felt that they are modest but sound results within the context of one-dimensional calculations. For example, this design is relatively insensitive to the thickness of the CHOW pusher — a 10-μm variation in the thickness leads to only a 40% reduction in the neutron yield. Finally, we note that the positions of the various shell interfaces as a function of time are shown in Fig. IV-65.

It is difficult to assess the complete role of illumination asymmetry in the low fuel-mass target. The results obtained in several LASNEX[26,27] simulations suggest that (a) the peak density can be degraded by a factor of 2 or more (from the one-dimensional result) and (b) the peak ion temperature can be reduced by a larger factor. Figure IV-66 illustrates the type of asymmetry in implosion hydrodynamics that can result from a large asymmetry in laser illumination. The conclusion of our two-dimensional study is that illumination asymmetry must be kept to a minimum if good performance is to be achieved with the low-mass-fuel target. However, we consider this to be largely an experimental question which can only be resolved in the laboratory.

In summary, it is found that a low-fuel-mass velocity-multiplying target (POLARIS B) can produce nearly 200 times solid density for EBS parameters when the laser illumination is highly symmetrical. The exact role of illumination asymmetry is an uncertainty which must be resolved empirically.

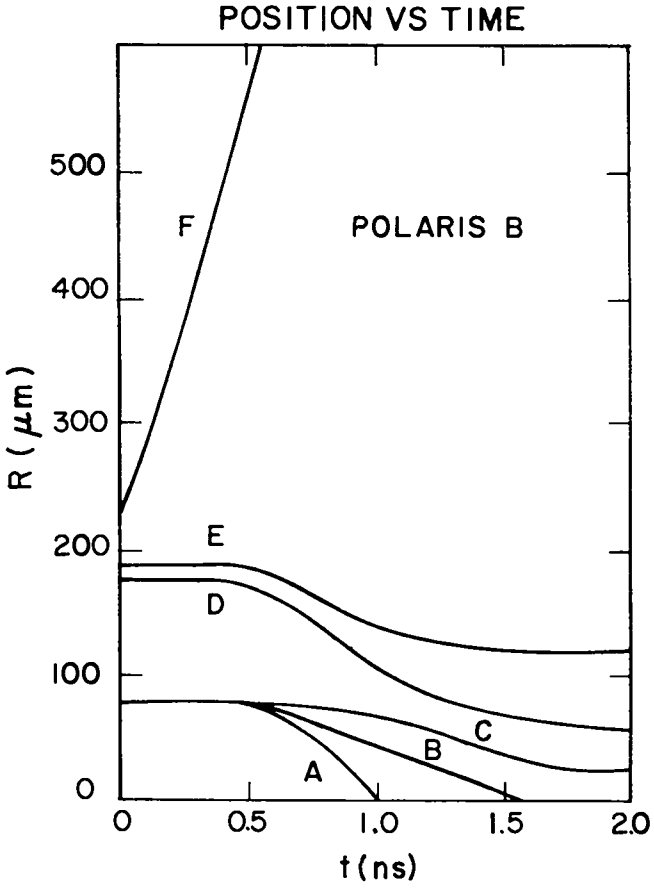

Fig. IV-65.
Plot of radii as a function of time for the design shown in Fig. IV-64.

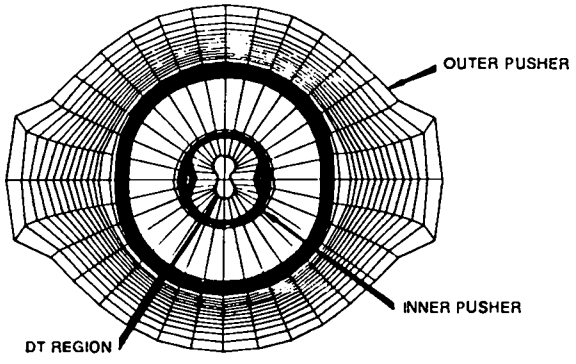

Fig. IV-66.
Two-dimensional velocity-multiplying target design with a large illumination asymmetry.

DOC - A Linear Stability Analysis Code (J. Scannapieco)

The viability of an inertial confinement fusion target design is dependent upon the fluid stability of that design. The problems faced in obtaining stability information about a target are copious, and have shown themselves to be analytically intractable.

To consider, in a realistic fashion, the fluid stability of an imploding fusion pellet, one must deal with (at least) effects due to real equations of state, asymmetric energy deposition, thermal conduction, shock propagation, time-dependent zeroth-order states, and spherical geometry. The necessity of considering the above-mentioned complications renders even a linear analytic perturbation analysis impossible.

Given the hopefulness of ever obtaining an analytic result, and the necessity of understanding the fluid stability of the fusion pellet, a computational procedure has been employed. The culmination of this computational procedure is the code, DOC.

DOC is a spherical harmonic linear stability code that integrates, in time, a set of Lagrangian perturbation equations. The necessary information describing the time-dependent zeroth-order state is obtained from the code LASNEX by dumping this information onto disk every timestep. DOC then operates as a postprocessor on the LASNEX-generated data.

DOC in its present form is a one-temperature code; however, it will be upgraded to a three-temperature code in the very near future. A physical viscosity will also be treated in the near future. This last feature is important for systems in which the materials are in a solid or liquid state during the pellet implosion.

The DOC is currently undergoing extensive testing on a few carefully selected target designs, but results are too preliminary to be reported at this time.

THEORETICAL SUPPORT AND DIRECTION

Introduction

As mentioned in our preceding discussion we are using the LASNEX code extensively in designing various targets for our laser fusion experiments. However, some relevant areas of target-related physics are not handled in LASNEX. These areas may be grouped into three catagories: (1) new insight into target physics, which will eventually modify LASNEX, such as the results of electron-transport and hot-electron production studies, (2) target physics that are outside the scope of LASNEX but are important for target diagnostics, such as studies on coronal rarefaction shocks, and (3) studies that are important in the diagnosis of target experiments, such as the physics of ion diagnostics and the design of a computerized data file. These areas are discussed in the following pages.

Physics of Ion Diagnostics (H. Brysk and S. J. Gitomer)

Results obtained from ion diagnostics depend upon the interplay of conditions at the target with the processes in the course of the subsequent expansion of the plasma over enormously larger distances and interaction of the plasma with components of the measuring apparatus. Deductions as to target characteristics depends on taking adequately into account the latter effects.

Thomson-parabola data at LASL indicate that the highest velocity ions are all protons (and hence that the energy content of the fast-ion component is much less than would be deduced from a free expansion of a single-ion-species plasma)[32]. This finding has been confirmed at Naval Research Laboratory with different instrumentation[33] and accounted for heuristically in calculations with a two-ion-fluid model. Fine structure in the fast-ion group is not yet

understood. Thomson-parabola traces of different charge states of nonhydrogenic ions (specifically, carbon in polyethylene) have the same high-energy cutoff[33], which is explained by an initially fully ionized plasma undergoing some recombination during its expansion; this interpretation is confirmed by the reported detailed analysis of a Lockheed experiment[34].

Slater has observed a laser fusion plasma with an ion pinhole camera[35]. He reports an image size almost an order of magnitude larger than would be expected from a radial expansion, more nearly compatible with isotropic emission of ions from the surface of the microballoon. We have analyzed the interaction between a plasma beam and a pinhole and computed the effect under the conditions of Slater's experiment[36]. The pinhole is modeled as a grounded conducting cylindrical tunnel. Within a Debye length of the tunnel wall, the electrons and ions in the plasma are uncorrelated. Considering uniformly distributed ions and randomly distributed electrons, we calculate the image charge induced in the wall. The resultant electric field deflects some of the electrons into the wall. The plasma emerging from the pinhole is no longer electrically neutral and the space charge effect causes it to expand on the way to the recording plane. Using parameters corresponding to Slater's experiment, we compute an image size comparable with that observed. This does not exclude the possibility that there *are* anomalies in the ion source, however. To settle the issue, further experiments will be required with a large dynamic range in pinhole dimensions and/or plasma densities at the pinhole.

Theoretical Model for Hot-Electron Production (B. Bezzerides, D. F. DuBois, and D. W. Forslund)

We have developed analytical and numerical methods to understand in detail how hot electrons are generated by large-amplitude electrostatic waves. These waves are created in the region of the critical surface through resonance absorption of intense laser light. The basic assumption of our work is that the waves may be characterized by a few simple parameters making it unnecessary to solve the full self-consistent problem. The great potential of this work, along with the microscopic understanding it provides, is a very inexpensive procedure for calculating hot-electron spectra as compared with a complete particle-in-cell wave plasma simulation.

In the simulations, the heated particles originate at some early time on a fixed boundary upstream of the field where they have a Maxwellian distribution with a temperature of the cold background. These particles stream into the region where the localized fields exist, are accelerated, and reflect off the sheath, returning to the overcharge region as shown in Figs. IV-67 and IV-68. Because the distribution function f is constant along a phase space trajectory, we have

$$f(v_2) = f(v_1)$$
downstream Maxwellian

where v_1 is the velocity that the particle must have had to arrive at (x,t) with velocity v_2. We have numerically calculated the backward trajectory to

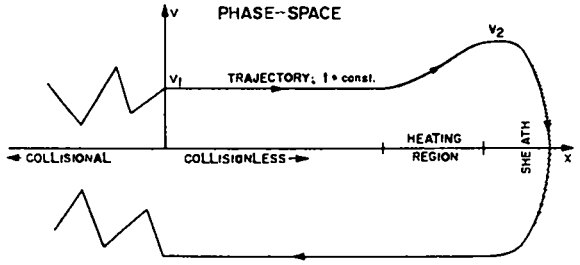

Fig. IV-67.
Typical phase space trajectory for a heated particle.

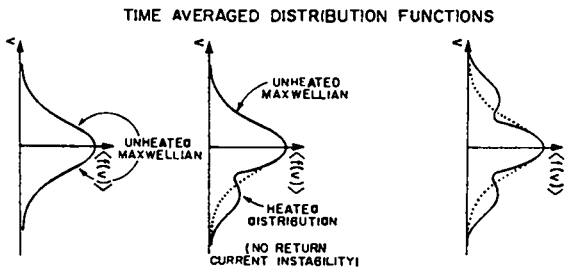

Fig. IV-68.
Schematic representation of distribution function downstream of field and upstream of field due to reflection off the sheath.

obtain v_1 given v_2 once the field is known. A typical example is shown in Fig. IV-69. The contour lines in v_1 vs v_2 correspond to a range of final times at which the distribution function is measured. Given such a contour plot, f is easily determined.

We find that a standing-wave model for the field leads to a scaling of $T_H \sim v_{oc}/\omega L$, where L is the field scale length. This scaling is inconsistent with the results observed in simulations. Also, far less suprathermal electrons are produced than is needed to explain the simulation results. Including a traveling-wave component to the field does not significantly alter these conclusions. Extensive comparative studies show that agreement is possible only if we include the inhomogenous phase of the field along with its correct amplitude.

To account for the effects of wave phase we have constructed a set of dynamical equations that describe the guiding center motion of the electrons, but include the effects of localized wave-particle resonance. From the structure of these equations we see that the particle has large-amplitude oscillations in velocity about its guiding center motion. However, in the neighborhood of the resonance, $v = v_{phase}$, the coherent oscillatory motion is interrupted by resonant acceleration. Thus, the final acceleration a particle experiences is due to a ballistic contribution from the coherent oscillatory motion and localized resonant acceleration. These qualitative features of the heating process have been confirmed by exact phase space trajectories. Progress is being made in obtaining scaling laws from the parameters of the field by these calculations.

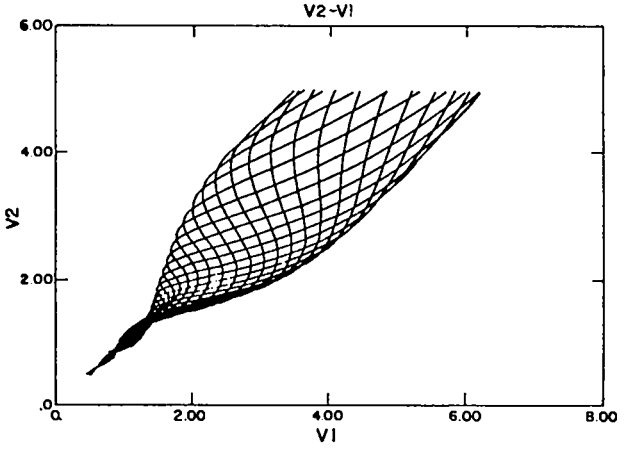

Fig. IV-69.
Initial velocities v_1 vs final velocities v_2 for a given time t_2. Each contour corresponds to a particular time t_2, ranging over a period.

Electron Transport (K. Lee)

It has been well established that the majority of the laser light energy absorbed is carried away to higher densities by energetic electrons. Therefore, it is crucial to describe the transport and thermalization of energetic electrons accurately so that prediction of preheat or decoupling is representative of the physics and not the numerical methods. A program of careful comparisons of different methods of electron transport has begun at LASL. The objectives are to identify situations where multigroup diffusion might be deficient, to study numerical methods that improve upon the accuracy of multigroup diffusion, and to determine whether or not the more accurate methods can be economically implemented in a design code.

The electron transport equation is obtained from the Boltzman equation. Assuming collisions are dominated by small-angle scattering, the Boltzman equation can be approximated by the Fokker-Planck equation. Separating the electrons into energetic and thermal electrons and neglecting interaction among energetic electrons the Fokker-Planck equation is linearized. Furthermore, making the asymptotic approximation, the following electron transport equation is obtained,

$$\frac{\partial f}{\partial t} + v\mu \frac{\partial f}{\partial r} + \frac{v(1-\mu^2)}{r} \frac{\partial f}{\partial \mu} = \frac{n}{v^2} \frac{\partial f}{v}$$

$$+ \frac{n(Z+1)}{2v^3} \frac{\partial}{\partial \mu} (1-\mu^2) \frac{\partial f}{\partial \mu} \quad . \qquad \text{(IV-43)}$$

We have initially restricted our study to one dimension in either plane or spherical geometry. The distribution function $f(t,r,v,\mu)$ is a function of time t, radius r, speed v, and cosine of the angle μ between the radius vector and the velocity vector; n and Z are the electron density and ionic charge of the cold background. The transport equation is in normalized units where r is in unit of λ, v is in units of hot thermal velocity A_H, t is in units of λ/A_H, and n

is normalized to the critical density n_o; λ is defined by

$$\frac{1}{\lambda} = \frac{4\pi e^4}{m_e^2 A_H^4} N_o \ln \Lambda \ . \qquad \text{(IV-44)}$$

For simplicity in the initial comparison calculations we have assumed $\ln \Lambda$ is constant and equal to 10. Initially we have also neglected the electric field and magnetic field.

We have studied the above equation in the flux-limited multigroup diffusion approximation and by Monte Carlo and have made some preliminary comparisons. The multigroup diffusion equation can be obtained from the transport equation by a truncated expansion of the distribution function's angular dependency in spherical harmonics

$$f = \sum_\ell \frac{(2\ell+1)}{2} \psi_\ell P_\ell(\mu) \ . \qquad \text{(IV-45)}$$

The expansion is truncated by assuming $\psi_1 = 0$ and by neglecting the time derivative and velocity derivative of ψ_1. In this expansion ψ_o and $V\psi_1$ physically represent, respectively, the density and flux of particles. By neglecting the time derivative, the flux can get unphysically large when the scattering mean free path is larger than the density scalelength. A limit is imposed on the flux either by setting

$$|\psi_1| = \text{minimum} \left\{ |v^4(\partial\psi_o/\partial r)/3n(Z+1)|, \alpha\psi_o \right\} \qquad \text{(IV-46)}$$

or by setting

$$\psi_1 = \frac{\alpha\psi_o v^4 \frac{\partial\psi_o}{\partial r} / 3n(Z+1)}{\alpha\psi_o + \left| v^4 \frac{\partial\psi_o}{\partial r} o/3n(Z+1) \right|} \ . \qquad \text{(IV-47)}$$

In the Monte Carlo calculation, the distribution function is represented by a collection of particles. The equations of motion for these particles in the same normalized units as the transport equation are

$$\frac{d\underline{v}}{dt} = -\frac{n\underline{v}}{v^3} \qquad \frac{d\underline{r}}{dt} = \underline{v} \qquad \text{(IV-48)}$$

and these particles are scattered in pitch angle $\delta\theta$ where $\delta\theta$ is picked from a distribution

$$P(\delta\theta, \Delta t, v) = \frac{v^3 \delta\theta}{(Z+1)n\Delta t} e^{-v^3(\delta\theta)^2/2(Z+1)n\Delta t} , \qquad \text{(IV-49)}$$

and in azimuthal angle $\delta\phi$, where $\delta\phi$ is a uniform distribution function distributed over 2π.

Bethe's[37] solution of the steady-state one-speed transport equation in plane geometry is compared with Monte Carlo calculations in Fig. IV-70. The one-speed approximation implies that the energy loss by the particles or, equivalently, the velocity derivative of the distribution function in the transport equation is neglected. Figure IV-70 shows the dependency of the inverse of the transmitted flux as a function of foil thickness in units of the scattering mean free path for a unidirectional beam incident normally on a foil. The solid line is Bethe's solution obtained by separation of variables and the dash line is the solution to the transport equation in the diffusion approximation. The points are Monte Carlo for the indicated free-streaming path length between scattering. For sufficiently small free-streaming path length between scattering Bethe's solution is reproduced. For large free-streaming path length between scattering the Monte Carlo solution goes over to the diffusion limit.

Figure IV-71 compares the Monte Carlo solutions against multigroup-diffusion solutions. Figure IV-71 gives the percentage of energy thermalized as a function of time from a constant 20-keV monoenergetic isotropic source emitted at the outer surface. The electrons are transported and thermalized against a background density profile, which has a density of 1×10^{20} cm^{-3} at a radius 300 μm and increase in density as $(1/r)^3$. The upper solid and lower dashed curves give, respectively, the multigroup diffusion and Monte Carlo solutions for Z = 1. The intermediate curves are solutions for Z = 100. The results indicate multigroup diffusion couples more energy into the background. Basically, in the low-density region where the mean free path is large compared to the local scale length, the flux-limited multigroup diffusion approximation requires that all the electrons move radially inward with a speed αv, where α and v are, respectively, the flux-limiting

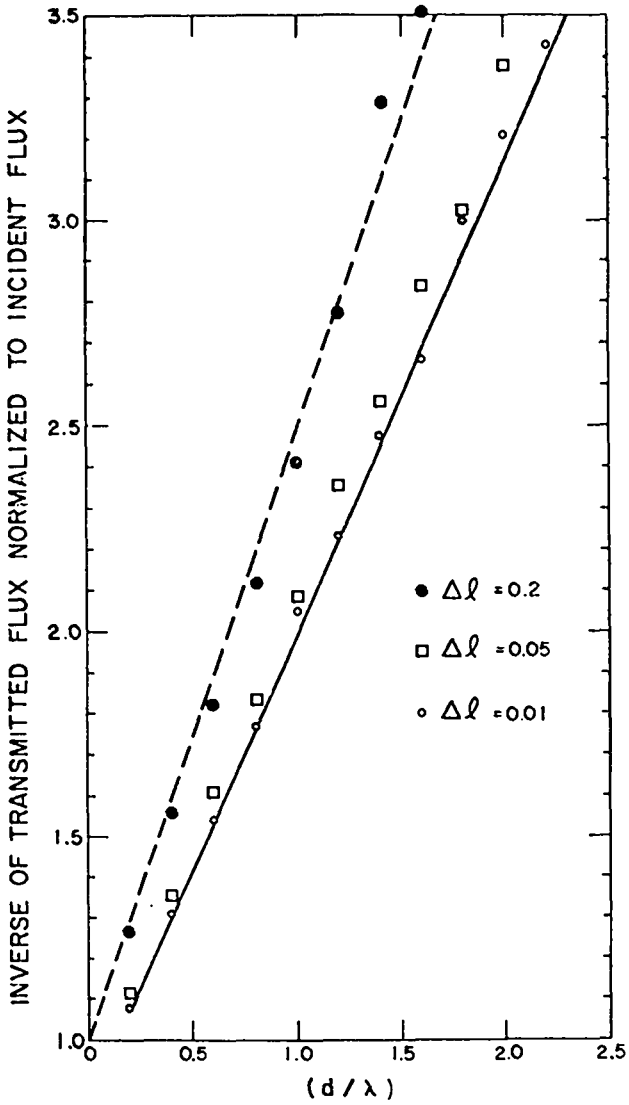

Fig. IV-70.

Steady-state one-speed Monte Carlo solutions in plane geometry with scattering only are compared with diffusion solution (dashed line) and Bethe's solution (solid line). The graph plots the inverse of transmitted flux vs foil thickness in units of scattering mean-free path. The points are Monte Carlo solutions for the three indicated free-streaming path lengths in units of mean free path between scattering.

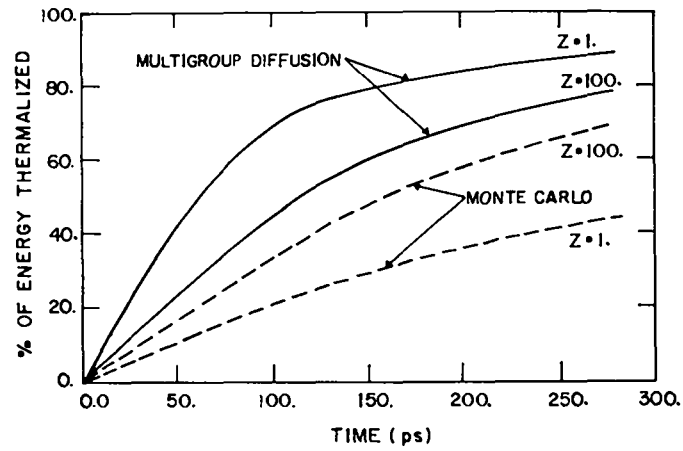

Fig. IV-71.

Percentage of emitted hot-electron energy thermalized as a function of time from a constant isotropic source of 20-keV electrons transported through a fixed density profile in spherical geometry which varies inversely as the cube of the radius. Multigroup diffusion overestimates the coupling of hot electron energy in comparison to Monte Carlo. Closer agreement is achieved by increasing the scattering for Z = 100.

factor (picked to be 1/ 3 in these calculations) and the average speed of the group.

All the energetic electrons are coupled to the high-density region after a transit time. In reality, a large fraction of the electrons with large angular speed and small radial speed remains in the low-density region and will not couple to the high-density region until significant radial velocity component is acquired due to cummulative scattering. These electrons in the low-density region can expend a larger fraction of their energy accelerating ions than flux-multigroup diffusion predicts. Thus, the smaller fraction of energy in fast ions as predicted by hydrodynamic codes in comparison with experiments may be due to inaccuracy in the treatment of electron transport and may not be due to existence of anomolous heat-conduction inhibition as suggested by many authors. It is true that increased scattering will decrease the energy coupling as predicted by multigroup-diffusion and bring about closer agreement with the Monte Carlo prediction. But, actually, increased scattering increases energy coupling as shown by the Monte Carlo calculation when the Z of background material is arbitrarily increased to one hundred.

In conclusion, flux-limited multigroup diffusion treatment of electron transport tends to overestimate preheat and underestimate decoupling.

Rarefaction Shocks in a Laser-Plasma Corona (B. Bezzerides, D. W. Forslund, and E. L. Lindman)

Direct measurements of the electron energy spectrum in a laser-irradiated target are extremely difficult to obtain. Presently, the spectrum is inferred from the x-ray spectrum and from fast ions and electrons collected far from the target. We have found,[38] however, that an interferometric measurement of the electron density profile could, in some cases, provide local information about the electron energy spectrum.

In particular, if the electrons have two distinct approximately Maxwellian components, a shock can be set up in the corona that depends on the relative size and energy of these components. This shock is known as a rarefaction shock[39] and occurs at the point where the plasma abruptly changes from primarily cold to hot, in analogy with a phase transition in more conventional thermodynamic fluids.[40]

The onset of the rarefaction shock can be seen by looking at the general rarefaction solution written in terms of the electrostatic potential ϕ and similarly variable $\xi = x/t$,

$$\frac{d\phi}{d\xi}\left[1 + \frac{1}{2}\frac{\partial c_s^2}{\partial \phi}\right] \pm c_s \approx 0$$

where $c_s^2 = dP/d\rho$ is the usual speed of sound. Note that if the quantity in brackets goes to zero the potential as a function of ξ becomes double valued. Typical rarefaction solutions are shown in Fig. IV-72. Double-valued solutions are unphysical, of course, and, in fact, result in the formation of a shock as indicated by the dashed lines in Fig. IV-72.

In the shock-frame jump conditions can be derived that determine the basic shock properties. These are just the usual Rankine-Hugoniot relations. For a two-component isothermal electron plasma, solutions for the shock waves that match onto a rarefaction wave are shown in Fig. IV-73. Note that the typical jump in potential across the

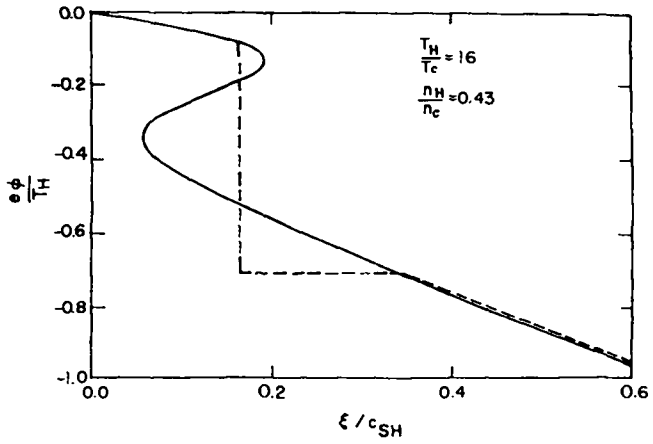

Fig. IV-72.
Rarefaction wave solutions with singularity in the flow illustrating the potential ϕ as a function of the similarity variable ξ for the initial parameters, $T_H T_c = 16$ and $n_H/n_o = .3$. Note the double-valued character of ϕ vs ξ. The dashed lines show the actual solutions with the rarefaction shock embedded in the flow.

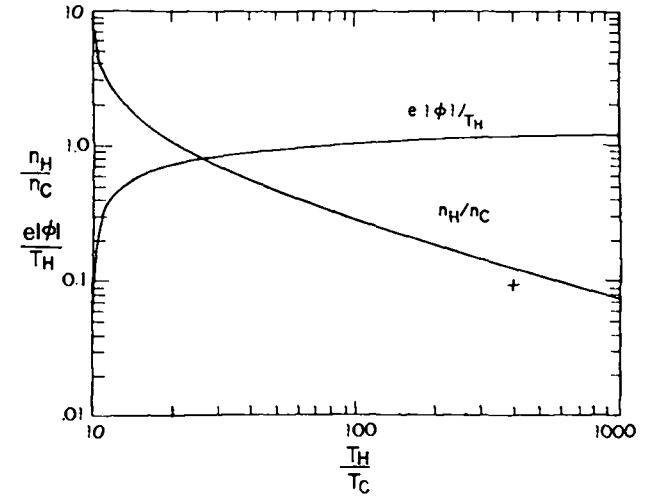

Fig. IV-73.
Rarefaction shock solutions which match onto rarefaction wave solutions. The potential jump $e|\phi|/T_H$ and hot-electron density n_H/n_C on the upstream side are plotted as a function of T_H/T_c.

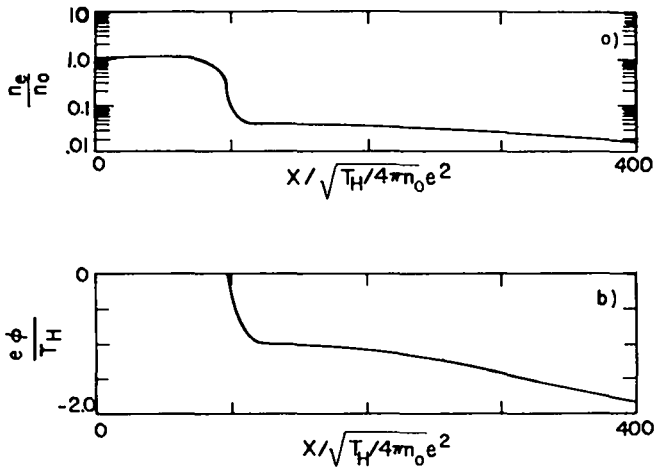

Fig. IV-74.
Numerical solution of a rarefaction shock for T_H/T_c = 100 and n_H/n_o = 0.1 showing a) the electron density as a function of position and b) the electrostatic potential as a function of position at a time t = 2500 ω_{po}^{-1}. Note the uniform region just below the step.

shock is $e\phi \sim T_H$ and that the shock can only occur if $T_H/T_C > 10$. The value of n_H/n_c plotted here is the ratio of hot-electron to cold-electron density on the high-density side of the shock. In Fig. IV-74 we illustrate the typical total electron-density profile which occurs in the presence of one of these shocks. Note that such a density discontinuity should be observable by interferometric means and by the magnitude of the jump and the size of the density at which it occurs, the density and temperature of the hot electrons can be inferred.

Finally, we note that the sharp gradient induced by the ponderomotive force can be described by the same formalism mentioned here. The transition from a high-density plasma to a low-density plasma in the presence of the intense laser field can be considered a phase transition between two plasma states.

Computerized Data File (H. Brysk)

A computer program has been written in the MCP (Master Control Program) data-base-management language for recording and manipulating laser-target shot information. The file consists (on a shot-to-shot basis) of a directory of diagnostics in use (x-ray, ion, neutron, optical) and a display of data available in digitized form from these diagnostics and target parameters. Input is at present manual but will be obtained from the output of the PDP 11/70 computer that the experimental equipment is being tied into. A target-fabrication inventory MCP file is planned next, and the two programs will communicate with each other.

The program produces a formatted report, including data on x-ray spectra, neutron yields, laser energies and temporal and spectral characterizations, target dimensions and materials, etc. The order of presentation of the shots can be varied from table to table according to the values of any specified variable (e.g., neutron number, laser energy). A subset of the shots can be selected by specifying a desired range of a succession of parameters. Output files can be extracted from MCP in a form suitable as input to FORTRAN programs or graphics packages. The combination of digital readout and data reduction on the PDP 11/70 with the link to the MCP data file will provide enhanced accessibility of the data for analysis and correlation.

MILITARY APPLICATIONS, EXPERIMENTS, AND STUDIES

Introduction (A. G. Engelhardt and R. Robertson)

We are conducting laser experiments to simulate and study, on a miniature scale, the blast- and shock-wave phenomena of nuclear explosions. These experiments, performed almost exclusively on our Nd:glass laser system, include equation-of-state studies, materials strength experiments, multiburst simulations, and opacity studies as described below.

Equation-of-State Studies (J. C. Solem and L. Veeser, P-Division)

We used the GEAR Pico V camera to observe shock emergence in plane, one-step, and two-step foils in much the same manner in which we used

previous streak cameras. In general, the performance of the Pico V was superior. The greater dynamic range allowed us to observe detailed structure of shock luminosity that was previously obscured by camera saturation. Specifically, we can now measure 50-ps risetimes by taking densitometer traces of streak records with confidence that the record was always within the semilinear response function of the camera. These observations also cleared up some mysteries about the duration of the bright portion of streak records in previous experiments. The results portend a bright future for detailed shock-structure studies. We hope to undertake these as soon as laser time and instrumentation are available.

Although the GEAR camera had noticably higher sensitivity than previous cameras, we were still unable to observe shock emergence across two steps. This was more the result of limited experimental time than limitations of the camera or laser.

Opacity Studies (N. Hoffman, L. Miller, J. Mack, J-Division)

We have devoted attention to a theoretical study of the limb-darkening technique of measuring relative opacity information. In this technique, one observes the specific intensity I_ν of radiation at frequency ν emerging from an emitting layer, as a function of θ, the angle with respect to the layer normal. The function $I_\nu(\mu)$, where $\mu = \cos\theta$, is called the limb-darkening function. The variation of the radiation source function with optical depth τ_ν at frequency ν is then given by the inverse LaPlace transform of $\mu I_\nu(\mu)$. In LTE the source function equals the Planck function, $B_\nu(\tau_\nu)$, which may then be solved for the temperature $T(\tau_\nu)$. One makes observations at two different frequencies ν_1 and ν_2 to determine $T(\tau_{\nu_1})$ and $T(\tau_{\nu_2})$. Then, from the slope of temperature functions, one determines the opacity ratio

$$\frac{\kappa_{\nu_2}(T)}{\kappa_{\nu_1}(T)} = \left.\frac{dT/d\tau_{\nu_1}}{dT/d\tau_{\nu_2}}\right|_T , \qquad \text{(IV-50)}$$

since $d\tau = \kappa\,\rho\,dx$. The density ρ and differential geometric distance dx cancel out of the division, and leave just the opacity κ. Observations at many frequencies give the shape of the opacity coefficient over that frequency range. For example, the relative height of a photoionization edge may be measured by performing limb-darkening observations in narrow bands on either side of the edge.

We have performed numerical simulations of the limb-darkening experiment. The radiation-hydrodynamics code F[3] was used to simulate a hot, expanding aluminum plasma. The multigroup spectral transport code SNAPD then calculated the emergent specific intensity at various angles. Finally, this limb-darkening function was analyzed as described above, and the original input opacity data were successfully recovered.

We have also done an analytical investigation of the form of the limb-darkening function in the case that $h_\nu \gg kT$ for all T in the emitting layer; this limit is applicable in our present optical observations and will also be true in the x-ray region. An alternative to the usual Eddington-Barbier relation is found, and various conclusions about the temperature structure of the emitting layer can be drawn.

The latest series of laser experiments included attempts to measure time-resolved spectral information using a Hadland Imacon streak camera. Even broadband filters attenuate the target light so much that streak-camera recording is impossible. Thus, we are considering using image intensifiers or television recording systems to enhance our signal. Another possibility is that the limb-darkening experiment can be done using the plasma on the front side of the target, which is much hotter and brighter than the back of the target.

Material Strength Experiments (J. Mack, J. Petrovic, CMB-Division)

Fifteen separate experiments were completed with various target materials (aluminum foils, aluminum oxide, silicon nitride, silicon carbide) to ascertain the feasibility of using high-power lasers to induce strong shocks through these materials, and thereby cause material changes, which can be investigated after the fact.

We have enough information to state that this technique does produce the desired magnitudes of material alterations (through laser shocks) necessary for detailed studies of the mechanical and

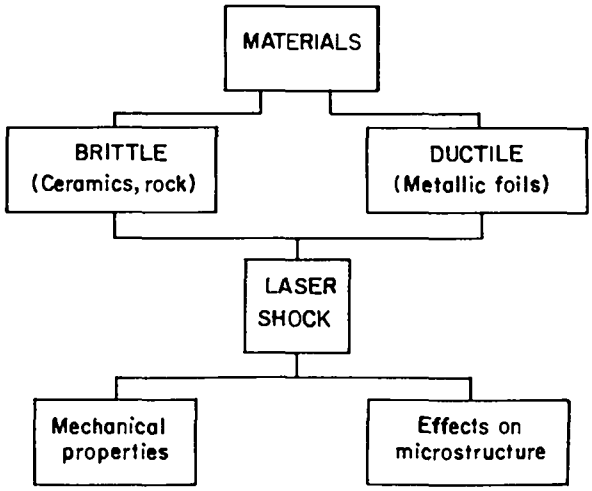

Fig. IV-75.
Laser-shock materials experiment.

microstructural effects on materials of interest. Figure IV-75 summarizes in a broad manner the program we would like to establish. A more comprehensive report on these experiments is presently being prepared.

Simulation of Blast and Shock-Wave Phenomena (A. G. Engelhardt, R. Robertson, and I. V. Johnson, L-Division)

The Two-Beam glass laser facility has been used extensively for military applications experiments. Approximately 80% of the target shots were useful, on-target shots, with a typical on-target energy of 20 J/beam. Some shots, however, produced energies of 40 to 50 J, which caused considerable damage to the rods of the final 51-mm Line-B and -C amplifiers and to some preceding mirrors. The damaged components are being replaced.

Several beam splitters did not conform to the specified reflection-to-transmission ratios. The mirrors had been checked interferometrically to ensure they meet the wave-front distortion specification. Future purchases will be monitored more strictly.

The new CAMAC unit for the NOVA control computer has been received, so that we will be able to record calorimeter energy readings on two separate, independent computer systems. The new CAMAC unit allows readings to be taken by the Wang 600 computer, by the Nova, or by both, and eliminates equipment malfunctions occasionally caused by Wang misreadings triggered by spurious noise.

Multiburst Simulation, Blast-Wave Interactions (G. E. Barasch, S. N. Stone, M. D. Wilke, J-Division)

Our optical diagnoses of laser-driven simulations of the nuclear multiburst environment have shown shock-wave phenomenology closely matching that of full-scale, atmospheric nuclear explosions. Holographic interferometry using a pulsed ruby laser was successfully added to the shadowgraph and high-speed framing photograph of the disturbed air surrounding laser-induced microfireballs. This diagnostic technique records in great detail the refractive-index changes in the test volume. These records are amenable to quantitative analysis for air density distributions over the outer blast-wave region. At moderate and late times high-electron densities with accompanying large refractive-index changes are limited to the smaller central volume. The later addition of a frequency doubling crystal to the ruby laser system will provide two-wavelength holographic interferometry to permit unfolding both the electron density and gas density profiles over the entire shocked region.

Coordinated records of both the holographic interferometry and time-resolved shadowgraphy were obtained on about 50 laser shots. Various target geometries and air pressures were fired, to include single target-single beam, single target with nearby reflecting plane, two target-two beams, and two target-two beams with reflecting plane. Air pressures were 20, 50, 200, and 580 torr, the last being ambient air at LASL with the microfireballs being air breakdown sparks. In Fig. IV-76 we show a holographic interferogram of a microfireball with reflecting ground plane that simulates to a remarkable degree the shock features of the full-scale, atmospheric nuclear explosion. An interferogram of a multiburst simulation is shown in Fig. IV-77.

Some 1-D RADFLO microfireball calculations have been run to check out the computer code for the small energies (1-40 J), small distances (0.5-5 cm), and short times (1-50 μs) involved in these MAL experiments. It should be noted that the

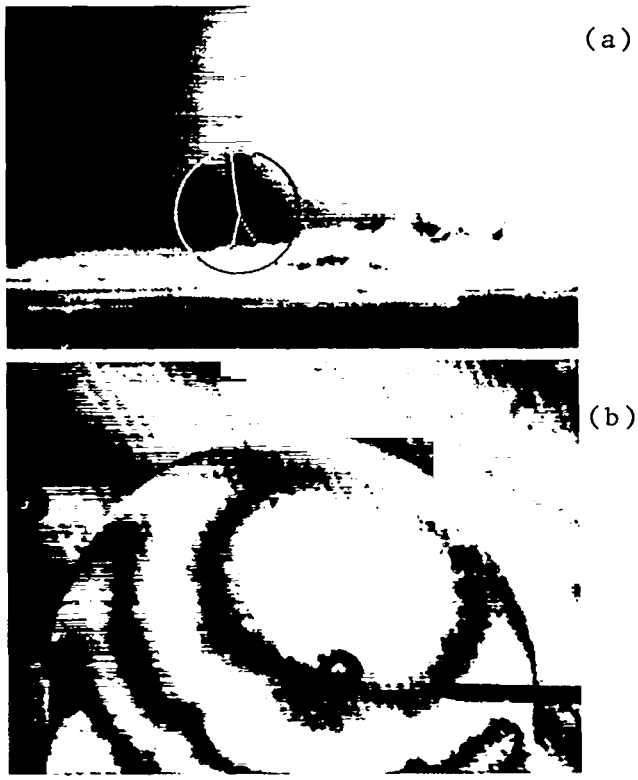

Fig. IV-76.
Full-scale nuclear explosion at Nevada Test Site: Met event of Operation Teapot, 1955, 22 kt on a 122 m tower. Frame recorded 170 ms after detonation. (a)

Laser-induced fireball simulation in 50 torr air pressure 9 mm above ground reflecting plane. Holographic interferogram recorded 17 μs after microfireball initiation by 20-J, 300-ms Nd: glass laser pulse. (b)

energy scaling factor for these microfireballs relative to full nuclear fireballs is of the order of 10^{12}.

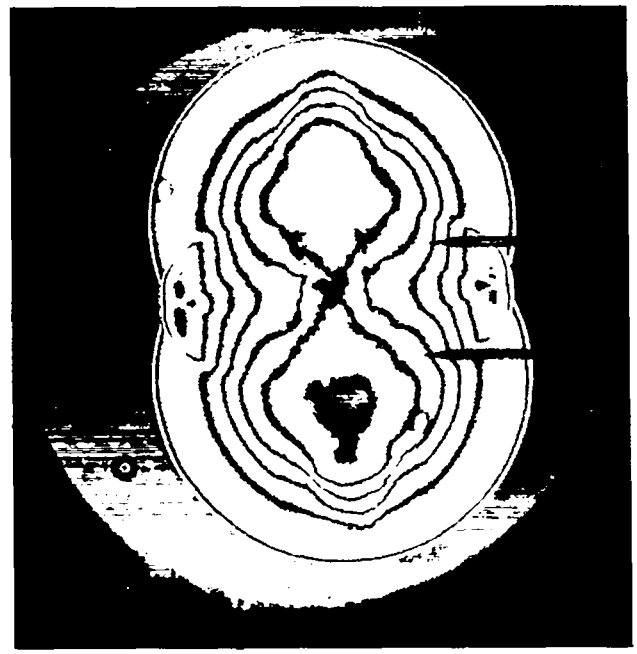

Fig. IV-77.
Multiburst simulation in 200 torr air pressure, with air spark fireballs separated 3 cm. Holographic interferogram recorded 30 μs after initiation of each microfireball by 20-J, 300-ms Nd:glass laser pulse.

REFERENCES

1. R. K. Osborn and F. J. Mayer, Am. J. Phys. **44**, 149 (1976); E. K. Storm, J. T. Larsen, J. H. Nuckolls, and H. G. Ahlstrom, Bull. Am. Phys. Soc. **22**, 1086 (1977).

2. V. Cottles, Bull. Am. Phys. Soc. **22**, 1090 (1977).

3. F. Young and G. H. McCall, Bull. Am. Phys. Soc. **22**, 1129 (1977).

4. S. Glasstone and R. H. Lovberg, "*Controlled Thermonuclear Reactions* (D. Van Nostrand Company, Inc., 1960), p. 20.

5. R. F. Benjamin, P. B. Lyons, and R. H. Day, "X-Ray Calibration of RAR-2490 Film for Application to Laser, Plasma Experiments," Appl. Opt. Vol. 16, No. 2 (February 1977), pp. 293-297.

6. H. Keppel, Naval Research Laboratory, and P. Griem, University of Maryland, personal communication.

7. T. H. Tan, Proceedings from Fourth International Workshop on Laser Interaction and Related Plasma Phenomena, Vol. 4B, 677 (Plenum Publishing Corp. 1977). See also Los Alamos Scientific Laboratory report LA-6510-PR (November 1976), p. 81.

8. E. Stark and F. Skoberne, Los Alamos Scientific Laboratory report LA-6982-PR (April 1978).

9. J. E. Crow, P. L. Auer, and J. E. Allen, J. Plasma Phys. 14, 65 (1975).

10. C. W. Cranfill, "One-Dimensional Computer Simulations of the Implosion of Simple-Shell Targets with the Los Alamos Two-Beam CO_2 Laser, Series I," Los Alamos Scientific Laboratory report, LA-6827-MS (June 1977).

11. V. M. Cottles and D. V. Giovanielli, "The Absorption of 1-NS CO_2 Laser Pulses by Plane Targets," 3rd Int. Congress on Waves and Instabilities in Plasmas, Palaiseau, France, June 27-July 1, 1977.

12. V. M. Cottles, "Measurements of Absorption and Ion Production in Laser Fusion Experiments," American Physical Society Division of Plasma Physics, November 7-11, 1977.

13. C. G. M. van Kessel, J. N. Olsen, P. Sachsenmaier, R. Sigel, K. Eidmann, and R. P. Godwin, "Diffuse Scattering from Laser-Irradiated Plane Targets", 10th European Conference on Laser Interaction with Matter, Ecole Polytechnique, Palaiseau, France, October 18-22, 1976.

14. D. R. Kohler and P. B. Weiss, "Use of Pyroelectric Vidicons for Measurements on CO_2 Laser Systems," Inertial Confinement Fusion Conference, San Diego, California, February 7-9, 1978.

15. J. S. Pearlman and M. K. Matzen, "Angular Dependence of Polarization - Related Laser-Plasma Absorption Processes," Phys. Rev. Lett. **39**, 3, July 1977, Sandia Laboratories.

16. K. R. Manes, V. C. Rupert, J. M. Aerbach, P. Lee, and J. E. Swain, "Polarization and Angular Dependence of 1.06-m Laser-Light Absorption by Planar Plasmas," Phys. Rev. Lett. **281**, Vol. 39, 3, August 1977.

17. R. P. Godwin, R. Sachsenmaier, and R. Sigel, "Angle-Dependent Reflectance of Laser-Produced Plasmas," Phys. Rev. Lett. **1198**, Vol. 39, 3, November 1977.

18. Dale B. Henderson, "Theoretical and Practical Aspects of Laser Fusion," Bull. Am. Phys. Soc. 19 867 (October 1974); G. S. Fraley, W. P. Gula, D. B. Henderson, R. L. McCrory, R. C. Malone, R. J. Mason, and R. L. Morse, "Implosion, Stability, and Burn of Multi-Shell Fusion Pellets," 5th International Conference on Plasma Physics and Controlled Nuclear Fusion Research, Tokyo, Japan, November 11-15,1974, I.A.E.A. Vol. II, 543 (1975).

19. J. Nuckolls, J. Lindl, W. Mead, A. Thiessen, L. Wood, and G. Zimmerman, "Laser-Driven Implosion of Hollow Pellets," Ibid., p. 535.

20. R. C. Kirkpatrick, C. C. Cremer, L. C. Madsen, H. H. Rogers, and R. S. Cooper, "Structured Fusion Target Designs," Nucl. Fusion **15**, 333 (1975).

21. Michael A. Stroscio, "Structured Pellet Design for Laser Fusion: A Numerical Determination of the Optimum Mass Ratio," Los Alamos Scientific Laboratory report LA-6986-MS (October 1977).

22. Charles W. Cranfill, "One-Dimensional Computer Simulations of the Implosion of Simple-Shell Targets with the Los Alamos Two-Beam CO_2 Laser," Los Alamos Scientific Laboratory report LA-6827-MS (June 1977).

23. F. J. Mayer, R. R. Goforth, R. R. Johnson, and T. A. Crispin, "Yield Scaling in Laser-Driven Target Experiments," Bull. Am. Phys. Soc., **20**, 1237 (1975).

24. J. T. Larsen, "Computer Simulation of Laser-Driven Implosion of DT Filled Glass Microshells," Bull. Am. Phys. Soc. **20**, 1267 (1975).

25. G. S. Fraley and R. J. Mason, "Preheat Effects on Microballoon Laser-Fusion Implosions." Phys. Rev. Lett. **35**, 520 (1975).

26. G. A. Zimmerman, "Numerical Simulation of the High Density Approach to Laser-Fusion," Lawrence Livermore Laboratory report UCRL-74811 (1973).

27. G. B. Zimmerman and W. L. Kruer, "Numerical Simulation of Laser-Initiated Fusion," Comments in Plasma Phys. Controlled Nucl. Fusion Res. **2**, 51, (1975).

28. D. W. Forslund, J. M. Kindel, and K. Lee, "Theory of Hot-Electron Spectra at Higher Laser Intensities," Phys. Rev. Lett. **39**, 284 (1977).

29. R. J. Mason, "Performance of Structured Laser Fusion Pellets," Los Alamos Scientific Laboratory report LA-5898-MS (February 1975); Nucl. Fusion **15**, 1031 (1975).

30. V. M. Cottles, "Measurements of Absorption and Ion Production in Laser Fusion," Bull. Am. Phys. Soc., **22**, 1090 (1977).

31. V. M. Cottles, Los Alamos Scientific Laboratory, personal communication, 1977.

32. F. Young and G. H. McCall, Bull. Am. Phys. Soc. **22**, 1129 (1977).

33. R. Decoste and B. H. Ripin, Phys. Rev. Lett. **40**, 34 (1978).

34. G. L. Payne, J. E. Perez, T. E. Sharp, and B. A. Watson, "Recombination Effects in an Expanding Laser Produced Plasma" (submitted to J. Appl. Phys.)

35. D. C. Slater, Appl. Phys. Lett. **31**, 196 (1977).

36. S. J. Gitomer and H. Brysk, "Space Charge Effects in Laser Plasma Particle Diagnostics (submitted to Appl. Phys. Lett.)

37. H. A. Bethe, M. E. Rose, and L. P. Smith, Proceedings of the American Philosophical Society, Vol. 78, **4**, pp. 573-585, 1938.

38. B. Bezzerides, D. W. Forslund, and E. L. Lindman, "The Existence of Rarefaction Shocks in a Laser-Plasma Corona", to be published in Phys. Fluids, 1978.

39. Y. B. Zel'dovich and Y. P. Raizer, *Physics of Shock Waves and High Temperature Hydrodynamics Phenomena*, (Academic Press, 1966).

V. LASER FUSION TARGET FABRICATION

Our pellet fabrication effort, supported by extensive theoretical investigations, supplies the thermonuclear fuel packaged in a form suitable for laser-driven compressional heating experiments. These targets range from simple deuterated-tritiated plastic films to frozen DT pellets to complex DT-gas-filled hollow microballoons, mounted on ultrathin supports and coated with various metals and/or plastics. Numerous quality-control and nondestructive testing techniques for characterizing the finished pellets are being developed.

INTRODUCTION (R. J. Fries, E. H. Farnum)

In our target fabrication effort, we are developing techniques and methods to fabricate spherical targets containing DT fuel in a variety of chemical and physical forms. High-pressure DT gas has been used extensively as the fuel because it can be conveniently packaged in glass or metal microballoons for use as laser fusion targets. However, the designers and experimentalists would prefer a higher density of DT fuel than can be obtained conveniently in gaseous form. In addition, significantly better yields are predicted if the fuel can be formed as a high-density shell surrounding either a vacuum or a low-pressure spherical core because it is then unnecessary to work against the high pressure of the inner fuel core during the compression of the spherical fuel shell. These considerations have led to our development of methods to condense layers of cryogenic DT, either liquid or solid, on the inside surfaces of microballoons. In addition, we are developing techniques to prepare room-temperature solids containing fuel atoms at high density (e.g. polyethylene, lithium hydride, and ammonia borane, in each of which the hydrogen has been replaced by an equiatomic mixture of deuterium and tritium) and to form these into microspheres and/or microballoons. The non-fuel atoms in these room-temperature solids (carbon, lithium, nitrogen, and boron) must also be compressed and heated to fusion conditions along with the deuterium and the tritium, but, because they do not participate in the fusion reaction, they act as diluents of the fuel. As a result, targets fueled with these room-temperature solids are not expected to perform as well as those with cryogenic DT fuel shells. However, the fuels that are solid at room temperature are considerably easier to work with, both in target fabrication and in laser target interaction experiments; they also enlarge the parameter space available for exploration in our interaction experiments.

Along with the development of techniques to fabricate the fuel pellets, we also are developing methods to apply a wide variety of coatings to the fuel pellet and to support the pellets for irradiation by the laser beam using thin plastic films or glass fibers so as to introduce a minimum of extraneous material into the system. Finally, we are continuously developing techniques to select, characterize, and measure the various pieces of the target both before and after assembly.

TARGET ASSEMBLY, ALIGNMENT, AND POSTSHOT ANALYSIS

General

Our primary assignment in target fabrication is the assembly, delivery, and postshot analysis of targets for our three operating laser systems. We therefore devote whatever fraction of our effort is required to meet delivery requests from experimenters on these systems. In addition, we try to maintain a large and very flexible inventory of materials and techniques so that we can respond rapidly to changes in target design or specifications. As part of target assembly, we also mount and align the targets on the appropriate target-changing

mechanism before their insertion into the target chamber to eliminate the need for any further position adjustment in the target chamber. If desired, we photograph and analyze any remnants to supplement target diagnostics.

Assembly Technique Improvement

General. We have added assembly capabilities that permit us to produce new types of targets as well as to improve the quality of those built to existing designs.

Hole Drilling (J. Feuerherd). We must often drill pinholes of exact size for diagnostic devices. Although some pinholes were made with our ruby laser, their size and edge quality were difficult to control. As a result, we acquired a Najet microdrill which, with the aid of a microscope, can produce holes as small as 5 μm in diameter. This machine is in routine use for fabricating parts for both targets and diagnostic devices.

Lead-Cone Targets (B. Cranfill, J. Feuerherd, M. Campbell). The difficult lead-cone target design[1] was finally successfully fabricated and tested in October 1977. This target (a 60° DT-filled cone in lead, covered with a plastic film ablator/pusher) appeared deceptively simple. However, we soon realized that the high permeability of all plastic films to DT would inconveniently shorten fuel-gas retention lifetimes of the target. In addition, the plastic with the lowest DT permeability we could use, polyvinyl alcohol (PVA), could not be glued to lead. Our solution avoided, rather than solved, both problems. As shown in Fig. V-1, we put the target into a clamp assembly; glue was eliminated by sealing the PVA film with a clamp and O-ring seal and the fuel-gas-retention half-life was improved by adding a fill tube as a buffer volume. With the increased amount of gas trapped in the fill tube and in part of the O-ring groove, the calculated half-life for fuel-gas retention was several days.

Several of these targets were filled to 2 atm with DT gas and were shot within 6 h of filling. However, because our x-ray counting method for nondestructive gas assay showed very little activity from any of the targets, we were unable to verify their fuel content although some targets produced neutrons. We are checking the outgassing half-life of some dummy targets with a mass spectrometer and are redesigning our photon-counting system.[2]

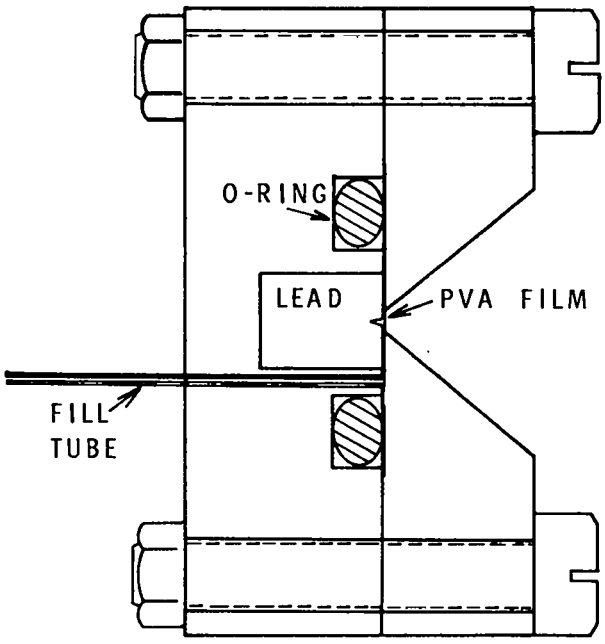

Fig. V-1.
Lead-cone target. The basic body is stainless steel, bolts are 0-80 size.

Miscellaneous New Designs. Several new targets required coating techniques not previously attempted. Among these targets were concentric rings of metal films with different atomic number (Z) on a beryllium substrate (called Bulls-eye targets; the rings had to be well aligned, with sharp edges and no overlap of the metal rings); flat targets of elements ranging across the entire periodic table (some were available in foils, others were evaporated onto removable substrates); multilayered flat targets of various materials; and targets coated with LiF and Nextel to reduce target reflectivity.

Postshot Analysis (B. Cranfill)

We mounted a large number of gas-filled GMBs for two low-power laser interaction experiments. In

one set of these experiments we measured the alignment accuracy of our prealignment jig and of the Hartmann mask test, whereas in the other we measured the threshold for laser prepulse damage of glass and metal microballoons. After the experiments we conducted a quantitative photographic analysis of the damaged targets, which verified our alignment accuracy and conclusively showed that GMB damage arises from laser-light absorption and subsequent melting of the glass wall.

MICROBALLOON SEPARATION, MEASUREMENT, CHARACTERIZATION, AND FABRICATION

Introduction

Almost all our DT-filled targets use a microballoon as the central, fuel-filled core. We therefore devote considerable effort to develop methods for separating, measuring, and characterizing glass or metal microballoons. In addition, we are developing techniques to alter the size and/or the quality of existing microballoons, as well as to directly fabricate microballoons.

Separation Techniques

General. Commercially available microballoons, both of glass and metal, are generally of very poor quality, with as few as one in 10^6 possessing the sphericity and wall-thickness uniformity required for laser fusion targets. We have therefore developed elaborate procedures to recover the few high-quality microballoons[3] and are continuously striving to improve these separation and recovery techniques.

Surface Acoustic-Wave Separator (W. Bongianni, Rockwell International; S. Butler). We are evaluating the use of surface acoustic waves (SAWs) in separating microballoons according to their size and geometric perfection. Consideration of the electrostatic forces acting on glass microspheres led to the development of a multiple-contact adhesion model (based on the work of Kunkel)[4] which is in good agreement with the observed adhesion of microspheres and microballoons. We are thus able to predict the amount of charge on a given microballoon, which, in turn, allows us to estimate the ultrasonic force necessary to overcome such adhesion.

Our theoretical analyses led us to the conclusion that surface acoustic waves could overcome the electrostatic adhesion between a particle and a surface, and could be used to move the particle along the surface in a controlled fashion. This possibility has been demonstrated experimentally, using a SAW transducer deposited on a single-crystal bismuth-germanium-oxide ($Bi_{12}GeO_{20}$) substrate. We also found that particles colliding with each other agglomerated and could not be broken apart with SAWs.

To alleviate this agglomeration problem, we have mechanized the one-at-a-time particle feeder described in LA-6982-PR to dispense single microballoons at variable rates. The automatic feeder is highly reliable and, at feed rates of several hundred per hour, has functioned unattended for 12 h with no GMB breakage or decreased reliability.

Density Separation of Nickel Microballoons (S. Butler). We originally investigated the technique of density separation by terminal-velocity differences in 1975, but abandoned the method because of particle interaction problems. When the technique was subsequently used in a qualitative density separation elsewhere,[5] we reevaluated this method, but found it unsatisfactory, as outlined below.

We observed some interesting behavior of metal microballoons (MMBs) rising in an alcohol column. When several MMBs were released simultaneously at the bottom of the column, the spheres interacted through hydrodynamic coupling, and the fastest rising group always arrived at the top of the column in about the same length of time. When the first half of the group arriving at the top was captured and discarded, and the experiment was repeated with the slower spheres, the MMBs arriving at the top first had the same rise velocity as those arriving first in the preceding experiment.

The length of time of an individual MMB, released under a column of liquid, to rise a specified distance is very reproducible (±1%), but the terminal rise velocity is about half that predicted by Stoke's law. In addition, when analyzed according

to Stoke's law ($v/r^2 \propto \rho$, where v is the terminal rise velocity, r is the sphere radius, and ρ is the density computed from the weight and diameter of the MMB) the data show more scatter than is accounted for by uncertainty in the measurements. The cause of this scatter was not investigated, but nonsphericity or surface effects are suspected. We found comparable sensitivity of the terminal rise velocity to particle density and to these nondensity effects. Thus, these facts plus the necessity of using a range of radii due to the screening process, indicate that only gross density separation of MMBs is possible with this technique.

X-ray Microradiography (D. Stupin, R. H. Day, R. L. Whitman, R. P. Kruger)

Both the size and the uniformity of laser target microballoons must be measured with the highest accuracy, i.e., with a resolution at least good enough to meet the required level of uniformity of 1% for sphericity, between 1 and 10% for wall thickness, and between 10 and 100 nm for small-scale surface defects such as dimples and warts. Optical interferometry is very useful for GMBs, but cannot be used for MMBs or for other opaque microballoons. For these specimens we are using micro-x radiography, and are developing a technique that is easy and convenient to use.

We have continued the development of photometrically analyzed microradiography (PAM) and an assessment of the resolution attainable with our TV-vidicon image-analysis system.[6] The microballoon images are formed as contact microradiographs on Kodak HRP plates using as an x-ray source either a monochromatic Henke tube[7] or a low-voltage tungsten bremsstrahlung source.[8] Day et al[9] have shown that monochromatic sources produce radiographs several times more sensitive to wall-thickness variations than those made with bremsstrahlung sources.

In previous experiments, we have established that optical interferometry and PAM are in excellent agreement when used to measure wall thickness and wall-thickness nonuniformities in GMBs. Recent very careful experiments have shown that PAM resolution is equally good with other materials. For example, a Solacel (Ni/Mn/Si-alloy metal microballoon), which showed 10% wall nonuniformity in our radiographic image, was metallographically sectioned in the plane perpendicular to the image and examined with a scanning electron microscope (SEM). The SEM image also indicated 10% nonuniformity. The SEM method was also used to determine the spatial resolution of microradiographs made with a bremsstrahlung x-ray source of platinum-rhodium wire whose diameter was measured on the SEM to be 0.51 ± 0.05 μm.

We have previously discussed a computer program which measures wall-thickness uniformities of microballoons from digitized photometer scans of their radiographs. We have now added a subroutine, which allows determination of small-scale blemishes on the microballoon surface by automated image analysis. The subroutine compares the average optical density of small areas at the same radius and uses test statistics to determine whether the average density of any area is abnormal. In this manner, the subroutine is sensitive to blemishes as small as 3 μm in diameter when the image has been digitized in 1-μm steps.

Microballoon Fabrication and Quality Upgrading (S. Dunn, Bjorksten Research Laboratory, Madison, WI)

We are supporting work at Bjorksten Research Laboratory to develop techniques for levitating and spinning microballoons in a reduced-pressure, elevated-temperature environment. Potential benefits of such capability are improved microballoon surface finish and/or increased strength by a fire-polishing type treatment. Additionally, we might be able to expand the microballoons to larger diameters and thinner walls and, perhaps, improve their wall-thickness uniformity. Finally, by randomly spinning the microballoon about an axis horizontal in space while rapidly changing the position of the heavy spot of the microballoon with respect to the axis of rotation, it might be possible to improve wall-thickness uniformity by means of centrifugal forces. (The required rotational behavior has been observed for ping-pong balls levitated on an air stream, but not for microballoons.)

We have been able to levitate and rotate microballoons in a controlled manner by using a specially machined collimated-hole structure (CHS) made up of 130-μm-i.d. tubes located in a hexagonal close-packed array on 190-μm center-to-center spacing.[10] A dimple machined into the upper surface of the CHS forms a potential-energy well, which will locate a microballoon stably. A single tube, with a separately controllable gas flow, inserted in the CHS bore at the center of the dimple provides the shear forces needed to spin the microballons. With the addition of a heater and an absolute pressure controller to this CHS, we have been able to levitate and melt GMBs simultaneously by heating the levitating gas issuing from the CHS. This heated CHS is enclosed in a hermetically sealed glass housing which permits us to control absolute pressure with a single vacuum valve.

By using this microlevitating furnace, we have been able to heat GMBs to their softening point under reduced pressure and to increase their volume by more than 80%. Measurements of surface quality and uniformity are in progress.

Further investigation of the rotational behavior of levitated GMBs caused by a single controllable air jet in the CHS showed that the axis of rotation changes from vertical to horizontal as rotational speed is increased. Further, by tilting the CHS axis, we can displace the GMB from the jet, thereby also causing changes in rotational speed and axis orientation. For the first time, we have been able to levitate a GMB on the jet alone (the CHS field gas supply was gradually reduced to zero).

Fuel Fill and Permeation Measurements

General. Many of our targets use uncoated, individual microballoons as the primary structure. We are therefore engaged in a continuing study of specific microballoon properties such as strength and permeation rate for various gases at elevated, room, and cryogenic temperatures.

Fuel Filling System (E. H. Farnum). We have built a high-pressure, high-temperature DT gas system for filling laser targets (Fig. V-2). Pressures of up to 600 atm at temperatures up to 673 K may be applied to microballoons with an overall volume of 2 cm^3. If desired, we can mix DT, Ne, and/or D_2 to any desired proportion. The high-pressure system is contained in a glove box, which acts as a secondary container to catch any accidentally released tritium gas. In case of a spill, the tritium is removed from the glove-box atmosphere by a state-of-the-art recovery system that converts the gas to water and absorbs it on molecular sieve for later reclamation. We are now routinely filling GMBs with DT gas in this system.

Fuel-Gas Leakage From GMBs (B. Cranfill, J. Fries). We have continued our measurements of gas loss rates from several types of GMBs (initially filled to pressures of 10 and 100 atm) stored at room temperature (300 K), in a freezer (253 K), or in liquid nitrogen (76K).[10] Gas-retention half-lives calculated from the data at 300 and 253 K are plotted in Fig. V-3. Conclusions to be drawn are:

In contrast to Types-BXX8s and B18As, none of the Type-B40A GMBs exhibited short half-lives at room temperature (minimum observed, $\simeq$ 1 yr).

Freezer storage significantly increases the fuel-retention half-lives of all GMBs studied, even the Type-B40As.

Smaller, thinner-walled Type-B18As and -B40As specimens exhibit higher gas-loss rates than larger, thicker-walled shells from the same batch, but this result may only reflect the effect of thinner walls on permeation rate.

In addition, examination of preliminary data for the GMBs stored at 76 K indicates gas-retention half-lives in excess of three years.

The second conclusion suggests that the variations in gas loss rate for different GMBs within a batch arise because of variations in chemical composition from shell to shell.[10] The order-of-magnitude decrease in loss rate we obtain by cooling the GMBs from 300 to 253 K is comparable to that predicted for fused silica shells (which should have a lower activation energy than our soft-glass GMBs)[11] for which we calculate a fourteen-fold half-life increase if shells are stored at 253 K rather than at room temperature.

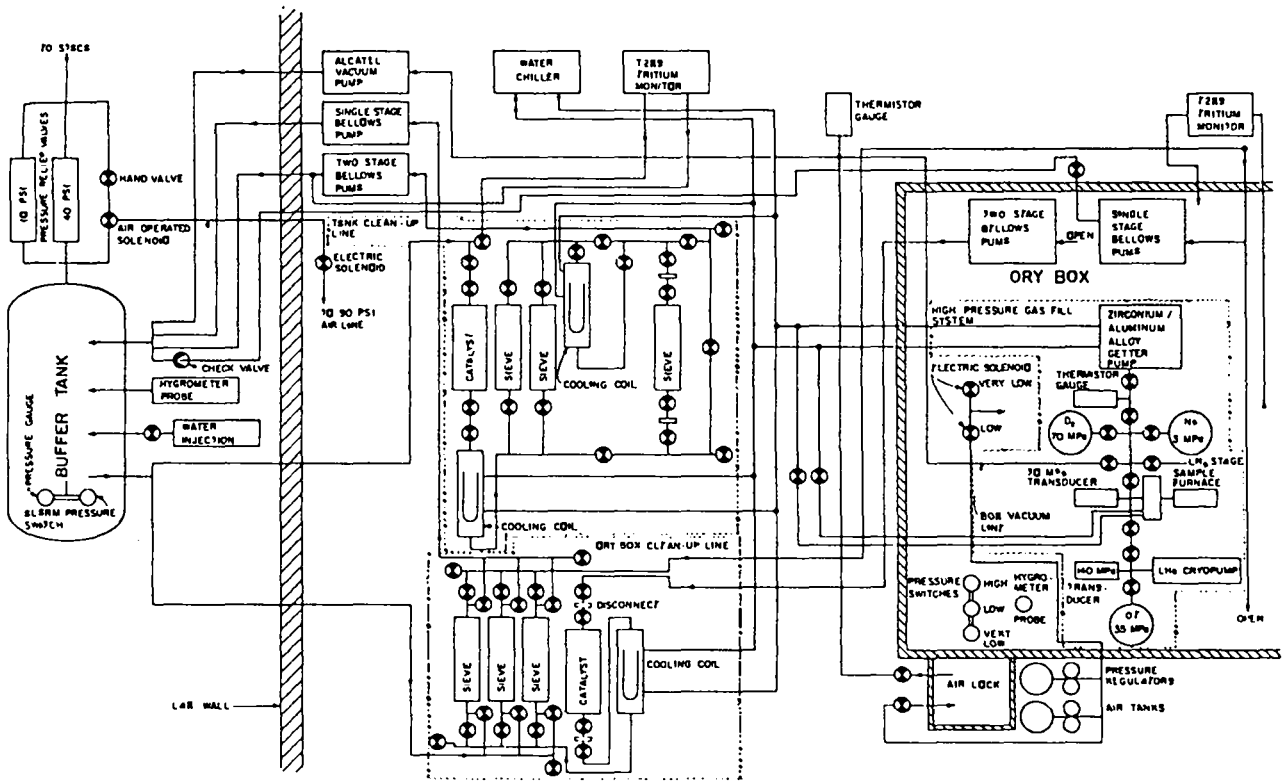

Fig. V-2.
Plumbing diagram of our high-pressure DT fill system showing the high-pressure system, the dry-box secondary container, and the air-scrubbing/T_2-recovery system.

One set of observations appears to be inconsistent with our suggestion that variations in composition are responsible for the variations in gas permeation rate from microballoon to microballoon. We are measuring the wall-gas retention half-life of several GMBs that had been filled with DT gas and then vented so that we could measure only the tritium retained in the walls of the GMBs. In no case did we find half-lives of less than ~1 yr. For 100-μm-diam B18A GMBs, for instance, the wall gas-retention half-lives at 300 K ranged from 350 to 1375 days. In comparison, three out of five similar GMBs had void-gas retention half-lives of less than 100 days. The contrast with the BXX8 GMBs is even more striking, with half-lives for wall gas of 1025 to $\simeq$ 4500 days while that for void gas measured 30 to 110 days. We are considering several mechanisms, which are consistent with all of these observations, and will soon conduct experiments to identify the cause.

In an associated experiment, we vented gas from two shells (originally containing 1 atm of DT gas at 300 K) whose apparent tritium content had stabilized (see Ref. 10, Fig. IV-9). These had been vented through an ~10-μm hole drilled in the shell with a pulsed ruby laser. Count rates taken before and after venting indicate that ~70% of the before-venting counts resulted from tritium dissolved in the glass shells, amounting to ~11% of the total initial count rate for these shells. Comparison of specific activities of tritium dissolved in the walls of these and other long-storage-time GMBs with those from similar GMBs vented immediately after filling suggests that the tritium content of the GMB walls increases with increasing time of exposure to the tritium-containing gas. We are continuing experiments to better quantify our understanding of tritium-GMB interactions, as well as the contribution to the total x-ray count from tritium contained in the glass wall.

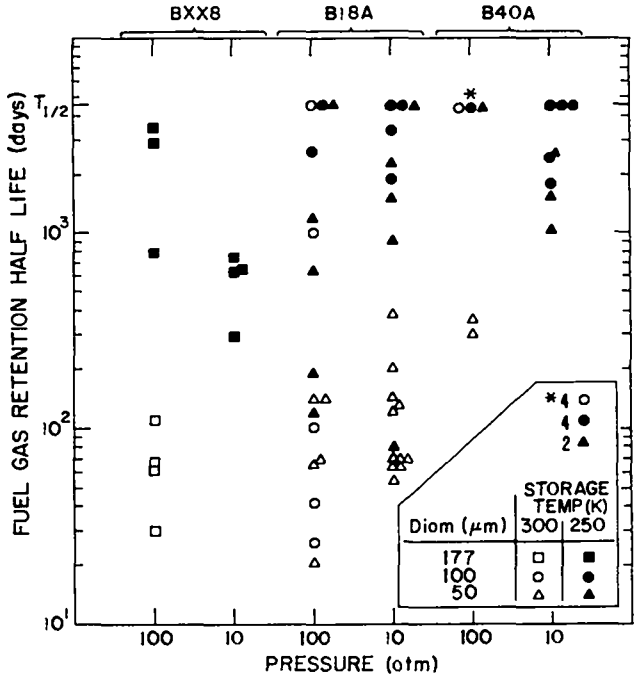

Fig. V-3.
Half-lives for DT outgassing from glass microballoons vs microballoon type at 300 and 250 K. All microballoons were purchased from 3M Co. and types refer to 3M nomenclature.

DEVELOPMENT OF NEW TARGET MATERIALS

Introduction

We are continuing our development of new materials for targets required in high-yield experiments. One class of these materials comprises high-density fusion fuels that are solids at room temperature. They are hydrogen-containing compounds which have been deuterated and tritiated. Although DT density is very high in these compounds, nonfuel atoms dilute the fuel, absorb energy, and degrade target performance. Their convenient physical properties, however, often outweigh these disadvantages. The other class of materials includes those for nonfuel parts of complex targets, which are required to couple the laser to the fusion pellet. For instance, low-density plastic foam acts as a hydrodynamic buffer between concentric multiple pusher shells.

Fusion Fuel Development — Ammonia Borane (H_3NBH_3) (R. Geanangel, U. of Houston)

General. Ammonia borane is a promising fusion fuel because its ratio of fuel to nonfuel atoms is very high and because it is a stable air-compatible solid at room temperature. We have previously synthesized and isolated this substance, and have measured its thermal properties.[12] Recent progress at LASL and at the University of Houston permitted us to fabricate free-standing microballoons of high-purity ammonia borane for the first time.

H_3NBH_3 Synthesis. Ammonia borane is prepared by the reaction of $(NH_4)_2\ CO_3$ and $NaBH_4$ in carefully purified tetrahydrofuran.[12] The crude H_3NBH_3 generally has a melting point around 378 to 385 K. Several purification methods have been used, but the most troublefree is purification with a simple zone sublimer (Fig. V-4). A vacuum of at least 10^{-3} torr must be used for best results.

The product obtained from the zone sublimer has a melting-temperature range of 387 to 389 K after one run. Physically, the substance shows a low level of crystallinity and appears almost waxy. This condition seems best for microballoon production.

H_3NBH_3 Microballoon Formation. Because H_3NBH_3 begins to decompose slowly[13] at 343 K, the task of heating H_3NBH_3 to its melting point without significant decomposition is of paramount importance. The first step in preparing microspheres is to determine the melting point of the H_3NBH_3 to be used, so as to establish the most favorable temperature range for microsphere formation. Temperatures exceeding the melting point by as little as 5 K can cause major decomposition of the H_3NBH_3.

Removal of the microballoons from the dodecane after the fabrication was difficult. Methods that work with glass microballoons are not effective for the immersed H_3NBH_3 microballoons. However, the use of vacuum chucks (microcapillary probes evacuated to a moderate vacuum) finally allowed us to remove microballoons from the dodecane at a rate of about one per minute.

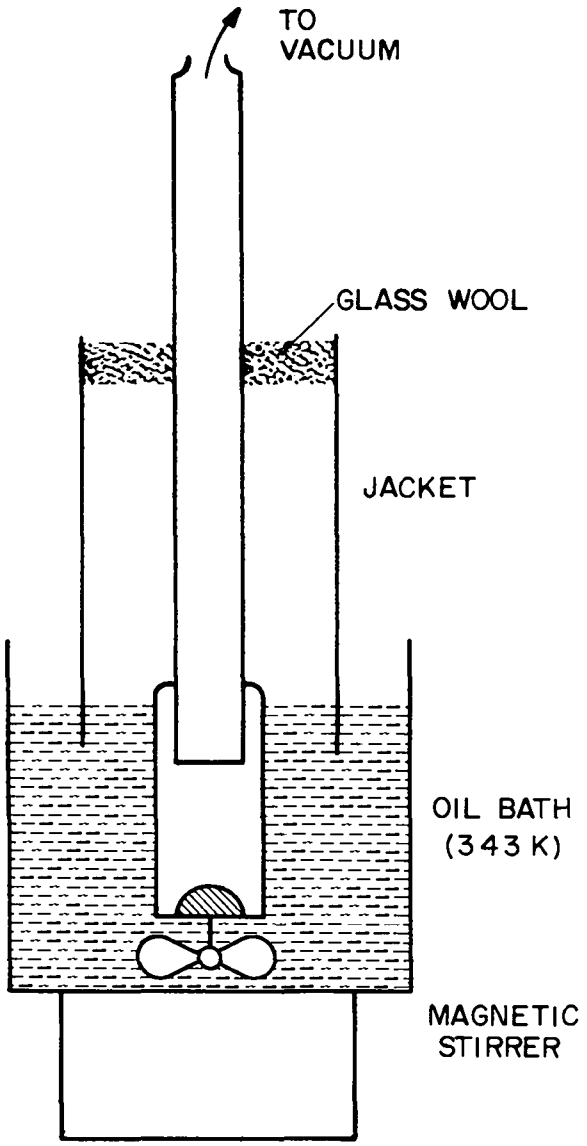

ZONE SUBLIMER FOR NH_3 B H_3

Fig. V-4.
Zone subliming apparatus used to purify H_3NBH_3.

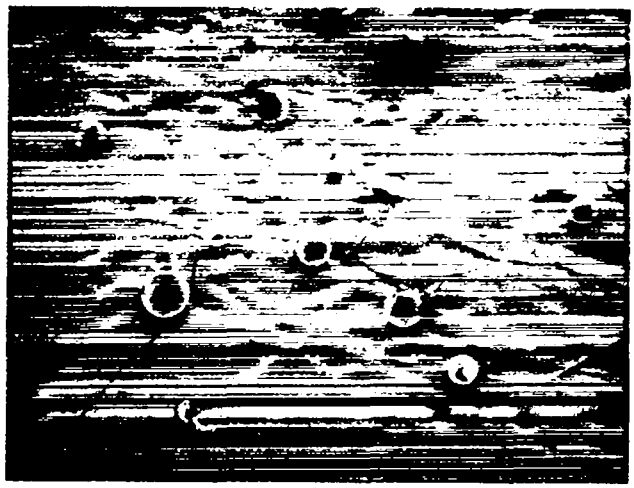

Fig. V-5.
SEM at 20 X of several microballoons of H_3NBH_3 formed by heating the material in dodecane under H_2 pressure.

Fig. V-6.
SEM of shard edge of an H_3NBH_3 microballoon at 972 X showing uniformity of wall thickness.

SEM Examination. Scanning-electron microscope (SEM) images of representative ammonia borane microballoons and of their fragments are shown(Figs. V-5 through V-7). A closeup of a fragments edge (Fig. V-6) shows a wall thickness ranging from ~2.2 to 4.4 μm. In addition, a few small pores are evident in the cross section. None of the microballoons observed thus far gave evidence of large pores or blisters although numerous small irregularities were seen.

Fig. V-7.
SEM of H_3NBH_3 microballoon at 208 X showing several features of interest.

Figure V-7 shows a microballoon with several features of interest. First, a sharp-edged hole is seen in the lower left quadrant, which we believe to be a fracture caused by handling. In contrast, the elliptical hole seen in the upper right is quite different, which may indicate that it was formed during cooling and formation of the spherical shell. Such a hole could be due to H_3NBH_3 shrinkage during solidification, but this phenomenon is still largely unknown. At least one small dimple is evident on the surface of the balloon (upper left quadrant), but more observations will be needed to determine whether dimples are common surface features of these microballoons. Finally, the surface of this microballoon is wrinkled, which, however, does not detract significantly from its overall sphericity and did not appear consistently on other specimens. Wrinkling may also be associated with solidification.

The average size of the microballoons in this sample was 205 μm, with an observed range of ~160 to 300 μm. The observed range of wall thicknesses was ~2.2 to 7.0 μm. Additional samples are being prepared for SEM investigation to determine whether the characteristics and parameters herein reported are representative.

Proposed Mechanism of Microballoon Formation. The microballoons were formed by heating highly purified ammonia borane to slightly above its melting point in a rapidly stirred dodecane suspension under 600 psi hydrogen pressure. Our previous investigation[13] has shown that ammonia borane decomposes slowly, but measurably, under these conditions. This decomposition seems to prevent small particles of H_3NBH_3 from melting and forming microdroplets in the stirred suspension. Cooling such a suspension would yield solid microspheres, a few of which have been observed.

However, during slow decomposition, the hydrogen released may form bubbles in the ammonia borane droplets, and should equalize with surface tension forces to form a symmetrical bubble. If the suspension is then rapidly cooled so that the H_3NBH_3 solidifies before it can crystallize effectively, the microbubbles could form microballoons.

Only a small portion of the sample is converted into microballoons, but careful investigation of the conditions should permit optimization of the yield. At present we can produce microballoons whenever desired, but the yield varies widely, from a few to hundreds per run. We expect to improve our control by optimizing the temperature profiles, hydrogen overpressure, and stirring rates during the melting cycle.

Plastic-Foam Development (J. L. Schwendeman, Monsanto Research Corp.)

General. Several advanced laser fusion target designs require ~250-μm-thick spherical shells of low-density foam (0.05 to 0.3 g/cm^3) with very small cells (1 to 2 μm). Ideally, the foams should consist of carbon and hydrogen. However, to increase the chances for producing the desired foams, we are using polymers containing nitrogen and/or oxygen atoms. This broadens the choice of polymers greatly. Heavy metals and other elements with atomic numbers higher than 20 are considered undesirable. Because the foams should have a uniform structure throughout, cell size and density should not vary greatly.

Several systems have shown promise of being capable of producing the desired foams, but they need further development to optimize their properties and methods of preparation. Techniques for applying these foams to small target spheres are under

investigation. The most promising approaches involve a continuous film or casting, which contains a component that can be subsequently removed by drainage, extraction with a solvent, or evaporation leaving vacant sites in the structure. Examples of such approaches are the removal of water from water-extended polyester resins (WEP resins), the removal of volatile components from aqueous gelatin/toluene emulsions, coagulation of cellulose-acetate solution as developed by Rinde and Stone,[14] and leaching out of a solid filler in a polyurethane casting.

Water-Extended Polyester Resins (WEP). Foams with open cells of ~2 μm were prepared from WEP resin* with water loadings up to 80%.

Foams with such small cells are formed simply by adding water containing 0.75% hydrogen peroxide (H_2O_2) to cobalt octoate-promoted WEP resin. Proper agitation and water addition rates are critical in obtaining an emulsion that is not inverted and does not contain large air bubbles.

The best foam from water extended polyester was obtained by emulsifying 32% WEP resin with 68% H_2O containing H_2O_2 and using a laboratory disperser. After vacuum-drying, this foam (Fig. V-8) had a density of 0.34 g/cm^3 and cell sizes ranging from 0.2 to 3 μm.

*A product of Ashland Chemical Company.

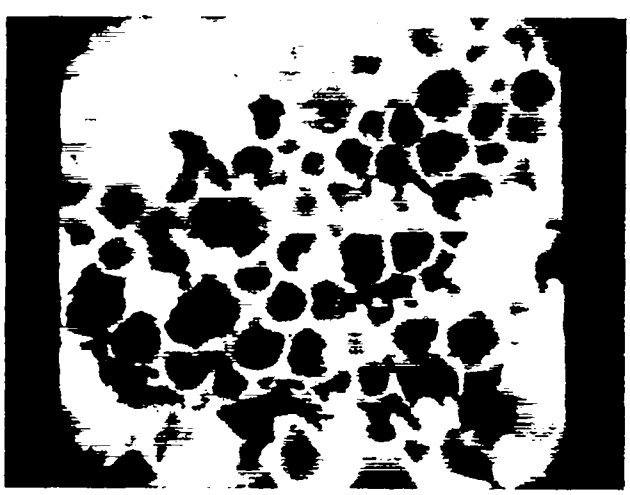

Fig. V-8.
SEM of water-extended polyester foam (best sample) at 3600 X. Density, 0.34 g/cm^3; cell size, 0.2-3 μm.

Work on lowering the density is continuing, e.g., by increasing the water content of the mixture, completely removing the water, and finding volatile organic extenders that do not cause structure collapse.

Foams Made From Aqueous Gelatin/Toluene Emulsions. This approach is based on a simple aqueous gelatin/toluene emulsion in which the toluene is the discontinuous phase and furnishes the sites for the open cells in the foam. It is an attractive approach because fairly concentrated (5 to 20%) solutions of high-molecular-weight gelatins have relatively low viscosities at moderately elevated temperatures, and because gelatin solutions go through a sol-to-gel transition at ~300 to 310 K.

Because of their low viscosity, gelatin solutions are easy to work with and easily mixed with other materials. The sol-gel transition (reversible) permits gelatin solutions to be handled as liquids at easily attainable temperatures and allows the production of castings and drawn films. The transition to a gel in the temperature range of ~300 to 310 K (depending on solution concentration and molecular weight) causes the casting or film to set up and to stablize the structures. Gelatin is unique among natural and synthetic polymers: it combines low viscosity with high concentration, it can be handled as a liquid at moderately elevated temperatures, and it gels at a convenient temperature (slightly higher than room temperature) below which it becomes an easily handled solid.

We have produced foams with small cells and low densities of 0.12 to 0.36 g/cm^3. Cell sizes ranged from 1 to 2 μm up to 20 μm. The wide range of cells sizes is probably caused by the equipment used for producing these emulsions (Waring blender vs laboratory disperser), which permits large amounts of air to be whipped into the emulsion. A typical gelatin foam is shown in Fig. V-9.

COATING TECHNIQUE DEVELOPMENT

General

Because nearly all future targets will require layers and shells of metal or plastic, we have continued the development of a wide variety of coating techniques. Metal coatings have been applied by

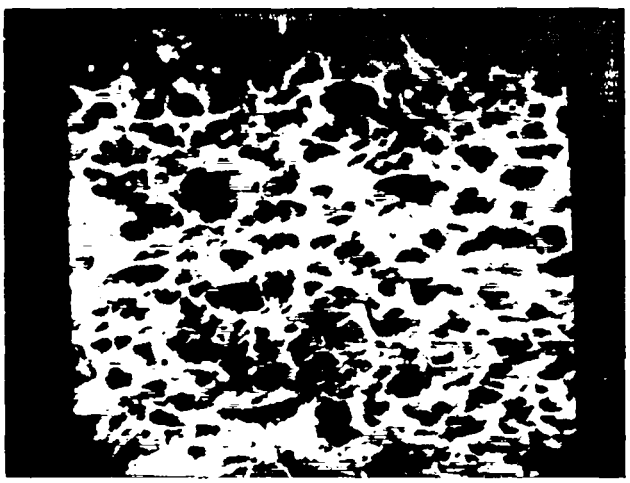

Fig. V-9.
SEM of a gelatin foam of density 0.24 g/cm³. Cell size, 1 to 15 μm; 720 X.

the wet chemical methods of electro and electroless plating, by the thermochemical method of chemical vapor deposition, and by physical vapor deposition from an electron-beam source and by sputtering. In addition, we have improved our plastic coating facility in an attempt to deposit layers of CH plastic to thicknesses of > 10 μm. We have focused our attention on high-quality coatings and on the recovery of a small number (~100) of coated preselected glass or metal microballoons.

Metal Plating (S. Armstrong, A. Mayer)

Electroless Plating Fixture Development. Our attempt to coat a few GMBs (~100 pellets) in the plating fixtures[15] that had been designed for bulk plating of many spheres was not successful. Yields were erratic and low and coating quality was poor. The original electroless plating fixtures were constructed from Lucite plastic. This material was adequate to demonstrate the feasibility of plating microparticles, but the fixtures could not be fabricated to the close tolerances needed to effectively lock and retain a small number of pellets in the reaction chamber of the fixture during plating. We have redesigned the electroless plating apparatus, which should make it possible to reliably plate a small number of parts with a high yield.

The critical components of the new device (Figs. V-10 and V-11) will be constructed from glass or glass ceramic with compatible thermal expansion coefficients. A threaded connection between the plating chamber and the end plates will permit loading the pellets into the reaction cavity just before assembly and will align the cavity with the screen-retaining rings. An enlarged pneumatically operated cylinder-and-piston chamber will enhance solution flow and increase the force to the solution to expel the evolved hydrogen from the plating chamber.

Metallization of Glass Microspheres. We have conducted preliminary experiments on metallizing GMBs in aqueous solutions to serve as conductive or catalytic substrates for subsequent electroless plating or electroplating. In our first attempt we coated the spheres with a thin film of silver by a mirror silvering process. The glass spheres were fully metallized, but a large number of silver particles were clinging to the surface (Fig. V-12). An adequate surface might be obtained if the parts could be withdrawn from the solution before the precipitation of the silver flakes. Further work is required.

We are also investigating the feasibility of metallizing the glass surfaces and rendering the surfaces catalytic by either colloidal or ionic palladium chloride.

Electroplating. We are installing a 20-ℓ gold-plating solution to improve the coating quality and recoverability of microspheres in the electrolytic plating process.

Chemical Vapor Deposition (CVD) (W. McCreary, D. Carroll)

The CVD process involves the chemical or thermal reduction of a metal-containing compound at the surface of a substrate. The method has been useful for coating microsphere substrates in a gas-fluidized-bed coating apparatus, which mixes the substrates well and allows us to apply useful metal coatings to these otherwise difficult-to-handle particles.

We needed a thin, high-Z coating on ~100 preselected GMBs and evaluated the possibility of depositing tungsten from WF_6. Before a protective

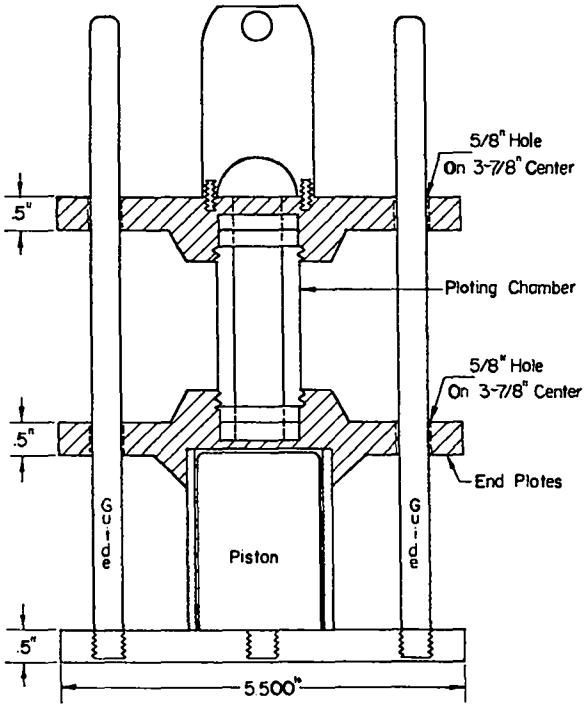

Fig. V-10.
Electroless plating fixture.

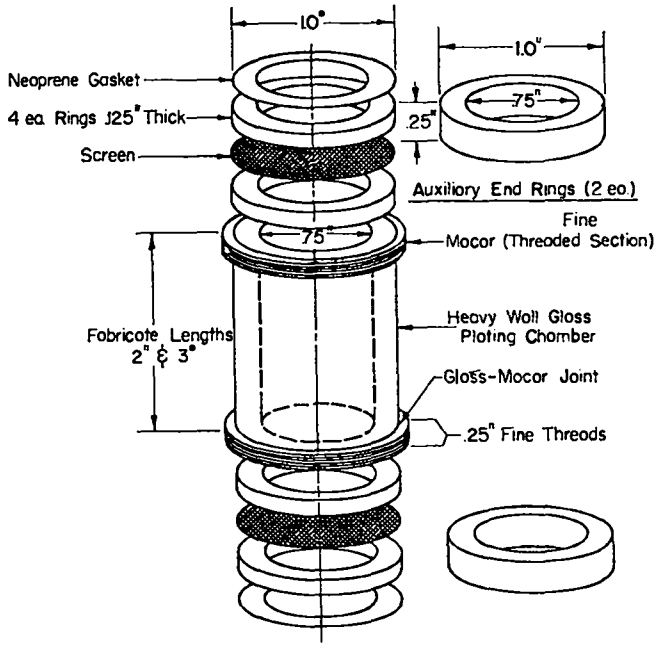

Fig. V-11.
Exploded view of plating chamber for electroless plating fixture. Design should eliminate loss of particles during coating.

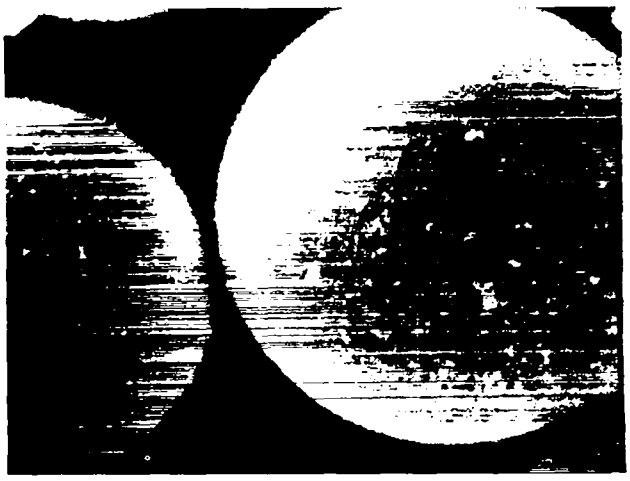

Fig. V-12.
Glass microballoons coated with silver by a mirror silvering process. SEM, 576 X.

tungsten film could be formed, the bare GMBs were eroded to an unacceptable amount by the HF formed from the hydrogen reduction of the WF_6. A 2-μm precoating of Mo_2C prevented this problem.

Work was continued on the development of techniques to coat a small number of preselected mandrels with CVD nickel from $Ni(CO)_4$ while mixed in with a bed of carrier particles that are separated from the desired particles after the run. Although we had previously coated ~200-μm-diam GMBs, our current efforts to coat ~120-μm-diam GMBs have not been very successful. We are evaluating other sizes and materials as carriers.

Sputtering (A. Lowe)

Our development of a sputtering technique to coat microspheres with a uniform layer of metals and/or oxides was continued, further exploring the use of combined electromechanical and plasma agitation of the microsphere substrates. We have previously established that short, alternating coating and cooling cycles enabled us to maintain good bouncing motion of the microspheres during metal deposition and to obtain 1.5-μm-thick aluminum coatings on beryllium-copper microspheres, uniform to at least 0.2 μm (the resolution limit of the measurement technique used).

We suspected that the high substrate temperatures (575 to 675 K) encountered during the diode sputtered deposition softened the nickel and aluminum coatings and made them sticky enough to capture the low-mass microballoons. To decrease substrate temperature, we installed a magnetically confined sputtering system (Fig. V-13), and to increase vibration strength we replaced the shaker table with a variable-frequency electromechanical shaker and an oscillator, which allow continuous sweep of frequency.

For solid metal spheres the best bouncing frequency is 44 Hz. However, because GMBs drift to one side of the shaker table, reduce their motion, and do not coat evenly at a single frequency, we tried sweeping the table frequency between 40 and 45 Hz. As the frequency varies, the microballoons are bounced and rolled back and forth across the table. Although electrostatic attraction continues to be a problem early in the run, GMB motion becomes excellent as soon as a thin metal layer is deposited. Soft metals such as aluminum and gold cause sticking problems for heavy coatings even with a water-cooled shaker table, but high-modulus metals such as molybdenum do not exhibit this problem.

Initial experiments with molybdenum indicate continuous motion throughout the deposition of a 1-μm coating. Although molybdenum can be deposited with either rf or dc sputtering, the lower deposition rate (~20 nm/min) obtainable with rf sputtering resulted in much better adherence of the molybdenum film to the GMB substrate. Metallographic sections of a molybdenum coating on a Be/Cu sphere and on a GMB are shown in Fig. V-14 a and b, respectively. Coating uniformity is better than $\pm 0.2\ \mu$m and adherence is excellent, but surface finish is poor.

Experiments are under way to increase coating thickness and improve surface finish by premetallizing the GMBs and by increasing the surface hardness of the shaker table.

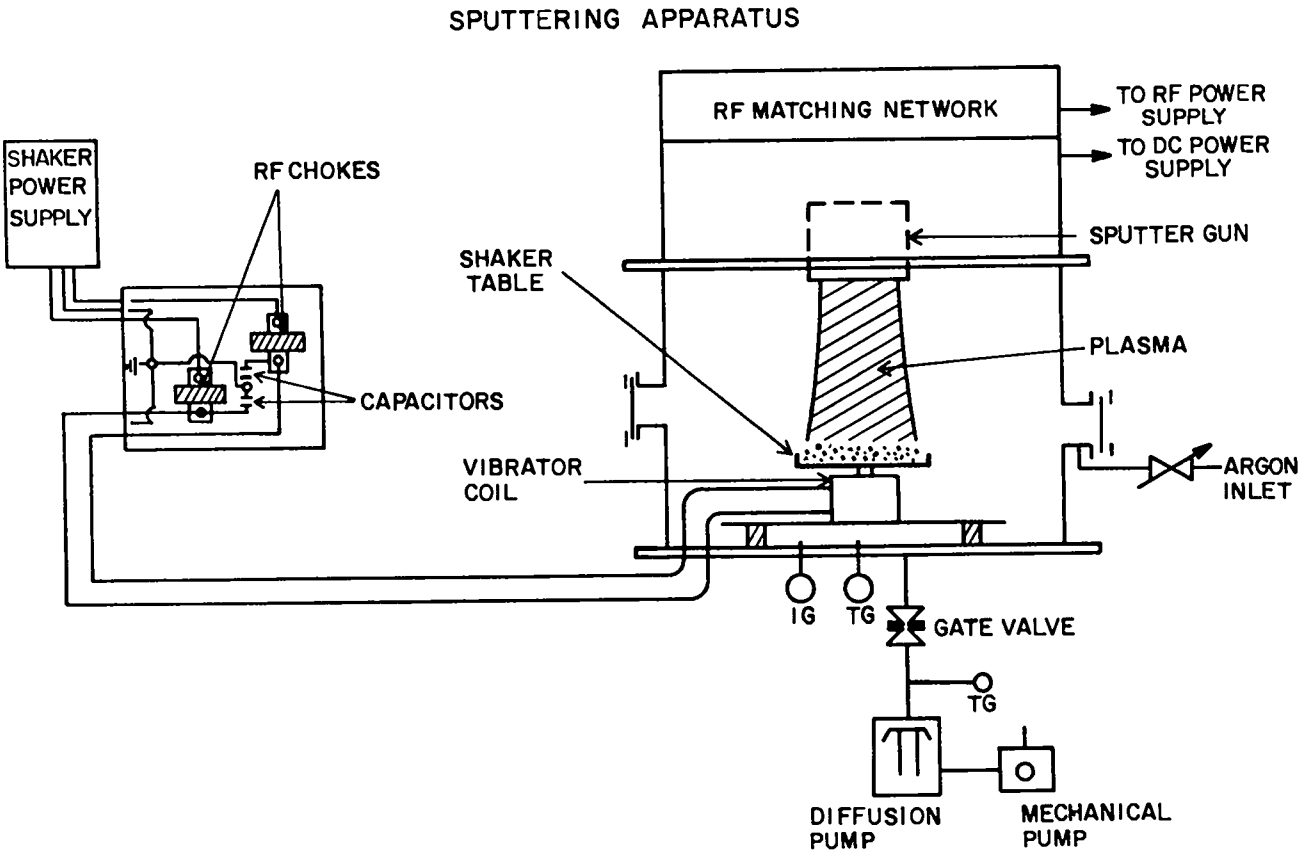

Fig. V-13.
Magnetically confined sputtering system.

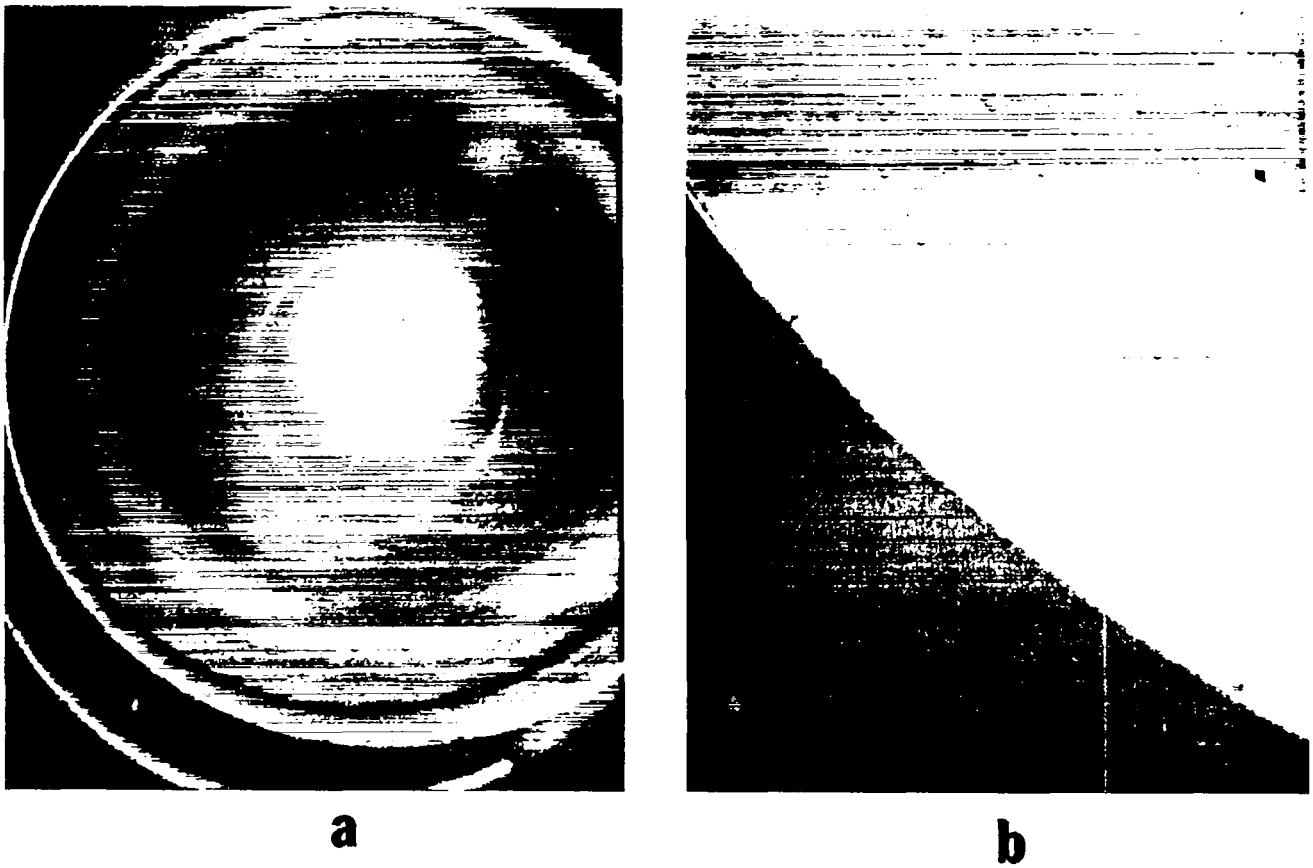

Fig. V-14.
Metallographic sections of spheres coated by sputtering showing good uniformity but poor surface finish. a) Mo-coated GMB (720 X). b) Mo-coated copper sphere (720 X).

Inorganic Films (A. Lowe, C. Hosford)

We are fabricating a wide range of inorganic films, both freestanding and on substrates, for use as targets and in diagnostic devices. A wide variety of metals were deposited on laser targets, as lens coatings, x-ray filters, and scintillator coatings. We acquired the capability of depositing LiF by electron-beam evaporation and applied it to various EBS targets as a means of reducing the reflectivity of targets to 10-μm CO_2 laser light.

Organic Coatings

Many of our multilayered laser-fusion targets use an outer shell of low-density, low-Z material as an absorber/ablator layer. This layer absorbs energy from the incident laser, is heated and vaporized, and streams away from the pusher shell causing the pusher shell to implode via the rocket reaction forces. For designs that do not depend on the strength of this absorber/ablator to contain the fuel-gas pressure, we generally use plastic. We also frequently provide freestanding cylindrical and spherical shells of plastic as targets and for special diagnostic measurements. These latter are generally fabricated by coating appropriate mandrels, which are then dissolved in acid to leave the freestanding plastic shells.

Glow Discharge Polymerization (GDP).

Apparatus Development for Deuterated Films (A. Lowe). We have extended our capabilities and our understanding of the GDP technique that we

use for plastic deposition.[18] We have modified the GDP apparatus in anticipation of using expensive, deuterated p-xylene by valving off the vacuum line and creating a "static" system wherein a small amount of p-xylene vapor is introduced and the bell jar is isolated from the vacuum pump for the duration of the run. Polmerized p-xylene films of good quality have been deposited at a rate of 300 Å/min.

Parameter Studies (A. Lowe). Because the plasma discharge is composed of several vertically stratified regions, each with different characteristics, we suspected that the vibration amplitude (effectively, the bounce height of the target spheres) would affect the coating rate and made a series of runs to determine this effect. Changes in vibration amplitude caused a wide variation in coating rate as shown in Table V-I. Therefore, we have standardized the vibrator settings to reduce variations from run to run.

Parylene Coating (R. Liepins). Parylene is the generic name for members of a polymer series consisting of poly-p-xylylene and its derivatives developed by Union Carbide Corp. Parylene is produced by vapor-phase polymerization of a unique class of monomers, i.e., of di-p-xylylene and its derivatives:

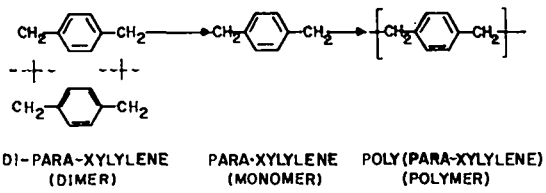

The polymer is a straight chain compound, highly crystalline, insoluble below 423 K, exhibiting superior dielectric strength, low gas permeabilities (similar to epoxies), and good mechanical properties. It can be used at temperatures from 75 to 450 K and has molecular weight approaching 500 000.

TABLE V-I

EFFECT OF VIBRATION APPLICATION ON COATING RATE OF MBLS

Run	Shaker Setting*	Deposition Rate (Å/min)	Type of Motion	Average Location of Spheres
278	58	266	Rolling	In cathode glow region only
276	62	366	Bouncing	Small percentage of time spent in negative glow region (high-current-density glow)
277	70	450	Vigorous Bouncing	Approximately 50% of time spent in negative glow region

*Arbitrary

Several targets designed to achieve high compression with moderate laser power incorporate layers of CH ablator up to 100 μm thick. We have determined that usable coatings of GDP p-xylene as thick as 10 μm can be applied to microsphere substrates, but the brittleness of these films increases with coating thickness and flaking becomes a problem for thicknesses greater than ~10 μm.

Because of this limited thickness range for GDP p-xylene, we evaluated the possibility of obtaining thicker plastic coatings using Parylene. In previous work with Parylene, we encountered serious difficulties in coating GMBs because of interparticle and particle-to-support-plate agglomeration.[17] For our current application, we were able to mount microspheres on support stalks and hold these individual assemblies stationary during the coating process.

Our current Parylene processor is shown in Fig. V-15. With this processor we have coated several sets of GMBs with Parylene. Deposits up to 5 μm thick are uniform to 0.1 μm. We are modifying the apparatus to permit more conservative use of the Parylene monomer and greater coating thicknesses.

Deuterated Polyethylene (B. Cranfill, R. Liepins). We have previously developed methods of making films of deuterated polyethylene from 20 nm to 0.3 mm thick by coating and casting with solutions of polyethylene in heated xylene. In these studies we discovered that the H/D exchange rate between deuterated polyethylene and undeuterated solvent at 400 K considerably reduced the deuterium concentration in the resulting films. Consequently, we obtained deuterated p-xylene to use as the solvent.

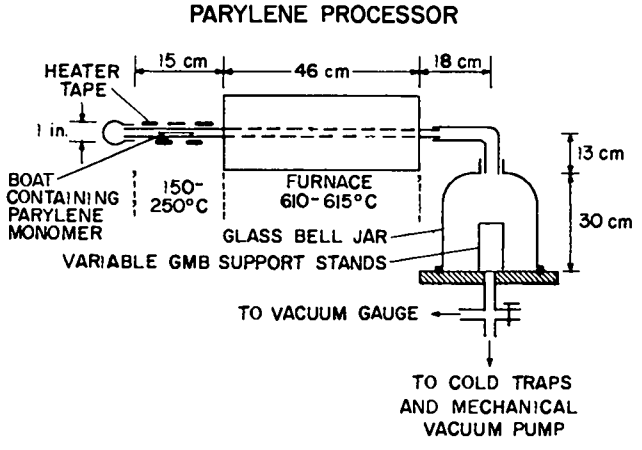

Fig. V-15.
Parylene processor.

Hydrogen concentration in a "perdeuterated" compound may be determined by direct conversion of the compound to H_2, HD, D_2, HD_2, D_3 and by mass-spectrometric determination of the D/H ratio. It can also be determined from density measurements on the water formed in complete combustion of the test compound, by NMR, ion microprobe, or ir techniques. We have chosen the ir technique because of its inherent simplicity.

Analysis of the polyethylene, poly(ethylene-1,2-d_2), and perdeuterated polyethylene ir spectra indicated that three major absorptions could be used for the determination of the H/D ratio in the "perdeuterated" polyethylene. The absorption bands considered are summarized in Table V-II. Of the three pairs of absorptions considered, the 3150-to-4450-cm^{-1} absorption appears best for analysis. The 5000-cm^{-1} region is accessible with a Michelson interferometer with a beam splitter consisting of a layer of germanium evaporated on a salt plate and covered by another salt plate. We are using this method in our work.

Microballoon Strength Measurements (J. V. Milewski)

A new approach is being evaluted for testing the tensile strength of microballoons. The present procedure involves filling a batch of balloons with D_2 gas and then acoustically determining the pressure at which they break as the background pressure is slowly released. The filling, which must be done in stages, is a time-consuming procedure.

The new approach tests balloons individually by potting them, one hemisphere at a time into specially prepared microgrips that are then pulled apart. The breaking load is measured on a microdynamometer and the cross-sectional area of the balloon wall is measured after breaking.

Preliminary tests have proven the feasibility of this method for GMBs, and stronger glues with improved gripping procedures are being developed for metallic microballoons.

TABLE V-II

ABSORPTION BANDS FOR DETERMINATION OF H/D RATIO

Band Type	Band Location in Spectrum (cm^{-1}) Polyethylene	Perdeuterated Polyethylene	Comments
CH_2 Stretching	4150-4450	3100-3320	No interferences.
CH_2 Bending	1462-1473	1072-1081	Possible C-C stretching and C-C-C bending interferences.
CH_2 Rocking	720-730	520-530	Not as sensitive as the other two absorptions.

MANDRELS FOR FREESTANDING METAL MICROBALLOON FABRICATION (S. Butler)

Many advanced targets require thin, high-quality metal pusher shells filled to high pressure. In such cases, the shell must be highly uniform and made of very strong material. Because freestanding MMBs are, except for nickel, not available commercially or, in the case of nickel, of poor quality and require arduous sorting to find a target-quality shell, various targets are fabricated by depositing the metal onto a GMB. However, the glass cannot be removed and forms an undesirable layer on the target. In preliminary work the problem was attacked by fabricating freestanding MMBs by coating a removable mandrel.[16] Thin coatings, which were strong enough for the mandrel to be leached out before being increased in thickness by recoating, were achieved with chemical vapor deposition, but the problem of obtaining high-quality mandrels remained. We have started work on producing suitable mandrels.

Uniform droplets are produced when a jet of liquid breaks up due to a repetitive disturbance and surface tension.[19,20] The size of the drop depends upon the velocity and radius of the jet and on the frequency of the disturbance. We have built an apparatus in which a liquid is forced through a capillary while the capillary is vibrated with a vibration exciter or an earphone. By using several capillary sizes, we formed water droplets with diameters ranging from 250 to 1100 μm. To prevent the falling drops from coalescing, we are charging and deflecting most of them by an electric field while not charging one out of every 8, 16, etc., which is allowed to fall freely. For water drops ~400 μm in diameter the charge induced by 120 V was $\geq 3 \times 10^{-12}$ which is in excellent agreement with the charge predicted by the theory of Schneider et al.[20] Drops this size and with this charge are deflected 0.25 cm when they fall 3.8 cm in a 1×10^{3}-V·cm^{-1} field. The apparatus can deflect much larger drops.

Solid spheres will be made by dropping either a melt that solidifies upon cooling or a solution that solidifies in a heated evaporation column. In initial experiments we will try molten sodium nitrite and solutions containing polymethyl methacrylate. Because the technique produces uniform spheres within a small size range and because metal coatings of uniform thickness and high strength can be deposited on spherical substrates, the freestanding MMBs thus produced should be of sufficiently high quality to obviate the need for sorting.

CRYOGENIC TARGETS

General

Laser fusion targets fueled with cryogenic, liquid or solid, DT offer the advantage of high initial fuel density without the disadvantage of diluent atoms

being present as they are in room-temperature solids having a high-hydrogen density [such as lithium in Li(D,T), carbon in $(\text{-CT})_n$, or boron and nitrogen in NH_3BH_3]. Calculations indicate that the yields from targets fueled with liquid or solid DT can be considerably higher than those from targets of the same design, but fueled with high-pressure DT gas. We are therefore actively pursuing the development of cryogenic targets despite the significant experimental complications encountered in their fabrication and in their use in laser target interaction experiments. We are also designing a cryogenic insertion mechanism for loading and cooling these targets in the EBS target chamber. In a modest program of determining the basic properties, we are measuring the compressibility and thermal expansion coefficient of the cryogenic deuterium-tritium system.

Cryogenic targets receiving greatest attention are uniform, hollow shells of solid or liquid DT condensed onto the inside surface of a glass or metal microballoon that serves as the pusher shell. We are concentrating on GMBs, simultaneously developing the techniques to condense the DT into a uniformly thick layer on the inside surface of the glass and to measure the thickness uniformity of the DT shell. We are also preparing to cycle multishell targets to cryogenic temperatures and study changes in shell concentricity and support-stalk straightness.

Fast Isothermal Freezing (FIF) Technique (J. R. Miller)

The FIF technique[21,22] for producing a uniformly thick layer of solid DT fuel on the inside surface of a GMB fuel core was studied further. A small resistance heater was used instead of the focused cw He:Ne laser. This heater vaporizes the DT in a GMB fuel core that is supported by a thin glass stalk in a copper cell filled with low-pressure helium heat-exchange gas at ~4 K. The FIF technique relies on rapid cooling of the fuel core in an isothermal environment. Because quasi-local resistance heating produces a temperature nonuniformity in the freezing cell, we are investigating the uniformity of the DT fuel layer produced by this type of fuel-core heating.

The FIF cell with this internal resistance heater in place is shown in Fig. V-16. The 1.25-Ω heater surrounding the fuel core is fabricated in two 3.18-mm-

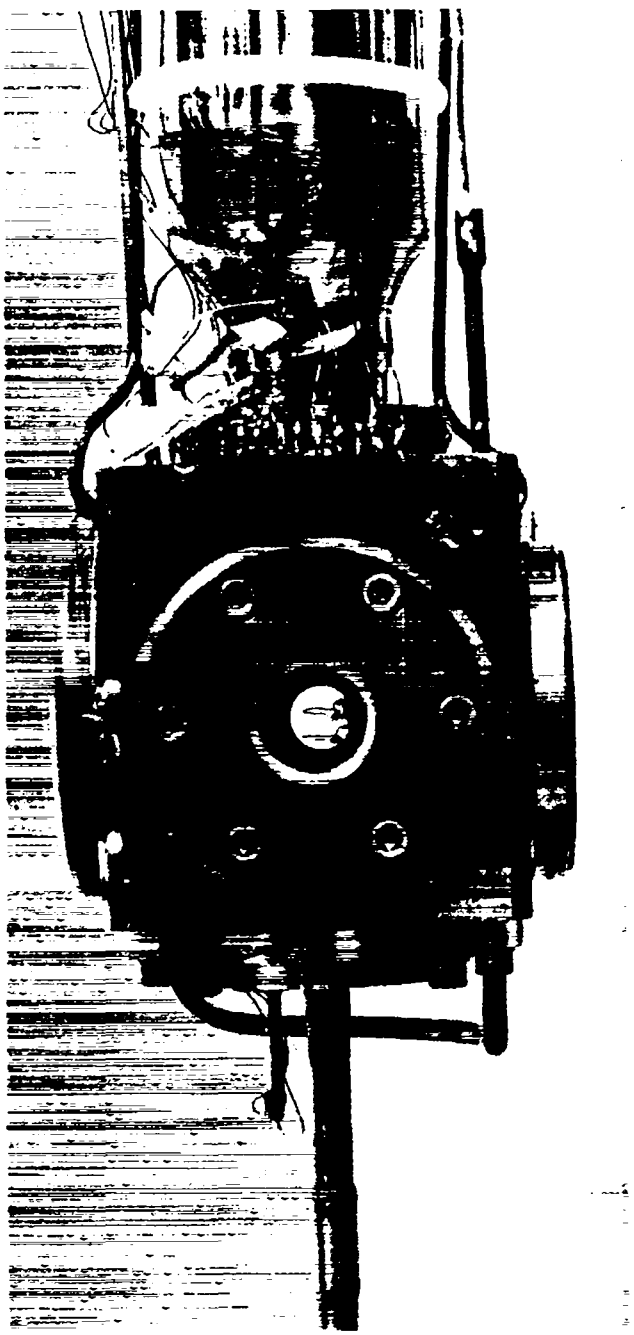

Fig. V-16.
Bottom end of cryogenic dewar with resistance heated FIF apparatus.

diam loops from 0.125-mm-diam wire. (The heater is visible through the cell window in the photograph.) A capacitor is discharged through the heater to vaporize the DT in the fuel core. For a given heat-exchange gas pressure, the energy required to completely vaporize the DT fuel is constant for a time constant of 0.4-8.1 ms. However, because this energy is not coupled directly to the fuel core, > 10 times as much energy is required for complete vaporization of the DT (as when local laser heating is used), causing a measurable cell-temperature increase.

Preliminary results show that quasi-local resistance heating can produce solid DT layers of good uniformity, but the results are far less consistent and reproducible than those obtained with local laser heating. Work in progress includes obtaining interferograms on two axes of the cryogenic fuel cores produced by FIF resistance heating.

Cryogenic-Target Insertion Mechanism

Substantial design progress has been made towards incorporating into the EBS target chamber the FIF technique for producing cryogenic targets. In the proposed design, the existing room-temperature target carrier will be modified to thermally isolate the target support from the micropositioner and to provide a cryogenic vacuum seal to the processing shroud. A single target at 300 K will be loaded on the target carrier, moved into the target chamber by the transport cart, and kinematically positioned. The liquid-helium-cooled processing shroud (Fig. V-17) is moved in from the opposite direction and is sealed against the target support. The sealed enclosure thus formed around the target (Fig. V-18) is then filled with gaseous helium. A pulse from the heating laser vaporizes the DT fuel and the desired cryogenic layer forms. The target can be repositioned with the existing micropositioner.

After the enclosure around the target is evacuated and the cryogenic seal is slowly broken to minimize vibration, the processing shroud is rapidly retracted milliseconds before the target is shot (Fig. V-19). In a 4-K environment, the uniformity of a processed cryogenic target should survive indefinitely. However, the solid DT will melt in a few milliseconds upon exposure to room-temperature radiation. This rapid melting demands the use of a fast-acting mechanism to remove the cryogenic processing shroud and to expose the target to ambient temperature for the shortest possible time before laser irradiation.

An experimental FIF target insertion apparatus is being constructed to test the various components of the proposed EBS. This apparatus will incorporate working components identical to those proposed for the final installation. Data necessary for complete evaluation of the system before its incorporation into the EBS target chamber will be obtained with this experimental apparatus.

Multishell Cryogenic Target Fabrication (B. Cranfill)

Because nearly all high-yield target designs contain both multiple shells and cryogenic DT layers, we are developing fabrication techniques for complex targets that will survive cycling to cryogenic temperature.

The simplest such target, the vacuum insulation target[23] (Fig. V-20), showed considerable distortion when cooled to 4 K. Differential thermal contraction combined with vacuum drying of the plastic shell caused displacement of parts and distortion at the glue joints. We have modified the support structure of this target by replacing the glass crosshairs with a single stalk inserted through a laser-machined hole in the plastic outer shell. This plastic shell is still fabricated as two hemispheres glued together over a GMB, as shown in Fig. V-21. Upon cooling, this target occasionally changed position because the glass support stalk bent, but no internal distortion occurred. We later discovered that thermally annealing the glass stalks prevented this motion.

We are presently investigating the cryogenic cycling behavior of other designs intended for the EBS laser.

Property Measurements of Cryogenic DT (E. Grilly)

We have continued our measurements of the properties of liquid and solid H-D-T systems. The

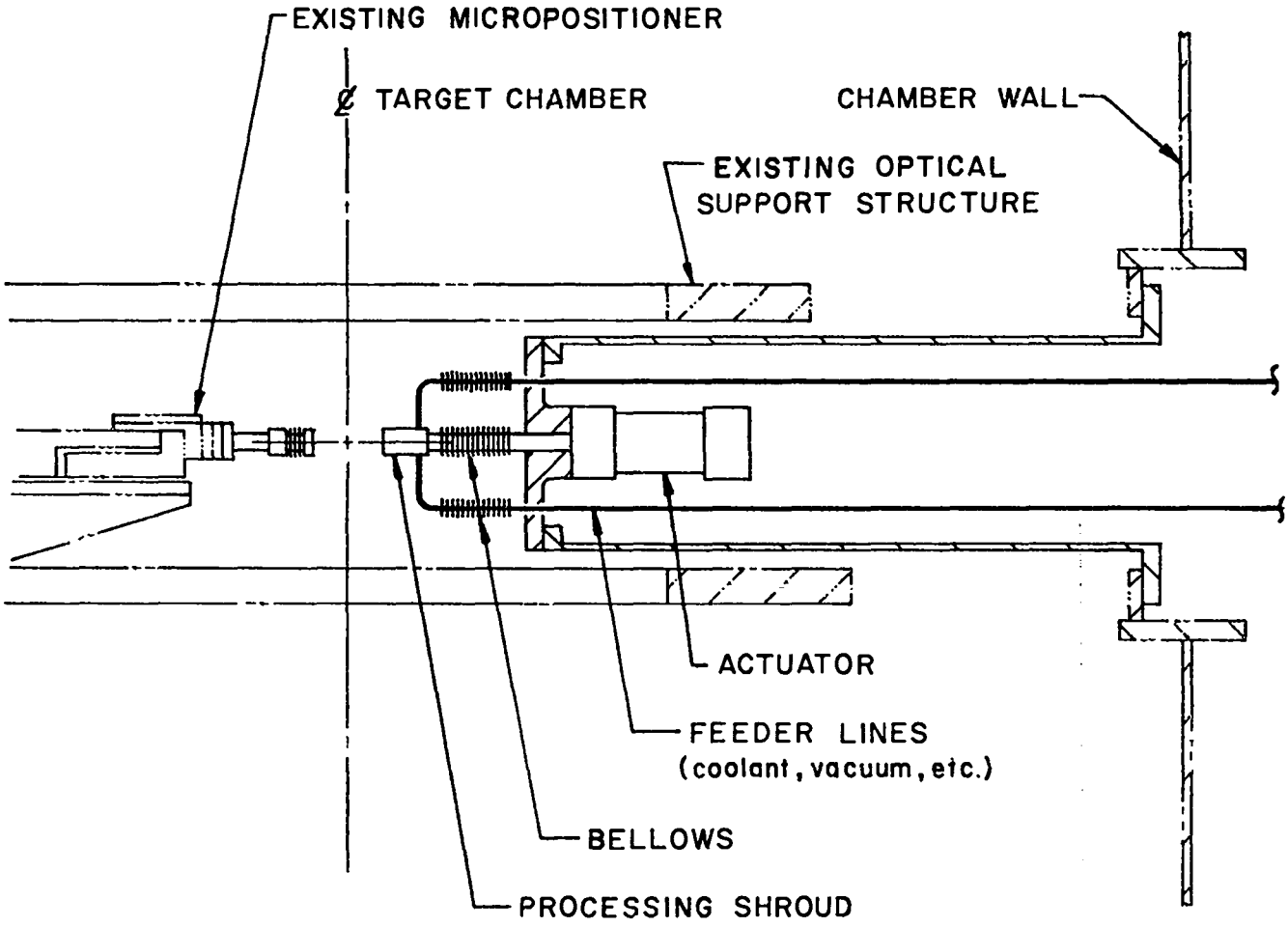

Fig. V-17.
Cryogenic target cooling mechanism for in situ *target cooling. Cooling stage approaching target.*

melting curve and three isothermal compressibility curves reported in LA-6982-PR were replotted by a different experimenter, yielding essentially the same results; this provides confidence in the melting curves, volume changes due to melting, and the properties of the liquids. However, the properties of solid D_2 could not be measured as carefully because the lack of plasticity of the solid restricts the bulk sample from following pressure changes. Solid hydrogen with an ortho-to-para fraction > 0.01 follows these changes more readily, and experiments on such D_2 will therefore continue.

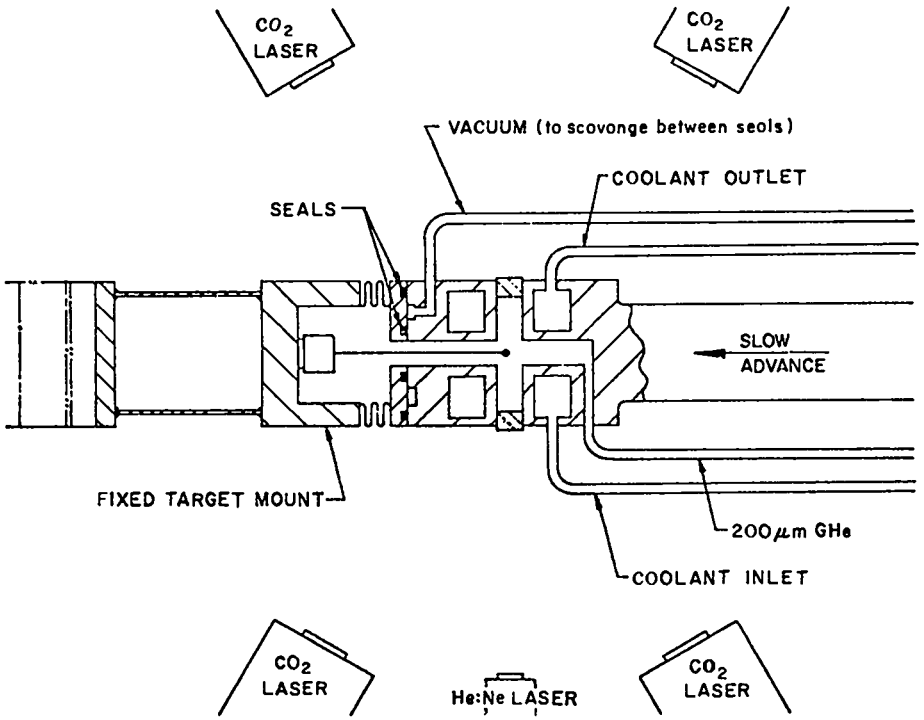

Fig. V-18.
Cryogenic target cooling mechanism in operation.

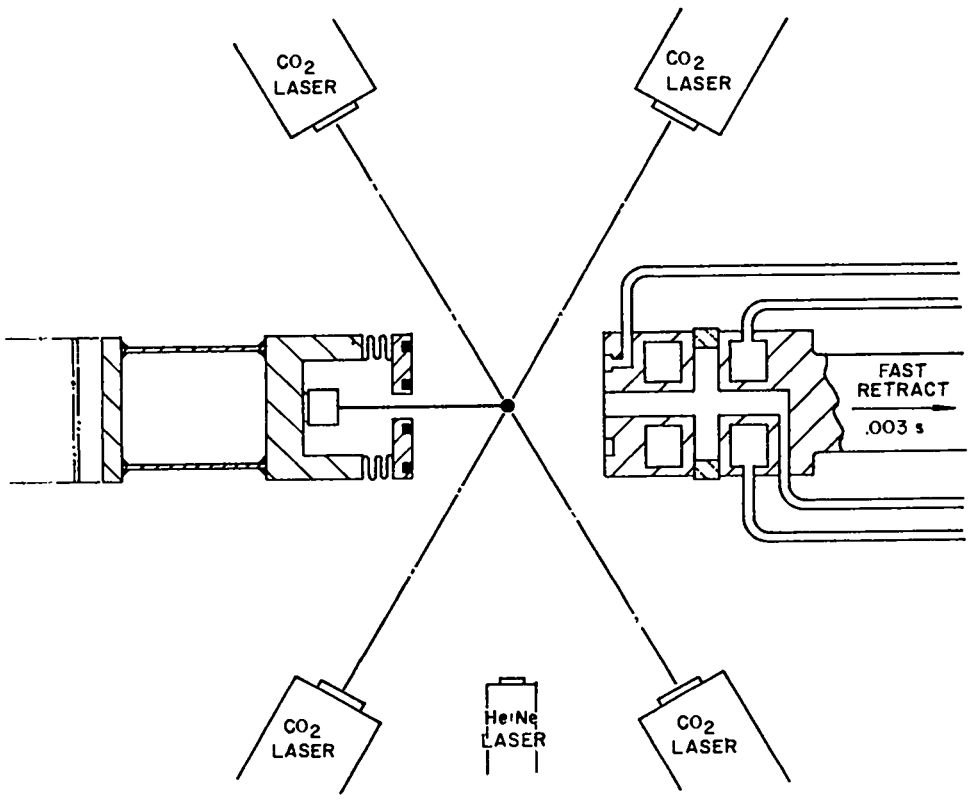

Fig. V-19.
Cryogenic target cooling mechanism retracted for laser shot.

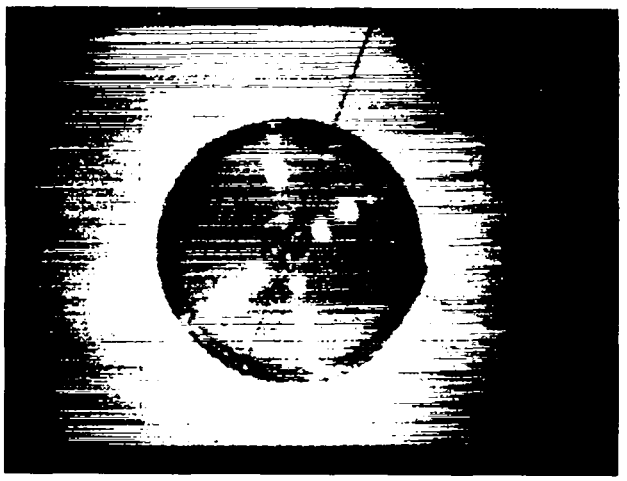

Fig. V-20.
Two-shell vacuum-insulation target mounted on crosshairs.

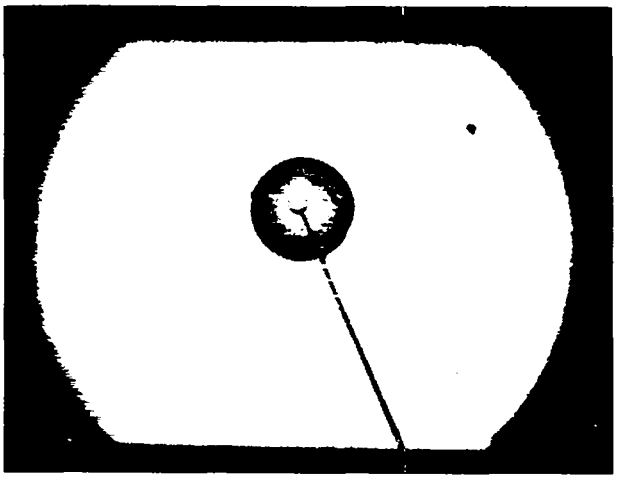

Fig. V-21.
Two-shell vacuum-insulation target mounted in the preferred configuration for cryogenic cooling.

REFERENCES

1. E. Stark and F. Skoberne, Los Alamos Scientific Laboratory report LA-6834-PR (October 1977).

2. V. Cottles, H. R. Maltrud, E. H. Farnum and R. J. Fries, "Nondestructive Assay of Fuel Content in Laser-Fusion Targets by Fluorescent Photon Counting," Paper 10B-10, Post Deadline Section, 18th Annual Meeting of the Plasma Physics Division of the American Physical Society, San Francisco, California, November 15-19, 1976.

3. R. Jay Fries and E. H. Farnum, Los Alamos Scientific Laboratory report LA-5703-SR Rev. (November 1974).

4. W. B. Kunkel, J. Appl. Phys. **21**, 820 (1950).

5. K. H. Turner, SSCD Memorandum No. 412, Chemistry Division, AWRE, Aldermaston, May, 1976.

6. E. Stark and F. Skoberne, Los Alamos Scientific Laboratory report LA-6616-PR (May 1977), Sec. IV.

7. R. H. Day and E. J. T. Burns, Adv. X-Ray Anal. **19**, 597 (1975).

8. M. A. Winkler, Los Alamos Scientific Laboratory internal document (June 1977).

9. R. H. Day, T. L. Elsberry, R. P. Kruger, D. M. Stupin, R. L. Whitman, "X-Ray Microradiography of Laser Fusion Targets," presented at the Eighth International Conference on X-Ray Optics and Microanalysis, Boston, Massachusetts, August 1977.

10. E. Stark and F. Skoberne, Los Alamos Scientific Laboratory report LA-6982-PR (April 1978), Sec. IV.

11. R. T. Tsugawa, I. Moen, P. E. Roberts, and P. C. Souers, J. of Appl. Phys., Vol. 47, No. 5, May 1976.

12. Final Report, Contract E-(40-1)-5176, June 1, 1976-May 31, 1977.

13. First Quarterly Report (ORO-5176-5) Contract E-(40-1)-5176, June 1, 1977-August 31, 1977.

14. J. A. Rinde and R. S. Stone, UCRL report 51708, January 9, 1975.

15. A. Mayer and D. S. Catlett, "Plating Discreet Microparticles for Laser Fusion Targets," to be published in "Plating and Surface Finishing," March 1978.

16. A. T. Lowe and R. J. Fries, Los Alamos Scientific Laboratory internal document (July 1977).

17. E. Stark and F. Skoberne, Los Alamos Scientific Laboratory report LA-6834-PR (October 1977) p. 8.

18. F. Skoberne, Los Alamos Scientific Laboratory report LA-5739-PR (October 1974).

19. Lord Rayleigh, Proc. R. Soc. **29**, 71.

20. J. M. Schneider, N. R. Lindblad, C. D. Hendricks, Jr., and J. M. Crowley, J. Appl. Phys. **38**, 2599 (1967).

21. E. Stark and F. Skoberne, Los Alamos Scientific Laboratory report LA-6616-PR (May 1977).

22. E. Stark and F. Skoberne, Los Alamos Scientific Laboratory report, LA-6834-PR (October 1977).

23. E. Stark and F. Skoberne, Los Alamos Scientific Laboratory report LA-6616-PR (May 1977), p. 56.

VI. TARGET DIAGNOSTICS

The tiny volume and brief duration involved in the laser fusion process create needs for new diagnostic techniques having spatial and temporal resolutions in the submicrometer and 1- to 100-ps regime, respectively. These needs are being met with a vigorous program of diagnostics in such areas as laser calorimetry, charged-particle and neutron detection, x-ray spectrometry, and subnanosecond streak-camera development.

INTRODUCTION

In addition to the development of ultrafast x-ray diodes (XRD), spatially resolved x-ray line spectrographs, filtered pinhole cameras, and elaborate fast-ion detection schemes described in the Target Experiments section, a number of new diagnostics are in various stages of design, fabrication, or test.

Vacuum uv (VUV) imaging gratings, which allow extension of the spectral and imaging capabilities to the VUV portion of the photon energy spectrum, are currently being tested at the TBS.

Calorimeters which can selectively measure laser light or total target emissions of ions, electrons or x rays, have been developed. They have demonstrated linearity and sensitivity surpassing all other integral methods.

The alignment and focusing of CO_2 lasers is now possible, using ir microscopes and pyroelectric vidicon cameras, to an accuracy of better than 20 μm. It is possible to verify alignment to an accuracy of 5 μm.

The synchronization of a Nd:glass oscillator to a CO_2 oscillator has been accomplished to within 30 ps, making possible the use of accurately timed visible light pulses to probe 10.6-μm-generated plasmas. This kind of probe will be essential for interferometric measurements of density profile modification.

An additional technique for determining average density profile scale lengths between narrow density limits eliminates the need for costly interferometric unfolding.

Improved diagnostics for neutron yield and spectral analysis, plasma fast-ion expansion, and low-energy spectrally resolved calorimetry have been developed and are now being tested and calibrated. These will allow greatly increased accuracy in the measurement of important laser fusion target parameters. A laser beam alignment technique based on measured results of the microballoon damage study allows verification of alignment of 10.6-μm laser beams to a greater accuracy than earlier techniques.

DEVELOPMENTS

Vacuum uv Imaging of a Laser Produced Plasma (A. W. Ehler)

An image of a laser-produced plasma can be produced by a pinhole camera, by transmitting optics, or by reflecting optics. The pinhole camera, usually filtered to view the soft x-ray emission from the plasma, has the advantage of simplicity,but the disadvantage of a very small aperture and limited resolution. Transmitting or reflecting optics are capable of a 10^5 increase in light collection efficiency over the pinhole and are relatively inexpensive. However, transmitting optics are limited in spectral range from ir to uv, while the reflecting optics extend the range down to the vacuum uv. Grazing-incidence reflecting optics can operate in the soft x-ray region but with considerable loss of collection efficiency, greater expense, and alignment difficulty.

The compromise of normal incidence reflecting optics was chosen for this experiment. An elliptical

mirror would have given better spatial resolution, but a spherical mirror was selected because of its off-the-shelf availability and low cost. Also the spherical mirror could be purchased as a concave grating. The grating has the advantage that the plasma image can be dispersed to provide VUV spectral images[1] as well as the zero-order image. The power radiated by the plasma at 40 eV is about the same as that radiated at 1 keV. Although the normal-incidence mirror is a less efficient reflector, its greater collection efficiency provides about the same power at the focus as the grazing-incidence mirror. The time duration of the plasma radiation at 1 keV is about 1 ns for a 1-ns laser pulse, and about 1.5 ns at 40 eV. Consequently, for a time-integrated VUV image, the spatial smear due to the plasma motion would be almost negligible.

The laser used in this experiment was the LASL Two-Beam CO_2 laser. The laser energy of 250 J per beam in a 1-ns pulse was focused on the target with an irradiance of about 10^{13} W/cm^2. The concave grating used to image and disperse the plasma had a 40-cm radius of curvature, 5-cm blank diameter with 600 grooves/mm blazed at 750 Å with a platinum overcoat. The grating, target, and image were placed in line with the grating on one side of the target and the image focused on the opposite side of the target 140 cm from the grating. The plasma image was magnified six times and the plate factor was 12 Å/mm. A15-cm-diam vacuum window, coated on the inside with NE 111 plastic with an 800-Å aluminum overcoat, was used to convert the vacuum uv to visible light. A camera placed outside the vacuum chamber recorded the image through the window. The camera and film were not sensitive enough to record the spectroheliograms. Consequently, a new camera and film are being fitted to the experiment to give 12 times the present sensitivity.

Calorimetry (A. H. Williams)

The specialized calorimeters described below were developed to operate in a laser target vacuum chamber. They are designed to measure and record 10-μm laser energy and laser target interaction products for 1-ns pulses. The first calorimeter to be discussed is a reaction product calorimeter that can be filtered for selective sensitivity to ions, electrons, x rays, or 10-μm radiation. The second is an inverse-black-body calorimeter, which is highly linear over a large range of input energies and is used to measure 10-μm radiation from finite f-number ($\sim$ 1) systems. The third calorimeter is a high-precision, low-f-number calorimeter capable of accepting and measuring the 10-μm radiation from highly divergent systems. The fourth type of calorimeter is a conical, f/2, 10-μm-radiation, energy monitor used to measure absolute laser energy output with high linearity.

The multipurpose calorimeter shown in Fig. VI-1 can be used to measure the angular distribution of particular laser plasma reaction products by the use of selective filters. The basic calorimeter consists of a Ta disk 25 μm thick by 1.6-mm diameter supported by an intrinsic thermocouple fabricated with 25-μm chromel-constantan wires. The unit shown is a dual model of the basic calorimeter configuration that allows differential measurements of the reaction products at a given observation angle relative to the target. To filter the calorimeter and make it selectively sensitive to electrons, ions, x rays, or 10-μm radiation, one uses a beta-ray magnetic spectrometer, a positive-ion magnetic spectrometer, a Be foil or a crystal spectrometer, or a NaCl window, respectively. The very low mass of the basic unit (i.e., 0.947 mg for the Ta disk) makes it possible to achieve intrinsic sensitivities of 2.35 J/V. Efficiencies are $\sim$ 100% for electrons, ions, or x rays (i.e., 10-keV photons), and $\sim$5% for 10-μm radiation. If one assumes that the selected species of reaction product illuminates the energy-absorbing disk uniformly, the thermal equilibration time is $\sim$10 μs.

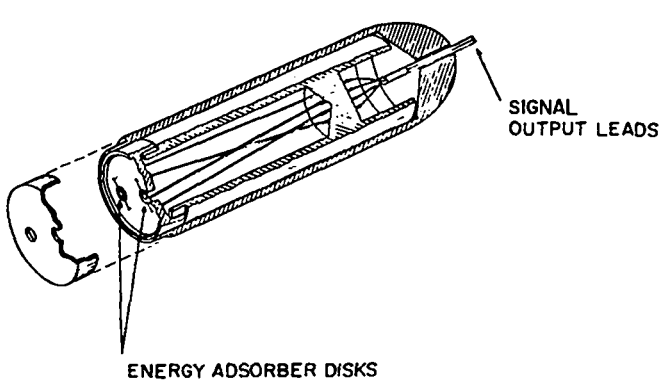

Fig. VI-1.
Multipurpose calorimeter.

Because the thermal decay constant (i.e., decay time to a temperature of $(1/e)T_o$) is ~12 s, the peak measured temperature rise is directly proportional to the absorbed energy, and extrapolation techniques used for calorimeters with long equilibration times are not necessary. When using this calorimeter in a differential mode, both elements are viewing a laser target with one element left totally unfiltered and the other element filtered with a polyethylene window. The unfiltered element is sensitive only to 10-μm radiation and to most of the x-ray spectrum. With suitable corrections for the transparency of the polyethylene window, one can deduce from the differential reading the intensity of the electron-ion energy flux at the position of the detector.

Figure VI-2 shows an inverse-black-body calorimeter that was developed to handle focused high-flux, 10-μm laser energy that would drive conventional surface or volume absorber calorimeters nonlinear for irradiances ~ 10^9 W/cm^2, even when the divergent beam is intercepted past the focus so that it just fills the entrance of the calorimeter to minimize the irradiance. Focused 10-μm radiation enters the thermally isolated can through the aperture and is totally absorbed despite any plasma formation within the cell. The temperature is monitored as a function of time. Using a single thermocouple and readings from the data after the equilibration time, the effective temperature rise at irradiation time can be obtained through extrapolation and the incident energy can be deduced. This type of calorimeter was used to monitor energies of 1 to 75 J with a linearity of better than 4.3% standard deviation for an f/2 laser beam. It was also used to measure the refocused, scattered light collected by an elliptical mirror in an energy balance measurement for intense 10-μm light incident on plane slabs of various materials at total energies on target of ~100 J.

Figure VI-3 shows a precision, low-irradiance calorimeter optimized for low-f-number systems. This unit contains an electrical heater for primary calibration and is thermopiled for increased sensitivity and resolution. For 10-μm radiation, this calorimeter absorbs ~99% of the incident energy from a low-f-number (i.e., 2 π) system with focus near the cylindrical axis of the unit and in the plane of the front entrance. The inside is coated with NEXTEL paint which has $R \simeq 0.04$, but multiple bounces of specularly and diffusely scattered light drop the effective value for the system to $R < 0.02$. Because the thermopile is localized on a small area of the absorbing cylinder, the effective temperature rise must be extrapolated from temperature data points taken after the equilibration time because the initial time dependence of the temperature is highly influenced by the energy deposition profile on the inner surface of the absorbing cylinder. This calorimeter is currently being used with a low-f-number, scattered-light collection system to measure 10-μm light absorption.

Figure VI-4 shows an incident energy calorimeter that is being developed to make f/2 high-energy measurements where multiple beams restrict the

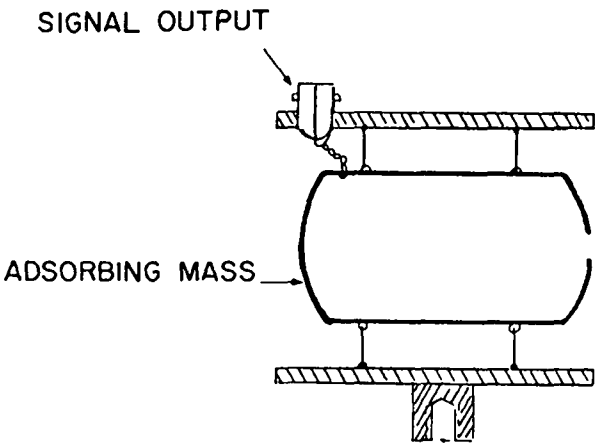

Fig. VI-2.
Inverse-black-body calorimeter.

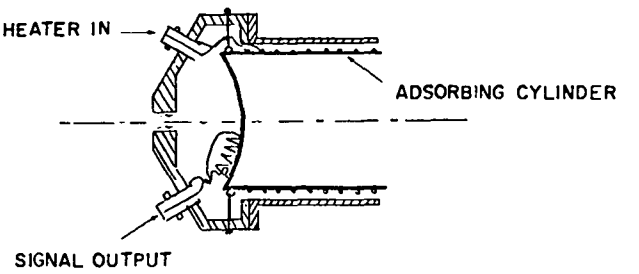

Fig. VI-3.
Precision low-irradiance calorimeter optimized for low-f-number systems.

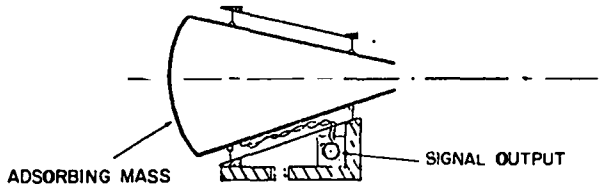

Fig. VI-4.
Incident-energy calorimeter being developed for f/2 high-energy measurements.

space available. A prototype unit was tested to 200 J and found to have a linearity of ± 4%, but the absorption efficiency was found to be ≃ 93%. This design is being studied to determine its scaling properties and to develop modifications to bring its efficiency closer to 100%.

Infrared Microscope (D. R. Kohler)

The infrared microscope described previously was used to examine the focus of the CO_2 laser beam in the SBS. As a result of being able to observe the focus spot of the oscillator beam directly, we were able to readjust the focusing mirror to improve the focal spot from that shown in Fig. VI-5 to the spot shown in the top view in Fig. VI-6. The signal on one horizontal scan line was also displaced on an oscilloscope as shown in Fig. VI-6. The oscilloscope trace was recorded for different amounts of beam attenuation so that both the wings and the peak of the distribution could be measured.

The camera tended to overheat so that the signal-to-noise ratio was poor. Nevertheless, data from the three photographs were combined in a semi-log plot that covered a factor of 100 in irradiance. The curve in Fig. VI-7 is plotted so that a Gaussian would appear as a straight line. Surprisingly, over the range of the measurement, the spot is very nearly diffraction limited. However, we did not take measurements over a sufficient range to be sure that a significant fraction of the energy was not spread into long, low wings around the central core.

The prototype of an improved pyroelectric-vidicon camera was used in a similar manner to

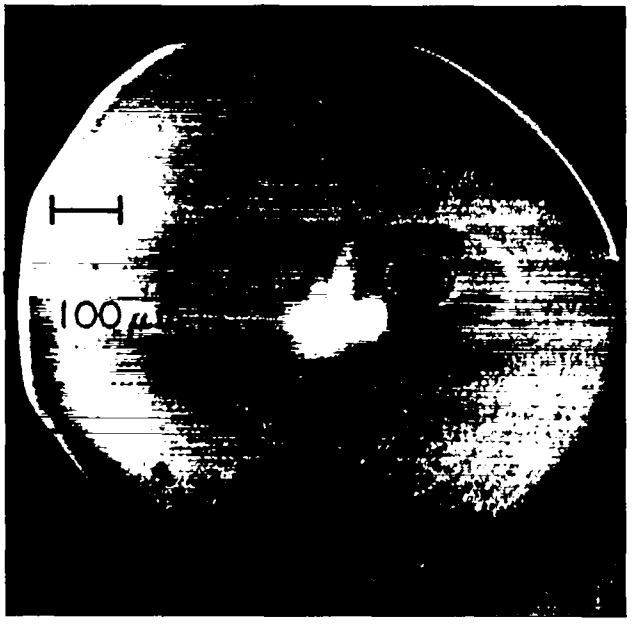

Fig. VI-5.
Focal spot of SBS observed through ir microscope.

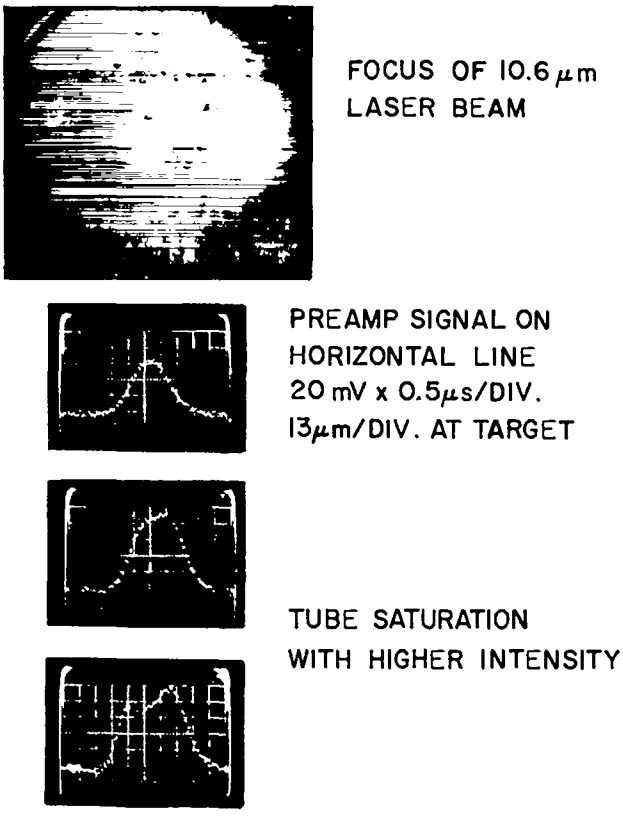

Fig. VI-6.
Focal spot of SBS as adjusted after viewing through ir microscope; traces illustrate different amounts of beam attenuation.

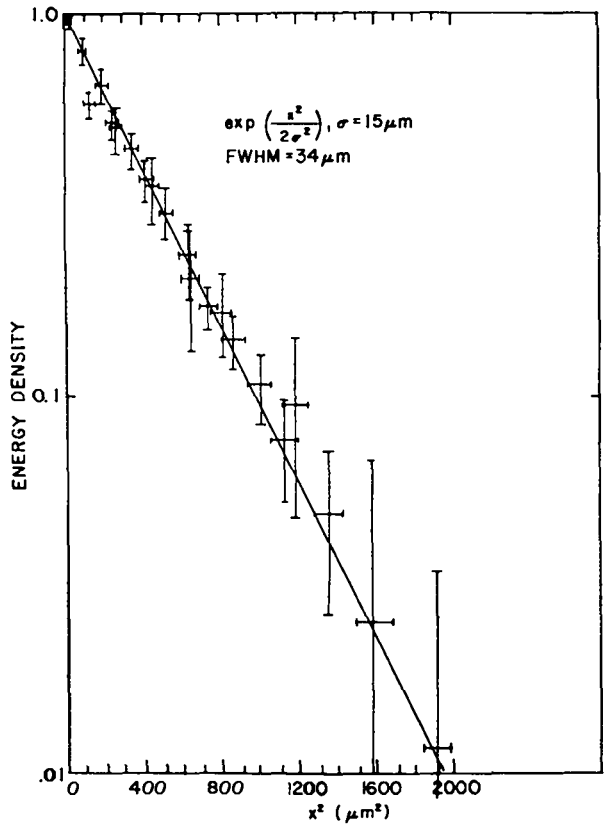

Fig. VI-7.
Energy density at focus of SBS oscillator beam (composite from 3 shots).

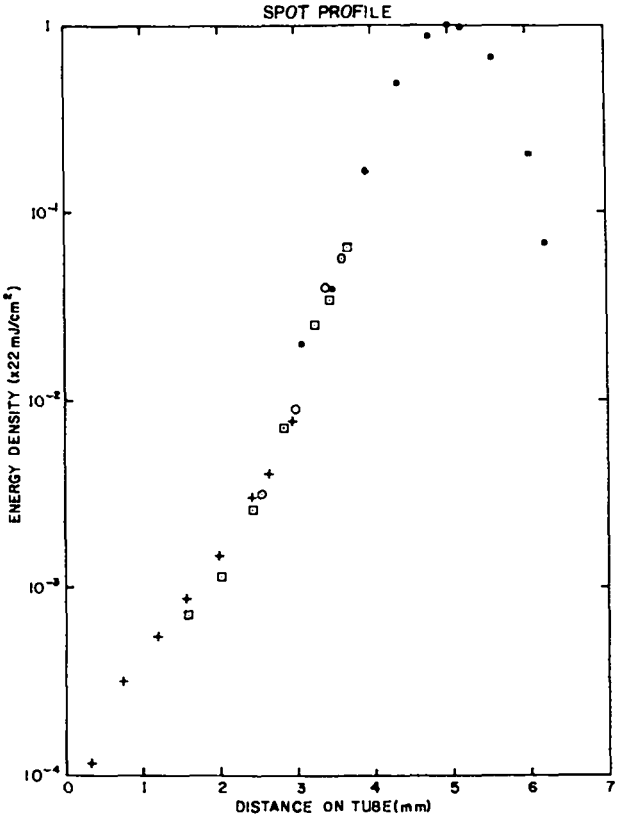

Fig. VI-8.
Composite data showing beam profile of a small CO_2 laser as plotted by pyroelectric-vidicon camera.

measure the profile of the beam from a small CO_2 laser. To measure the wings, the center of the beam was blocked and the gain of the oscilloscope was increased on separate pulses. By combining the data, a profile of the beam was obtained that covered a range of 10^4 in irradiance as shown in Fig. VI-8. Infrared microscopes using the improved cameras are currently being installed on the TBS.

Calculations of Neutron Detector Efficiences (F. Young)

The use of scintillation neutron detectors aids our analysis and understanding of basic physical processes in laser induced fusion. In scintillators, neutrons are detected by the scintillation light produced by the charged products of interactions between the incident neutrons and the nuclei of the scintillator. A central problem in the use of the scintillation neutron detector is the determination of its efficiency.

In recent years a number of measured and calculated neutron detector efficiencies have been reported.[2] In some cases there is significant disagreement between calculation and experiment.

Furthermore, calculations have been devised for scintillators with specific light output yields, hydrogen/carbon ratios, and geometries.

A substantially revised version of Kurz's neutron detector efficiency computer program[3] was written to generate absolute efficiencies for organic scintillators with arbitrary chemical and geometric properties.

The efficiency program calculates for a specified series of neutron energies, E, the total efficiency, $\xi(E)$, which is the result of a folding integration over the detection threshold, T,

$$\xi_{\text{total}}(E) = \int_0^\infty dte^{-\frac{(T-T_D)^2}{\tau T_0}} [\varepsilon_H(E,T) + \varepsilon_C(E,T)]; \quad \text{(VI-1)}$$

where T_o is the mean threshold, τ is the fractional resolution, $\xi_H(E,T)$ is the efficiency for an initial neutron interaction with hydrogen, and $\xi_L(E,T)$ is the efficiency for an initial interaction with a carbon nucleus. The essential elements of the program used to compute ξ_H and ξ_C are the subroutine HYD(E,T), which computes the single-scattering efficiency for n-p collisions and CAEV(E,T), which computes the single-scattering efficiency for n-C collision from the (n,α), C(n,n') 3α and (n,p) reactions. Rescattering contributions from (n,p) and C(n,n') 3α and (n,p) reactions are computed. Rescattering contribution from (n,p) and C(n,n')3α are also computed.

Results of a CDC 7600 computer run are shown in Fig. VI-9. The detector geometry was a cylinder 12.7 cm thick and 15.24 cm in diameter; the detector material was "Pilot-F" plastic scintillator. Figure VI-9 shows that the efficiencies for detecting 2.45-MeV and 14.1-MeV fusion neutrons are 54% and 35%, respectively.

Veeser[4] conducted measurements on neutron detection efficiencies at LASL's Tandem Van de Graaff facility. His results show that the experimental and calculated values for detection efficiencies agree within 10% for a similar scintillator type and geometry and for neutron energies at 2.45 MeV and 14.1 MeV.

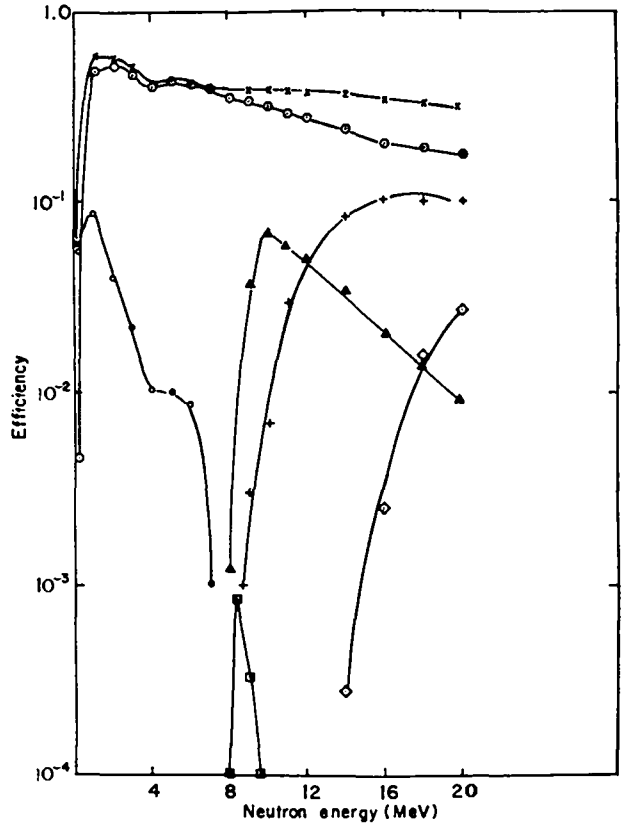

Fig. VI-9.
Neutron detection efficiency as a function of neutron energy, x = total efficiency; ⊙ = n-p scattering; o = n-p rescattering; Δ = c(n,α); ◇ = c(n,p); + = c(n,n'3α); □ = c(n,n'3α) rescattering.

Measurement of Alignment Accuracy (R. Benjamin, P. Goldstone, J. Carpenter)

The difficulty of aligning 10.6-μm wavelength beams on target has led to the development of the Hartmann test and an infrared transmission microscope. These developments are discussed elsewhere in this report and previous progress reports. To measure the accuracy of these techniques, as well as the optical stability of the laser, we performed the "Snout" test based on the prepulse damage measurement on GMB targets.

The Snout test involved carefully perforating GMB s with the aligned laser beam and then measuring the relative location of the holes. Figure VI-10 shows a typical GMB following the test on the TBS. Note that the two holes, one drilled by each beam, are clearly discernible. The holes are 40-to 80-μm diameter, enabling measurement of hole location to be made with a precision of 5 μm.

The Snout test performed at the TBS measured the accuracy of the Hartmann test as the alignment tool. The principal result is that there is a 45-μm rms pointing error in each beam. Fig. VI-11 shows

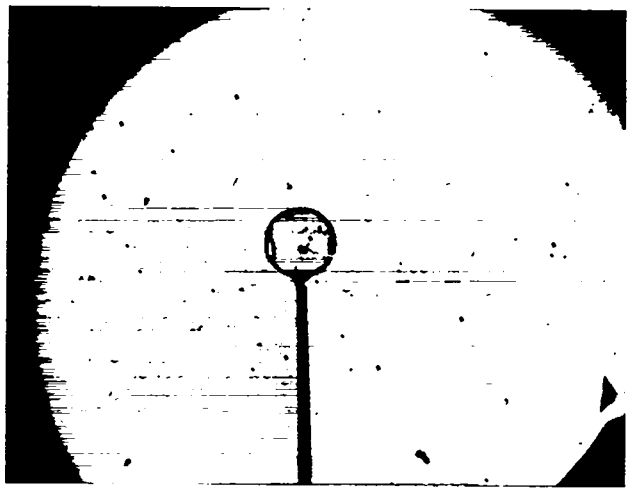

Fig. VI-10.
Typical glass microballoon after alignment accuracy test on TBS.

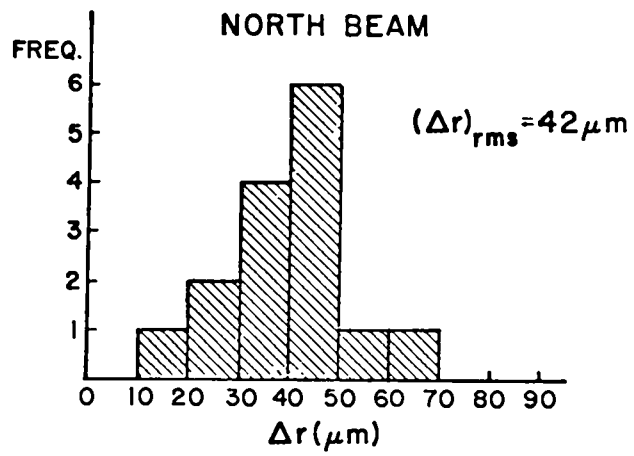

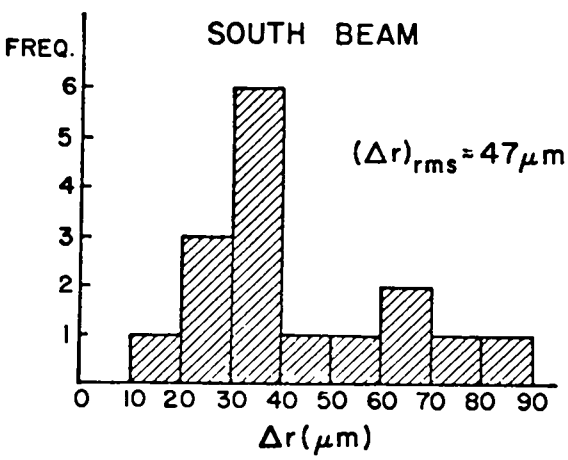

Fig. VI-11.
Histograms of Snout Test used to verify accuracy of Hartmann target alignment.

histograms of the data while Fig. VI-12 is a scatter plot of the same data. In Table VI-I, we estimate the relative amount of random and systematic error, finding that most of the error is random. We believe that beam aberration is the major source of alignment error since aberration makes interpretation of the Hartmann pattern quite difficult. On several shots the alignment changed between Hartmann test and the Snout shot (over several minutes) as diagnosed by a postshot Hartmann test. The 45-μm pointing error will be included in considerations for future target design and fabrication for the TBS.

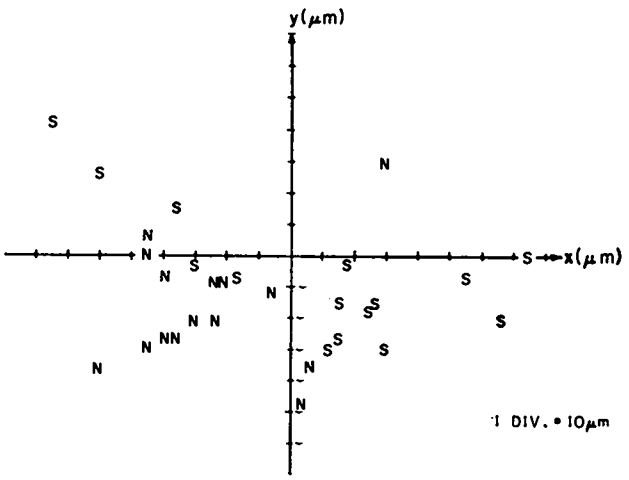

Fig. VI-12.
Scatter plot of path in Fig. VI-11.

TABLE VI-I

ESTIMATED RELATIVE AND SYSTEMATIC POINTING ERROR FOR THE TBS

	Pointing Error Relative To:	
Beam	Ball's Center	Average of Hole's Location
North	42 μm	30 μm
South	47 μm	46 μm

Dual Thomson Parabola Ion Detector (F. Young)

In the past several years, the Thomson parabola has served as a valuable diagnostic tool at LASL in the analysis of ions from laser-produced plasmas.

A single-channel Thomson parabola instrument has been used to measure velocity distributions[6] of different ion species. Its limited dynamic range, however, has allowed only partial velocity distributions to be recorded.

In an attempt to solve this dynamic range problem, a two-channel Thomson parabola instrument has been designed and is being fabricated. In the two-channel instrument, the electrostatic and magnetostatic fields, and the entrance apertures, can be independently adjusted so that the total velocity distribution of the ions can be observed. The instrument incorporates the "Watson" magnet design[6] and each channel has the same "view" angle of the target. The ion detector for this instrument will be cellulose-nitrate nuclear-track emulsions. A schematic of the two-channel instrument is shown in Fig. VI-13.

Track Size Measurement and Counting Instrument (F. Young)

An image analysis system designed and manufactured by Bausch and Lomb[7] is now being used to process images recorded on cellulose nitrate nuclear track detectors.[8]

A block diagram of the image analysis system is shown in Fig. VI-14. The images of ion tracks on the cellulose nitrate film are optically relayed through a microscope to a scanner head mounted on top of the microscope. The scanner head generates and transmits analog video signals (video bandwidth = 10 MHz) representing the images to the scanner control. Processed video signals are then transmitted from the scanner control to the basic module where the analog signal is converted into a two-level binary signal. Adjustment of controls in a gray-level detection module determines gray-level values and boundaries of the image. The basic module transmits the binary video into the measurement module which performs the following functions:

a. Total count; with detected tracks identified by count tags.
b. Total area of tracks.
c. Oversize count; useful for generating track diameter distribution functions. See Fig. VI-15.
d. Tangent count; will discriminate overlapping tracks.

The instrument has been designed to meet the following specifications on track-size detection limits as a function of microscope objective power:

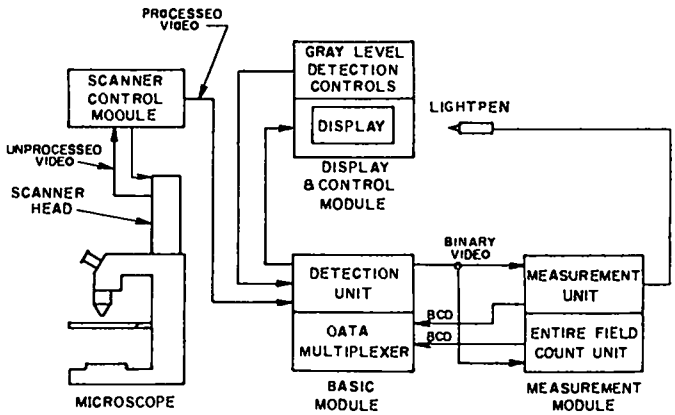

Fig. VI-14.
Block diagram of the image analyzer with microscope.

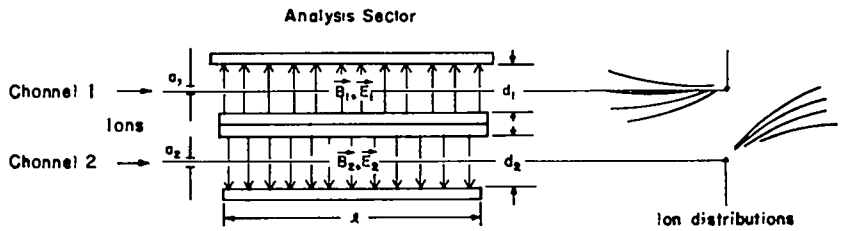

Fig. VI-13.
Two-channel Thomson parabola instrument. a_1 = aperture 1; a_2 = aperture 2; d_1 and d_2 can be adjusted; ℓ = constant.

Objective Magnification	Minimum Size Detectable (μm)
4	9 to 10
10	5 to 5
40	1 to 2
100 (oil immersion)	0.5 to 0.8

A television display is provided to monitor the performance of the image analysis instrument. The instrument will also be interfaced to a PDP-11/70 computer so that ion-track data can be immediately stored on disk or tape.

The instrument has greatly reduced the data reduction time for analyzing ion data from laser induced plasma experiments. Figure VI-15 is a photo of ion tracks in cellulose nitrate film. The image analysis system identified 195 tracks with diameters $> 2.5\ \mu m$, and indexed each one with a count tag, in approximately one second.

Computer Based Data Acquisition (R. C. Peck and M. Laymen)

Target experiment data from the TBS are being read into the PDP-11/70 data computer by means of CAMAC modules and a CAMAC serial highway which connects the TBS with the computer. This capability is limited at present, as extension of the serial highway to the diagnostics screen room awaits an acceptable means of cabling, which will be compatible with laser operation and other analog data channels.

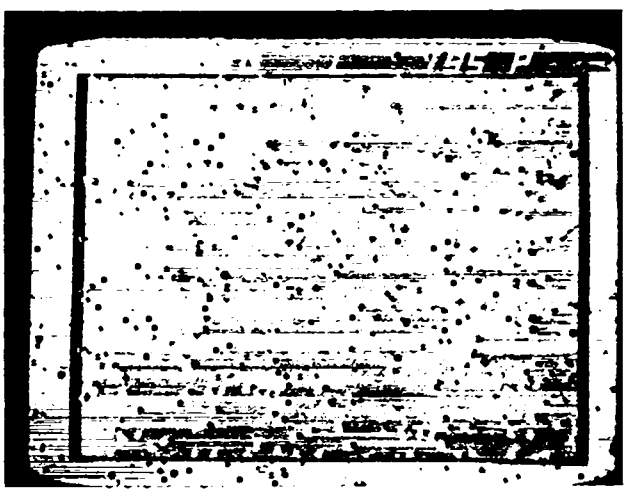

Fig. VI-15.
Display demonstrating count of oversize ion tracks (195 tracks with diameters > 2.5 μm).

A single program now provides for the acquisition of new data from all users and for its storage in orderly fashion. The next programming step, just under way, provides for retrieval of raw data as input to user data-analysis programs. One such user program has been translated from Nova FORTRAN and is running. Others have been moved to the PDP-11/70, and have been partially translated.

Eleven persons have established accounts as time-sharing users. Six graphics terminals are available for their use. Although a formal schedule has not been set, computing facilities are normally available during regular working hours with an operator on duty. Evening hours can be accommodated when the need arises.

It is anticipated that data acquisition using the PDP-11/70 can begin at the EBS on April 1, 1978. The necessary hardware is being collected on a rather tight schedule and the software is operating now.

Rainbows from Spherical Plasmas with Sharply Steepened Density Profiles (M. M. Mueller)

Interferometric diagnostics, while very useful in certain situations, are not generally useful[9] in determining the height and steepness of the density "cliff" expected in the laser-fusion regime. What is needed is a diagnostic which will accept very large scattering angles so that a given probe frequency can penetrate much deeper into the plasma and still be detected. To pursue this desideratum, the scattering of probe rays by spherical plasma has been investigated in some detail using an elaboration of the computer code developed previously.[10] Among other modifications and additions, a folding routine was developed to calculate the resultant light intensity on a screen as a result of the irradiation of a given spherical plasma with a beam of specified intensity distribution.

The results to be shown here are based on the assumed electron density profile for a spherical

plasma displayed in Fig. VI-16. This profile is moderately steepened (electron density drops to half in 1.5 μm),with the top of the cliff at 10^{21} cm^{-3}. For a one-radian acceptance half-angle, the minimum radii attained for 0.53- and 1.06-μm probe beams incident on the assumed profile are shown as vertical lines in Fig. VI-17. Note that at this acceptance angle, 1.06-μm radiation does not penetrate as far as the steepened region, while 0.53-μm radiation goes much deeper. By comparison, an f/2 optical system would receive 0.53-μm radiation from a minimum radius about where the 1.06-μm line is in Fig. VI-17.

The ray paths for a range of impact parameters are shown in Fig. VI-16 for 0.53-μm radiation incident on the assumed density profile of Fig. VI-17. Note that the steepened portion of the profile causes irregular ray distribution so that the ray density in angle space is sharply augmented in one region and depleted in another. This effect is graphically shown in Fig. VI-18 in which a cusp is evidently produced by the modified density profile. The sharpness of the cusp is due to the use of ray optics instead of wave optics; if a wave-optics solution were obtained, one might expect a somewhat more rounded peak.

Pronounced as the effect shown in Fig. VI-18, it is regrettably not accessible to experiment because

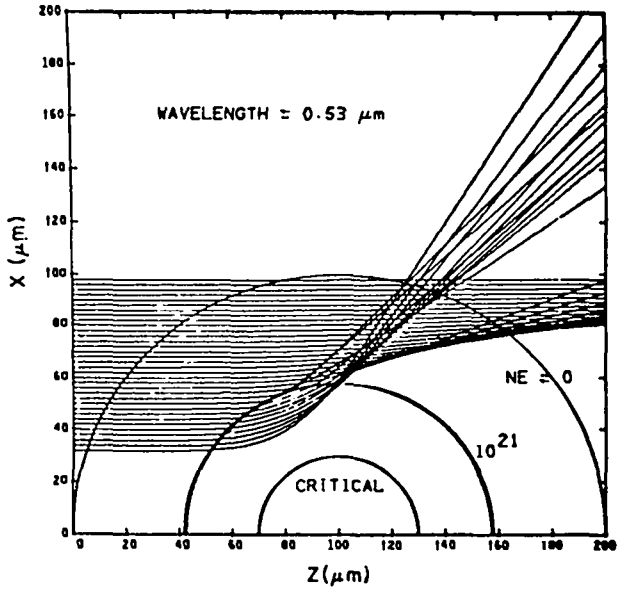

Fig. VI-16.
Optical refraction in a spherical plasma.

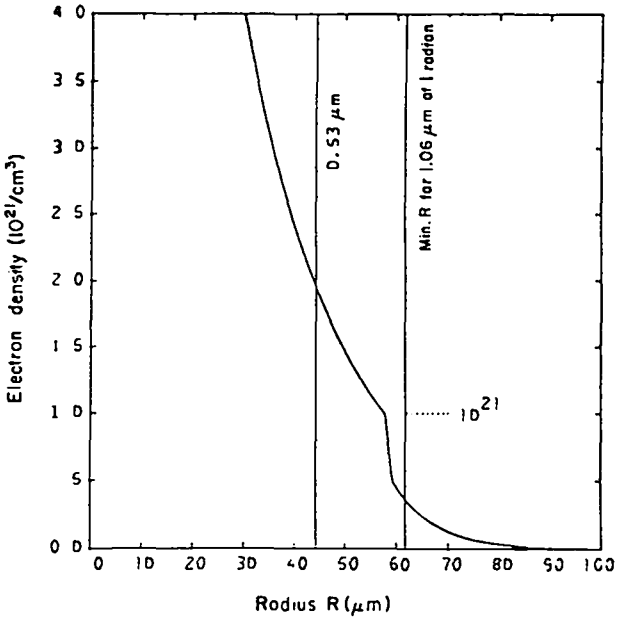

Fig. VI-17.
Assumed electron density profile in a spherical plasma.

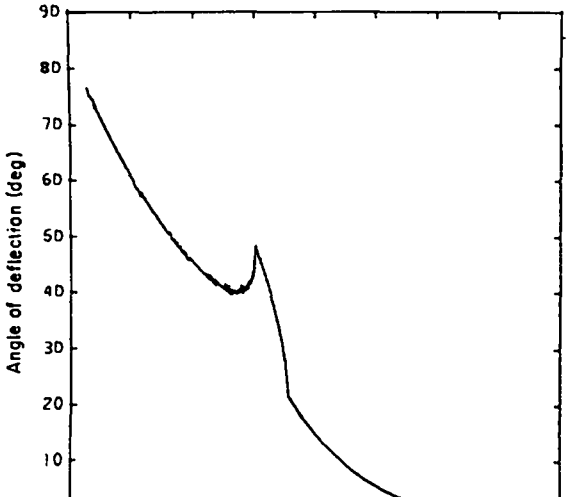

Fig. VI-18.
Scattering angle as a function of impact parameter for rays incident on spherical plasma.

there is no way of determining the impact parameter of a particular ray incident on a detector. What can be measured (for example, by a strip of photographic film) is the scattered intensity as a function of the angle of deflection. To obtain this function, the angle-vs-impact-parameter function (Fig. VI-18) must be numerically folded with the beam intensity (assumed to be Gaussian) shown in Fig. VI-19.

The result of using one thousand rays in such a folding operation is displayed in Fig. VI-20. The rainbow effect is a direct consequence of the sharply steepened region of the density profile. Note that the 1.06-μm radiation, which does not penetrate to the steepened region, does not exhibit a peak for this profile and this angular acceptance. Thus, if a sharply steepened spherical plasma were irradiated with a white-light probe beam, the scattered light would appear as a very wide and bright rainbow, which could be photographed (without imaging lenses) on a strip of color film. The half-angle acceptance is not critical and should exceed 45° in most circumstances. Of course, the larger the acceptance angle, the larger the probe wavelength can be. It is also evident that white light is neither necessary nor

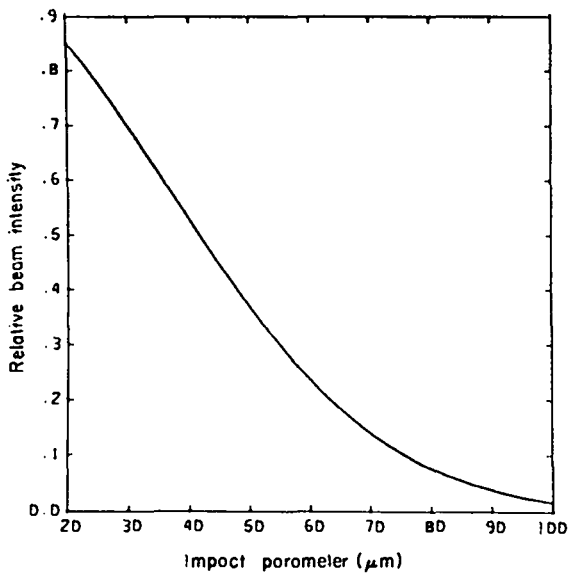

Fig. VI-19.
Intensity distribution of beam incident on spherical plasma.

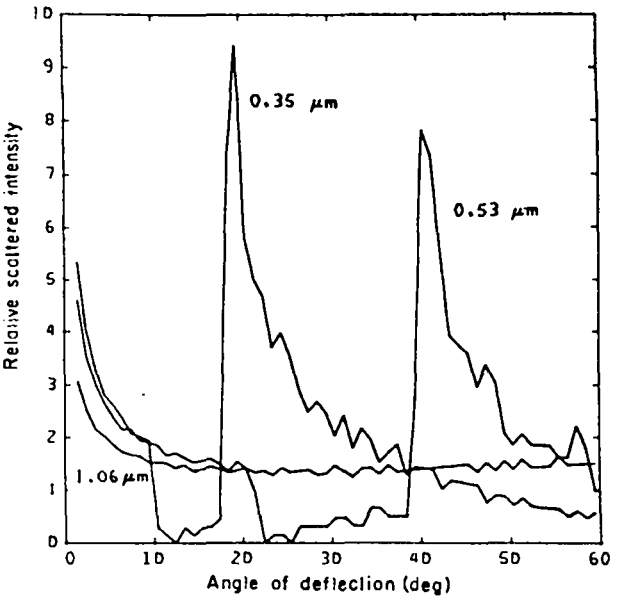

Fig. VI-20.
Rainbow from a spherical plasma with a sharply steepened density profile.

desirable for the experiment—any number of discrete probe wavelengths would provide valuable information.

The most important information is the existence of a sharply steepened region in the profile, and this could be ascertained simply by noting wavelength-dependent intensity bands on the detector filmstrip. However, exact and model-free reconstruction of the density profile in the spherical plasma from the measured scattered-intensity distribution appears to be rather difficult, and has not yet been carried out. Particularly, problems of uniqueness appear prohibitive. Probably the most fruitful approach would be model-dependent and iterative—assuming a profile model and iteratively varying parameters until the predicted scattered intensity-vs-angle function best fits the experimental data.

But most promising is the joint application of this rainbow method and the reflectance method in quasi-planar plasmas described previously[11] to determine both the electron density profile and the microscopic plasma absorption profile. For this to work, one must start with spherical and quasi-planar plasmas which, on physical grounds, can

reasonably be assumed to be very similar. Then the rainbow method is used to unfold the electron density profile of the spherical plasma, and this information is then used to unfold the microscopic absorption profile of the quasi-planar plasma.

Generalization of the Wave-Optics Code (M. M. Mueller)

The wave-optics code developed previously[12] calculates resonance absorption in a gradient planar plasma using an exact solution of Maxwell's equations across multiple boundaries; the plasma is approximated by a very large number of thin strata. However, this code was restricted to inverse bremsstrahlung absorption, p-polarization, and a linear electron density gradient.

The code was extended and rewritten to eliminate these restrictions. The new code can handle arbitrary polarization and arbitrary analytical profiles, but is still restricted to planar plasmas.

The main purpose of this code generalization is to provide a tool which should prove useful in a scheme to estimate resonance absorption in a spherical gradient plasma. For this purpose, arbitrary polarization and arbitrary profiles will be necessary to "bootstrap" from ray optics to wave optics by means of relating enhanced absorption to the depth of penetration of the ray in the planar case and then applying this relation to the spherical case. Because steep plasma profiles are expected, this also pushes the limits of validity of ray optics itself; but, as we see in the next section, ray optics is a somewhat better approximation in these circumstances than was anticipated.

Test of Ray Optics in Steep Planar Gradients (M. M. Mueller)

Because the only practical general solutions of radiation propagation in spherical absorbing plasmas exist in the eikonal approximation, and because the gradients of interest to laser fusion are very steep for distances around one wavelength or less, determining the accuracy of ray-tracing under these conditions is rather important. Simple analysis, in the approximation of ignoring absorption, indicates that ray optics start to break down when the index of refraction changes appreciably over a distance of about one wavelength. We decided to test the accuracy of ray optics in fairly realistic planar plasmas by comparing absorption calculated from ray-tracing with that calculated using the wave-optics code described above. Another benefit of such comparisons is the precise cross-checking of the ray-optics and wave-optics codes for s-polarized light and fairly realistic plasma models.

For the tests, we chose a density model that is smooth and potentially steep,

$$N = (x/s)^p,$$

where N is the electron density relative to the critical density, x is the distance, and s is the depth of the critical surface. The conventional plasma scale length can be shown to be $L = s/p$. For the absorption model we somewhat simplistically used inverse bremsstrahlung at an electron temperature of 0.1 keV, which gives absorptions of about the magnitudes observed experimentally. In the tests, we used both $p = 1$ and $p = 7$; $p = 7$ is, of course, much more realistic. The tests used only s-polarized light since the ray-optics treatment cannot take optical resonance into account.

For $p = 7$, runs were made using s values of 1.75, 3.5, 7, and 17.5 wavelengths, corresponding to plasma scale lengths of 0.25, 0.5, 1, and 2.5 wavelengths. Four thousand zones (strata) were employed in each run. The deviations between the absorptances calculated by the ray optics and wave-optics codes are a weak function of angle so we have chosen an angle of incidence of 20° for the percentage deviations reported here. For the plasma scale lengths of 2.5, 1.0, 0.5, and 0.25 wavelengths, the respective deviations are 0.10, 0.72, 2.9, and 10.7%. Thus, absorption calculated from ray optics is reasonably accurate down to plasma scale lengths of about one-third wavelength.

Multidimensional Empirical Formulas Describing Electronic Backscattering from 7 to 300 keV (M. M. Mueller)

An attempt has been made to develop a set of empirical formulas which describe the most important behavior of electron backscattering over a large volume of multidimensional parameter space. Particle backscattering (integrated over 2 π sr) and energy reflection are described as functions of atomic number, incident electron energy, angle of incidence, and film thickness. Composite-film backscattering is treated at normal incidence only. Our success in this complicated effort has been modestly good, but the paucity of consistent data in many regions poses a threat to the general reliability of these formulas.

Reflection of Planckian X-Ray Spectra from Surfaces (M. M. Mueller)

To interpret and reduce the data from x-ray reflection calorimeters, detailed information is needed on the reflectances of surfaces as a function of incident angle and photon energy, as well as the integrated response to specified spectral distributions as a function of angle incidence. A computer code was written for these purposes, and used to calculate reflected energy as a function of angle for Au and SiO_2 surfaces with incident radiation of arbitrary black-body temperature.

Deconvolution to Determine Source Diameter from the Spatial Profiles of Lines in X-Ray Spectrograms (M. M. Mueller)

A slit x-ray spectrograph produces images of the source in the direction on the detector plane normal to the dispersion direction. These images contain information about source diameter (normal to the view axis and to the slit direction) and source structure. Even with relatively wide slits, deconvolution can provide an estimate of source diameter; but it cannot provide detailed information on source structure unless rather narrow slits are used. We shall be deconvolving slit images of a circular source disk of uniform radiance, so the problem can be solved analytically.

The intensity distribution on the detector plane is essentially the projected convolution of a rectangle with a semicircle, and can readily be expressed analytically. However, because the expressions are transcendental, analytical deconvolution is not feasible. But the first derivative of the intensity distribution is algebraic, and may readily be solved for the source diameter when the geometry of the system is known. Indeed, a plot of the first derivative exhibits a sharp cusp, the location of which is simply related to the source diameter. Therefore, finding the source diameter from actual intensity data should present no problem so long as the first derivative can be even roughly determined.

REFERENCES

1. U. Feldman, G. A. Taschek, D. K. Prinz, and D. J. Nagel, J. Appl. Phys. **47**, 168 (1976).

2. S. T. Thornton and J. R. Smith "Measurements and Calculations of Neutron Detector Efficiencies," NIM, Res. Rep. **96**, 551-555 (1971).

3. R. J. Kurz, "A 709/7090 FORTRAN II Program to Compute the Neutron Detection Efficiency of Plastic Scintillator for Neutron Energies from 1 to 300 MeV." E. O. Lawrence Radiation Laboratory report UCRL-11339 (March 1964).

4. L. R. Veeser, Los Alamos Scientific Laboratory, personal communication.

5. F. Young and G. H. McCall, "Measurement of Charged Particle Velocity and Population Distributions in Laser-Produced Plasma Experiments," Bull. Am. Phys. Soc. **22**, 1129 (1977).

6. B. Blecke, Indiana General Corp., Valparaiso, Indiana, personal communication.

7. Analytical Systems Division, Bausch and Lomb, Rochester, New York, personal communication, 1977.

8. F. Young, "Ion Distributions from Thomson Parabola with Plastic Track Detector," Los Alamos Scientific Laboratory report LA-6834-PR (October 1977).

9. E. Stark and F. Skoberne, Los Alamos Scientific Laboratory report LA-6982-PR (April 1978).

10. M. M. Mueller, "A Ray-Tracing and Simulated Interferometric Fringe-Shift code for Gradient—Index Media with Spherical Symmetry," Los Alamos Scientific Laboratory internal document, May 25, 1976.

11. E. Stark and F. Skoberne, Los Alamos Scientific Laboratory report LA-6982-PR (April 1978).
Also, M. M. Mueller, "New Optical Methods for Determining Profiles in Spherical or Quasi-Planar Plasmas," Los Alamos Scientific Laboratory internal document, November 1977.

12. M. M. Mueller, "Enhanced Laser-Light Absorption by Optical Resonance in Inhomogeneous Plasma," Phys. Rev. Letters, **30**, 582-5 (1973).

VII. APPLICATIONS OF LASER FUSION—FEASIBILITY AND SYSTEMS STUDIES

Our systems studies are being performed to analyze the technical feasibility and economic aspects of various commercial and military applications of lasers and laser fusion. The direct production of electricity in electric generating stations is of major concern. The general objectives of the studies are: the conceptualization and preliminary engineering assessment of laser fusion reactors and other generating-station subsystems; the development of computer models of generating-station subsystems for economic and technology tradeoff and comparison studies; and the identification of problems requiring long-term development efforts. Emphasis in military applications studies is placed on relatively near-term weapons-effects simulation sources and facilities.

HYDRODYNAMIC WAVES IN A LIQUID LITHIUM BLANKET (I. O. Bohachevsky)

Introduction

In this section we present results of our continual study of parametric dependencies of ICF reactor characteristics. The objective of this phase of investigation was to model the transient response of the system of two concentric structural shells with liquid (lithium) between them (shown in Fig. VII-1) to impulsive mechanical and thermal loads applied from the interior of the inner shell and from the liquid blanket region. In particular, the following two problems were analyzed:

1. propogation of pressure waves in the blanket generated by the pressure pulse resulting from fuel pellet microexplosion and their reflections from the elastic walls;
2. generation of waves in the liquid blanket as a consequence of nonuniform energy deposition.

In both cases the wave motion has been characterized with analytic solutions, and expressions have been derived for the values of parameters required in the mathematical modeling of ICF reactor systems.

Response of a Two-Shell Reactor Vessel to a Pressure Impulse

We consider the model of the reactor vessel shown in Fig. VII-1 consisting of two elastic structural

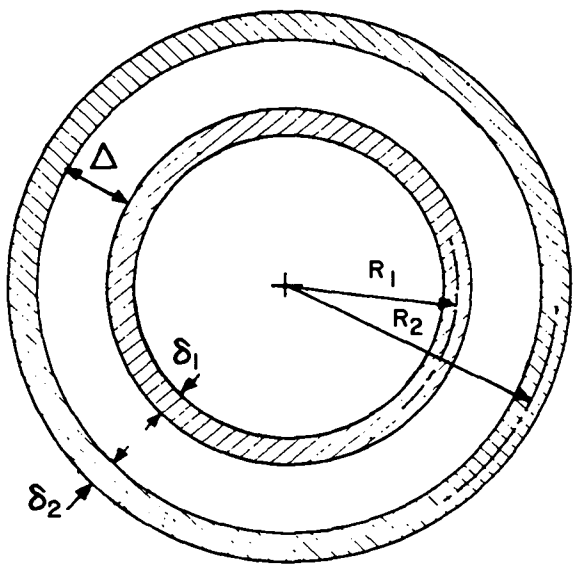

Fig. VII-1.
Reactor vessel model.

shells with liquid in the region between them. At a time $t = 0$ the fuel pellet microexplosion generates an impulse I_1, which is applied to the interior shell; the problem is to determine the response of the system.

The response of the system is governed by the two equations describing the elastic behavior of the structural shells and one-wave equation describing the behavior of the liquid between them. These equations are:

$$\frac{d^2 w_i}{dt^2} + \frac{\rho_o a_o}{\rho_i \delta_i} \frac{dw_i}{dt} + \frac{2E_i}{\rho_i R_i^2 (1-\nu)} w_i = 0 \quad , \qquad \text{(VII-1)}$$

$$\frac{\partial^2 u}{\partial t^2} - a_o^2 \frac{\partial^2 u}{\partial r^2} = 0 \quad , \qquad \text{(VII-2)}$$

where w is the radial displacement of the shell, δ is the shell thickness, ρ is the density of shell material, E is the Young's modulus, ν is the Poisson's ratio, R is the mean radius of the shell, ρ_o is the undisturbed liquid density, a_o is the sound speed in the liquid medium, u is the local particle velocity in the liquid medium, r is the variable radial coordinate, and i = 1 for the interior shell, i = 2 for the exterior shell.

The initial conditions for Eqs. (VII-1) are

at $t = 0$ $w_i(0) = 0$

$$\frac{dw_1}{dt} = \frac{I_1}{\rho_1 \delta_1} \qquad \text{(VII-3)}$$

and at

$$t = \frac{\Delta}{a_o} \quad w_2 \left(\frac{\Delta}{a_o}\right) = 0 \qquad \text{(VII-4)}$$

$$\frac{dw_2}{dt} = \frac{I_2}{\rho_2 \delta_2} \, .$$

where Δ is the liquid-blanket thickness and I_2 is the impulse carried by the wave through the blanket to the outer shell.

For Eq. (VII-2) the initial and boundary conditions are:

$$u \equiv 0 \qquad \text{at } t = 0$$

$$u = \frac{dw_1}{dt} \qquad \text{at } r = R_1 \qquad \text{(VII-5)}$$

$$u = \frac{dw_2}{dt} \qquad \text{at } r = R_2 \, . \qquad \text{(VII-6)}$$

Condition (VII-6) expresses the assumption that cavitation does not occur.

The pressure perturbation in the liquid blanket is given by the acoustic relations:

$$p = \pm \rho_o a_o u \qquad \text{(VII-7)}$$

where (+) corresponds to outward and (-) to inward propagating waves.

The assumptions leading to the derivation of Eq. (VII-1) have been discussed in Ref. 1,and additional details of the model and analysis will be included in a forthcoming Los Alamos Scientific Laboratory report.

The above presented system of equations (VII-1) through (VII-7) has been solved explicitly and in closed form. The solution, however, is too cumbersome to be included in this report. We will only summarize the relevant results.

Shown in Fig. VII-2 are the shape and outward propagation of the impulse-generated pressure wave. Its reflection at the exterior shell and the subsequent inward propagation of the reflected wave are illustrated in Fig. VII-3. The results show that the hyrodynamic wave is strongly attenuated during the reflection process; this is a consequence of the elastic response of the structural shell.

In the design and analysis of structural shells for the containment of microexplosions of particular interest are impulses delivered to the walls. These have been calculated with the aid of the explicit solution to be:

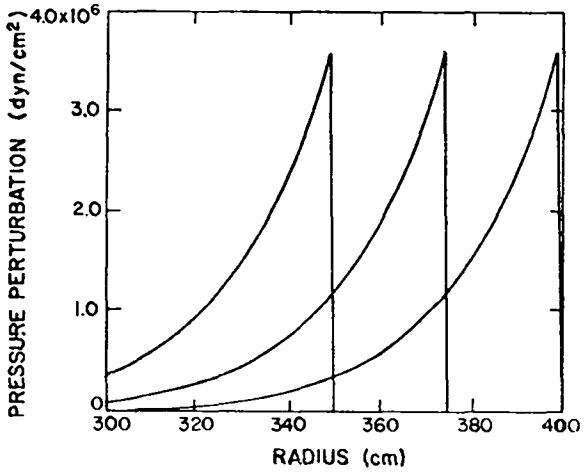

Fig. VII-2
Shape and outward propagation of pressure wave through lithium blanket.

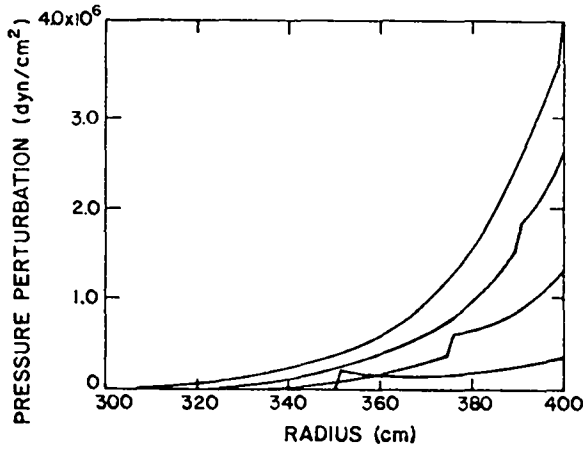

Fig. VII-3
Wave reflection at outer shell of reactor vessel.

$$\frac{I_2}{I_1} = - \frac{\rho_o a_o \left(e^{-\omega_1 t_b} - e^{-\omega_2 t_b} \right)}{2\rho_1 \delta_1 \sqrt{\frac{\rho_o^2 a_o^2}{4\rho_1^2 \delta_1^2} + \frac{2E_1}{\rho_1 R_1^2 (1-\nu)}}} \qquad \text{(VII-8)}$$

where $\omega_{1,2}$ are the roots of the polynomial associated with Eq. (VII-1) for the interior shell and t_b is the wave transit time Δ/a_o. For the values of parameters characterizing designs of containment vessels for commercial ICF reactors, the value of the ratio I_2/I_1 is in the neighborhood of 0.94 indicating that the impulse is transmitted through the liquid blanket with very little (6%) dissipation. However, after the wave reflection at the exterior shell, the impulse carried back to the interior shell, I_3, is given by:

$$\frac{I_3}{I_2} = 1 - \frac{C_2 \left(e^{-\Omega_1 t_b} - e^{-\Omega_2 t_b} \right)}{C_1 \left(e^{-\omega_1 t_b} - e^{-\omega_2 t_b} \right)} , \qquad \text{(VII-9)}$$

where $\Omega_{1,2}$ are roots of the polynomial associated with Eq. (VII-1) for the exterior shell and $C_{1,2}$ are constants contained in the solution of the system of Eqs. (VII-1) through (VII-7). For the values of parameters relevant to the commercial reactor designs the value of the ratio I_3/I_2 is in the neighborhood of 0.04; such small value indicates that most of the original impulse is expended to accelerate the exterior shell. This is consistent with the result illustrated in Fig. VII-3.

The above results indicate that within the framework of the present model the response of the two-shell vessel to pressure generated impulses is strongly overdamped and the vessel vibrations will be highly unlikely. It is necessary to point out, however, that the solution described here will not remain valid in the case when the denominator in Eq. (VII-8) vanishes; the case of such "resonance" will require special analysis.

Thermally Generated Pressure Waves

Thermonuclear neutrons deposit their energy nonuniformly in the reactor blanket and thereby induce nonuniform temperature distribution that results in an instantaneous pressure imbalance that must be resolved with wave motion. The wave motion is determined in this section.

For this analysis the model is that of a liquid region between two immovable walls located at r = R_1, and r = R_2 (see Fig. VII-1). The assumed instantaneous neutron energy deposition produces an initial pressure perturbation given by:

$$p = p_1 e^{-\frac{r-R_1}{\lambda}} , \qquad \text{(VII-10)}$$

where λ is the e-folding distance of the exponential energy deposition profile ($\lambda \approx 70$ cm for lithium) and P_1 is the pressure generated at $r = R_1$,

$$p_1 = \frac{\beta b}{c_p} \quad \frac{(1-f-x)\,Y}{\pi(R_1+R_2)^2\,\lambda} \,. \qquad \text{(VII-11)}$$

Here β is the adiabatic bulk modulus, b is the volume coefficient of thermal expansion, c_p is the heat capacity and ρ the density of the liquid medium, Y is the fuel pellet energy yield, f is the fraction of yield in debris ions, and x the fraction of yield in photons. The derivation of these expressions and the details of further analysis will be described in a separate technical report; here we will present only the formulation and the final results.

The motion of the liquid blanket medium resulting from the initial pressure imbalance is governed by the following set of linearized equations,

$$\frac{\partial}{\partial t}\begin{pmatrix} p \\ u \end{pmatrix} = \frac{\partial}{\partial r}\begin{pmatrix} 0 & a_o^2\rho_o \\ 1/\rho_o & 0 \end{pmatrix}\begin{pmatrix} p \\ u \end{pmatrix} = 0 \qquad \text{(VII-12)}$$

with the initial conditions at $t = 0$ given by Eq. (VII-10) and by $u(0) = 0$ and the boundary conditions by $u(R_1,t) = u(R_2,t) = 0$. The general solution of Eq. (VII-12) may be written in terms of outward and inward propagating waves as follows:

$$\begin{pmatrix} p \\ u \end{pmatrix} = f_1(r-a_o t)\begin{pmatrix} a_o\rho_o \\ 1 \end{pmatrix} + f_2(r+a_o t)\begin{pmatrix} -a_o\rho_o \\ 1 \end{pmatrix}, \qquad \text{(VII-13)}$$

where the arbitrary functions f_i are to be determined from initial and boundary conditions.

Using the standard Fourier series expansion technique the solution is given by

$$f_1 = \frac{1}{2}\sum_{n=0}^{\infty} b_n \sin\left\{\frac{\pi n}{\Delta}(r-a_o t) - \pi\left(\frac{1}{2} + n\frac{R_1}{\Delta}\right)\right\}$$

$$f_2 = \frac{1}{2}\sum_{n=0}^{\infty} b_n \sin\left\{\frac{\pi n}{\Delta}(r+a_o t) + \pi\left(\frac{1}{2} - n\frac{R_1}{\Delta}\right)\right\} . \qquad \text{(VII-14)}$$

Since from Eq. (VII-13)

$$p = a_o\rho_o\,(f_1-f_2),$$

the expression for the pressure perturbation can be written as

$$\frac{p}{a_o\rho_o} = -\sum_{n=0}^{\infty} b_n \cos\left[n\pi\frac{r-R_1}{\Delta}\right]\sin\left[\pi\left(\frac{1}{2} + \frac{n a_o t}{\Delta}\right)\right], \qquad \text{(VII-15)}$$

where the Fourier coefficients b_n are given by

$$b_o = -\frac{\beta b}{a_o\rho_o^2 c_p} \quad \frac{(1-f-x)Y}{\pi(R_1+R_2)^2\Delta}\,(1-e^{-\Delta/\lambda}) \qquad \text{(VII-16)}$$

$$b_n = -\frac{2\beta b}{a_o\rho_o^2 c_p} \cdot \frac{(1-f-x)\,Y}{\pi(R_1+R_2)^2\lambda} \quad \frac{\Delta/\lambda}{(\Delta/\lambda)^2 + (n\pi)^2}$$

$$\left[1 - (-1)^n e^{-\Delta/\lambda}\right] n \geq 1 \,. \qquad \text{(VII-17)}$$

Several observations can be made on the basis of this solution. First, the leading constant term, b_o, gives the pressure rise that would obtain if the energy was added so slowly that waves do not develop; this checks with the result obtained in Ref. 1 (Eq. 19). Second, the first two terms describe the motion with less than 10% error; this is illustrated in Fig. VII-4 in which plotted are approximations to the initial pressure distribution obtained by evaluating Series (15) at $t = 0$ with 1, 2, 3, and 4 terms successively.

Because the first harmonic component characterizes the motion with sufficient accuracy for our purposes, we will examine the variation of its amplitude, b_1, in some detail. Figure VII-5 shows the dependence of this amplitude on the blanket thickness, Δ, normalized with the e-folding scale λ. Because the current conceptual ICF reactor designs have values of Δ/λ in the range between 1.0 and 1.5, the amplitude of the pressure wave for these designs will increase steeply and approximately linearly with the blanket thickness. This result indicates the

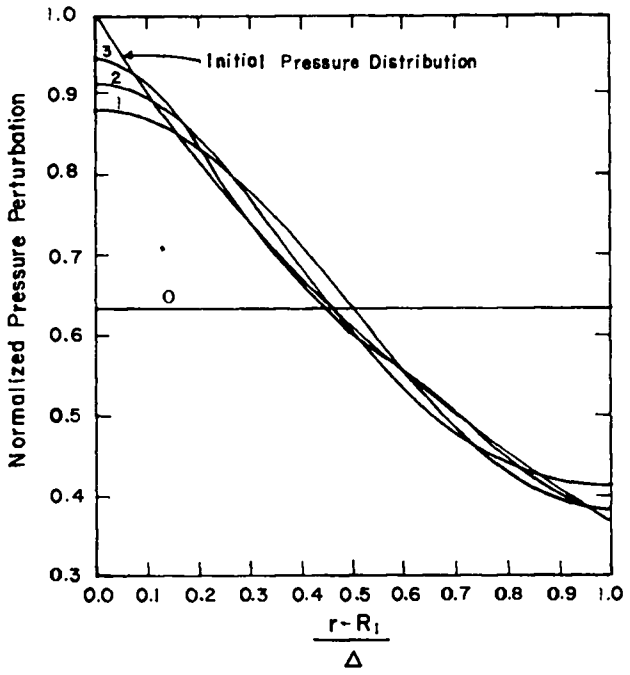

Fig. VII-4.
Successive approximations to initial pressure distribution in lithium blanket.

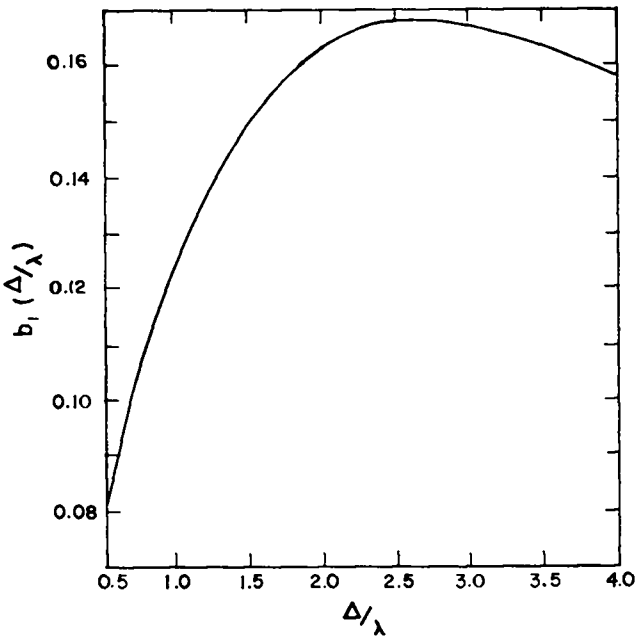

Fig. VII-5.
Amplitude of first harmonic component of pressure wave in the blanket.

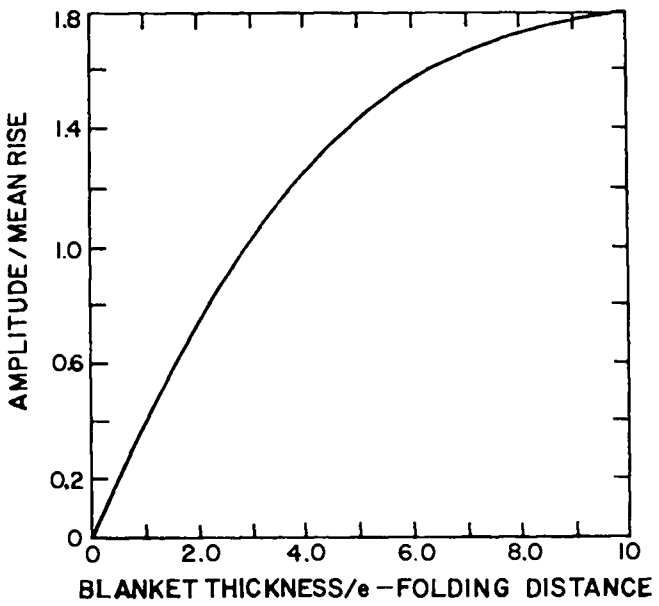

Fig. VII-6.
Relative amplitude of first harmonic component of pressure wave in the blanket.

incentive to design blankets as thin as possible consistent with the needs of energy extraction. A more convenient form of this result is presented in Fig. VII-6 where the ratio of the amplitude b_1 to the mean pressure rise b_o is plotted. We note that this ratio also increases with the blanket thickness.

The impulse delivered by the first harmonic component to the inner shell is easily calculated by integrating the pressure at the wall, $r = R_1$, over the compression phase of the wave. The result is

$$I_1 = -\frac{\Delta b_o}{2a_o}\left(\frac{1}{2} + \frac{1}{\pi}\frac{b_1}{b_o}\right); \qquad \text{(VII-18)}$$

it shows that the impulse is proportional to the blanket thickness, Δ, and the mean pressure rise, b_o, and increases as the ratio b_1/b_o increases. Substitution of explicit expressions for b_o and b_1 shows that the impulse is proportional to the inverse square of the acoustic impedance $a_o\rho_o$.

Concluding Remarks

The explicit results presented in this section are very useful for rapidly estimating dynamic loads on the microexplosion containment vessels and establishing the dependence of loads and wall stresses on different parameters of the system. As the next step in the analysis of phenomena discussed here we will extend the model of the thermally generated pressure waves to include the cases of free-falling thick liquid-curtain walls and of blankets contained by elastic walls. The discussion of the elastic response of a two-shell reactor vessel to external impulses presented above showed that the inertia and the elastic effects should not be neglected in the determination of the hydrodynamic wave motion and of the resulting wall stresses.

PROPAGATION OF LASER LIGHT IN A COMMERCIAL REACTOR CHAMBER (J. J. Devaney)

The wide range of light intensities encountered in the propagation of focused laser beams in a large gas-filled chamber gives rise to a multitude of competing processes that might affect delivery of light energy onto a tiny pellet. These processes include multiphoton (and tunneling) ionization, cascade ionization, absorption, Rayleigh scattering, Brillouin scattering, Raman scattering, stimulated Raman scattering, refraction, self-focusing, inverse bremsstrahlung, ion polarization, ponderomotive force, thermal blooming, inverse blooming or trapping, and laser-induced detonation. For the proposed commercial reactor chamber parameters some effects are expected to be negligible, but prudence requires that at least the orders of magnitude of all effects be checked. At the present time the dominant effects are ill understood and some are controversial. Henderson's excellent analysis[2] of the defocusing of the laser beam by the reduction of the index of refraction by ionization provides both a convenient rule of thumb and a code for detailed calculation of this effect. The multi-photon-tunneling theory of Keldysh,[3] upon which Henderson's work is based, however, rests on the crude approximation of a square well in place of the Coulomb well. Whereas this model will describe the gross features correctly, it may be an oversimplification. There are claims that Keldysh's theory disagrees with experiment by several orders of magnitude, and that it has been extended beyond its proper range.[4] Indeed, the entire subject of multiphoton ionization is in a rapid state of flux.[5] Although it seems likely that Henderson has identified a major effect, others[6,7] have argued that stimulated Raman scattering is dominant and that longer wavelengths are more affected. The findings of Eimerl[8] and Forslund[9] do not substantiate such dominance. Both find errors in work yielding large Raman effects, and Forslund asserts that simulations at LASL have shown that stimulated Raman plasmon scattering saturates at a very low light level. Therefore, although Raman scattering seems at present to be negligible, it is evicent that a complete, reliable, uncontentious, theoretical resolution of the behaviour of high-energy laser beams that are highly focused to extreme intensities in a gas, requires considerable study that will not be completed in the near future. Indeed, generally, the multitudinous processes of the interaction of plasmas with laser light are far from being completely understood and these are but a part, albeit the major part, of the transmission problem.

Because theory is unlikely to provide the needed answers soon, we examine a direct experimental approach. Our experimental requirements appear minimal and the results would be directly useful. We need only to learn how much laser energy from a focused beam can be transmitted through a pinhole as a function of chamber gas type and density. Unscrambling of each of the effects is of course necessary for a full understanding and for optimum, knowledgeable planning, especially for the most innovative and efficient compensation of beam degradation. (We can optically compensate to some extent for defocusing and scattering, for example.) However the immediate need is only for measurement of beam total transmission through an aperture representing a pellet target. Conceptually this is the simplest measurement to make.

Unfortunately the laser intensities considered for commercial design are only now being approached

by the largest lasers. Because the effects are intensity, fluence, and distance dependent one cannot mock up the effects expected at commercial intensities with a small off-the-shelf laser.

Typical parameters[10] for a single chamber of a 1000-MWe power plant are output of 100 MJ/pulse per chamber, 1 MJ per chamber input in 8 beams of 0.135 MJ each. Beam fluence is 10 J/cm^2; beam diameter is 1.4 m. Two optical designs are considered. One involves a final flat turning mirror, which has the advantages of a lower cost last optical surface, a more easily shielded surface, and having the capacity to correct pointing errors without abberation, but has the disadvantage of an additional optical surface in the laser train. This system might have a focusing optic as long as f = 15, f-number 10.7 together with a plane turning mirror 6 m from the pellet. The second system has the pointing and focusing optic combined in a final focusing mirror of focal length f = 6 m, f-number = 4.28. The former, for a perfect Gaussian beam, leads to a spot diameter of 72 μm, or for X4 diffraction limited spot of 288-μm diameter. The latter system would have a (Gaussian beam) minimum spot diameter of 29 μm, and for X4 diffraction limited of 116-μm diameter. For commercial pellets we anticipate a need to focus to a diameter of 1 mm (1000 μm). Thus, at that diameter the average fluence is 1.7×10^7 J/cm^2, and at 1-ns pulse length the intensity is 1.7×10^{16} W/cm^2.

Ideally, we would prefer the transmission experiment to have the same f-number and intensity, although not necessarily the same energy, in order that the same distances are allowed for development of the effects. Otherwise theoretical extrapolation must be used and that route is subject to all the uncertainties heretofore described, although of a lower order. At present we can approach f/4.3 optics and 1.7×10^{16} W/cm^2, but not f/10.7 *and* that intensity.

Required therefore are a large laser, about a kilojoule or more, and beam qualities of 2X diffraction limited or better to barely reach the parameter space of interest. Consequently, the transmission experiment will require (1) a large laser, (2) upgrading of the laser final optics particularly salt windows, if used, (3) a test chamber to contain gas, (4) gas flow and control plumbing, (5) irises, and (6) a total energy detector. When irises are used some lasers, with present technology, will have to operate at reduced intensity because of possible parasitics.

We envision that the experiment is performed as follows: the laser beam final focusing optic is placed as close to the gas-filled region as possible. The beam is focused to the desired intensity within the gas on to an iris if used (destructable) and then followed by a total energy detector located at or behind the focus. As a first objective, an intensity equivalent to that in the commercial reactor (see above) should be striven for. Then long focal lengths should be investigated. In the absence of focal lengths not quite as long as the commercial system, but achieving the same intensity, careful observation may enable good extrapolation over modest f-number differences. Effects at the highest intensity can be compensated somewhat by moving the detector behind the effective waist and thus obtaining a longer high intensity region, for the waist expands slowly. The iris is used to determine the precise energy transmitted through a given size hole. It is destroyed with each shot and may be made of several materials with the intent to evaluate some of the effects such as ponderomotive force and others. The results of interest for commercial reactor designs are the transmission of light through the selected iris aperture as a function of gas density. It is suggested to first use hydrogen, then neon, and argon as chamber gases. Then later, if warranted, measuring transmission for other gases, including lithium vapor.

Of next interest is the dependence of transmission on iris diameter near the gas type and density at which ransmission begins to be seriously affected. Such results will determine the possibility of, and the correction needed to, optically compensate for gaseous defocusing.

ECONOMIC MODELING FORTRAN PROGRAM INDEXER (J. H. Pendergrass)

Introduction

The program INDEXER has been developed to automate the computation of composite cost indexes used for projecting currently known or estimated costs of conventional, advanced thechnology, or conceptual facilities into the future. The availability of composite indexes greatly reduces the effort required

to obtain accurate cost updates while the extrapolation of their values into the future is necessary to obtain meaningful cost estimates for long-range projects. The cost indexes devised and calculated with INDEXER will be used to periodically update and predict capital, operating, and maintenance costs of conceptual laser fusion facilities for the generation of electric power, production of synthetic fuel or process heat, or for other applications.

A cost index is the ratio of the current cost of an item (i.e., a plant, a unit of a craft labor, a unit of a raw or finished material, a piece of equiment, etc.,) to its cost at some reference time multiplied by 100. Thus,a value greater than 100 corresponds to an increase in cost relative to its cost at the reference time and a value less than 100 to a decrease in cost. A composite cost index is a weighted, normalized sum of component indexes, i.e., indexes considered more basic in some sense. A value of a composite index is representative of the cost of the item composed of the components whose cost variations are represented by the component cost indexes and which contribute to the cost of the composite item in the proportions indicated by the weighting factors.

The effects of the changes in productivity on the costs are specified with productivity factors. A productivity factor is a divisor of a cost index which modifies its value to reflect the changes in productivity. Thus productivity values greater than one resulting from the introduction of superior techniques, acquisition of new machinery and equipment or experience lower the cost index values. Productivity factors less than one resulting from, for example, more restrictive work rules for reasons of health, safety, or environmental protection increase the cost index values.

Capabilities of INDEXER

Program INDEXER can be used to compute monthly, quarterly, or yearly values of composite cost indexes for arbitrary sequences of these time periods within the range of the data base provided for it. Users of INDEXER can specify that a set of weighting factors be used through the time period for which the composite indexes are to be computed or that the weighting factors be automatically adjusted to account for changes with time in the relative importance of the costs of component items.

Users can also add their own monthly, quarterly, or yearly cost index values to the data base provided for INDEXER and can alter rference values and reference times for both component and composite indexes.

Quarterly and yearly component index values provided by users are automatically distributed over the months included in each quarter and year, respectively. To reduce the amount of input data which users must supply, default values are provided for some of the input parameters when available information does not justify great detail. Various data input options are also provided.

In addition to computed composite index values, an automatic echo check on new input data is provided and, at user option, any part of the data base for INDEXER, whether or not used in computing composite index values can be output for arbitrary periods of time for which values are available in the data base.

Data Base for INDEXER

INDEXER data base contains several hundred cost indexes obtained directly from or computed on the basis of data published in:

- Bureau of Labor Statistics, *Wholesale Price Indexes*
- Bureau of Labor Statistics, *Monthly Labor Review*
- Bureau of Labor Statistics, *Earnings and Employment*
- McGraw - Hill, *Chemical Engineering*
- McGraw - Hill, *Oil and Gas Journal*
- McGraw - Hill, *Engineering News Record*
- Engineers Joint Council Engineering Manpower Commission Engineering Salary Surveys.

Wherever the information necessary for conversion of the cost index values in the data base to the common reference, which is the average for 1967, was available, the conversions have been made. Otherwise, the reference value is that which was associated with the cost index in the original source. In general, the latter category includes indexes for which values were not published before 1967. The time period presently covered by the data base, except for indexes for which values were not used before 1970, is January 1970 to May 1977. Periodic updating of the data base is planned.

Summary of the Composite Cost Index Computation

The INDEXER calculation of composite index values with constant weighting is summarized below:

- Monthly Index Values:

$$I_{C,M,k} = \sum_{n=1}^{N}\left[\frac{(\omega_n I_{M,n,k})}{(\sum_{n=1}^{N}\omega_n)(I_{C,R} I_{R,n} P_{C,k} P_{n,k})}\right].$$

$k = 1, \ldots, K$

$I_{C,M,k}$ = value of monthly composite index for $k^{\underline{th}}$ month, $k = 1, \ldots, K$

$I_{M,n,k}$ = value of $n^{\underline{th}}$ monthly component index, $n = 1, \ldots, N$, for $k^{\underline{th}}$ month, $k = 1, \ldots, K$

$I_{C,R}$ = reference value for composite index

$I_{R,n}$ = reference value for $n^{\underline{th}}$ component index, $n = 1, \ldots, N$

ω_n = constant weighting factor for $n^{\underline{th}}$ component index, $n = 1, \ldots, N$

$P_{C,k}$ = productivity factor for composite index for $k^{\underline{th}}$ month, $k = 1, \ldots, K$

$P_{n,k}$ = productivity factor for $n^{\underline{th}}$ component index, $n = 1, \ldots, N$, for $k^{\underline{th}}$ month, $k = 1, \ldots, K$

- Quarterly Index Values:

$$I_{C,Q,j} = \left[\sum_{k=3j-2}^{3k} I_{C,M,k}\right]/3, \quad j = 1, \ldots, J$$

$I_{C,Q,j}$ = value of quarterly composite index for $j^{\underline{th}}$ quarter, $j = 1, \ldots, J$

- Yearly Index Values:

$$I_{C,Y,i} = \left[\sum_{k=12i-11}^{12i} I_{C,M,k}\right]/12, \quad i = 1, \ldots, I$$

$I_{C,Y,i}$ = value of yearly composite index for $i^{\underline{th}}$ year, $i = 1, \ldots, I$

The automatic updating of initial component cost index weights is summarized below:

- Normalized cost of $n^{\underline{th}}$ component item, $n = 1, \ldots, N$, during $k^{*\underline{th}}$ month, $k^* = 1, \ldots, K$:

$$I_{M,n,k^*}/(I_{R,n} P_{n,k^*})$$

- Contribution of normalized cost of $n^{\underline{th}}$ component item, $n = 1, \ldots, N$, to normalized cost of composite item (without composite item reference value and productivity conversions) during $k^{*\underline{th}}$ month, $k^* = 1, \ldots, K$ (where ω_n, $n = 1, \ldots, N$, are weighting factors appropriate for $k^{*\underline{th}}$ month):

$$\frac{[\omega_n][I_{M,n,k^*}]}{(\sum_{n=1}^{N}\omega_n)(I_{R,n} P_{n,k^*})}$$

- Normalized cost of $n^{\underline{th}}$ component item, $n = 1, \ldots, N$, during $k^{\underline{th}}$ month, $k = 1, \ldots, K$:

$$I_{M,n,k}/(I_{R,n} P_{n,k})$$

- Updated contribution of normalized cost of $n^{\underline{th}}$ component item, $n = 1, \ldots, N$, to normalized cost of composite item (without composite item reference value and productivity conversions) during $k^{\underline{th}}$ month, $k = 1, \ldots, K$:

$$\frac{(\omega_n |I_{M,n,k}/P_{n,k}|/|I_{M,n,k^*}/P_{n,k^*}|)(I_{M,n,k})}{(\sum_{n=1}^{N}\omega_n |I_{M,n,k}/P_{n,k}|/|I_{M,n,k^*}/P_{n,k^*}|)(I_{R,n} P_{n,k})}$$

ELECTROTHERMOCHEMICAL HYDROGEN PRODUCTION BY WATER-SPLITTING USING LASER FUSION REACTORS AS THE SOURCE OF HIGH-TEMPERATURE PROCESS HEAT (J. H. Pendergrass and L. A. Booth)

Introduction

The primary goal of the fusion programs of the DOE is commercial electric power production. However, about 75% of the energy consumption in the United States is for space heating, industrial

process heat, and transportation. Consequently, a major mismatch between production capacities for required and desired energy forms and demands for these energy forms may develop if fusion reactors are not also adapted to satisfy nonelectrical needs directly. Therefore, it is important that potential uses for fusion-generated energy other than electric power production for direct transmission and distribution be identified and their feasibility be assessed. The potential utility of fusion-generated energy for the manufacture of synthetic fuels as substitutes for the use of our dwindling supplies of oil and natural gas is especially important. Among these fuels hydrogen is of particular interest.

Hydrogen produced by water-splitting using fusion-generated energy has many potential uses, including:

- a chemical feedstock for synthetic fuel production by coal liquefaction and gasification, for ammonia production, for metal-ore reduction, and for other industrial chemical processes;
- a primary transportable fuel;
- an energy storage medium for electrical energy generation systems when used in fuel cells.

The supply of the basic fuel, deuterium, for fusion reactors and the supply of the raw material, water, for hydrogen production by water-splitting are, for practical purposes, inexhaustible. In addition, water from which hydrogen is liberated is returned to the hydrosphere when hydrogen or synthetic fuels made with hydrogen are burned. The use of hydrogen as a primary transportable fuel and the generation of electricity by fusion power plants would allow the remaining supplies of fossil fuels to be used primarily as feedstock for the organic chemicals industry.

The first generation of fusion reactors will use tritium (T) and deuterium (D) as fuels because the conditions for efficient thermonuclear burn are least extreme for this fuel combination. The energy forms characteristic of fusion reactors that burn tritium and deuterium are x rays, high-temperature plasmas, and high-energy (14 MeV) neutrons. The neutrons, which carry approximately 80% of the energy released by the fusion reactions, can penetrate thin reactor structural members with little energy loss and hence can be utilized in blanket regions essentially independent of reactor cavity constraints. The potential availability of the major fraction of total energy release outside reactor cavities is a unique characteristic of DT-burner fusion reactors.

Evaluations have been made of the potential for producing hydrogen or methane by direct radiolytic decomposition of water or carbon dioxide.[11] The results of these studies indicate that for commercial feasibility, conversion efficiencies for these processes must be higher by a factor of 2 to 3 than available experimental values indicate can be achieved. However, application of laser fusion reactors in combination with selected thermochemical cycles appears more promising.

A recent evaluation of fusion energy applied to synthetic fuel production recommends further studies of hydrogen production by high-temperature electrolysis, by thermochemical cycles, or by combined electrothermochemical processes.[12] Our studies will include these processes and, to date, we have concentrated on a combined electrothermochemical cycle described below.

For this cycle we have developed a conceptual design of a very simple, nonbreeding laser fusion process heat source, which consists of a graphite blanket to absorb fusion-born neutrons and radiate thermally with surface temperatures in excess of 2000 K to process heat tubes.[13]

We have also made a preliminary evaluation of the use of thermionic direct-conversion topping cycles to produce low-voltage, direct-current electricity for electrochemical processing.[14] The results of this study indicate that very high overall efficiencies can be obtained for fusion plants producing both direct current for electrolysis and conventional alternating current for power grid transmission and distribution.

Electrothermochemical Cycle

The approach adopted by LASL to develop practical cycles for hydrogen production from water has been to verify proposed reaction schemes by experiment. This verification includes careful determinations of reaction rates and equilibria, as well as the thermochemistry and electrochemistry for each reaction step in the cycle under a wide variety of operating conditions. Many potentially useful cycles have proved to be infeasible upon experimental examination of kinetics, equilibria, energetics, etc.

The experimental work is being conducted by LASL and is supported by other DOE offices. A portion of this effort is directed toward identification of potential thermochemical cycles using temperatures of 1500-2000 K from fusion reactor heat sources.

After demonstration of a cycle's scientific feasibility, a preliminary engineering analysis is attempted to evaluate cycle thermal efficiency and economics. Further experimentation is carried out to optimize cycles that still appear promising, with cost of hydrogen production as the principal figure of merit. Typically, enhanced yields at each reaction step, which means less energy expenditure per unit of product, and increased reaction rates, which results in lower residence time requirements and hence lower capital costs for equipment, contribute to low production cost.

If a cycle appears promising after the initial evaluation which has been described, the next phase would involve a bench-scale, closed-loop test to provide data for more realistic engineering and cost analyses. At the same time, an attempt would be made to match the electrical and thermal energy requirements of the cycle to the delivery capabilities of fusion ractors for these forms of energy.

The conceptual electrothermochemical (hybrid) cycle presently under development will be subjected to the evaluations described above. To drive the cycle, we will develop appropriate fusion reactor blanket and heat transport systems concepts. The hybrid cycle may be characterized by the following reactions. A low-temperature heat-rejecting, water-absorbing, electrochemical reaction step is

$$SO_2(g) + 2\ H_2O(\ell) \rightleftharpoons H_2SO_4(aq) + H_2(g).$$

The low-temperature, heat-rejecting precipitation step is the reaction

$$H_2SO_4\ (aq) + 1/3\ \text{metal oxide}(s) \rightleftharpoons 1/3\ \text{metal oxide sulfate}(s) + H_2O\ (\ell).$$

For the present study, the metal oxide being considered is Bi_2O_3 and the metal oxide sulfate is $Bi_2O_3.3SO_3$. The next reaction step, or steps, involves high-temperature, endothermic decomposition of the metal oxide sulfate and further decomposition of evolved SO_3.

$$1/3\ Bi_2O_3.3SO_3(s) \rightleftharpoons 1/3\ Bi_2O_3(\ell) + SO_2(g) + 1/2\ O_2(g).$$

To complete the cycle the $SO_2(g)$ and $1/2\ O_2(g)$ must be cooled rapidly to prevent back reaction and the $O_2(g)$ separated. For cycle efficiency, latent and sensible heat must be recovered from Bi_2O_3 and from the hot gaseous products.

A principal reason for introducing the metal oxide into the cycle is the potential for eliminating the large amounts of heat required for dehydration of sulfuric acid characteristic of the Westinghouse sulfuric acid hybrid and the General Atomic sulfuric acid iodine cycles. In the presence of metal oxide the separation is effected by precipitation of the solid metal oxide sulfate from a relatively low concentration sulfuric acid solution rather than by evaporation of water from a sulfuric acid solution up to concentrations approaching 100%. A preliminary evaluation of the energy efficiency of the bismuth oxide sulfate cycle relative to the sulfuric acid hybrid cycle adopted by Westinghouse for conceptual commercialization suggests that the bismuth oxide sulfate cycle offers a potential gain in efficiency of 12%. The introduction of the metal oxide has other potential benefits. For example, $Be_2O_3{\cdot}3SO_3$ decomposes by release of consecutive SO_3 molecules with increasing temperatures yielding a series of metal oxide sulfates terminating in Bi_2O_3 itself. The SO_3 pressure in equilibrium with $Bi_2O_3.2SO_3$ is 1 atm at ~860 K and the SO_3 pressure in equilibrium with $Bi_2O_3SO_3$ is 1 atm at ~1050 K, with final decomposition to Bi_2O_3 and SO_3 occurring at higher temperature. The option of generating SO_3 over a range of temperatures, i.e., of accepting large amounts of reaction heat, rather than smaller amounts of sensible heat, over a range of temperatures, may permit more efficient matching of cycle thermal energy requirements to laser fusion reactor thermal energy delivery characteristics.

The temperatures required for favorable equilibria between SO_3 and Bi_2O_3 are adequate for virtually complete decomposition of SO_3 to SO_2 and O_2, e.g.,

at 1500 K, SO_3 is ~ 99.8% decomposed to SO_2 and O_2.

However, the introduction of the metal oxide into the cycle also introduces an unusual engineering problem. For an efficient cycle, significant sensible heat and latent heat of fusion and of solid-phase transformation must be recovered from the Bi_2O_3 decomposition reaction product, which melts at ~ 1100 K, well below the 1500 K maximum cycle temperature presently being considered, and undergoes several crystalline transformations in the solid state upon being cooled to room temperature. Nonetheless, engineering problems presently do not appear to be insurmountable.

Principal criteria for selection of the particular metal oxide to be used in such a cycle are that the sulfate formed should have a low solubility and should be anhydrous under conditions of interest. A literature survey indicated that both bismuth and antimony, which will also be investigated in the future, form sulfate precipitates which satisfy these criteria.

Perhaps the most important unknowns at present are the rates at which the bismuth oxide sulfate decomposition reactions occur. Experiments to obtain these data are planned by the high-temperature chemistry group at LASL.

High-Temperature Laser Fusion Reactor Blanket Concepts

Two fundamental concepts have been selected for detailed study during the first phase of the investigation. The first of these is illustrated schematically in Fig. VII-7. Preliminary neutronics studies indicate the following.

- The use of a lead neutron multiplier region, (lead is identified as the most promising nonfissioning multiplier material with beryllium having been eliminated from consideration at present), is less effective than an equivalent thickness of natural lithium with respect to both tritium breeding and the fraction of the initial fusion neutron energy which passes through to the high-temperature blanket region.
- Pure lithium in the tritium breeding region is more effective with respect to breeding of tritium than are mixtures of lead and lithium, but the the lead-lithium mixtures allow deposition of more of the neutron energy in the high-temperature blanket region.
- Less than 50% of the initial neutron energy can be deposited in the high-temperature blanket region if breeding ratios of one or greater must be achieved.

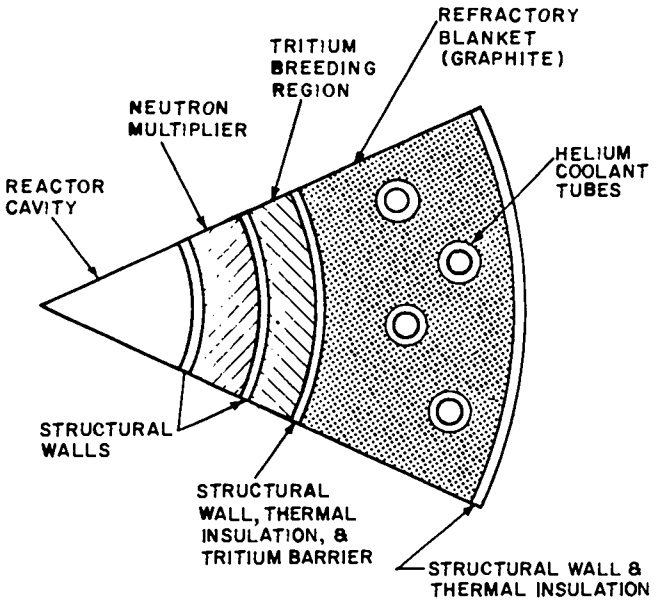

Fig. VII-7.
Helium-cooled, high-temperature refractory-blanket fusion reactor concept (first-wall protection concept yet unspecified).

In spite of the potentially lower efficience as a source of thermal energy for hydrogen production implied by the last of these conclusions, this concept will be investigated in greater detail because

- it involves smaller extrapolation of technology from the present state of the art, and
- much of the fusion-generated thermal energy must be used to generate electrical power to operate the plant and for the electrolytic steps, therefore, the use of lower temperature heat recovered from the lower temperature region of the blanket to generate electricity in a conventional steam cycle may still prove to be cost effective.

We have also developed the basic ideas for a blanket concept, which we believe will permit achievement of breeding ratios in excess of unity while permitting all but the small fraction of the

neutron energy deposited in reactor structural members to be transformed into thermal energy at temperatures in excess of 1500 K. Such a concept would result in high efficiencies in generation of electricity and in utilization of thermal energy.

The primary obstacles to application of this concept appear to be in the realm of materials properties rather than heat transfer, tritium breeding, tritium recovery, escape prevention, product contamination, etc. However, we do not believe that these problems are insurmountable or even require great advances in materials technology.

REFERENCES

1. I. O. Bohachevsky, "Scaling of Reactor Cavity Wall Loads and Stresses," Los Alamos Scientific Laboratory report LA-7014-MS (November 1977).

2. D. B. Henderson, "Pulse Unfocusing within Laser-Fusion Reactors," Nucl. Eng. Design **30**, 111 (1974).

3. L. V. Keldysh, "Ionization in the Field of a Strong Electromagnetic Wave," Sov. Phys. JETP **20**, 1307 (1965).

4. T. B. Bystrova, "Multiphoton Ionization of Xenon and Krypton Atoms at Wavelength $\lambda = 1.06\mu$," JETP Pis'ma **5**, 223 (April 1967).
   Also U. Devi and M. Mohan, "Raman Processes in the Case of Multiphoton Excitation of an Helium Atom in an Intense Laser Beam," Phys. Lett **57A**, 38 (1976).

5. P. Lambropoulos, "Topics on Multiphoton Processes in Atoms," Adv. Atom. Mol. Phys. **12**, 87 (1976).

6. M. Sparks and P. N. Sen, "Possible Reduction of Laser Fusion Target Illumination by Enhanced Stimulated Raman Plasmon Scattering," Phys. Rev. Lett. **39**, 751 (1977).
   M. Sparks, "Optical Studies in Commercial Laser-Fusion Systems," Sonics Inc. informal report (November 1977).

7. J. J. Thompson, "Stimulated Raman Scatter in Laser Fusion Target Chambers," Bull. Am. Phys. Soc. **22**, 1138, 5E4 (1977).

8. D. Eimerl, "Enhanced Stimulated Raman Scattering Does Not Exist," University of California Radiation Laboratory report UCRL-80161 (October 1977).

9. D. W. Forslund, Los Alamos Scientific Laboratory, personal communication, November 1977.

10. J. Devaney, Los Alamos Scientific Laboratory internal document, September 1974.

11. E. Stark and F. Skoberne, "Laser Fusion Program," Los Alamos Scientific Laboratory report LA-6510-PR, (November 1976) (pp 120-122).

12. L. A. Booth, "Fusion Energy Applied to Synthetic Fuel Production" DOE Report CONF-770593, October 1977.

13. E. Stark and F. Skoberne, "Laser Fusion Program," Los Alamos Scientific Laboratory report LA-6245-PR (July 1976) pp. 107-109.

14. T. G. Frank, E. A. Kern, and L. A. Booth, "Commercial Application of Thermionic Conversion Using a Fusion Reactor Source" (A Preliminary Assessment) Los Alamos Scientific Laboratory report LA-6621-MS, (January 1977).

VIII. RESOURCES, FACILITIES, AND OPERATIONAL SAFETY

The design and construction of HEGLF Facilities continued. Safety policies and procedures continued to be applied successfully to minimize the hazards of operating high-energy lasers.

MANPOWER DISTRIBUTION

The distribution of employees assigned to the various categories of the DOE-supported Laser Fusion Research Program is shown.

APPROXIMATE STAFFING LEVEL OF LASER PROGRAM

DECEMBER 31, 1977

Task	Direct Employees (Actual)
CO_2 Laser Development	147
CO_2 Laser Experiments	55
Pellet Design	26
Pellet Fabrication	32
Diagnostics Development	29
Systems and Advanced Technology	12
Total	301

OPERATIONAL SAFETY

General

Historically, the Laser Fusion Research activities have never produced biological damage to any employee from laser radiation. This record continued. The special Laser Electrical Safety Committee continued inspection of electrical facilities. The development of laser protective eyewear for prescription specifications from Schott Optical Glass Co. color filter glass was continued.

FACILITIES

The following are summaries of present construction activities; in the interest of continuity, however, we have presented details in Section II.

High-Energy Gas Laser Facility

Construction Package-I work was started in September 1977. Included in this package are the laser building, mechanical building, office building, and warehouse. Earthwork and exterior utilities work are on schedule.

Construction Package-II, comprising mainly the target building, was awarded in December 1977.

Optical Evaluation and High-Voltage Laboratories

The construction contract for these two laboratories was awarded in December 1977.

IX. PATENTS, PRESENTATIONS, AND PUBLICATIONS

PATENT ISSUED

U.S. Pat. 4 038 125, issued July 26, 1977. "Method for Mounting Laser Fusion Targets on Thin Plastic Film," R. Jay Fries, Eugene H. Farnum.

APPLICATION FILED

S. N. 838 011, filed September 29, 1977, "Method for More Efficient Energy Extraction from Gas Laser Amplifiers," Eugene E. Stark, John F. Kephart, Wallace T. Leland, and Walter H. Reichelt.

PRESENTATIONS

The following presentations were made at the Nineteenth Annual Meeting, Plasma Physics Division of the American Physical Society, at Atlanta, Georgia, November 7-11, 1977.

M. M. Mueller, "New Optical Diagnostic Methods for Determining Profiles in Spherical or Quasi-Planar Plasmas."

A. H. Williams and T. H. Tan, "Imaging of Fast Ions from Laser Irradiated Targets."

K. B. Mitchell and J. V. Parker, "X-Ray Experiments on 10 μm Produced Plasmas."

A. W. Ehler and J. P. Carpenter "Ion Impulse Measurements."

T. H. Tan, D. Giovanielli, G. H. McCall, and A. H. Williams, "Plasma Expansion and Electron Preheating."

J. L. Shohet, D. B. vanHulsteyn, and P. Lee, "Stark Broadening of Hydrogen-Like and Helium-Like Transitions in CO_2 Irradiated Targets."

R. J. Mason, "Hot Electron Transport in Laser Produced Plasmas," also presented at the Eleventh European Conference on Laser Interaction with Matter, Oxford, England, September 17-23, 1977.

D. B. Henderson, "The Brightening Outlook for CO_2 Laser Fusion."

D. W. Forslund, J. M. Kindel, and K. Lee, "Hot Electron Generation in Resonant Absorption."

R. H. Day, P. Lee, D. vanHulsteyn, and T. E. Elsberry, "X-Ray Diodes for Laser Fusion Plasma Diagnostics."

R. L. Benjamin, D. B. Henderson, K. B. Mitchell, M. A. Stroscio, and J. Thomas, "Laser Target Retropulse Isolation Using an Aperture in Vacuum."

F. Young and G. H. McCall, "Measurement of Charged Particle Velocity and Population Distributions in Laser Produced Plasma Experiments."

P. Lee, D. B. vanHulsteyn, and R. H. Day, "Low-Energy X-Ray Emission Studies from Fusion Plasma."

D. B. vanHulsteyn, P. Lee, G. N. Minerbo, and J. G. Sanderson, "Three Dimensional Imaging of Laser Imploded Targets."

M. M. Mueller, "A New Optical Diagnostic Method for Determinating Profiles in Quasi-Planar Plasmas."

T. H. Tan, D. V. Giovanielli, G. H. McCall, and A. H. Williams, "Plasma Expansion and Electron Preheating."

A. H. Williams and T. H. Tan, "Imaging of Fast Ions from Laser Irradiated Targets."

V. M. Cottles, "Measurements of Absorption and Ion Production in Laser Fusion."

A. W. Ehler, "Ion Impulse Measurements."

K. B. Mitchell and J. V. Parker, "X-Ray Experiments on 10μm Produced Plasmas from Glass Microspheres."

M. A. Stroscio and E. L. Lindman, "Relativistic Derivation of Laser Induced Plasma Profiles."

K. Lee, "Comparison of Multigroup Diffusion and Monte Carlo Electron Transport."

D. W. Forslund, B. Bezzerides, and D. DuBois, "Calculation of Hot Electron Distributions in Resonant Absorption by Method of Characteristics."

B. R. Wienke, W. F. Miller, Jr., and K. Lee, "Electron Transport with Discrete Ordinates."

S. J. Gitomer, "Modeling of Layered Target Experiments," Simulation of Layered Target Experiments," "Hydrodynamic Stability of Laser-Driven Ablative Implosions."

J. M. Kindel, D. W. Forslund, and E. L. Lindman, "Critical Surface Rippling."

R. J. Fries, E. H. Farnum, and R. J. Mason, "Conical Targets for CO_2 Implosion Studies."

W. E. Gula and T. E. Thode, "Relativistic Electron Beam Heating of a 10^{16}-10^{20} cm^{-3} Plasma."

E. L. Lindman and J. M. Kindel, "Inertial Fusion Using Fast Ions."

The following presentations were made at the American Nuclear Society 1977 Winter Meeting, San Francisco, California, November 27-December 2, 1977.

T. G. Frank and L. A. Booth, "A Characterization of Laser Fusion Reactor Concepts."

L. A. Booth and I. O. Bohachevsky, "Requirements for Commercialization of Inertial Confinement Fusion."

I. O. Bohachevsky, "Thermonuclear Fusion Device LIME."

The following presentations were made at the AIChE Annual Meeting Symposium of Engineering Aspects of Laser Fusion, New York City, New York, November 13-17, 1977.

J. H. Pendergrass and L. A. Booth, "Chemical Engineering Aspects of the Tritium Fuel Cycle for Laser Fusion Reactors."

R. J. Fries, "Fabrication of Targets for the Los Alamos Laser Fusion Program."

The following presentations were made at the Gordon Research Conference on Laser Interaction with Matter, Tilton, New Hampshire, August 8-12, 1977.

D. V. Giovanielli, G. H. McCall, and T. H. Tan, "Laser-Plasma Interactions and Compression Experiments at 10.6μm." Also presented at the Eleventh European Conference on Laser Interaction with Matter, Oxford, England, September 19-23, 1977.

J. R. Miller, "Cryogenic Laser Fusion Targets."

R. J. Mason, "Design of Targets for CO_2 Lasers."

J. M. Kindel, "Light Pressure Effects in Laser Produced Plasmas."

E. L. Lindman, "Ion Driven Implosions."

The following presentations were made at the 1977 Fall Meeting of the Optical Society of America, Toronto, Canada, October 10-14, 1977.

D. R. Kohler and P. B. Weiss, "Measurements at 10.6 Microns with Pyroelectric Vidicon," and "Characterization of Pyroelectric Vidicons for Use with Pulsed CO_2 Lasers."

G. Lawrence, (Optical Sciences Center, University of Arizona Optical Science Center), I. Liberman, and V. K. Viswanathan, "Optical Analysis of the LASL 10 KJ CO_2 Laser Fusion System."

G. Lawrence, (Optical Sciences Center, University of Arizona Optical Science Center), and J. L. Munroe, "Effects of Window Segmentation on the LASL 100-kJ Laser-Fusion System."

K. C. Jones and J. L. Munroe, "Optical Design of a 100-kJ CO_2 Laser-Fusion Systems."

J. L. Munroe and K. C. Jones, "Optical Performance Calculations for a 100-kJ CO_2 Laser-Fusion System."

W. C. Turner, "Metallurgical Engineering Consideration for the 100-kJ CO_2 Laser."

J. E. Sollid, "Reflection Suppression for a High-Gain CO_2 Laser System."

R. R. Williamson and J. L. Munroe, "Optical Component Requirements for a 100-kJ CO_2 Laser Fusion System.

B. J. Feldman and R. A. Fisher, "Ultrashort CO_2 Laser Pulse Generation Using a Fabry-Perot Interferometer."

The following presentations were made at the Eleventh European Conference on Laser Interaction with Matter, Rutherford Laboratory, Oxford, England, September 19-23, 1977.

T. H. Tan, V. M. Cottles, D. V. Giovanielli, G. H. McCall, A. Williams, and F. Young, "CO_2 Laser Target Interaction Experiments."

D. V. Giovanielli, T. H. Tan, A. W. Ehler, G. H. McCall, A. Williams, D. vanHuylsteyn, and D. Bannerman, "Implosion Experiments Using the High Power CO_2 Laser System at LASL."

S. J. Gitomer, B. S. Newberger, A. J. Scannapieco, and R. L. Morse (University of Arizona), "Hydrodynamic Stability of Laser-Driven Ablative Implosions."

D. B. Henderson, S. J. Gitomer and R. N. Remund, "Laser-Fusion Interactions in a Self-Consistent Classical Light."

C. Cranfill, G. S. Fraley, S. J. Gitomer, D. B. Henderson, J. Kindel, R. Kopp, E. L. Lindman, E. Linnebur, and R. J. Mason, "CO_2 Laser Target Interaction Simulations at Los Alamos."

The following presentations were made at the Tenth International Quantum Electronics Conference, Atlanta, Georgia, December 19, 1977.

B. J. Feldman, R. A. Fisher, C. R. Pollock, S. W. Simons, and R. G. Tercovich, "Intense Sequence-Band and Hot-Band Lasing in a Atmosphere CO_2 Double Discharge."

E. J. McLellan, "A Reinjection CO_2 Oscillator."

The following presentations were made at the Seventh Symposium on Engineering Problems of Fusion Research, Knoxville, Tennessee, October 25-28, 1977.

K. B. Riepe, M. J. Kircher, "Design of the Energy Storage System for the High Energy Gas Laser Facility at LASL."

W. T. Leland, J. T. Ganley, M. Kircher, and G. W. York, Jr., "Large-Aperture Discharges in E-Beam-Sustained CO_2 Amplifiers."

J. Jansen and V. L. Zeigner, "Design of the Power Amplifier for the HEGLF at LASL."

D. B. Henderson. "Laser Fusion Interactions in a Self-Consistent Classical Light," Eleventh International Symposium on Shock-Tubes and Waves, Seattle, Washington, July 11-14, 1977.

In addition, the following presentations were made at various institutions.

J. R. Miller, "A New Method for Producing Cryogenic Laser Fusion Targets," 1977 Cryogenic Engineering Conference, Boulder, Colorado, August 2-5, 1977.

L. E. Thode and W. P. Gula, "Inertially Confined Plasma Heating by a 10-50 MeV Electron Beam," Second International Topical Conference on High Power Electron and Ion Beam Research and Technology, Cornell University, Ithaca, New York, October 3-5, 1977.

G. H. McCall, "Ion Emission and Light Absorption Measurements on Laser-Produced Plasmas," II Conference on Hot Plasma Diagnostics, Kharkov, USSR, September 22-27, 1977.

A. W. Ehler and J. P. Carpenter, "Vacuum UV Spectrum of Laser Plasma," American Physical Society, Gaseous Electronics Division, Palo Alto, California, October 18-21, 1977.

K. Lee, "Physical Processes in Laser Induced Fusion," Dept. of Physics and Astronomy, University of Wyoming, July 22, 1977.

M. D. Bausman, I. Liberman, J. P. Manning, and S. Singer, "Alignment System for Large High-Power Pulsed CO_2 Laser Fusion Systems," Society of Photo-Optical Instrumentation Engineers 21st Annual Technical Symposium, San Diego, California, August 22-26, 1977.

A. T. Lowe and R. J. Fries, "Plasma Polymerized Pxylene as a Laser Fusion Target," IV Rolla Conference on Surface Properties of Materials, Rolla, Rolla, Missouri, August 1-4, 1977.

D. C. Winburn, "Fast-Pulse Laser Biological Damage Threshold Studies at Los Alamos Scientific Laboratory—An Overview," LIA Laser Exposition and Conference, Anaheim, California, October 1977.

D. W. Forslund, J. M. Kindel, K. Lee, and E. L. Lindman, "Whence Cometh the Anomalous Flux-Limit," Conference on Transport Processes in Laser Plasmas, Acadia National Park, August 3-5, 1977.

R. K. Ahrenkiel, "Infrared Faraday Rotation Materials," Seminar at Sandia, Albuquerque, New Mexico, November 1977.

J. E. Sollid, W. H. Reichelt, S. Singer, R. N. Shagam (Optical Sciences Center, University of Ariz.), and R. E. Sladky (UCC, Nuclear Div., Y-12, Oak Ridge, Tennessee), "Copper Mirrors for the LASL 10-KJ Eight-Beam CO_2 Laser: Figure and Surface Evaluation," OSA San Mateo Fabrication and Testing Workshop, San Mateo, California, November 10, 1977.

T. F. Stratton, and W. H. Reichelt, "Optical Design and Components for a 100-kJ CO_2 Laser," Society of Photo-Optical Instrumentation Engineers 21st Annual Technical Symposium, San Diego, California, August 22-26, 1977.

H. Jansen, "High-Voltage Power Technology, Rep-Rated Systems and PFN's," Informal talk given at the Air Force Studies Group sponsored by the National Academy of Sciences at Kirtland AFB, Albuquerque, New Mexico, July 26, 1977.

R. A. Fisher, B. J. Feldman, C. R. Pollock, S. W. Simons, and R. G. Tercovich, "Megawatt Operation of an (0, 0°, 2) → (1, 0°, 1) Sequence-Band High-Pressure CO_2 Laser," 13th Annual Gaseous Electronics Conference, Palo Alto, California, October 23, 1977.

R. J. Feldman, R. A. Fisher, C. R. Pollock, S. W. Simons and R. G. Tercovich, "An Intense High-Pressure Sequence-Band CO_2 Laser," 1977 Gordon Conference on Nonlinear Optics and Lasers, Plymouth, New Hampshire, August 18, 1977.

S. J. Czuchlewski, A. V. Nowak, and E. Foley, "An Efficient Gas Isolator for CO_2 10-μm P-Branch Laser Operation," Electro-Optics/Laser 1977 Conference, Anaheim, California, October 25-27, 1977.

R. P. Godwin, "Wavelength Scaling in Laser-Plasma Experiments" and "Recent Absorption Measurements at Garching", Rutherford Laboratory Seminar, August 1, 1977. Abingelon, U. K.

R. P. Godwin, P. Sachsenmaier, and R. Sigel, "Reflectometry of Laser-Produced Plasmas," Bull. Am. Phys. Soc. **22**, 1119 (1977). (American Physical Society Division Of Plasma Physics).

R. P. Godwin, "Wavelength Scaling in Laser-Plasma Experiments" and "Recent Absorption Measurements at Garching," AWRE Aldermaston Seminar, August 3, 1977. Reading, U. K.

R. P. Godwin, "Recent Abosrption Measurements at Garching," Gordon Conference on Laser-Plasma Interactions; August 8, 1977, Tilton, New Hampshire.

PUBLICATIONS

C. A. Javorsky and D. S. Catlett, "Laser Fusion Target Fabrication—Metallographic Characterization of Micro-Sized Particles," Proc. International Metallographic Society, Annual Technical Meeting, Seattle, Washington, (1976), pp. 259-72; Microstructural Science 5, J. D. Braun, Ed., Elsevier North-Holland (1977).

A. Lieber, H. D. Sutphin, and C. B. Webb, "Subpicosecond Proximity—Focused Streak Camera for X-Ray," High Speed Optical Techniques Seminar, M. A. Duguay, Ed., San Dieto, California (1976); Proc. S.P.I.E. 534/H638S (1977), pp. 7-12.

R. F. Benjamin, D. B. Henderson, K. B. Mitchell, M. A. Stroscio, and J. Thomas, "Laser-Target Retropulse Isolation Using an Aperture in Vacuum," Appl. Phys. Lett. **31**, (1977), pp. 511-512.

W. H. Reichelt, D. J. Blevins, and W. C. Turner, "Metal Optics in Carbon Dioxide Laser Fusion Systems," Opt. Eng. **16**, (1977), pp. 381-386.

R. W. Getzinger, K. D. Ware, J. P. Carpenter, and G. L. Schott, "Nanosecond Switching and Amplification of Multiline HF Laser Pulses," IEEE J. Quantum Electron **QE-13**, No. 4 (1977), pp. 97-100.

D. B. vanHulsteyn and R. F. Benjamin, "X Ray Shadowgraphing in Laser Produced Plasma Experiments," Opt. Lett. **1**, (1977), pp. 76-78.

K. C. Kim, J. P. Aldridge, H. Filip, H. J. Flicker, R. F. Holland, and N. G. Nereson, "Laser Spectroscopy," TIC (1975), 19 pp.

G. H. McCall, "X-Ray Imaging in the Laser Fusion Program," TIC (1977) 18 pp.

R. L. McCrory (non-LASL), R. L. Morse, (non-LASL), and K. A. Taggart, "Growth and Saturation of Instability of Spherical Implosions Driven by Laser on Charged Particle Beams," 41 pp. Nucl. Sci. Eng. **64**, (1977), pp. 163-176.

T. G. Frank and L. A. Booth, "Characterization of Laser Fusion Reactor Concepts," Trans. Am. Nucl. Soc. **27**, (1977) p. 32.

E. Stark and F. Skoberne, "LASL Laser Fusion Program, October 1-December 31, 1976," Los Alamos Scientific Laboratory report LA-6834-PR (1977) 117 pp.

M. A. Stroscio, "Structured Pellet Design for Laser Fusion—A Numerical Determination of the Optimum Mass Ratio," Los Alamos Scientific Laboratory report LA-6986-MS (1977) 3 pp.

R. A. Fisher and B. J. Feldman, "Generation of Single Ultrashort Carbon Dioxide Laser Pulses in a Fabry-Perot Interferometer," Opt. Lett. 1, (1977) pp. 161-163.

I. O. Bohachevsky, "Scaling of Reactor Cavity Wall Loads and Stresses," Trans. Am. Nucl. Soc. **27**, (1977) pp. 64-65.

L. A. Booth and I. O. Bohachevsky, "Requirements for Commercialization of Inertial Confinement Fusion," Trans. Am. Nucl. Soc. **27**, (1977) pp. 15-16.

R. L. Carman, A. G. Engelhardt, and N. Clabo, "Multiwave Picosecond Laser Interferometry of Carbon Dioxide," Laser Interaction and Related Plasma Phenomena **4B**, H. J. Schwarz, Ed. (Plenum Press, 1977) pp. 619-38.

T. H. Tan, G. H. McCall, A. H. Williams, and D. V. Giovanielli, TIC (1976) 12 pp. Related Plasma Phenomena **4B**, H. J. Schwarz, Ed. (Plenum Press, 1977) pp. 677-687.

T. G. Frank and L. A. Booth, "Remote Systems for Inertial Confinement Fusion Generating Stations," Trans. Am. Nucl. Soc. **27**, (1977) pp. 1011-1012; Proc. ANS Remote Systems Technology, 1977, 25th Conf., San Francisco, California, Wojoiechowski, Ed., 626/H832C 25th, (1977) pp. 307-314.

M. D. Bausman, I. Liberman, J. P. Manning, and S. Singer, "Alignment System for Large High-Power Pulsed Carbon Dioxide Laser Fusion Systems," S. P. I. E. Clever Optics **126**, (1977) pp. 23-31.

R. L. Carman, "Advanced Laser Technology for Laser-Induced Fusion Applications," TIC (1976) 34 pp. Proc. Laser Interaction and Related Plasma Phenomena, 1976, 4th Workshop, Troy, New York **4A**, H. J. Schwarz, Ed. (Plenum Press, 1977) pp. 43-66.

D. H. W. Carstens, "Tritium Handling and the Preparation of DT-Containing Micro-Targets for Laser Fusion Experiments," Proc. Laser Interaction and Related Plasma Phenomena, 1976, Workshop, Troy New York **4A**, H. J. Schwarz, Ed. (Plenum Press, 1977) pp. 317-331.

S. Singer, "Carbon Dioxide Laser Systems for Fusing Experiments," Proc. Laser Interaction and related Plasma Phenomena, 1976, Workshop, Troy New York **4A**, H. J. Schwarz, Ed. (Plenum Press, 1977) pp. 121-142.

B. J. Feldman, R. A. Fisher, C. R. Pollock, S. W. Simons, and R. G. Tercovich, "Intense High-Pressure Sequence-Band," Opt. Lett. **2**, (1978) pp. 16-18.

R. P. Godwin, P. Sachsenmaier, and R. Sigel, "Angle Dependent Reflectance of Laser-Produced Plasmas," Phys. Rev. Lett. **39**, 1198 (1977).

R. P. Godwin, C. G. M. vanKessel, J. N. Olsen, P. Sachsenmaier, R. Sigel, and K. Eidmann, "Reflection Lasers from Laser-Produced Plasmas, Z. Naturforsch **32**, 1100 (1977).

D. C. Winburn, "Lightweight, Comfortable, Prescription Spectacles for Use in Laser Laboratories," Los Alamos Scientific Laboratory Mini-Review, LASL-77-32, (December 1977).

D. C. Winburn, "Fast-Pulse Laser Biological Damage Threshold Studies at the Los Alamos Scientific Laboratory—An Overview," Electro-Optical Systems Design Magazine, (November 1977).

☆ U. S. GOVERNMENT PRINTING OFFICE 1978 — 677-907

Printed in the United States of America. Available from
National Technical Information Service
US Department of Commerce
5285 Port Royal Road
Springfield, VA 22161

Microfiche $3.00

001-025	4.00	126-150	7.25	251-275	10.75	376-400	13.00	501-525	15.25
026-050	4.50	151-175	8.00	276-300	11.00	401-425	13.25	526-550	15.50
051-075	5.25	176-200	9.00	301-325	11.75	426-450	14.00	551-575	16.25
076-100	6.00	201-225	9.25	326-350	12.00	451-475	14.50	576-600	16.50
101-125	6.50	226-250	9.50	351-375	12.50	476-500	15.00	601-up	

Note: Add $2.50 for each additional 100-page increment from 601 pages up.